Quantitative Analysis of Membrane Components using Super-Resolution Microscopy

Dissertation zur Erlangung des
naturwissenschaftlichen Doktorgrades
der Julius-Maximilians-Universität
Würzburg

vorgelegt von

Sebastian Letschert

geboren in Kassel

Würzburg, 2018

Eingereicht am: .....

Mitglieder der Promotionskommission:

Vorsitzender: .....

Gutachter: Prof. Dr. Markus Sauer

Gutachter: Prof. Dr. Jürgen Seibel

Tag des Promotionskolloquiums: .....

Doktorurkunde ausgehändigt am: .....

Zusammenfassung

Die Plasmamembran gehört zu den am meisten untersuchten, gleichzeitig aber auch zu den komplexesten, vielfältigsten und am wenigsten verstandenen biologischen Strukturen. Ihre Funktion wird nicht nur durch die molekulare Zusammensetzung bestimmt, sondern auch durch die räumliche Anordnung ihrer Bestandteile. Selbst nach Jahrzehnten intensiver Forschung und der Veröffentlichung dutzender Membranmodelle und Theorien bleibt die genaue strukturelle Organisation der Plasmamembran ein Rätsel. Moderne Bildgebungsverfahren wie etwa die hochauflösende Fluoreszenzmikroskopie gehören mittlerweile zu den effizientesten Techniken der Lebenswissenschaften und werden immer öfter verwendet, um die räumliche Anordnung als auch die Anzahl von Biomolekülen in fixierten und lebenden Zellen zu studieren. Im Rahmen dieser Arbeit wurde die hochauflösende Mikroskopie-Methode *d*STORM (*direct* stochastic optical reconstruction microscopy) angewendet, um die räumliche Verteilung von Membranmolekülen mit annähernd molekularer Auflösung zu untersuchen. Schwerpunkte dieser Arbeit sind dabei verschiedene Präparations- und Färbemethoden für die mikroskopische Untersuchung von Zellmembranen sowie lokalisationsbasierte quantitative Analysemethoden von Membranmolekülen.

Eine Voraussetzung für die räumliche als auch quantitative Analyse von Membranmolekülen ist die Vermeidung von Photoschalt-Artefakten in rekonstruierten Lokalisationsmikroskopie-Bildern. Um dies genauer zu demonstrieren, wurden die Auswirkungen von Anregungsintensität, Markierungsdichte und verändertem Photoschalten auf die räumliche Verteilung von Proteinen der Plasma- und Mitochondrienmembran in *d*STORM-Bildern analysiert. Es wird gezeigt, dass eine dicht markierte Plasmamembran in Kombination mit ungeeigneten Photoschaltraten zu artifiziellen Clustern in der Membran führt. Es sind vor Allem oft die Projektionen dreidimensionaler Membranstrukturen wie etwa Mikrovilli und Vesikel dafür verantwortlich, dass lokale Unterschiede in der Lokalisationsdichte entstehen, wodurch unter Umständen Bildartefakte generiert werden können. Darüber hinaus werden alternative Mikroskopie-Methoden und Möglichkeiten,

Artefakte in Einzelmolekül-Lokalisationsmikroskopie-Bildern zu verhindern, präsentiert und ausführlich diskutiert.

Ein weiteres zentrales Thema dieser Arbeit ist die räumliche Anordnung von glykosylierten Membranmolekülen. Es wird demonstriert, wie ein bioorthogonales chemisches Reportersystem bestehend aus modifizierten Monosacchariden und organischen Fluorophoren für die spezifische Markierung von Membran-assoziierten Glykoproteinen und –lipiden eingesetzt werden kann. Mittels *d*STORM wird gezeigt, dass die Verteilung von Glykanen in der Plasmamembran unterschiedlicher Zelllinien homogen und frei von Clustern ist. Des Weiteren zeigt eine quantitative Analyse, dass sich in etwa fünf Millionen Glykane auf einer einzigen Zelle befinden. Die Ergebnisse demonstrieren, dass die Kombination aus metabolisch markierten Zielmolekülen, Click-Chemie und Einzelmolekül-Lokalisationsmikroskopie effizient genutzt werden kann, um Glykokonjugate auf Zelloberflächen zu untersuchen.

In einem dritten Projekt wurde *d*STORM zur Untersuchung von Rezeptormolekülen auf Krebszellen verwendet. Die Expression dieser Oberflächenproteine ist so gering, dass sich nur wenige Moleküle auf einer Zelle befinden, die jedoch als Zielmoleküle in der personalisierten Immuntherapie dienen könnten. Dafür wurden primäre Tumorzellen aus dem Knochenmark von Patienten, die am Multiplen Myelom erkrankt sind, auf die Expression des CD19-Oberflächenproteins als potentielles Ziel für CAR-modifizierte T-Zellen (*chimeric antigen receptor*) untersucht. Es wird gezeigt, dass sich, abhängig vom untersuchten Patienten, auf einer Zelle 60 bis 1600 CD19-Moleküle befinden. Funktionale in-vitro-Experimente demonstrieren, dass weniger als 100 CD19 Moleküle ausreichen, um CD19-CAR-T-Zellen zu aktivieren. Diese Ergebnisse werden mit Durchflusszytometrie-Daten verglichen und die wichtige Rolle von Lebendzellfärbung und geeigneten Kontrollexperimenten wird diskutiert.

Summary

The plasma membrane is one of the most thoroughly studied and at the same time most complex, diverse, and least understood cellular structures. Its function is determined by the molecular composition as well as the spatial arrangement of its components. Even after decades of extensive membrane research and the proposal of dozens of models and theories, the structural organization of plasma membranes remains largely unknown. Modern imaging tools such as super-resolution fluorescence microscopy are one of the most efficient techniques in life sciences and are widely used to study the spatial arrangement and quantitative behavior of biomolecules in fixed and living cells. In this work, *direct* stochastic optical reconstruction microscopy (*d*STORM) was used to investigate the structural distribution of membrane components with virtually molecular resolution. Key issues are different preparation and staining strategies for membrane imaging as well as localization-based quantitative analyses of membrane molecules.

An essential precondition for the spatial and quantitative analysis of membrane components is the prevention of photoswitching artifacts in reconstructed localization microscopy images. Therefore, the impact of irradiation intensity, label density and photoswitching behavior on the distribution of plasma membrane and mitochondrial membrane proteins in *d*STORM images was investigated. It is demonstrated that the combination of densely labeled plasma membranes and inappropriate photoswitching rates induces artificial membrane clusters. Moreover, inhomogeneous localization distributions induced by projections of three-dimensional membrane structures such as microvilli and vesicles are prone to generate artifacts in images of biological membranes. Alternative imaging techniques and ways to prevent artifacts in single-molecule localization microscopy are presented and extensively discussed.

Another central topic addresses the spatial organization of glycosylated components covering the cell membrane. It is shown that a bioorthogonal chemical reporter system consisting of modified monosaccharide precursors and organic

fluorophores can be used for specific labeling of membrane-associated glycoproteins and –lipids. The distribution of glycans was visualized by *d*STORM showing a homogeneous molecule distribution on different mammalian cell lines without the presence of clusters. An absolute number of around five million glycans per cell was estimated and the results show that the combination of metabolic labeling, click chemistry, and single-molecule localization microscopy can be efficiently used to study cell surface glycoconjugates.

In a third project, *d*STORM was performed to investigate low-expressing receptors on cancer cells which can act as targets in personalized immunotherapy. Primary multiple myeloma cells derived from the bone marrow of several patients were analyzed for CD19 expression as potential target for chimeric antigen receptor (CAR)-modified T cells. Depending on the patient, 60–1,600 CD19 molecules per cell were quantified and functional *in vitro* tests demonstrate that the threshold for CD19 CAR T recognition is below 100 CD19 molecules per target cell. Results are compared with flow cytometry data, and the important roles of efficient labeling and appropriate control experiments are discussed.

Contents

1 Introduction

1.1 The Plasma Membrane

As a response to internal and external impulses, biological systems act within a thoroughly adapted balance of opposing tendencies. Often, such ambivalent features are robustness and adaptability which can be found in each level of biological organization. The plasma membrane with its functions gives a perfect example of this duality, since it isolates the cell from its extracellular environment on the one hand and, simultaneously, allows the cell to communicate and interact with its surroundings on the other hand (Grecco *et al.*, 2011). It represents the cell's internal state to the outside by its structural and quantitative composition while informing the interior what happens outside by relaying messages through signal cascades. Plasma membranes operate selectively and regulate the uptake and secretion of metabolites, carrier molecules and other particles. They ensure that specialized cells are able to form tissues and organs, that immune cells can migrate into sites of inflammation, and that neurons are electrically excitable.

1.1.1 Composition of Plasma Membranes

A plasma membrane's function is determined by its molecular composition, which is the quantitative ratio of specific membrane proteins and lipids, and furthermore, the interplay between those. However, the presence of proteins and lipids at a particular membrane is normally not sufficient for its function. It is rather the spatial arrangement of its components which determines functionality. Most membranes consist in equal parts of lipid and protein. However, due to a substantially larger molecular mass of proteins, there are approximately 50 lipids per protein molecule. Lipids form a bilayer in which proteins are integrated or associated with. At the extracellular side, often, proteins and lipids are conjugated to carbohydrate groups or glycans through glycosylation.

Lipids. The cell membrane is composed of thousands of different lipid species. Its main components are glycerophospholipids which consist of a glycerol core esterified with two fatty acid tails and one phosphate group (the "head") which is often further modified. Due to the amphiphilic character —the chemical composition of a hydrophobic and a hydrophilic part— and an aqueous environment the formation of an energetically preferred bilayer is induced. This hydrophobic effect, furthermore, leads to the formation of micelles and liposomes (or vesicles). Further membrane lipids are sphingolipids and, in animal cells, sterols such as cholesterol (Berg *et al.*, 2018). Sphingolipids consist of the sphingoid base backbone sphingosine which is further modified to form ceramides and sphingomyelins, for example. In contrast to most biological phospholipids, sphingolipids contain long, largely saturated acyl chains which allow them to readily pack tightly together — a key feature which might result in raft formation (Brown and London, 2000). Sterols, such as Cholesterol, have a strong impact on basic membrane properties such as viscosity or interleaflet coupling, and, in mammals, can represent up to 40% of total lipid (La Bernardino de Serna *et al.*, 2016). Besides their function as structural membrane component, lipids often take part in signal transduction or serve as metabolic precursors for second messengers (Fernandis and Wenk, 2007). Moreover, they can act as cofactors for several membrane proteins, stabilize their structures, and thus are crucial for their function (Bowie, 2005).

Proteins. Membrane proteins constitute approximately half of the total plasma membrane mass (Dupuy and Engelman, 2008). They can be grouped into peripheral and integral proteins. Peripheral membrane proteins do not transverse the membrane but associate with the membrane surface to varying extents and with various moieties. These proteins are usually bound to the membrane indirectly by interactions with integral membrane proteins or directly by interactions with lipid polar head groups (e.g. GPI-anchored) or hydrophobic loops (Tan *et al.*, 2008). Conversely, integral membrane proteins are permanently attached to the membrane by either spanning the entire membrane (transmembrane proteins) or by attaching the membrane from only one side (Johnson and Cornell, 2009; Berg *et al.*, 2018). There is a vast variety of different membrane proteins and functions. One of them are transporter proteins that move molecules and ions across the membrane. This is realized by either pore-shaped channel proteins or carrier proteins which both are highly selective for the passing molecule, and most of them are strictly regulated. Carrier proteins allow molecules being actively transported through the membrane against their concentration gradient. This is realized by the use of chemical energy such as ATP, or by using an electrochemical gradient (Berg *et al.*, 2018). A further large protein class are membrane receptors which

are responsible for the binding of extracellular signaling molecules and the transduction of the message into the cell by signaling cascades. The cell then responds by changing or adapting its activity or metabolism. Signaling molecules or ligands are for example cytokines, hormones, neurotransmitters, nutrients, growth factors etc. Other membrane proteins are membrane enzymes which catalyze metabolic processes, as well as adhesion molecules which stabilize membranes by anchoring to the cytoskeleton and maintaining cell–cell contact (Tan *et al.*, 2008; Berg *et al.*, 2018). Plasma membrane proteins form key nodes in mediating the cell's interaction with the surroundings, which is one of the main reasons why the majority of drug targets are membrane proteins (Almén *et al.*, 2009).

Glycans. A biomolecule which is covalently linked to a carbohydrate is called glycoconjugate. Approximately 50% of the proteome is glycosylated (Berg *et al.*, 2018). Glycans —the carbohydrate portion of glycoconjugates— play key roles in numerous biological processes which is also reflected by their structural variety. This diversity can far exceed that of linear biopolymers, because glycans are built of monosaccharide building blocks that are connected in both linear and branched geometries. The totality of glycans that a cell produces, is termed the cell's glycome which reflects the physiological state of the cell (Laughlin and Bertozzi, 2009). The glycoside can be linked to a polypeptide backbone via *N*-linked glycosylation which is the attachment to the amide group of asparagine residues inside a specific sequence, or via *O*-linked glycosylation, the conjugation to the hydroxyl group of serine or threonine residues. *N*-linked glycans are composed of monosaccharides such as galactose, *N*-acetylgalactosamine, *N*-acetylglucosamine, neuraminic acid, mannose and fucose. Glycans are assembled mainly in the cytoplasm and subsequently migrate into the Golgi apparatus and the endoplasmatic reticulum for posttranslational modification of the respective protein. In some cell types such as epithelial cells, long membrane-associated glycans are building a pericellular matrix —the glycocalyx— which forms an envelope that surrounds the cell membrane. Glycoconjugates are substantially involved in cell–cell recognition, communication, and cell adhesion, and are involved in numerous diseases (Berg *et al.*, 2018).

1.1.2 Membrane Organization

After the discovery of the lipid bilayer as a biological membrane by Gorter and Grendel in 1925, Davson and Danielli proposed that biomembranes consist of lipid bilayers that are coated with proteins on both sides (protein–lipid–protein). They

assumed that the interaction between lipids and proteins is only based on absorption and they highlighted, for the first time, the importance of proteins in biological membranes (Danielli and Davson, 1935). With further improvements in electron microscopy the Davson–Danielli trilayer model was extended by Robertson in 1959. He demonstrated that the supposed inner and outer protein sheets flanking the lipid bilayer differ in their chemical compositions (Robertson, 1959). However, these earlier models had certain limitations in explaining existing data on membrane structure as for example the permeability for certain substances and the movement of membrane proteins (Nicolson, 2014).

Fluid Mosaic Model. In the beginning of the 1970s a range of crucial experiments as well as the ongoing development of electron microscopy led to new insights into the structural organization of the plasma membrane which were difficult to explain with the existing models of Davson, Danielli and Robertson. More exact measurements resulted in an asymmetric distribution of proteins in the membrane as well as heterogeneous membrane thicknesses. In 1970 Frye and Edidin could demonstrate by using fluorescence microscopy that fusing two cells results in an intermixing of membrane proteins which proved the fluidic character of plasma membranes Frye and Edidin, 1970). Based on this knowledge and on contradictions to existing membrane models, Singer and Nicolson proposed the fluid mosaic model in 1972 (Singer and Nicolson, 1972). They assumed that the underlying structure is also a lipid bilayer which, however, is not flanked by thin protein sheets, but rather is punctuated by various proteins that form a mosaic-like pattern in the lipid membrane. They postulated that the membrane's fluidity allows lateral movement of proteins and, furthermore, that proteins are anchored in the membrane or even spanning the entire plasma membrane (transmembrane proteins). Thus, the fluid mosaic model could explain the observations made by Frye and Eddin as well as many other phenomena observed by scientists at that time (Nicolson, 2014).

Picket Fence Model. In the early 1980s a couple of experiments demonstrated that the description of the structural membrane composition by Singer and Nicolson was incomplete. Observations of diffusing membrane proteins in erythrocyte membranes led to the assumption that the mobility of membrane proteins is strongly reduced which contradicted the fluid mosaic model (Sheetz *et al.*, 1980). Sheetz proposed that the reduction of lateral diffusion is induced by interactions with the cytoskeleton which could be shown by artificial membranes and actin defective cells that exhibited an enhanced protein mobility. As the name suggests, the picket fence model describes the plasma membrane as fluid bilayer which is compartmentalized by actin-based membrane-skeleton fences and anchored

transmembrane protein pickets (Kusumi *et al.*, 2005). With the help of single-particle tracking (SPT) approaches it could be observed that a large range of membrane receptors (e.g. the transferrin receptor) are temporarily confined within a compartment, and then these molecules hop to an adjacent apposed compartment where they again become trapped temporarily (Sako and Kusumi, 1994). This hop diffusion and a range of other experiments and observations further consolidated the picket fence model. However, hop diffusion is not only performed by membrane proteins as Fujiwara *et al.* could demonstrate in 2002. They proposed with the anchored-protein picket model that numerous transmembrane proteins which are attached to the actin membrane skeleton meshwork effectively act as rows of pickets, and temporarily confine the movement of other membrane molecules (including phospholipids) through steric hindrance and circumferential slowing effects (Fujiwara *et al.*, 2002; Kusumi *et al.*, 2005). Last but not least, the good agreement of plasma membrane compartment sizes determined by electron tomography of the actin meshwork on the cytoplasmic surface, and indirectly by calculations based on SPT experiments of phospholipid molecules highlighted the important role of the cytoskeleton in terms of structural membrane organization (Morone *et al.*, 2006).

Lipid Raft Hypothesis and other Membrane Models. Whereas the picket fence model holds the cytoskeleton accountable for substructuring membrane proteins and lipids, other theories postulate lipid microdomains as decisive factor for membrane organization. Thereby, sphingolipid and cholesterol molecules cluster in the plasma membrane's outer and/or inner leaflet to form lipid phases or lipid rafts. The physical properties of these lipid rafts lead to an accumulation of certain membrane proteins and other lipids (Simons and Ikonen, 1997). Only one year after the publication of the fluid mosaic model in 1972 first observations that cell membranes can be separated into detergent-labile and detergent-resistant fractions (Yu *et al.*, 1973) resulted in the assumption that distinct membrane compartments are present in plasma membranes. A range of following experiments, especially with biomimetic model membranes, consolidated the idea that certain lipids interact preferentially with each other, and thus generate lateral domains as a consequence of liquid–liquid phase separation (Sezgin *et al.*, 2017).

Due to the vast number of different observations and reconsiderations regarding the raft model, a general definition of lipid rafts was formulated in 2006 suggesting that rafts are heterogeneous, highly dynamic, cholesterol and sphingolipid-enriched membrane nanodomains of dimensions between 10 and 200 nm that compartmentalize cellular processes. Furthermore, these nanodomains have the potential to form microscopic domains (>300 nm) induced by protein–protein and

protein–lipid interactions (Pike, 2006)(Figure 1.1). However, due to the difficulty in preparation and microscopic detection of lipid rafts in living cells the existence and exact nature of rafts remain a subject of debate (Klotzsch and Schütz, 2013; Sezgin *et al.*, 2017).

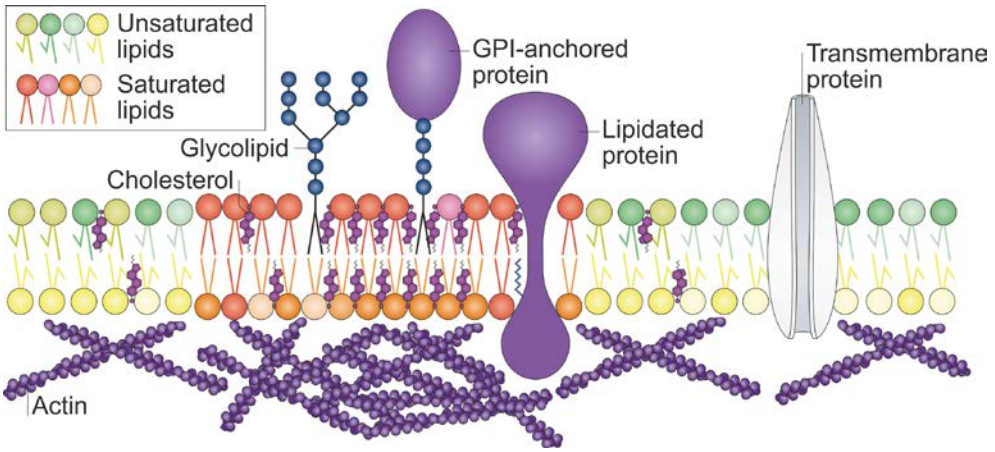

Figure 1.1: Lateral heterogeneity in the plasma membrane. Membrane components can be concentrated in hydrophobic lipid raft domains that consist of saturated phospholipids, sphingolipids, glycerolipids, cholesterol, lipidated proteins and GPI-anchored proteins. These enrichments feature increased lipid packing and decreased fluidity. In addition, cortical actin filaments play in important role in domain remodeling. Reprinted by permission from Macmillan Publishers Ltd: Nature Reviews Molecular Cell Biology, Sezgin *et al.*, 2017, copyright 2017.

Due to new findings on membrane organization and the development of new biophysical methods such as super-resolution fluorescence microscopy, a growing number of models and hypotheses are proposed which all try to explain membrane organizations. The tendency is towards a combination of existing models. One of them is the protein islands model in which all membrane-associated proteins are clustered in protein islands that are surrounded by a sea of protein-free membrane. The islands can be subdivided into raft and non-raft islands which is controlled by their lipid and protein composition. Moreover, the protein islands are connected to the actin meshwork which additionally controls island formation (Lillemeier *et al.*, 2006; Lillemeier *et al.*, 2010). Another highly discussed proposal for membrane organization is the protein cluster theory in which membrane proteins with the same or similar physical properties self-assemble to form clusters of highly-packed homophilic proteins. Cluster dimensions and dynamics are controlled by a balance between self-association and crowding induced steric repulsions which, for example, has been previously shown for syntaxin clusters (Sieber

et al., 2007; Bar-On *et al.*, 2012). The protein cluster theory does not conflict with the above described theories and may be seen as an extension or differentiation of existing membrane organization models.

1.1.3 Receptors as Targets in Cancer Immunotherapy

The evolution of unique cell-surface molecules that allow neighboring cells to communicate is considered as one of the major transitions from uni- to multicellular organisms. Plasma membrane receptors are able to recognize adjacent cells and extracellular structures, and to relay extracellular signals into the cell's interior. This has resulted in a vast variety of different membrane receptors and the ability of cells to differentiate and communicate (Kaiser, 2001; Ben-Shlomo *et al.*, 2003).

In immunology cell-surface molecules play an extraordinarily important role since each contact among immune cells, and between those and pathogens is receptor-mediated. During the last 35 years a large range of monoclonal antibodies has been produced which has facilitated the purification and functional characterization of many leukocyte surface molecules. Beyond that, monoclonal antibodies have been used as markers for cell populations, and thus have been used for counting, separation, and functional studies of various subsets of immune cells (Beare *et al.*, 2008). However, as the number of monoclonal antibodies detecting cell surface differentiation antigens grew, an international standardization was established in the 1st International Workshop and Conference on Human Leukocyte Differentiation Antigens (HLDA) which took place in Paris in 1982 (Fiebig *et al.*, 1984). There, the cluster of differentiation (CD) nomenclature was proposed as a protocol for the classification (or "clustering") of monoclonal antibodies against defined surface molecules of leukocytes (not necessarily the same epitopes). Until today, the human CD system is numbered up to 371 (CD371), and is commonly used in immunophenotyping, cell sorting and flow cytometry.

In addition to this, CD-based immunophenotyping can also be used to distinguish between healthy and malignant immune cells due to altered CD expression profiles. Furthermore, if the CD pattern of a certain cancer type is known, it can be used as therapeutic target, and the immune system of a patient can be adjusted in order to eliminate the tumor. This can be achieved by a couple of strategies which have been developed during the last decades. One of these is the administration of monoclonal antibodies directed against the target molecule (e.g. a CD) which results in a stimulation of immune response. However, monoclonal antibodies are unable to engage T cells which are considered as the most powerful

agent of the immune system (Zhukovsky *et al.*, 2016). Mobilization of T cells can be achieved with two strategies — activation of T cells via bispecific antibodies, and genetic modification of T cells.

Bispecific Antibodies. Bispecific antibodies such as BiTEs (bispecific T cell engagers) are antibodies with dual specificity. They are artificial fusion proteins that consist of two single-chain variable fragments of two different antibodies (Figure 1.2). Whereas one of the fragments binds to a T cell's CD3 receptor, the other one binds to a tumor associated antigen (the target molecule). Thereby, the T cell is not only crosslinked to the cancer cell, but also gets activated through CD3 binding which results in a subsequent elimination of the cancer cell (Wang *et al.*, 2014; Huehls *et al.*, 2015).

TCR. The other way is to genetically engineer T cells. There are two basic strategies that are being explored in clinical testing of engineered T cells. The first one involves that the T cell expresses the alpha and beta chains of a T cell receptor (TCR) known for recognition of a cell-type specific antigen. This therapy is potentially accessible to any patient whose tumor bears the human leukocyte antigen (HLA) allele and expresses the target antigen recognized by the TCR (Farkona *et al.*, 2016).

CAR. The second strategy is the use of chimeric antigen receptors (CARs) which also are fusion proteins and usually consist of at least three domains: an extracellular antigen-binding domain which is a single-chain variable fragment derived from monoclonal antibodies, a spacer (hinge) and transmembrane domain, and an intracellular signal transduction domain which is usually a CD3ζ chain (Figure 1.2). Beyond that, there is an ongoing development of new generations of CARs which are equipped with additional intracellular costimulatory domains such as CD28 to enhance sensitivity and activity (Sadelain *et al.*, 2013). The advantage of this strategy is that CAR engineered T cells (CAR T cells) obtain the antigen-recognition properties of antibodies and are thus potentially targeted against any cell surface target antigen (e.g. any CD or other surface molecules) (Wang *et al.*, 2014; Farkona *et al.*, 2016).

TCR and CAR T cell therapies are performed using adoptive cell transfer. Thereby, a patient's own T cells are harvested through leukapheresis, and transduced with a vector encoding the recombinant receptor. Following *ex-vivo* expansion of cells, modified T cells are reinfused into the patient where they can fulfil their task — the elimination of all target cells. This type of cancer treatment is also called personalized immunotherapy and is, due to its high specificity, a very promising approach in cancer treatment (Rosenberg and Restifo, 2015; Maus and June,

2016). However, the clinical use of highly avid TCRs and CARs has been associated with significant secondary destruction of healthy tissues expressing the same target antigen. Hence, safety issues regarding the selection of the target, serious adverse effects and the lack of long-lasting responses in many patients indicate that additional interventions may be necessary to appropriately control and activate T cells in personalized immunotherapies (Suzuki *et al.*, 2015; Farkona *et al.*, 2016).

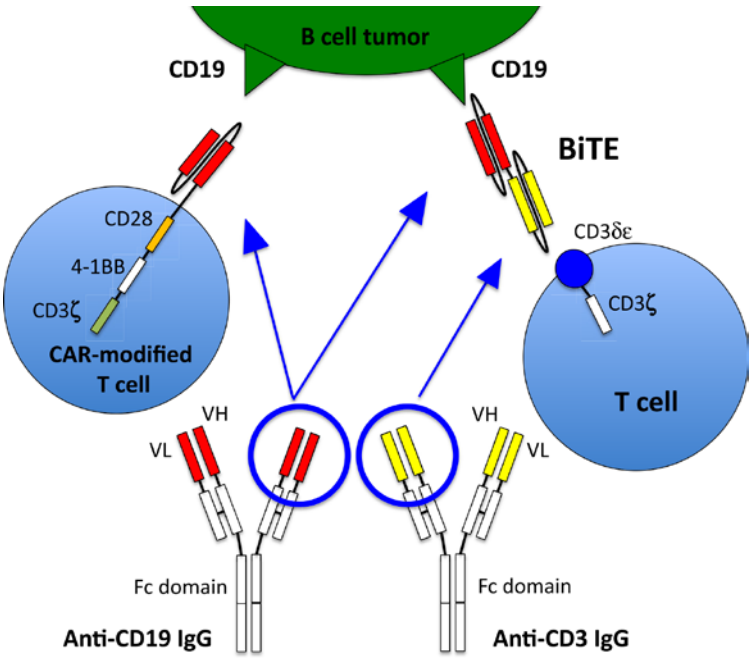

Figure 1.2: T cell recruitment and activation in cancer immunotherapy. Anti-tumor CAR T cells (in this case anti-CD19 CARs) recognize the antigen on a tumor cell via a single chain variable fragment binding domain (red) derived from a monoclonal anti-CD19 antibody (*left*). Anti-CD19–CD3 bispecific antibodies consist of two single chain variable fragments joined in tandem (red and yellow, *right*) which allows the recruitment and activation of T cells. Following binding and activation, (CAR) T cells subsequently induce apoptosis of the cancer cell. Adapted with permission from (Suzuki *et al.*, 2015).

One prominent example of CAR therapies are T cells expressing anti-CD19 CARs which have been the most widely used and successful among all chimeric antigen receptors to date. CD19 is a surface antigen expressed on the plasma membranes of precursor and mature B cells, but also on various B cell malignancies including B-acute lymphoblastic leukemia. CD19CART cells can cause complete remissions of B cell malignancies that are often durable (Kochenderfer and

Rosenberg, 2013). Compared to other anti-cancer therapies such as chemotherapies, side effects of CD19CAR therapies are relatively low. However, the most important toxicity which has been emerged is the cytokine release syndrome which induces e.g. hypotension, fever, and tachycardia. For that reason, one of the most important goals of the CAR field is to improve the efficacy-to-toxicity ratio of CAR T therapies (Mikkilineni and Kochenderfer, 2017).

1.2 Tools to Study Membrane Organization

The multitude of potential molecular interaction between and among lipids and proteins in plasma membranes results in an extraordinarily high complexity which has led to a vast variety of different theories, predictions, and hypotheses of membrane organization. Early on, researchers started to investigate biological membranes with different experimental approaches, and often, their observations and resulting theories had more relation to the way the experiment was actually performed than to the nature of the investigated object (Klotzsch and Schütz, 2013).

The range of different analytical tools to study cell membranes is continuously growing. In classical biochemical approaches membrane fragments and compounds are extracted with detergents or by sonication, and further analyzed with gradient centrifugation or immunoprecipitation. However, results are strongly dependent on the degree of solubilization, and despite precise details of membrane composition, they do not contain information about the structural organization of membrane components. A great step in membrane research was made by the introduction of electron microscopy which allowed scientists to observe membranes in their cellular context and with molecular resolution. For the first time, heterogeneities in membrane organization could be observed, and in combination with freeze-fracturing, the existence of transmembrane proteins could be proven (Robertson, 1981; see also Chapter 1.1.2).

Nonetheless, the investigation of dynamic cellular processes and structures prepared under less harsh and more native conditions could only be achieved by application of fluorescence microscopy and spectroscopy tools. Important fluorescence methods that have contributed in membrane research are particularly total internal reflection fluorescence microscopy (TIRFM), confocal laser scanning microscopy (CLSM), near-field scanning optical microscopy (NSOM), single-particle tracking (SPT), fluorescence resonance energy transfer (FRET), anisotropy-based homo-FRET, fluorescence recovery after photobleaching (FRAP), spot variation

fluorescence correlation spectroscopy (svFCS), as well as combinations of those (Lommerse *et al.*, 2004; Klotzsch and Schütz, 2013; van Zanten and Mayor, 2015). In addition to that, several far-field super-resolution microscopy tools have been evolved during the last 25 years which will be described in the following sections.

1.2.1 Fluorescence Microscopy

In biology, fluorescence-based methods belong to the most widely applied tools to study cellular structures and dynamic processes. During the last 30 years the usage of fluorescence has been substantially grown which is reflected by the vast variety of different applications in many fields such as biotechnology, flow cytometry, DNA sequencing, medical diagnostics, genetic analysis and forensics. The detection of fluorescence is highly sensitive, and due to the high contrast between signal and background it is well-suited for cellular and molecular imaging. In fluorescence microscopy, the Stokes shift between the absorption and emission spectra is used to filter out the excitation light, and thus detecting only the red-shifted emission light. Unlike conventional transmission light microscopy, the contrast is considerably improved which makes fluorescence microscopy a very sensitive, versatile, and non-invasive tool for helping biological mysteries to be unraveled (Lakowicz, 2006). Nowadays, there exist a large number of different fluorescent molecules (fluorophores) and labeling strategies which can be used to specifically label the cellular structure of interest. There are different types of fluorophores which all bear different biochemical and photophysical properties. The long list of different fluorophores starts with fluorescent proteins (e.g. GFP, the green fluorescent protein), over quantum dots, to organic fluorescent molecules such as cyanine and rhodamine dyes (see also Chapter 1.2.4).

Besides its various advantages, fluorescence microscopy has an important drawback which becomes obvious when trying to resolve small biological structures and processes beyond 200 nm — the diffraction of light. The diffraction barrier of optical systems is a physical limit, and is caused by the wave nature of light. As introduced by Ernst Abbe and Lord Rayleigh (Abbe, 1873; Rayleigh, 1896), the spatial resolution of optical microscopes was dictated for a long time by the diffraction barrier which seemed to be insurmountable. Abbe described that a light microscope's resolution is dependent on the emission wavelength (λ) and the numerical aperture (NA) of the objective which can be described as $d = \lambda/(2NA)$, where d is the distance between two lines of a periodic grid. However, an emitting fluorophore can be considered as a point-like light source appearing as a circular

diffracted spot with a centered maximum surrounded by concentric rings of decreasing intensity (Airy pattern). Its lateral intensity distribution is the result of the point object's convolution with the point spread function (PSF) of the optical system. Imaged emission patterns (spots) of single fluorophores are hereinafter referred to as PSFs. According to Rayleigh, two point light sources are still resolvable if the maximum of the first PSF coincides with the first order minimum of the second one (Rayleigh criterion). This minimum distance of two barely resolvable point sources can be described as $d_{\text{Rayleigh}} = 0.61\lambda/NA$. As an example, a fluorophore with an emission maximum of 670 nm and an objective with an *NA* of 1.40 results in a maximum lateral resolution of ~290 nm. By increasing *NA*, and decreasing the emission wavelength, the resolution of a microscopic system can be improved. However, due to technical limitations regarding the *NA* and the limitation of the visible spectrum, objects smaller than 200 nm are usually not resolvable with conventional fluorescence microscopy.

1.2.2 Super-Resolution Fluorescence Imaging

To overcome the diffraction barrier of optical microscopy, a range of optical tools have been developed during the last decades which can be separated into two different approaches. The first strategy to circumvent the diffraction limit consists of deterministic approaches, where defined illumination patterns are used, while the second one is of rather stochastic nature, where the emission of stochastically activated individual fluorophores is randomly separated in time. Examples of deterministic approaches are stimulated emission depletion (STED) microscopy (Hell and Wichmann, 1994; Hell, 2007) and structured illumination microscopy (SIM)(Heintzmann and Cremer, 1999; Gustafsson, 2000). In STED, which is based on confocal microscopy, the resolution is substantially improved by deexcitation of excited fluorophores. This is realized by a second red-shifted, donut-shaped laser beam which induces stimulated emission of fluorophores that are located in the outer parts of the focus, whereas those sitting in the center (which is far smaller than the diffraction limit) are still able to emit photons. On the contrary, the wide-field-based imaging technique SIM uses patterned light to illuminate the sample. This causes Moiré fringes in the detected raw image which can be mathematically extracted and further used to reconstruct an image with an up to twofold improved spatial resolution.

SMLM. The second type of sub-diffraction-resolution fluorescence imaging are stochastic approaches which use the time-separated emission of stochastically activated individual fluorophores to precisely determine their positions. Since each

single molecule is localized, these methods are grouped under the term single-molecule localization microscopy (SMLM). Time-separation is achieved by using photoswitchable fluorophores that are able to either reversibly or irreversibly switch between two fluorescent states of different spectral properties, or between a fluorescent *on* and a non-fluorescent *off* state. This ensures, that only a sparse subset of fluorophores are activated at one moment, and thus being placed further apart from each other than the distance resolved by the microscope camera. There are several different concepts that are based on switchable fluorophores, and mainly differ in their type of interconversion between the two states. One of these is photoactivated localization microscopy (PALM, Betzig *et al.*, 2006) or fluorescence PALM (FPALM, Hess *et al.*, 2006) which uses photoactivatable or photoconvertible fluorescent proteins (PA-FPs) such as PA-GFP and mEos2. Upon illumination with ultraviolet light, these proteins change from either an initial non-fluorescent *off*, or an initial fluorescent state into a fluorescent *on* or a fluorescent red-shifted state, respectively. Once PA-FPs are stochastically activated they emit photons and thus are detected by the camera until being irreversibly photobleached. Since PALM uses genetically expressed proteins it is very suitable for imaging intracellular structures and processes in living cells. (Patterson *et al.*, 2010; Sauer *et al.*, 2011)

Further prominent SMLM approaches are stochastic optical reconstruction microscopy (STORM, Rust *et al.*, 2006; Bates *et al.*, 2007) and *direct* STORM (*d*STORM, Heilemann *et al.*, 2008; Heilemann *et al.*, 2009; van de Linde *et al.*, 2011; Klein *et al.*, 2014) which both use photoswitchable organic dyes for time-separated localization. Experimental realization ensures that only a sparse subset of fluorophores populates the fluorescent *on* state while the majority is reversibly transferred to a stable non-fluorescent (dark) *off* state at a given time (Figure 1.3 A). In a next step, emitting fluorophores are transferred into the dark state and another subset is activated. This cycle continues until several thousand frames are recorded. Each frame contains information about spatially well separated single molecules whose coordinates are precisely determined by fitting a two-dimensional Gaussian function to their PSFs. The error in position determination (the localization precision) is a function of the PSF's standard deviation (σ), the number of collected photons (N), and different noise factors such as background signal. However, for bright fluorophores, and thus high photon numbers, the background noise can be neglected which results in an approximated localization precision of $\sigma/\sqrt{N}$ (Thompson *et al.*, 2002). Finally, after extracting the positions of all emitter spots from a raw data movie, localizations can be used to calculate a single reconstructed super-resolved image with a resolution that is substantially

enhanced —usually up to 20 nm in lateral dimensions— compared to the standard wide-field fluorescence image.

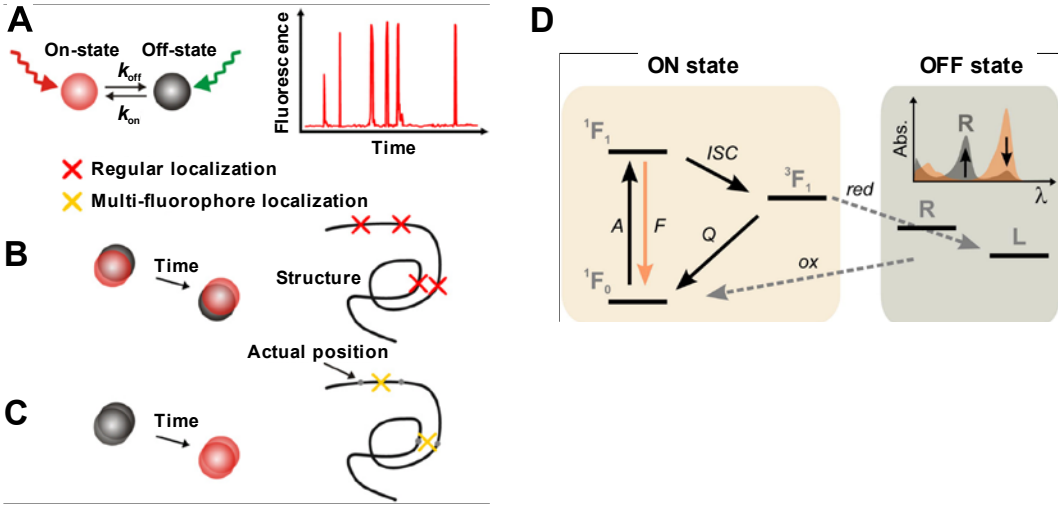

Figure 1.3 Principle of *d*STORM and reversible photoswitching. *d*STORM compatible fluorophores can be switched between a fluorescent *on* and a non-fluorescent *off* state (**A**) which enables the separation of fluorescence emission in time (**B**). In the case of inappropriately set switching rates it may happen that more than one fluorophores are fluorescent in the same diffraction limited area at the same time. This results in multi-fluorophore localizations (**C**) which may lead to the generation of reconstruction artifacts (Chapter 4.1). (**D**) The reducing environment ensures that, once a fluorophore has populated the triplet state ($^3F_1$) it forms a reduced non-fluorescent radical (R), and in some cases a fully-reduced leuco form (L). Both can be oxidized again to the singlet ground state ($^1F_0$) of the fluorophore (*ox*). Reprinted from van de Linde *et al.*, 2010, Copyright 2010, with permission from Elsevier (**A**–**C**), and van de Linde *et al.*, 2013 Copyright 2013, with permission from Elsevier (**D**).

Since the precise localization of an emitter is also dependent on the shape of its PSF as described above (standard deviation σ), it is highly important that, at a given time, only one emitter per diffraction-limited area resides in the *on* state. Otherwise overlapping PSFs result in elongated and asymmetric spots which either cannot be fitted anymore and are discarded, or lead to multi-fluorophore localizations (Figure 1.3 B–C, van de Linde *et al.*, 2010; van de Linde and Sauer, 2014). In the case of densely labeled structures, this can lead to the generation of artifacts in the reconstructed image which can be considered as potential source for misinterpretations regarding biological questions (see also Chapter 4.1 for a detailed description and discussion of these kinds of problems). The other way

around, a cellular structure that is too sparsely labeled will not be completely resolved as such in the reconstructed super-resolved image. This phenomenon can be described with the Nyquist-Shannon sampling theorem, which states that the average distance between neighboring molecules must be at least half of the desired resolution (Shannon, 1949). As an example, a spatial resolution of 20 nm necessitates that the structure of interest is fluorescently labeled every 10 nm. Consequently, the structural resolution that can be achieved with SMLM methods is not only dependent on the localization precision and photon yield, but also on the labeling density (Sauer *et al.*, 2011).

In *d*STORM, the experimental conditions ensure that a fluorophore is preferably transferred into its long-living *off* state which allows the low number of *on*-state-fluorophores to be localized. This is accomplished by the addition of reducing compounds such as thiols (e.g. β-mercaptoethylamine) in the millimolar range to the buffer. Once a fluorophore is irradiated it is transferred into the first excited singlet state, from where the excitation energy is either released via fluorescence emission, or the triplet state is occupied via intersystem crossing (Figure 1.3 D). In the latter case the fluorophore can be reduced by thiolates to form a radical anion which, in some cases, can be further reduced into its leuco form. Both reduced forms (semi- and fully-reduced) are stable, non-fluorescent, and thus form the *off* or dark state of the fluorophore. Since this process is reversible, *off*-state-molecules can be transferred back into their singlet ground states via oxidation with molecular oxygen (O_2), or irradiation with ~400 nm-light. Furthermore, through oxidation with O_2 the triplet state can directly be quenched which results in a subsequent transfer into the ground state, without the chance of being reduced and switched off (Figure 1.3 D). To prevent this, especially in the case of cyanine dyes such as Cy5 and Alexa Fluor 647, O_2 has to be removed in order to gain usable switching rates. A fine-tuned adjustment of thiol and oxygen concentration, pH value, excitation intensity, and additional irradiation with 400 nm permits the temporal separation of fluorophore emissions, which forms the basis for a good *d*STORM experiment (van de Linde *et al.*, 2011; van de Linde and Sauer, 2014).

1.2.3 Quantification of SMLM Data

Besides the ability of SMLM to generate super-resolution images by detecting emission patterns of individual fluorophores separated in time, it provides a second option which demonstrates its high potential in life sciences: the usage as a quantitative bioanalytical tool. Due to the mathematical relationship between the

positions of emitters in space and time, biologically relevant information can be extracted which helps to describe the patterning, topography and geometry of sub-diffraction features (Nicovich *et al.*, 2017). The output data generated with SMLM are lists of molecular coordinates, and other elements corresponding to the time, brightness, background, spot size etc. of a particular localization event. This feature introduces new possibilities for coordinate-based data analysis, particularly in the field of cluster analysis and biomolecular quantification (Fürstenberg and Heilemann, 2013). Especially in membrane biology, localization data are used to investigate the spatial arrangement of membrane molecules such as membrane proteins, lipids and glycans (Chapters 1.1.1 and 1.1.2)(Ehmann *et al.*, 2014; Letschert *et al.*, 2014; Fricke *et al.*, 2015; Hummer *et al.*, 2016; Patrizio and Specht, 2016; Kabbani and Kelly, 2017). Questions like "Are target molecules clustered or randomly distributed?" as well as "How many target molecules are expressed?" become more and more relevant for understanding membrane organization and function.

The distribution of localizations is often analyzed using Ripley's H, K and L functions (Ripley, 1977) which clarify whether a set of points is homogeneously distributed or not, as well as approximates the average size of spatial patterns like clusters, for example (Nicovich *et al.*, 2017). Due to the single-molecule information obtained by SMLM experiments, fluorophores can be counted, and absolute numbers of molecules can be estimated. Therefore, the fluorophore which is bound to the biomolecule of interest is ideally localized only once which would result in a quantitative 1:1 relation between localization and molecule. However, due to a range of biochemical and photophysical effects this relation is usually shifted to one of the two sides. If, for example, direct or indirect immunofluorescence is used as labeling method, it can be assumed that more than one primary antibodies are binding the target molecule, and several secondary antibodies might bind to one primary antibody. It also depends on the degree of labeling (DOL) which is usually >1 due to signal enhancement. Besides biochemical labeling-related issues, photophysical effects such as the reversible on- and off-switching of individual fluorophores ("blinking") which leads to the detection of repeated localizations, must be taken into account.

During the last couple of years various strategies have been evolved which try to correct for repeated localizations by determination of the localization–molecule ratio (Griffié *et al.*, 2016; Karathanasis *et al.*, 2017; Nicovich *et al.*, 2017). One approach is to group all localizations coming from individual molecules using cluster algorithms. This can only be conducted, if the sample is sparsely labelled knowing that only one target molecule is located in any diffraction-limited area. For

densely labeled samples, it is possible to first determine localization densities, and, in a second step, perform titration experiments under the same imaging conditions to calculate a conversion (correction) factor (at very low dye concentrations). However, in addition to properly correcting for blinking and labeling effects, it is indispensable to include appropriate control experiments, especially in cases where very low expressing target molecules are aimed to be quantified. The following section describes a very useful cluster algorithm which can be used to characterize spatially well-separated localization clouds for a precise quantification of biomolecules.

Alpha Shapes. There are several approaches for cluster analysis of localization data. One of them are alpha shapes which can be used to approximate the shape of a finite set of points —for example single-molecule localizations— in a plane (2D) or in space (3D). Alpha shapes are a generalization of the convex hull and were first introduced by Edelsbrunner and colleagues (Edelsbrunner *et al.*, 1983). In life sciences alpha shapes are especially used to calculate three-dimensional shapes of macromolecules (Li *et al.*, 2013) and recently also protein-related interactions (Zhou and Yan, 2014). They can be described by the eraser intuition (Edelsbrunner and Mucke, 1992): Imagine a blackboard ($\mathbb{R}^2$) which is completely whited out with blackboard chalk. Additionally, a finite set of positions (S) are marked with metal pins stuck into the board. Now, imagine trying to wipe the board with a circular sponge of radius α (the "eraser") by moving it around and against the pins. After this process, the area which is still white is called the alpha hull of S. In a last step, straightening of circular segments (or arcs) between two boundary pins results in linearization of the alpha hull which is called the alpha shape. An analogy for the third dimension is the ice cream scenario: Imagine a large amount of ice cream ($\mathbb{R}^3$) with solid chocolate chips (S). Now, imagine trying to curve out all parts of ice cream with a spherical ice spoon —the alpha ball of radius α— without touching the chocolate chips. Here, it is even possible to carve out holes in the inside (e.g. those parts which are not reachable by simply moving the spoon from the outside). After straightening the obtained hull, we will end up with the shape (alpha shape) formed by the set of chocolate ships (S).

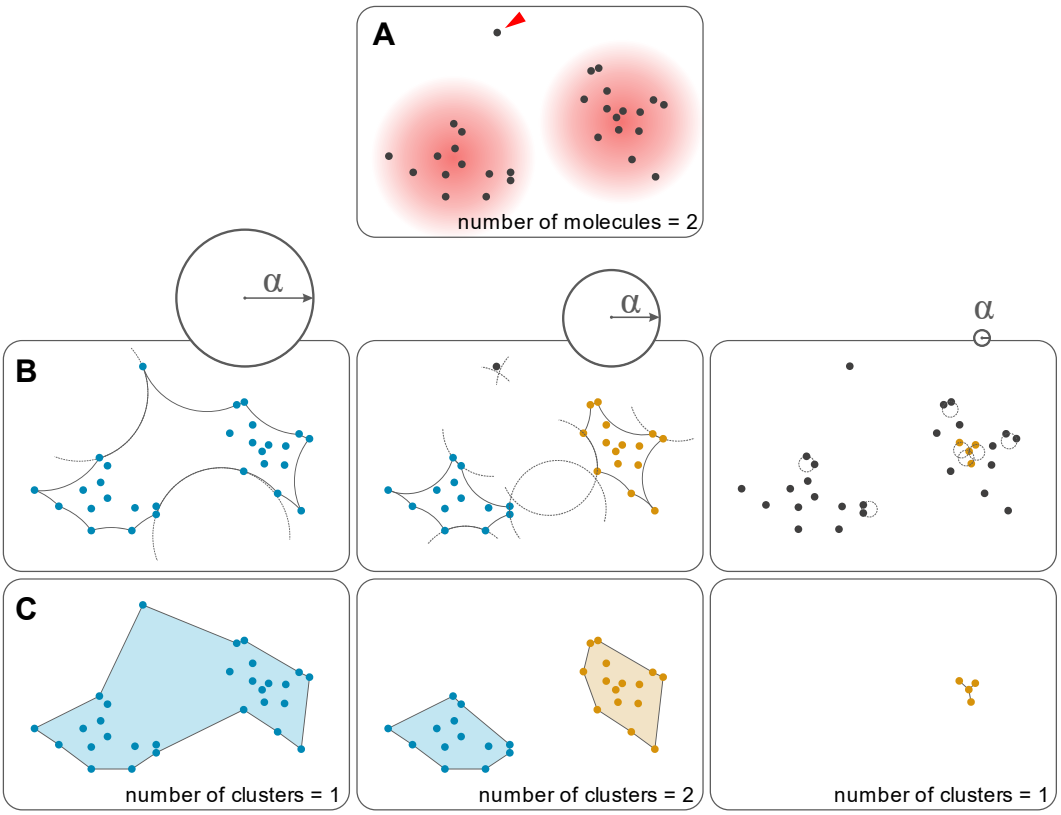

Figure 1.4: Schematic illustration of clustering localization data using alpha shapes. (**A**) Given are two point emitters (e.g. two fluorophores or two antibodies conjugated to several fluorophores) and their localizations (black dots) which are spread over an area (displayed in light red) depending on the localization precision. Background (e.g. detached and diffusing fluorophores) can lead to false localizations (red arrow head). (**B**) Erasers or discs with different radii (α) result in alpha hulls of different number, sizes and shapes. (**C**) Alpha shapes are generated by linearization of alpha hulls. Non-clustered localizations (single or pairs of localizations) are discarded. At very high α values (left panels), the probability of over-clustering increases whereas at low values (right panels) alpha shapes degenerate to their original point-sets which are then discarded. The number of obtained clusters in a defined area (region of interest) can be used to calculate the density of molecules (fluorophores, labeled antibodies, proteins of interest, etc.) whereas the alpha shape itself contains information about cluster size, cluster shape, number of localizations per cluster, etc.

These analogies can be easily transferred to SMLM data. Since repeated localizations from well-separated single molecules (e.g. fluorophores or fluorophore-conjugated antibodies) represent finite sets of points, it is possible to cluster those using alpha shapes (Figure 1.4). The level of detail as wells as the number of clusters are dependent on the alpha value. For $\alpha \to 0$ the alpha shape degenerates to the original set of points (S) without obtaining any information on the shape

(Figure 1.4, *right panels*). On the other hand, large alpha values ($\alpha \rightarrow \infty$) lead to the generation of the convex hull of S. Furthermore, the chance of over-clustering increases which means the grouping of several localization clouds coming from several neighboring emitters (Figure 1.4, *left panels*). The consequence of too low and high alpha values is an underestimation of the number of clusters and thus a wrong cluster and molecule density, respectively.

1.2.4 Metabolic Labeling and Click chemistry

Modern imaging tools such as fluorescent microscopy are one of the most efficient techniques in life sciences and are widely used to study the spatial arrangement and quantitative behavior of biomolecules in fixed and living cells (Stephens and Allan, 2003). The visualization of cellular structures has been revolutionized by the birth of immunofluorescence microscopy. Originally, a fluorescein molecule was chemically bound to a primary antibody which allowed the visualization of structures in tissue sections (Coons *et al.*, 1941; Coons and Kaplan, 1950). The optimization of antibody production and purification, the introduction of indirect immunohisto- and immunocytochemistry and the development of new organic fluorophores have immunofluorescence allowed to become the method of choice for visualizing cellular structures in fixed cells and tissues. Furthermore, the discovery and advent of fluorescent proteins such as the green fluorescent protein (GFP, Shimomura *et al.*, 1962) and its variants have revolutionized live-cell imaging by allowing the fusion to virtually any protein of interest (Tsien, 1998; Lippincott-Schwartz and Patterson, 2003).

However, while powerful, such genetic tools are not suitable for monitoring non-proteinaceous biomolecules, including glycans and lipids (Patterson *et al.*, 2014). Moreover, the molecular size of fluorescent proteins and antibodies is often as large as or even larger than the biomolecule of interest which can lead to manipulation of the original function, steric hindrances and antibody induced clustering effects which all cause problems when performing quantitative fluorescence imaging. An alternative to fluorescent protein tagging and antibody staining is the use of fluorescent chemical compounds. These chemical compounds have beneficial properties such as a small molecule size, various labeling positions and wide variation of their optical spectrum (Horisawa, 2014). This strategy relies on the installation of unique functional groups into target biomolecules that can be ligated in a second step. The chemical reactions must be selective and non-perturbing to biological systems. For these reasons, they have been collectively termed bioorthogonal (Prescher *et al.*, 2004; Patterson *et al.*, 2014).

Bioorthogonal Chemistry. The term "bioorthogonal" was first used in 2003 (Hang *et al.*, 2003) and describes the following requirements: the participating functional groups must be inert to biological moieties, must selectively react with each other under biocompatible conditions, and, for *in vivo* applications, must be nontoxic to cells and organisms. Furthermore, it is helpful if one reactive group is small and therefore minimally perturbing a biomolecule into which it has been introduced either chemically or biosynthetically (Sletten and Bertozzi, 2009). In a first step, the functional group (or chemical reporter) is incorporated into the target biomolecule using the cell's metabolic machinery. This process is called "metabolic labeling". Subsequently, the reporter is covalently tagged with an exogenous probe, e.g. a fluorophore, using a highly selective chemical reaction, often termed "click chemistry" (Agard *et al.*, 2006). This two-step procedure has been used to visualize and study proteins, glycoproteins, glycolipids and nucleic acids in cells, tissues and living organisms (Mahal *et al.*, 1997; Saxon and Bertozzi, 2000; Link *et al.*, 2006; Laughlin *et al.*, 2008; Tom Dieck *et al.*, 2012; Löschberger *et al.*, 2014). In the field of membrane biology, membrane-associated glycans, defined as the carbohydrate portion of a membrane glycoconjugate (e.g. glycoprotein or –lipid), can be visualized by treating cells or tissue with unnatural monosaccharide substrates. Often, these sugar derivatives are azide-functionalized monosaccharides such as tetraacetylated N-azidoacetyl–mannosamine (Ac_4ManNAz), –galactosamine (Ac_4GalNAz) and –glucosamine (Ac_4GlcNAz) which, upon cellular uptake and deacetylation are incorporated by the biosynthetic machinery into sialic acids, mucin-like O-linked glycans and O-GlcNac modified proteins, respectively (Laughlin and Bertozzi, 2009; Homann *et al.*, 2010). Additional approaches to metabolically engineer membrane proteins are the incorporation of amino acid analogs into proteins by genetic encoding and site- specific modification (Uttamapinant *et al.*, 2013), or by replacing a native amino acid by its non-natural analog (e.g. azido-functionalized alanines, Tom Dieck *et al.*, 2012).

Following the Staudinger ligation between azides and phosphines (Staudinger and Meyer, 1919) and its modified form, the Staudinger-Bertozzi reaction (Saxon and Bertozzi, 2000, Figure 1.5 A(i)), a large range of different chemical reactions between functionalized biomolecules (e.g. azido–sugar derivatives) and reactive reporter molecules (e.g. fluorophore–alkynes) have been developed which are termed "click" reactions or in general "click chemistry" (Kolb *et al.*, 2001). One of the most prominent example for click chemistry is the reaction between azides and alkynes which will be described in the following sections.

Copper-catalyzed Click Chemistry. The chemical reaction between an azide and an alkyne belongs to the family of 1,3-dipolar cycloadditions and was established in 1963 (Huisgen, 1963). During this reaction which is also termed Huisgen cycloaddition, a 1,3-dipole, the azide, reacts with a dipolarophile, the alkyne, to form a 1,2,3-triazole (Figure 1.5 B). However, due to a lack of reactivity, high temperatures or pressures are required to promote this reaction which disqualifies it for use in most biological samples and living systems.

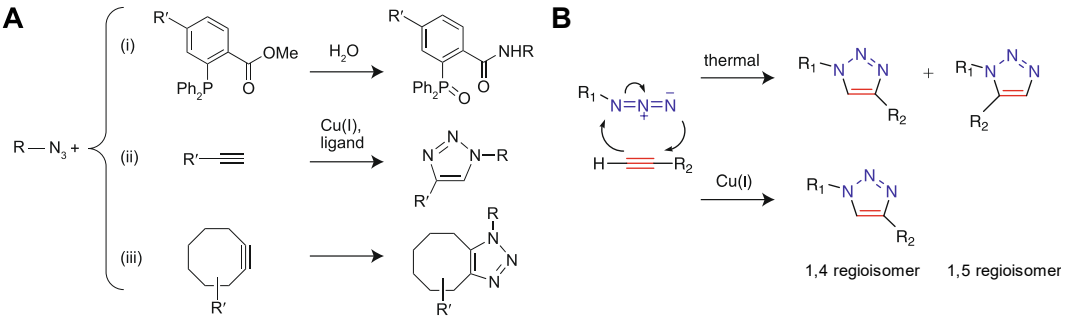

Figure 1.5: Bioorthogonal reactions using azides as chemical reporter groups. (**A**) Azide-functionalized biomolecules react via the Staudinger-Bertozzi ligation (i), a copper-catalysed (ii) or a strain-promoted (iii) cycloaddition resulting in ligated products. (**B**) 1,3-dipolar cycloaddition of an azide (blue) and a terminal alkyne (red). Without using copper (Cu(I)) as a catalyst, the cycloaddition needs high temperatures and is non-regiospecific. Adapted with permission from Agard *et al.*, 2006, Copyright 2006 American Chemical Society (**A**) and Evans, 2007 (**B**).

Still, due to its high potential, the relatively stable and small azide group, and the formation of stable aromatic triazole products, further investigations and optimizations have been made. Sharpless and colleagues as well as Meldal and coworkers discovered in 2002 independently from each other that the formal 1,3-dipolar cycloaddition of azides with terminal alkynes to produce 1,4-disubstituted 1,2,3-triazoles could be effectively catalyzed by copper(I) (Rostovtsev *et al.*, 2002a; Tornøe *et al.*, 2002). During the so called copper-catalyzed azide–alkyne cycloaddition (CuAAC) terminal alkynes are activated by the formation of copper acetylides which then react with azides (Figure 1.5 A(ii) and B, Figure 1.6). The advantage of CuAAC is its reaction speed which is about seven orders of magnitude higher than the uncatalyzed Huisgen cycloaddition. Moreover, the addition of specific Cu(I) ligands further accelerates the reaction (Uttamapinant *et al.*, 2012). The CuAAC exhibits all essential properties of a click reaction which are efficiency,

simplicity, and selectivity. In this way, CuAAC has become a widespread and versatile tool in many fields of chemistry and biology (Wang *et al.*, 2003; Sletten and Bertozzi, 2009).

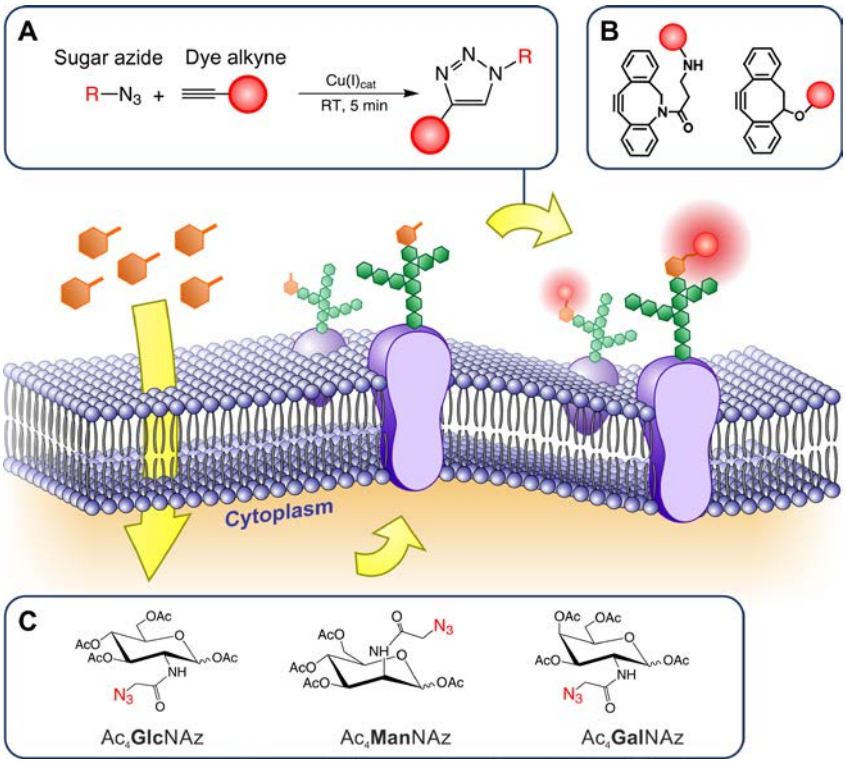

Figure 1.6: Metabolic labeling and click chemistry. Specific labeling of glycan subtypes with fluorophores is carried out in a two-step procedure. First, cells are fed with chemically reactive azido-sugars (**C**). These monosaccharide derivatives are metabolically incorporated into the target glycoconjugate subtype. In the second step, the azide-labeled glycan can be detected with an alkyne modified fuorophore via CuAAC (**A**) or SPAAC (**B**). Adapted from Mateos-Gil *et al.*, 2016.

Copper-free Click Chemistry. Apart from its excellent reaction efficiency, CuAAC has a huge downside regarding its application in biology. The catalytically active copper(I) is toxic to biological samples and living organisms as has been shown in previous experiments (Sletten and Bertozzi, 2009). While there are some ways to alleviate copper(I)-induced toxicity by, for example, adding additional additives and copper-chelating ligands (Uttamapinant *et al.*, 2012; Gutmann *et al.*, 2016) or by removing oxygen (Löschberger *et al.*, 2014), a more elegant strategy is to activate the alkyne in a completely different way. Instead of using metal catalysts

such as copper(I), Bertozzi and colleagues developed and synthesized strained alkynes by incorporating the alkyne group into a cyclooctan and by using the ring strain effect. These cyclooctynes are highly reactive with azides without the need for additives and copper, and thereby have formed the basis for the so called copper-free click chemistry, or strain-promoted azide–alkyne cycloaddition (SPAAC, Figure 1.5 A(iii), Figure 1.6). Since the first application of SPAAC, a wide range of optimized cyclooctynes has been developed such as difluorinated cyclooctyne (DIFO, Baskin *et al.*, 2007), and azadibenzocyclooctyne (DBCO, Debets *et al.*, 2010) which exhibit substantially increased reaction rates compared to first generation compounds or the Staudinger ligation. A schematic overview about the two-step procedure of bioorthogonal chemistry is presented in Figure 1.6.

2 Materials and Methods

2.1 Sample Preparation

The microscopical visualization of different cellular structures requires different, well approved staining approaches. Staining starts with cell culture. Questions like which cell line is best for a certain structure should be addressed in the same manner as the question for the availability of appropriate control cell lines. Factors like the cell type (adherent vs. suspension), the location of the target (intra- vs. extracellular), the size of the label (antibody vs. chemical tag) and the intention of the approach (qualitative vs. quantitative) play important roles during the decision-making process. The following sections list several important protocols used mainly in this work. Project-related methods are described in detail in the respective manuscript (Chapter 3 and section "Publications" at the end of this work).

All buffers and solutions were prepared with phosphate buffered saline (PBS) unless stated otherwise. In general, between two preparation steps (e.g. fixation and permeabilization) cells were washed at least three times with PBS (3× 5 min) unless stated otherwise. All preparation steps were performed at room temperature (RT), unless stated otherwise, and on 8-well chamber slides (Nunc Lab-Tek II Chamber Slide System, Thermo Fisher Scientific), hereinafter referred to as Lab-Tek(s).

2.1.1 Cell Culture

As a model system for adherent human cells, the osteosarcoma cell line U2OS was predominantly used in this work. U2OS cells were cultured in DEMEM Ham's F12 containing 10% FCS, 100 U/ml penicillin and 0.1 mg/ml streptomycin at 37 °C and 5% CO_2. The neuroblastoma cell line SK-N-MC was cultivated in RPMI-1640 medium supplemented with sodium pyruvate, 10% FCS, 4 mM glutamine, 100 U/ml penicillin and 0.1 mg/ml streptomycin at 37 °C and 5% CO_2. Cells were

grown in standard T25-culture flasks (Greiner Bio-One) up to a confluence of about 80–90%. For passaging, cells were washed once with PBS and treated with accutase for 5 min. Cells were seeded at a concentration of 1×10^4 cells/well into LabTeks and stained after two days of incubation. In the case of click chemistry experiments, cells were grown in medium supplemented with 25 μM sugar derivatives such as Ac_4GlcNAz, Ac_4GalNAz, and Ac_4ManNAz (Thermo Fisher Scientific) for two days (Letschert *et al.*, 2014; Burgert *et al.*, 2015; Mateos-Gil *et al.*, 2016; Mertsch *et al.*, 2016). Cell culture was mainly performed by Lisa Behringer-Pließ and Petra Geßner. A list of used cell lines is depicted in Table 2.1.

Table 2.1: List of used cell lines and corresponding projects.

Cell line	Cell type	Project
SK-N-MC	Neuroblastoma	Glycans
U2OS	Osteosarcoma	Glycans, Mitochondria
HeLa	Cervix carcinoma	Endocytosis
K-562	Chronic myeloid leukemia in blast crisis	CD19
MM.1S	Plasma cell myeloma	CD19
JeKo-1	B cell lymphoma	CD19
Raji	Burkitt lymphoma	CD19
NALM-6	B cell precursor leukemia	CD19

2.1.2 Immunofluorescence

CD19. To ensure an appropriate adherence of suspension cells to the microscope slide LabTeks were cleaned and coated with poly-D-lysine (PDL). In detail, LabTek chambers were incubated with 1 N KOH for 15 min. After three washing steps with mqH_2O, 0.05 mg/ml PDL was added. After 2–3 h of incubation, the PDL solution was removed and the open LabTek was dried for another hour at RT under sterile conditions. Next, LabTeks were filled with suspension cells, meaning primary cells as well as control cell lines and co-cultures, respectively which were let to adhere for 90 min at 37 °C. Afterwards, cells were cooled down slowly to 4 °C and washed three times with ice cold PBS to inhibit endocytosis. Then, cells were incubated with anti-CD38-AF488, anti-CD138-AF555 and anti-CD19-AF647 or AF647 isotype control antibodies for 30 min on ice (2.5 μg/ml each, see Table 2.2) before being washed with PBS and fixed with cold FA (4 % in PBS) for at least 2 h.

Mitochondria. For labeling of proteins in the mitochondrial inner membrane, antibodies have to pass through two membranes, the plasma membrane and the mitochondrial outer membrane. Furthermore, the crowded environment inside of

mitochondria coming from the extremely folded inner membrane which is deeply packed with huge protein complexes of the electron transport chain, impedes a sufficient access to the desired structure (in this case cristae). For that reason, it was necessary to permeabilize cells sufficiently without destroying the cellular structure at the same time. U2OS and HMLE cells were fixed in 4 % FA at RT for 10 min. After washing, ice cold methanol (−20 °C) was added and the LabTek was placed in the freezer for 20 min at −20 °C. Alternatively, cells were permeabilized in 0.2 % TritonX-100 at RT for 10 min. To prevent unspecific binding cells were blocked with 5 % bovine serum albumin (BSA, blocking buffer) for 30 min. Next, a cocktail of primary antibodies (Mouse anti-human OxPhos Complex I–V, Thermo Fisher Scientific, Table 2.2) was added for 90 min to address all subunits, that is Complexes I–V of the respiratory chain in the inner membrane. The antibody mixture was diluted in blocking buffer to a final concentration of 7.5–15 μg/ml. Cells were then incubated with 10 μg/ml of secondary antibody diluted in blocking buffer which was goat anti-mouse F(ab')$_2$ fragments coupled to Alexa Fluor 647 (Thermo Fisher Scientific, Table 2.2). Between each antibody incubation step cells were washed three times with PBS supplemented with 0.05% Tween 20. To prevent antibody detaching a post-fixation step in 4 % FA for 10 min was performed.

Table 2.2: List of used primary and secondary Antibodies

Type	Specificity	Conjugate	Used concentration	Company
Primary Antibodies	Mouse anti-human OxPhos Complex I–V Ig mix (Mitochondria)	–	7.5–15 μg/ml	Thermo Fisher Scientific, 458199
	Mouse anti-ATPase α subunit IgG	–	5 mg/ml	Thermo Fisher Scientific, 459240
	Mouse anti-human CD38 IgG	Alexa Fluor 488	2.5 μg/ml	BioLegend, 303512
	Mouse anti-human CD138 IgG	Alexa Fluor 555*	2.5 μg/ml	BioLegend, 356502
	Mouse anti-human CD19 IgG	Alexa Fluor 647	2.5 μg/ml	BioLegend, 302220
	Mouse Isotype Control	Alexa Fluor 647	2.5 μg/ml	BioLegend, 400130
Secondary Antibodies	Goat anti-mouse F(ab')$_2$	Alexa Fluor 647	10 μg/ml	Thermo Fisher Scientific A-21237

*Unlabeled antibody which was conjugated to Alexa Fluor 555 NHS ester (Thermo Fisher Scientific)

Labeling of Antibodies. Because of a limited range of commercially available primary antibodies coupled to a fluorophore of interest, some primary antibodies were conjugated to Alexa Fluor NHS esters with subsequent purification. This was achieved in a two-step procedure. In the first step, the antibody storage buffer was replaced by the use of desalting columns (Zeba Spin Desalting Columns 40K MWOC, Thermo Fisher Scientific) with a conjugation buffer which consisted of 100 mM sodium hydrogen carbonate ($NaHCO_3$, pH ~8.4). Typically, 0.06–0.1 mg protein (IgG) was incubated with a 10 fold molar excess of dye NHS ester (e.g. Alexa Fluor 555 NHS ester, Thermo Fischer Scientific) in conjugation buffer for 2–3 h at RT and in the dark. In a second step, the protein was separated from unconjugated dye by size exclusion chromatography (Zeba Spin Desalting Columns 40K MWOC, Thermo Fischer Scientific) and stored in PBS with 0.02% sodium azide as a preservative. The degree of labeling (DOL) was calculated based on the absorption at 280 nm and the particular peak wavelength of the used fluorophore (NanoPhotometer, Implen). The DOL was on average between three and four fluorophors per IgG antibody.

2.1.3 Click Chemistry

Neuroblastoma and U2OS cells were fed with azido sugar derivatives for two days (Chapter 2.1.1, Cell Culture). For CuAAC, cells were washed once with PBS and incubated with a premixture of 50 μM $CuSO_4$, 250 μM THPTA, 2.5 mM sodium ascorbate and 20 μM Alexa Fluor 647 alkyne in PBS for 5 min at RT. Regarding the premixture, it is essential that first, THPTA (stock solution) is added to the copper stock solution, next, a freshly prepared ascorbate solution is added following PBS, and last but not least the dye–alkine (DMSO stock) is added. For SPAAC cells were incubated with 30 μM of Alexa Fluor 647 DIBO for 1 h, and with Cy5 DBCO for 15 min, respectively. Next, cells were washed three times with PBS and fixed with 4 % FA and 0.2 % GA in PBS for 1 h at RT. Stained cells were either directly used for *d*STORM measurements or stored at 4 °C for a maximum of two weeks.

2.2 Localization Microscopy

2.2.1 Microscopy Setups

For *d*STORM measurements two custom-built wide-field setups were used, dependent on the needed excitation light. Both setups consist of an inverted wide-field fluorescence microscope (IX-71, Olympus) that was placed on an air-damped optical table (Linos). The first setup which was used for imaging membrane-associated glycans and mitochondria (Manuscripts 1, 2 and 3) will be described in the following. For excitation of Alexa Fluor 647 and Cy5, a 641-nm diode laser (Cube 640-100C, Coherent) was used whose light was spectrally cleaned by a clean-up filter (Laser Clean-up filter 640/10, Chroma). The laser beam was focused onto the back focal plane of an oil-immersion objective (60×, NA 1.45; Olympus). Drift was reduced by the usage on a nosepiece stage (IX2-NPS, Olympus). The emission light was separated from the illumination light using a dichroic mirror (HC 560/659, Semrock), spectrally filtered by a bandpass filter (HC697/75 and LP647, Semrock) and projected onto an electron-multiplying CCD camera chip (iXon DU-897, Andor). Placing additional lenses in the detection path, a final pixel size of 134 nm could be generated.

The second setup was used for multi-color imaging of cell surfaces stained with anti-CD19, -CD38, and -CD138 antibodies (Alexa Fluor 647, 555 and 488, respectively; Manuscript 4). The setup was equipped with an oil-immersion objective (APON 60XOTIRF, NA 1.49, Olympus) and a nosepiece stage (IX2-NPS, Olympus). Alexa Fluor 647, 555 and 488 were excited with the appropriate laser systems (Genesis MX 639 and MX 561, both Coherent, and iBeam smart 488 nm, Toptica). The excitation light was spectrally cleaned by appropriate bandpass filters and then focused onto the back focal plane of the objective. To switch between different illumination modes (epi and TIRF illumination), the lens system and mirror were arranged on a linear translation stage. A polychromatic mirror (HC 410/504/582/669, Semrock) was used to separate excitation (laser) and emitted (fluorescent) light. The fluorescence emission was collected by the same objective and transmitted by the dichroic beam splitter and several detection filters (HC 440/521/607/700, Semrock; HC 679/41, Semrock, for Alexa Fluor 647; HQ 610/75, Chroma, for Alexa 555; ET 525/50, Chroma, for Alexa 488), before being projected onto two electron-multiplying CCD cameras (both iXon Ultra 897, Andor; beam splitter 635 LP, Semrock). A final pixel size of 128 nm was generated by placing additional lenses in the detection path.

2.2.2 *d*STORM Measurement

To enable reversible photoswitching of Alexa Fluor 647, fixed cells were exposed to a thiol-containing buffer at pH 7.4–7.8. This switching buffer contained 80–100 mM β-mercaptoethylamine (MEA; cysteamine hydrochloride, Applichem) in PBS. The pH was adjusted with potassium hydroxide (KOH). For appropriate switching rates of Alexa Fluor 647, oxygen was removed with the help of an oxygen scavenger system containing 3% (*w*/*v*) glucose, 4 U/mL glucose oxidase and 80 U/mL catalase (Uppoor and Niebergall, 1996). Efficient oxygen reduction in aqueous solution is also possible with mere MEA at mM concentrations (Schäfer *et al.*, 2013). However, in order to ensure a stable and robust oxygen scavenging, especially in cases of very densely labeled structures, the above described enzyme-based system was additionally used. Samples (LabTeks) were placed on the microscope's sample holder, and, after recording a conventional fluorescent image, fluorophores were illuminated with excitation light of 3–7 kW/cm^2 for being transferred into the photoswitching mode. Typically, 15,000 frames were recorded with frame rates ranging from 100 to 50 Hz (10–20 ms exposure time).

2.2.3 Image Reconstruction and Data Analysis

Position Determination and Reconstruction. From the recorded image stack, a table with all localizations as well as a reconstructed *d*STORM image was generated using the freely available localization software rapi*d*STORM 3.3 (for details see Wolter *et al.*, 2010; Wolter *et al.*, 2012). In short, rapi*d*STORM identifies, among other parameters, the position and intensity of individual fluorophores by fitting a two-dimensional Gaussian function to the PSF-blurred emission patterns. The extracted localizations of a *d*STORM movie can be used to reconstruct a single, super-resolved image (see also Chapter 1.2.2). Moreover, rapi*d*STORM provides correction, filtering, and post processing features such as linear drift correction, intensity thresholding, z-position determination for 3D imaging, tracking, and many more. Here, localizations containing less than 800–1,000 photons were typically discarded to discriminate from background noise and false-localizations. All localizations were saved in a single text file (localization file) which was used for further analyses.

Quantification. Quantification of plasma membrane molecules was mainly conducted with the software Locan. This software package is based on the Wolfram language Mathematica and has been developed by PD Dr. Sören Doose (Department of Biotechnology and Biophysics, University of Würzburg). It offers a

broad range of different tools for analyzing SMLM data, starting with simple plotting of localization coordinates to more complex features such as localization-based cluster analysis (Ripley functions, alpha shapes, DBSCAN, etc.). Moreover, it implements tools for determination of localization precision, comparison of subpopulations, spectral demixing, and many more. In this work, Locan was used for the quantification of CD19 molecules on multiple myeloma cells (for details see Manuscript 4). Briefly, repeated localizations coming from individual fluorescence-labeled CD19 molecules were grouped using the alpha shape algorithm (Chapter 1.2.3). By a serial cluster finding tool, it was confirmed that the overall density of detected antibodies was small enough to yield well-separated alpha-shapes (for details on parameter finding see Chapter 4.2.2).

Further software tools. The open-source platform Fiji (an ImageJ distribution) offers a large number of standard features and additional plugins for scientific image analysis (Schindelin *et al.*, 2012). In this work, it was used for general image analysis and image processing procedures such as contrast adjustment and normalization, bit-depths and file format conversion, Gaussian blurring for display optimization, channel alignment, adjustment of pixels sizes, analysis of pixel intensities, addition of scale bars, color adjustment, etc. Furthermore, Fiji is very suitable for automatization of repeated standard operations using its java-based macro language. Besides Fiji, a range of Python scripts (Python 2.7) were written and implemented for various data analysis and automatization procedures. Final images and figures suitable for publication were made with CorelDraw Graphics Suite X7 (Corel).

3 List of Publications

This thesis is based on the following four publications:

1. Letschert, S., Göhler, A., Franke, C., Bertleff-Zieschang, N., Memmel, E., Doose, S., Seibel, J., Sauer, M. (**2014**): Super-Resolution Imaging of Plasma Membrane Glycans. *Angewandte Chemie International Edition* 53 (41), 10921–10924

2. Burgert, A.*****, Letschert, S.*****, Doose, S., Sauer, M. (**2015**): Artifacts in single-molecule localization microscopy. *Histochemistry and cell biology* 144 (2), 123–131
   **authors equally contributed*

3. Mateos-Gil, P., Letschert, S., Doose, S., Sauer, M. (**2016**): Super-resolution imaging of plasma membrane proteins with click chemistry. *Frontiers in Cell and Developmental Biology*. 4, 98

4. Nerreter, T.*****, Letschert, S.*****, Doose, S., Danhof, S., Einsele, H., Sauer, M., Hudecek, M.: CD19CART cells eliminate myeloma cells expressing very low levels of CD19 (**in submission**)
   **authors equally contributed*

Further publications

Eyss, B. von, Jaenicke, L.A., Kortlever, R.M., Royla, N., Wiese, K.E., Letschert, S., McDuffus, L.-A., Sauer, M., Rosenwald, A., Evan, G.I., Kempa, S., Eilers, M. (2015): A MYC-Driven Change in Mitochondrial Dynamics Limits YAP/TAZ Function in Mammary Epithelial Cells and Breast Cancer. *Cancer Cell* 28 (6), 743–757

Mertsch, A., Letschert, S., Memmel, E., Sauer, M., Seibel, J. (2016): Synthesis and application of water-soluble, photoswitchable cyanine dyes for bioorthogonal labeling of cell-surface carbohydrates. *Zeitschrift für Naturforschung. C, A Journal of Biosciences* 71 (9-10), 347–354

Jung, L.A., Gebhardt, A., Koelmel, W., Ade, C.P., Walz, S., Kuper, J., Eyss, B. von, Letschert, S., Redel, C., d'Artista, L., Biankin, A., Zender, L., Sauer, M., Wolf, E., Evan, G., Kisker, C., Eilers, M. (2017): OmoMYC blunts promoter invasion by oncogenic MYC to inhibit gene expression characteristic of MYC-dependent tumors. *Oncogene* 36 (14), 1911–1924

Lukeš, T., Glatzová, D., Kvíčalová, Z., Levet, F., Benda, A., Letschert, S., Sauer, M., Brdička, T, Lasser, T., Cebecauer, M. (2017): Quantifying protein densities on cell membranes using super-resolution optical fluctuation imaging. *Nature Communications* 8, 1731

4 Results and Discussion

4.1 Artifacts in SMLM

This chapter describes a project that addresses the generation of artifacts and the risk of its misinterpretation when using *d*STORM imaging for analysis of plasma membranes. The full description of results can be found in detail in Manuscript 2 (Burgert *et al.*, 2015) and to a minor extent in Manuscript 3 (Mateos-Gil *et al.*, 2016).

Since single-molecule localization microscopy provides the ability to resolve subcellular structures with high precision and in the nm-range, it has become more and more popular. Photoswitching microscopy such as *d*STORM requires fluorophores that can be reversibly switched between a fluorescent *on* and a non-fluorescent *off* state. The fluorescence emission of individual fluorophores must be separated in time in order to ensure precise single-molecule localization. Nevertheless, especially in the case of densely labeled structures, such as membrane-associated glycans (chapter 4.2.2), the *off* state should have a lifetime τ_{off} which is considerably longer than the lifetime of the fluorescent *on* state τ_{on}. Photoswitching can be described as the ratio $r = \tau_{off}/\tau_{on}$ and furthermore as the ratio between the *off* rate k_{off} (transfer to the metastable *off* state) and k_{on} (conversion into the singlet ground state). For a precise localization, τ_{on} should be very short while, at the same time, the fluorophore should have ideally a high photon yield (Thompson *et al.*, 2002). As a result, the denser a structure is labeled with fluorophores, the higher the rate-ratio r has to be to ensure temporally well separated fluorescence emissions from single fluorophores, and thus allowing a distinct localization of individual emitters (van de Linde *et al.*, 2010). The rate-ratio r can be controlled by a range of parameters such as irradiation intensity, the composition of switching buffer (pH, reductant concentration) as well as the choice of the fluorophore. Furthermore, the emitter spot density per frame is dependent on the exposure time of the camera. As a rule of thumb and in the case of classical single-molecule fitting algorithms, the emitter density should not exceed 0.6 emitter per μm^2 and

frame (Wolter *et al.*, 2011). Is the emitter density too high so that r cannot be controlled sufficiently, the fluorophore density has to be decreased by reducing the label concentration (e.g. antibody concentration). However, it has to be mentioned that in any case, the Nyquist-Shannon sampling theorem must be fulfilled in order to resolve the structure of interest appropriately (Chapter 1.2.2).

If more than one emitter are simultaneously in the *on* state and, additionally, are located in the same diffraction-limited area, their PSFs will overlap which results in a blurred or asymmetric emission pattern. These multiple emitter spots are either sorted out during software analysis or, in cases of only small irregularities, are fitted and counted as one localization whose coordinates do not match the real position of the fluorophores. In the latter case, these false or multiple emitter localizations will lead to a loss of structural information and to the generation of artifacts in the reconstructed image. This effect can be imposingly demonstrated by simulations and super-resolution imaging of linear cytoskeleton polymers such as microtubules and actin filaments as has been previously reported (van de Linde *et al.*, 2010; Sauer, 2013; van de Linde and Sauer, 2014). Whereas the operator expects single, parallel, and crossing lines when imaging cellular filaments and thus is able to evaluate the quality of the reconstructed image, it gets more difficult when the structure of interest is unknown and more complex.

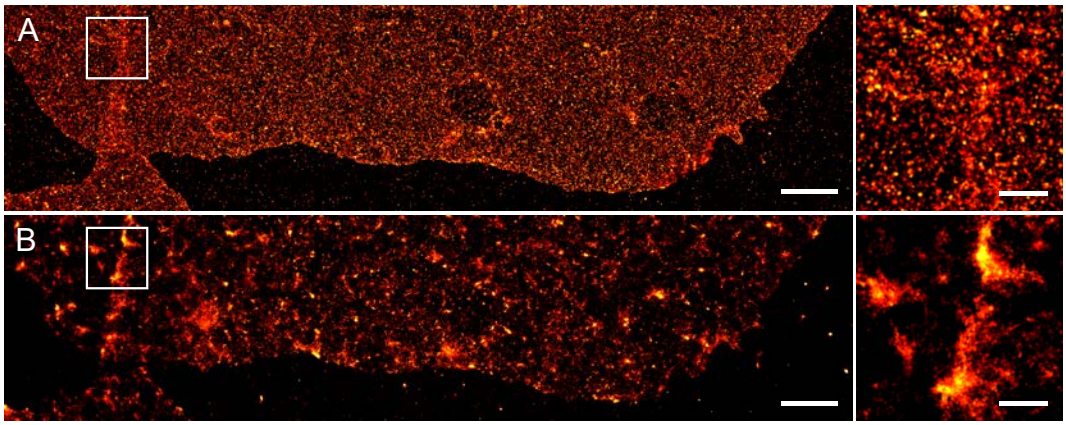

Figure 4.1: Photoswitching induced artifacts in localization microscopy images of plasma membranes. *d*STORM imaging of densely labeled structures with low irradiation intensities results in reconstruction of artificial membrane clusters. Homogeneously distributed glycans in the plasma membrane of U2OS cells were irradiated with 7 kW/cm^2 (**A**) and ~0.5 kW/cm^2 (**B**). Scale bars, 2 μm (left panels) and 500 nm (right panels). Adapted from Burgert *et al.*, 2015.

For that reason, the impact of inappropriate photoswitching rates on reconstructed images of membrane-associated glycans and other cellular structures such as mitochondria and microtubules were analyzed (Manuscript 2, Burgert *et al.*, 2015). To obtain densely labeled membrane samples, U2OS cells were metabolically glycoengineered and bioorthogonally labeled as described in Chapters 2.1.3 and 4.2.2. Additionally, Alexa Fluor 647–conjugated wheat germ agglutinin (WGA) was used to visualize specific membrane glycans. By imaging the bottom plasma membrane of stained U2OS cells with different irradiation intensities, the effect of too low photoswitching rate-ratios could be intentionally induced and observed (Figure 4.1). Whereas high irradiation intensities (up to 7 kW/cm^2) resulted in appropriate photoswitching rates and thus, a virtually homogeneous distribution of membrane-associated glycans (Figure 4.1 A), intensities of $\leq$ 1 kW/cm^2 led to the generation of artificial clusters (Figure 4.1 B). Moreover, with decreasing irradiation intensity (and thus decreasing r) the size of artificial clusters increased substantially due to a considerably increased spot density per frame. Especially in areas with extremely high spot densities, such as overlapping membranes or 2D-projections of filopodia and microvilli, large artificial clusters could be observed which might be misinterpreted as laterally organized nanodomains or protein clusters (Figure 4.1 A and B, right panels). These observations led to a more refined analysis of two-dimensional (2D) projections of labeled structures above and below the image plane. When a three-dimensional (3D) structure is projected on a 2D image, local inhomogeneities in the localization density pattern are induced while the actual density of fluorophores in the membrane structure remains constant. Combined with inappropriate switching rates, artifacts are generated at locations where the projection is at its highest level. In most cases, the risk of misinterpreting such artificial structures can be prevented by slightly lifting the image plane and by changing the illumination mode from TIRF to HILO or Epi (Figure 4.2). Thereby, structural membrane inhomogeneities such as budding vesicles (Figure 4.2 A and B) or membrane invaginations (Figure 4.2 C and D) can be easily detected and defined as such.

The results of this project (Manuscript 2, Burgert *et al.*, 2015) demonstrate that imaging plasma membranes with photoswitching localization microscopy is prone to user errors and misinterpretations. Even if the sample is efficiently labeled, wrong buffer conditions, inappropriate fluorophores or low irradiation intensities can cause super-resolution imaging artifacts. Nevertheless, if the distribution and organization of membrane components, especially in regions with inhomogeneous and locally high emitter densities, is interpreted with caution and imaging parameters are controlled in a proper way, super-resolution by *d*STORM can be a powerful tool to visualize, analyze and quantify plasma membrane molecules. In order

to evaluate the quality of reconstructed *d*STORM images, it is recommended to investigate the raw data movie which reveals information about photoswitching behavior, emitter density (<1 spot per μm^2 and frame) and robustness of the microscope setup (e.g. drift, illumination pattern etc.)(Burgert *et al.*, 2015).

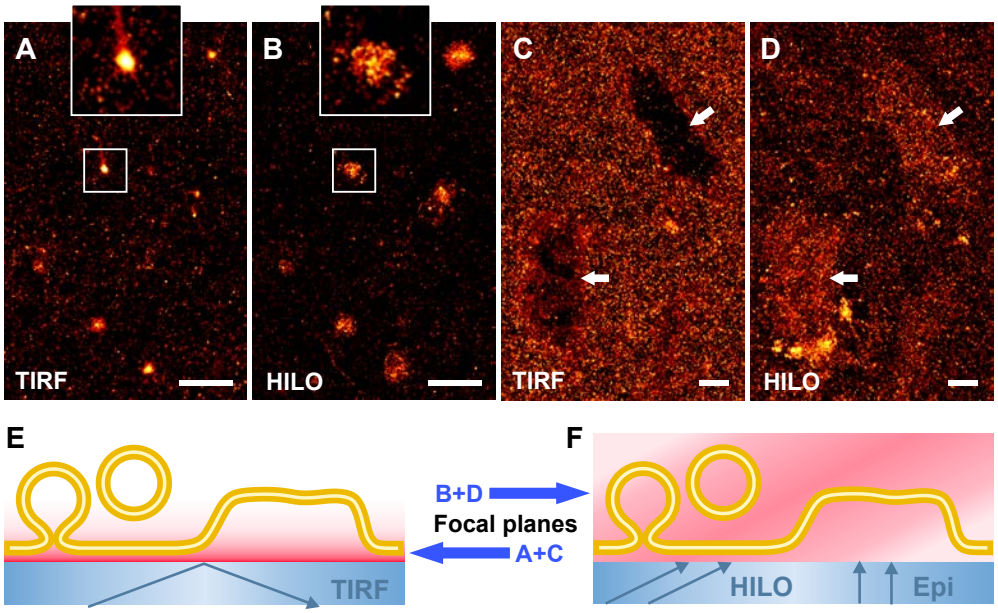

Figure 4.2: Artificial clusters and 2D projections in the plasma membrane induced by vesicles (**A**) and membrane invaginations (**B**). *d*STORM imaging was performed with high irradiation intensities (~7 kW/cm^2) on bioorthogonally labeled glycans in the bottom plasma membrane of osteosarcoma cells. (**A**, **C**) TIRF and (**B**, **D**) HILO illumination with slightly shifted focal planes (**E**, **F**). Artifacts in (**A**) are generated due to non-switching background signal resulting from budding vesicles filled with fluorophores that are located right above the plasma membrane and being detected as such with HILO or Epi illumination (**B**). 2D projections of plasma membrane invaginations (arrows) and modulations may create the impression of local inhomogeneities in the expression pattern of membrane-associated glycans (**C**, **D**). Scale bars, 1 μm.

Further analysis of membrane components could be performed using 3D single-molecule localization microscopy with high axial resolution such as astigmatism or biplane imaging (Huang and Jones *et al.*, 2008; Huang and Wang *et al.*, 2008; Klein *et al.*, 2014), lattice light-sheet and PAINT imaging (Legant *et al.*, 2016), and photometric intensity-based imaging (TRABI, Franke *et al.*, 2017). Especially in the case of a highly structured and modulated plasma membrane, novel 3D microscopy techniques in combination with localization-based quantification could substantially contribute to an improved deciphering of plasma membrane organization. Another promising approach in order to prevent artifact generation due to inappropriate switching rates is the use of specialized algorithms that are

capable of fitting multiple emitter spots such as DAOSTORM (Holden *et al.*, 2011), Bayesian statistics (Quan *et al.*, 2011), and compressed sensing (Zhu *et al.*, 2012). These methods, additionally, allow for an increased temporal resolution (shorter acquisition times) due to the ability of processing and assessing high emitter densities. Alternatively, super-resolution optical fluctuation imaging (SOFI) can be applied to high emitter density images or in cases where r cannot be controlled anymore (Dertinger *et al.*, 2009). Instead of fitting isolated or overlapping PSFs, SOFI is based on the temporal correlation of independently fluctuating fluorescent emitters and was recently used to extract structural and quantitative information out of highly and densely labeled plasma membrane glycoproteins in T cells without the generation of artifacts (Lukeš *et al.*, 2017). However, besides its advantages of SOFI especially when it comes to imaging speed and low SNR, localization microscopy delivers the highest resolution in wide-field light microscopy if sample requirements are met and photoswitching rates are set appropriately (Geissbuehler *et al.*, 2011).

4.2 Quantification of Plasma Membrane Components

In the following Chapter, two projects are described in which *d*STORM is used to investigate the molecular distribution and quantity of plasma membrane components. The topic of the first project is the combination of a bioorthogonal chemical reporter strategy with structural and quantitative analysis of membrane-associated glycoconjugates using *d*STORM. The results of this project are described in detail in Manuscript 1 (Letschert *et al.*, 2014) and Manuscript 3 (Mateos-Gil *et al.*, 2016). The second project is about the identification and quantification of the immune-relevant membrane receptor CD19 on multiple myeloma cells. A detailed description can be found in Manuscript 4 (Nerreter *et al.*, in submission). From a methodological point of view, these two projects highlight two completely different labeling strategies for visualizing plasma membrane components. Nevertheless, they both have in common that for super-resolution microscopy plasma membranes are difficult to prepare and that one has to be cautious in interpreting results. On that account, this chapter starts with the description and discussion of observations and results in relation to the preparation of plasma membranes for super-resolution fluorescence microscopy.

4.2.1 Preparation of Biomembranes for Super-Resolution Imaging

The aim of cell preparation (i.e., fixation, staining, washing, etc.) is to change as little as possible between the initial, native state and the final state of a membrane component and its environment. Therefore, a series of requirements must be observed. First of all, the cell needs to be immobilized on the cover slip surface. Adherent cells are doing this on their own whereas suspension cells must be immobilized by changing the surface's physical or biochemical properties using coating compounds like polylysine, glycine, gelatin, laminin or fibronectin (Mazia, 1975; Khan and Newaz, 2010). In this work, poly-D-lysine (PDL) was used to attach mainly myeloma cells (MM cell lines and primary MM cells) to the cover slip surface (Figure 4.3, see also Manuscript 4, Nerreter *et al.*, in submission). To study membrane protein distributions and quantities, the bottom (or "basal") plasma membrane of adherent or surface-attached suspension cells can be efficiently visualized by TIRF microscopy in which only the first 100–200 nm above the glass surface get illuminated (Figure 4.3 A–C). In this way, the signal-to-background ratio is enhanced by reduction of background fluorescence coming from higher planes. Furthermore, unspecific binding of antibodies or other labeling compounds to the surface can be analyzed by counting fluorescent spots next to the cell (Figure 4.3 A). Unspecific binding can be reduced by usually coating the surface with BSA or in some cases glycine, for example (Klein *et al.*, 2011). However, antibodies and other labeling compounds ideally should not be attracted by cover slip surfaces and thus being washed away during washing steps.

The probably biggest issue in cell preparation is the fixation of membrane components. The aim of cell or tissue preparation is to fix target molecules at the location where they exist in living cells at the moment of interest (Takatori *et al.*, 2014). For staining intracellular structures —as for example actin or microtubule filaments— the membrane must be permeabilized to allow large molecules, such as antibodies to pass through. Therefore, the cell is usually fixed in a first step followed by permeabilization, blocking with e.g. BSA, antibody incubation and postfixation (Small *et al.*, 1999). As opposed to that, staining of membrane components requires a completely intact plasma membrane, so that permeabilization caused by reagents and additives should be avoided. Otherwise, fluorophores and antibodies can diffuse into the interior which causes high background. Furthermore, it can no longer be ensured that the detected fluorescence signal originates from the membrane or from right behind it (Figure 4.3F). To prevent this, in all projects described in this work, staining of membrane compounds was performed with living cells and before the fixation step (Manuscripts 1–4). Additionally, in

Manuscript 4 live-cell labeling was performed on ice to prevent endocytosis (for more information and details see Chapter 4.3).

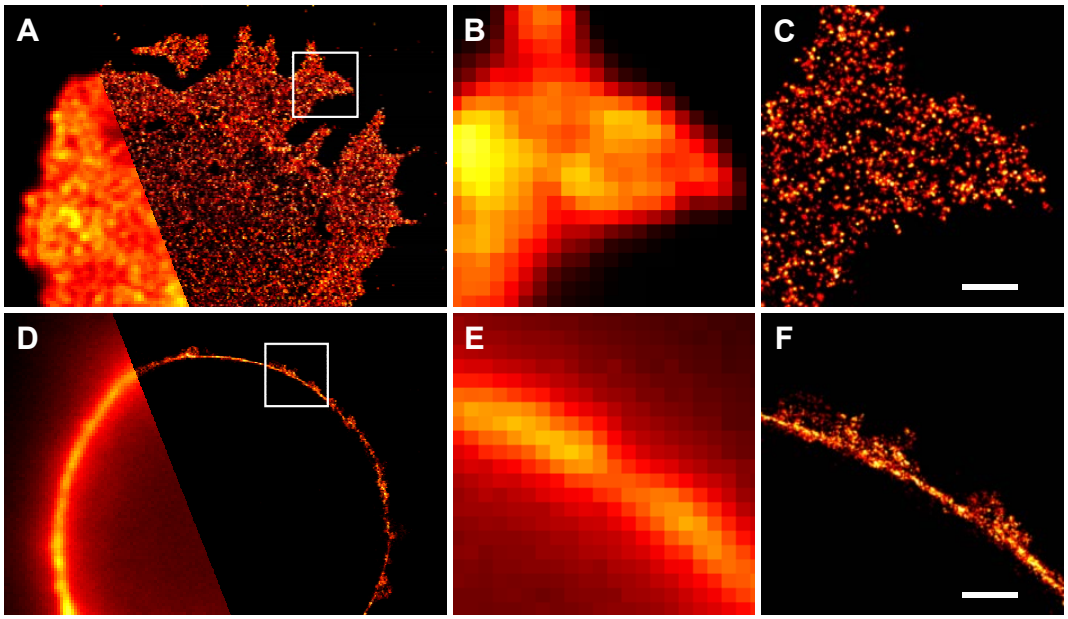

Figure 4.3: Staining and imaging of plasma membrane components. (**A**, **D**) Conventional fluorescence (*left part*) and *d*STORM images (*right part*) of a suspension cell attached to a PDL-coated cover slip. Living MM.1S cells, a human multiple myeloma cell line, were treated with anti-human CD38–Alexa Fluor 647 primary antibodies for 30 min on ice before being fixed with cold PFA. Whereas TIRF illumination of the cell's bottom membrane provides information about the structural arrangement of proteins (**A**–**C**), HILO illumination at the "cell equator" produces a cross section of the cell containing information about the membrane's condition and the quality of membrane staining (**D**–**F**). (**B**, **C**, **E**, **F**) Enlarged sections of boxed regions. Scale bars, 500 nm.

After staining, cells were chemically fixed. Membrane fixation is indispensable for the prevention of membrane protein and lipid mobility especially in the case of structural analysis and quantification approaches. Usually, formaldehyde (FA) or paraformaldehyde (PFA) is used to crosslink proteins. These aldehyde fixatives react with thiol and amino groups in proteins and immobilize proteins by forming cross-linkages (Melan, op. 1994; Takatori *et al.*, 2014). In a series of staining protocols it is recommended to use glutaraldehyde (GA) in addition to FA which cross-links proteins more efficiently during fixation. Furthermore, Tanaka *et al.* could demonstrate by conducting single-molecule tracking experiments that membrane molecules (proteins and lipids) are mobile even after chemical fixation. In order to block the lateral diffusion of membrane proteins they recommended using a

mixture of 4% PFA and 0.2% GA for at least 30 min of incubation. Though, chemical fixation of lipids (e.g. cholesterol) was not possible at all (Tanaka *et al.*, 2010; Takatori *et al.*, 2014).

However, in spite of the good fixation properties of aldehydes, Harper et al. showed that GA induces strong membrane permeabilization which results in high background in the cytoplasm (Harper, 1986). Moreover, Leyton-Puig *et al.* stated that for proper SMLM, a range of cellular structures should be fixed only with PFA because GA would often make tertiary structures unrecognizable by antibodies (Leyton-Puig *et al.*, 2016). An alternative to conventional fixatives such as PFA and GA could be the dialdehyde glyoxal which recently was tested for immunostaining in super-resolution microscopy (Richter *et al.*, 2018). Their results showed a substantial improvement in fixation efficiency and quality compared to PFA, especially for membrane and soluble proteins, when using a 3% glyoxal solution at pH 4.

These findings elucidate the complexity and significance of fixation and permeabilization. They clarify that there is no golden standard method and that protocols have to be adjusted on a case-by-case basis and dependent on the cellular structure of interest (Whelan and Bell, Toby D M, 2015). Last but not least, results of plasma membrane approaches (e.g. colocalization studies, analysis of raft-based interactions, etc.) are very sensitive to subtle variations in experimental conditions employed in different laboratories, so that results should always be treated with considerable caution (Kusumi and Suzuki, 2005).

4.2.2 Quantification of Glycoconjugates

Besides its role in cell protection and compartmentalizing, a plasma membrane operates as organizing center for tasks such as signal transduction, cell adhesion, immune response and metabolism. A plasma membrane's function is determined by its molecular composition, that is the quantitative ratio of specific membrane proteins and lipids, and furthermore, the interplay between those. However, the presence of proteins and lipids at a particular membrane is normally not sufficient for its function. It is rather the spatial arrangement of its components which determines functionality. This is usually realized by oligomerization or clustering of membrane components such as glycoproteins, GPI-anchored proteins and sphingolipids, for example. However, the precise molecular architecture remains unclear. (Kusumi *et al.*, 2005; Grecco *et al.*, 2011; La Bernardino de Serna *et al.*, 2016; Mateos-Gil *et al.*, 2016)

The following chapter addresses a new, bioorthogonal labeling strategy for visualizing glycans on plasma membrane-associated proteins and lipids in a native way. Therefore, metabolic labeling in combination with click chemistry was used in a first step before super-resolution imaging by *d*STORM was conducted in a second step. Localization-based cluster analysis as well as quantification of membrane components was performed in order to unravel the nanoscopic arrangement of membrane-associated glycoconjugates. The here described results are presented in full detail in Manuscript 1 (Letschert *et al.*, 2014) and Manuscript 3 (Mateos-Gil *et al.*, 2016).

Click Chemistry. Initially, different labeling conditions were tested in order to optimize the CuAAC protocol for live-cell labeling of neuroblastoma cells. Therefore, SK-N-MC cells were fed with different azidoacetyl monosaccharides before being treated in presence and absence of copper (Cu(I)) and its stabilizing ligand THPTA, respectively (Figure 4.4 A–C). It could be shown that Cu(I) is essential for click reactions between azides and terminal alkynes under physiological conditions (Figure 4.4 C). In presence of Cu(I) and absence of THPTA, a faint plasma membrane staining could be detected (Figure 4.4 B). However, strong intracellular background was observed, probably due to destructive reactive oxygen species (ROS) produced by ascorbate-induced reduction of Cu(II) to Cu(I) (Fry, 1998; Wang *et al.*, 2003). As a side reaction, ascorbate also reduces O_2 to H_2O_2 which then reacts with Cu(I) to form hydroxyl radicals ($^{\bullet}OH$) (Fry, 1998). Copper-mediated ROS-generation causes strong cytotoxicity which can be prevented by adding copper-chelating ligands, like THPTA, for example, as has been shown by Hong *et al.*, 2009 and Presolski *et al.*, 2011. Water-soluble ligands, such as THPTA and BTTAA accelerate the cycloaddition reaction and, furthermore, act as sacrificial reductants, helping to protect cells and molecules from ROS and thus, maintaining bioorthogonality (Besanceney-Webler *et al.*, 2011; Uttamapinant *et al.*, 2012).

The best condition could be observed when cells were treated with 50 μM $CuSO_4$, 250 μM THPTA and a ten-fold excess of sodium ascorbate (2.5 mM) (Figure 4.4 A, see also Letschert *et al.*, 2014). All labeling optimization experiments were performed with Alexa Fluor 647 alkyne. To investigate the effect of different dyes and their charges on the reaction efficiency, additional dye alkynes, such as Alexa Fluor 488, Atto 532 and Alexa Fluor 555 alkynes were used for CuAAC (Figure 4.4 E–G). Moreover, a highly water-soluble cyanine dye–alkyne conjugate with an absorption maximum of 648 nm, synthesized at the Institute of Organic Chemistry in Würzburg, was used to test the impact of water solubility on click reaction and *d*STORM imaging (Mertsch *et al.*, 2016). Interestingly, in all cases no difference in comparison to Alexa Fluor 647 alkyne or further negative

effects such as less reaction efficiency or cell penetration could be observed. This elucidates the high efficiency of CuAAC reactions in combination with ligands like THPTA even when differently charged fluorophores are used which, additionally, are much larger in size in relation to the reactive azide group (Hong *et al.*, 2009). Benefiting from more than a million-fold acceleration by using copper(I) catalysis, this process allows labeling of a cell's complete glycome in less than five minutes (Rostovtsev *et al.*, 2002b; Kolb and Sharpless, 2003; Letschert *et al.*, 2014; Gutmann *et al.*, 2016).

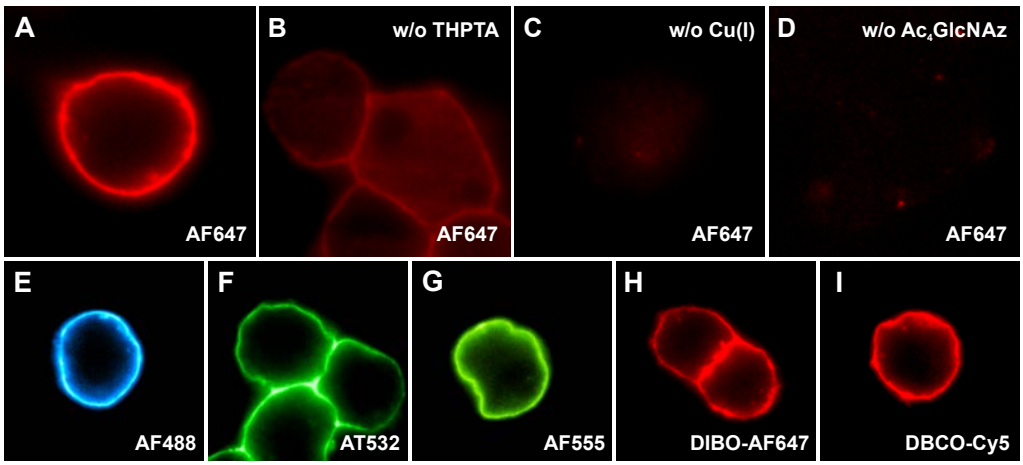

Figure 4.4: Visualizing cell membranes with click chemistry. Conventional wide-field fluorescence microscopy images (HILO) of metabolically engineered neuroblastoma cells. (**A**–**D**) In order to optimize copper-catalyzed azide–alkyne cycloaddition (CuAAC) on living cells, different labeling conditions were tested. After two days of incubation with Ac_4GlcNAz, cells were treated with 20 μm Alexa Fluor 647 alkyne for 5 min in presence of THPTA and Cu(I) (**A**), absence of THPTA (**B**) and absence of Cu(I) (**C**). (**D**) Control cells that were not being fed with Ac_4GlcNAz but treated in the same way as cells in (**A**). (**E**–**G**) Besides AF647, further dye-alkynes were tested for live-cell CuAAc compatibility that were Alexa Fluor 488 alkyne (**E**), Atto 532 alkyne (**F**) and Alexa Fluor 555 alkyne (**G**). (**H**–**I**) Copper-free click chemistry by SPAAC: Alexa Fluor 647 DIBO alkyne (**H**) and DBCO-Cy5 (**I**). (**A**–**D**) adapted from Letschert *et al.*, 2014.

In addition to CuAAC, copper-free strain-promoted cycloaddition (SPAAC) was applied on metabolically engineered cells by using cyclooctynes instead of terminal alkynes. Therefore, cells were incubated for 60 min with DIBO–Alexa Fluor 647 and for 15 min with DBCO–Cy5, respectively (Figure 4.4 H, I). On conventional fluorescence images, a distinct staining of the plasma membrane could be observed which shows that dye-coupled cyclooctynes are a suitable and less toxic alternative for CuAAC as has been shown by a couple of experiments (Jewett *et al.*, 2010; Sletten and Bertozzi, 2011; Saka *et al.*, 2014). However, due to a lesser

efficiency of SPAAC, reaction times have to be dramatically increased depending on the cyclooctyne which must be taken into account when performing staining of living cells in terms of endocytic uptake of dye molecules. The second order rate constant of DIBO was measured to be ~0.06 $M^{-1} s^{-1}$ (Poloukhtine *et al.*, 2009), whereas that of DBCO is about 0.31 $M^{-1} s^{-1}$ (Debets *et al.*, 2010), at least five-times faster. This explains the longer labeling time for DIBO which was 60 min compared to 15 min for DBCO (Letschert *et al.*, 2014; Mateos-Gil *et al.*, 2016). Besides glycoproteins, there are additional ways to metabolically engineer membrane components as, for example, azide-functionalized ceramides for visualization of sphingolipids (Walter *et al.*, 2017) and non-natural amino acids to image newly synthesized proteins (Mateos-Gil *et al.*, 2016). A detailed protocol and a step-by-step instruction of metabolic labeling in combination with copper-catalyzed as well as copper-free click chemistry can be found in Manuscript 3 (Mateos-Gil *et al.*, 2016).

Quantitative *d*STORM Imaging. After establishing an optimized click chemistry protocol, *d*STORM imaging with structural analysis and localization-based quantification was performed. By applying Ripley's K analysis (Ripley's H function), it could be demonstrated that ManNAc-, GalNAc- and GlcNAc-modified plasma membrane conjugates are homogeneously distributed in the plasma membrane of osteosarcoma and neuroblastoma cells (Figure 4.5 B–G and Letschert *et al.*, 2014). Same observations were made with membrane proteins modified with non-natural amino acids and independent on the type of click chemistry (CuAAC or SPAAC)(Mateos-Gil *et al.*, 2016). Furthermore, it could be shown that localization densities are in the range of 600–1700 localizations/μm^2 depending on the cell line and the type of sugar-derivative (Figure 4.5 A).

In order to determine the absolute number of glycans and proteins in the plasma membrane, the number of localizations must be converted into molecule numbers. However, the handling of multiple localizations remains challenging, as it is known that fluorophores change their photophysical properties, including photoswitching performance, depending on their nanoenvironment (Endesfelder *et al.*, 2011). Single fluorophores located outside of the investigated cellular compartment cannot be used as reference due to a different environment. Nevertheless, the number of localizations per fluorophore can be precisely extracted by performing calibration experiments in the same cellular nanoenvironment (e.g. in the plasma membrane and attached to glycans) with different concentrations of fluorophores (Sauer, 2013).

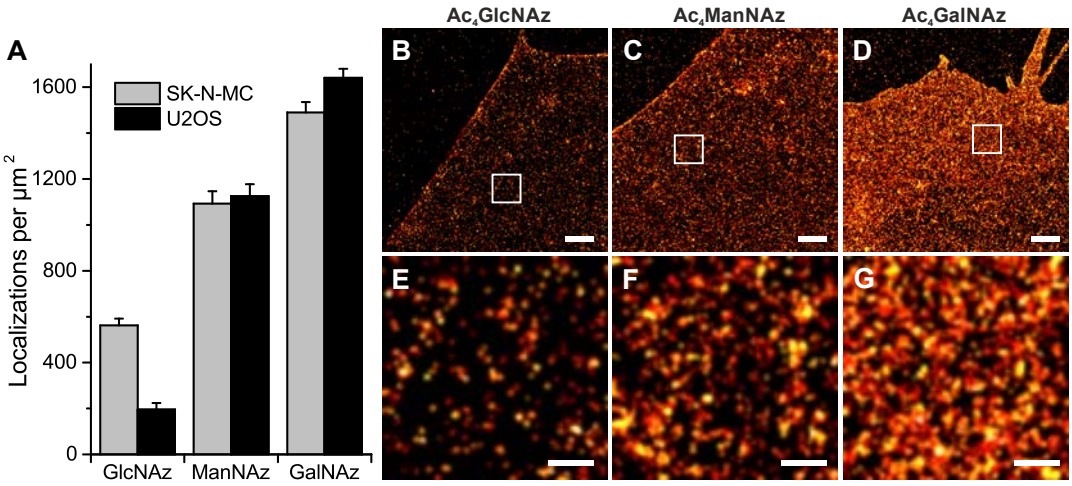

Figure 4.5: Quantification of glycoconjugates using *d*STORM. SK-N-MC and U2OS cells were metabolically engineered with three different azido-sugar derivatives and stained with Alexa Fluor 647 alkyne using copper-catalyzed azide–alkyne cycloaddition (CuAAC). (**A**) Localization density of fluorescently labeled, membrane-associated glycoproteins and –lipids using click chemistry. Error bars show the SEM of 12–32 cells. (**B**–**D**) *d*STORM images of bottom membrane areas of SK-N-MC cells fed with Ac_4GlcNAz (**B**), Ac_4ManNAz (**C**) and Ac_4GalNAz (**D**) before being clicked with dye–alkyne. (**E**–**G**) Magnified sections of boxed regions. Scale bars, 1 μm (**B**–**D**) and 200 nm (**E**–**G**). Adapted from Letschert *et al.*, 2014.

By grouping repeated localizations from identical fluorophores and at different dye–alkyne concentrations a conversion factor could be calculated which varied between 2.7 (Figure 4.6) and 6.7 localizations per fluorophore (Mateos-Gil *et al.*, 2016). This value highly depends on many factors such as photophysical properties of the dye, its nanoenvironment, the excitation intensity, the exposure time of the camera and the length of the recorded *d*STORM image stack. Therefore, when quantifying densely packed membrane molecules, it is recommended to always determine a new conversion factor under the same conditions as in the actual experiment. A conversion factor of 2.7 localizations per fluorophore and an estimated average cell membrane area resulted in extrapolated glycan densities of 280,000 (GlcNAc) to 2,400,000 (GalNAc) molecules per cell. Taking all glycans together one ends up with a total number of $\sim 5 \times 10^6$ fluorophore-labeled plasma membrane glycans per neuroblastoma cell (Further details are reported in Manuscript 1 Letschert *et al.*, 2014 and Manuscript 3 Mateos-Gil *et al.*, 2016).

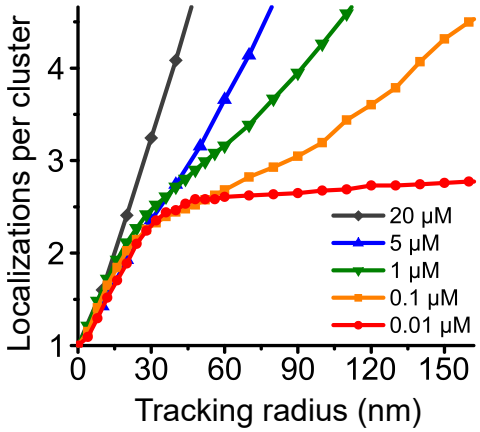

Figure 4.6: Quantitative *d*STORM analysis. Alexa Fluor 647 alkyne was titrated between concentrations of 0.01 and 20 μM. Spots of isolated glycans were tracked with different tracking radii over all frames. At low concentration (0.01 μM) the saturation level remains constant at ~2.7 localizations per cluster. Data points represent mean values of all tracks from a single experiment. Adapted from Letschert *et al.*, 2014.

In summary, the results of Manuscript 1 and Manuscript 3 show that membrane-associated glycoconjugates as well as the majority of membrane proteins are homogeneously distributed without the formation of clusters and nanodomains of specific sizes. Furthermore, bioorthogonal chemistry in combination with super-resolution by *d*STORM can be used as an efficient tool for quantification of glycans and membrane proteins. However, there is an ongoing debate about the structural arrangement of the plasma membrane and the existence of protein clusters, lipid rafts, picket-fences, lipid shells etc. (Saka *et al.*, 2014; Möckl *et al.*, 2015; La Bernardino de Serna *et al.*, 2016; Burgert *et al.*, 2017). Due to its complexity and difficulties in membrane preparation little is known about the real organization of plasma membranes. Much evidence suggests that there is no existence of a single overarching membrane model (La Bernardino de Serna *et al.*, 2016). This motivates for the development and application of new technologies such as quantitative super-resolution microscopy but also new staining and preparation methods to get further insights and additional puzzle pieces of membrane organization. Since many pathogens and tumor cells display glycan structures and quantities not normally found on healthy human cells and tissue, there is need for tools that can monitor the density of specific glycan structures in the context of cellular surfaces (Hudak and Bertozzi, 2014).

4.2.3 Quantification of CD19 on Multiple Myeloma Cells

Since a couple of years, SMLM methods such as *d*STORM have become a general tool to not only visualize cellular structures on a sub-diffraction scale but also to quantify the absolute number of molecules (Fürstenberg and Heilemann, 2013; Nicovich *et al.*, 2017). Of special interest is the quantification of tumor-associated antigens on cancer and healthy cells which might be potential targets for personalized immunotherapies (see Chapter 1.1.3). New immunologic anti-cancer treatments using bispecific antibodies as well as tumor-specific, genetically engineered T cells (CAR- and TCR-modified) are of ever-increasing sensitivity and substantially enhance antitumor efficiency (Hudecek and Einsele, 2016; Maus and June, 2016). In this project, single-molecule sensitive fluorescence microscopy and *d*STORM-based quantification was employed to investigate the expression of the membrane protein CD19, and the impact of CD19-specific CAR-engineered T cells on primary multiple myeloma (MM) cells (Manuscript 4, Nerreter *et al.*, in submission). The B-lymphocyte antigen CD19 (Cluster of Differentiation 19) is a membrane protein that is largely found on the surface of B cells. During maturation to plasma cells it usually gets lost or its expression is extensively downregulated. There is an ongoing debate about the existence of CD19 on MM cells and about CD19 as a potential target for MM CAR T cell therapy (Garfall *et al.*, 2015; Atanackovic *et al.*, 2016; Garfall *et al.*, 2016; Ghosh *et al.*, 2017; Mikkilineni and Kochenderfer, 2017).

The prevailing detection method in clinical routine is flow cytometry (FC) which has a detection limit in the order of thousands of molecules per cell (Truneh and Machy, 1987; Zola, 2004). In consequence, it may be possible that MM cells express very low levels of CD19 that are below the detection limit of routine flow cytometric approaches and thus are not being detected. To test this, we performed *d*STORM imaging and localization-based quantification of anti-CD19 antibody treated primary MM cells out of 14 patients to establish expression profiles of CD19. The results were compared with FC data as described in detail in Manuscript 4 (Nerreter *et al.*, in submission). It could be demonstrated that, in a subset of patients, CD19 is expressed on a large fraction of MM cells (Figure 4.7 A, F), but remains undetected by FC. To verify the detection of MM cells and to exclude false-positive CD19 cells due to impurities (e.g. B cells), purified bone marrow aspirates were additionally stained with antibodies against CD138 and CD38 (Figure 4.7 C, D, H, I). Using *d*STORM, we were able to identify isolated, well-separated CD19 molecules in the bottom plasma membrane of CD19-positive MM cells (Figure 4.7 B, panels 1 and 2), as well as CD19-negative MM cells with antibodies bound unspecifically to the glass surface (Figure 4.7 G, panels 3 and 4).

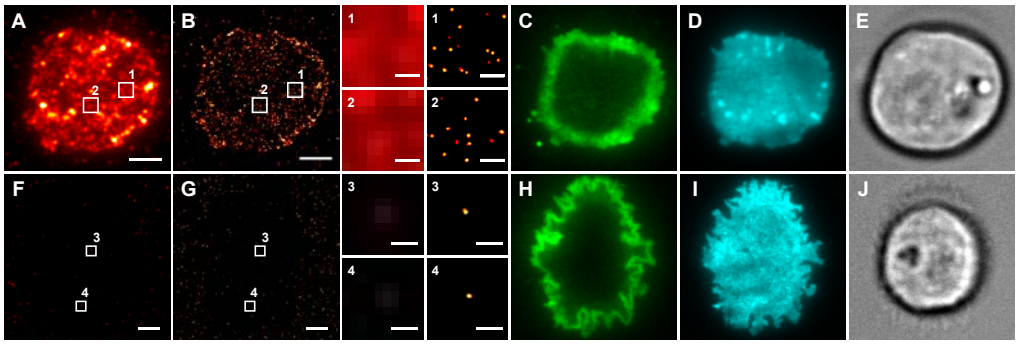

Figure 4.7: CD19 is present on primary MM cells. Single-molecule sensitive multicolor fluorescence imaging was used to identify myeloma cells ($CD38^+/CD138^+$) and to detect CD19 molecules on the plasma membrane of primary MM cells. (**A** and **F**) Conventional TIRF and (**B** and **G**) *d*STORM images of Alexa Fluor 647-conjugated antibodies on a $CD19^+$ (*upper row*) and $CD19^-$ (*bottom row*) cell, respectively. Small panels (**1**–**4**) show enlarged sections of boxed regions. For verification of the correct cell type (MM), CD138–Alexa Fluor 555 (**C** and **H**) and CD38–Alexa Fluor 488 (**D** and **I**) antibodies were used. (**E** and **J**) Transmitted light images of surface-immobilized MM cells. Both cells (*upper* and *bottom row*) are from the same patient. Scale bars, 3 μm (*large panels*) and 0.4 μm (*small panels*). Adapted from Nerreter *et al.*, in submission.

In a next step, *d*STORM localization files were used to quantify absolute numbers and densities of CD19 molecules on MM cells as well as on those which were additionally co-incubated with CD19-specific CAR T cells and non-transfected control T cells, respectively (Figure 4.8 A–H). Moreover, to distinguish between CD19 low-expressing MM cells and CD19-negative MM cells, fluorescently labeled isotype control antibodies were used which allowed determination of absolute numbers of unspecifically bound antibodies (Figure 4.8 B, F). Examples of CD19 expression profiles from two different patients, i.e. distributions of antibody densities on MM cells, are presented in Figure 4.8 A–H.

Surprisingly, we observed a complete elimination of CD19-positive MM cells in all patients when treated with CD19-specific CAR T cells whereas those treated with control T cells remained unaffected (Figure 4.8 C, G and D, H, respectively). These observations demonstrate the precise functionality of the CAR T cell system and underline its high specificity and efficiency. A summary of results from all patients including mean CD19 densities and the amounts of CD19-positive cells per patient is given in Figure 4.8 I and J. In order to compare *d*STORM results with data derived from FC experiments, the number of CD19 molecules per cell was calculated using CD19 densities and cell surface areas (determined with the help of transmitted light images). As a result, CD19 expression among all CD19-positive patients varied between on average ~60 and ~1600 molecules per cell. Moreover, the results of co-incubation experiments with CAR T cells suggest that

the here used CD19-specific CAR T cells are able to eliminate myeloma cells that express far less than 100 CD19 molecules on their surface. This value can now be used as sensitivity threshold for further experiments and clinical applications, especially in CAR design and CAR T immunotherapy.

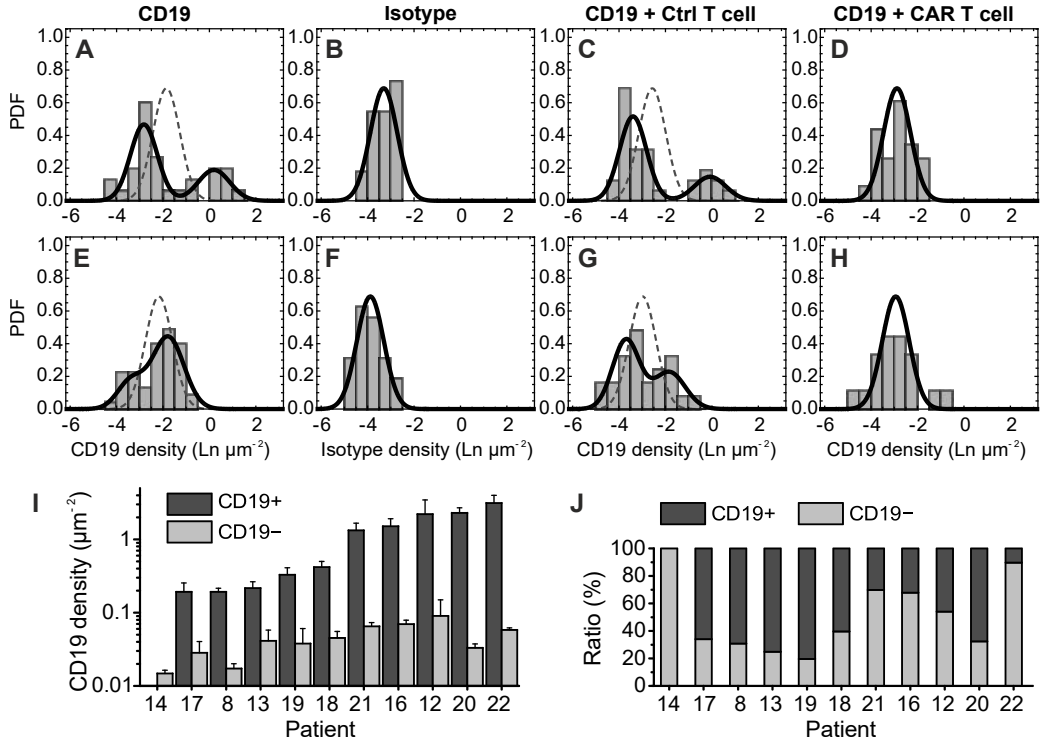

Figure 4.8: Localization-based quantification of CD19 on primary myeloma cells. (**A**–**H**) Histograms illustrate the distribution of CD19 and isotype antibody densities on MM cells. Representative data from two patients (*first* and *second row*) are shown and densities are given in logarithmic numbers per μm^2. Four different conditions were analyzed: (**A** and **E**) CD19 and (**B** and **F**) isotype control antibodies on myeloma cells, and additionally, CD19 on MM cells co-cultivated with (**C** and **G**) non-transfected control T cells and (**D** and **H**) CD19-CAR T cells. Antibody density distributions were fitted to a one- or two-component log-normal distribution (solid lines) depending on the fit accuracy. Density distributions were divided into a $CD19^+$ subpopulation ($CD19^+$ cells) and $CD19^-$ subpopulation ($CD19^-$ cells) by comparing distributions with those of isotype control antibodies. In the case of two components, discarded one-component log-normal fits are displayed as dashed lines. PDF: probability density function; Ln: natural logarithm. (**I** and **J**) Summarized presentation of CD19 expression on all $CD19^+$ patients and one representative $CD19^-$ patient (P14). (**I**) Antibody densities of $CD19^+$ (dark grey) and $CD19^-$ (light gray) subpopulations of CD19 stained MM cells. (**J**) Ratio of $CD19^+$ and $CD19^-$ cells illustrating strong variation in CD19 expression pattern among MM patients (range: 10–80%). Adapted from Nerreter *et al.*, in submission.

A comparison with FC data resulted in an estimated minimum number of ~1350 molecules per cell that is necessary for detection by conventional FC. These findings would explain the discrepancy between super-resolution fluorescence microscopy and FC concerning the number of as CD19-positive classified cells and patients. Furthermore, it shows that FC can be insufficient as analytical method in cases of detecting cells with low-expressing target molecules. For more details and the complete set of results see Manuscript 4.

In addition to the results described in Manuscript 4, a range of control and data analysis experiments was performed to obtain correct parameters for quantification. The in Chapter 1.2.3 introduced alpha shape algorithm was used to cluster repeated localizations from one CD19 molecule. Because of the importance of this step, a detailed description can be found in the following section:

Alpha shape clustering. The alpha shape algorithm is a very robust method to cluster sets of points such as localizations for example, and a good method to obtain information about the shape and size of clusters (for details see Chapter 1.2.3). In this work, clustering was defined as the grouping of repeated localizations coming from one fluorophore-conjugated antibody. Since the degree of labeling (DOL) is usually given as a mean value (e.g. a DOL of 4 means 4 fluorophores per antibody on average) and additionally, the on- and off-switching is a stochastic process depending on many parameters (see Chapter 4.1), the number of localizations per antibody can vary substantially. A critical issue is the impact of the alpha value on cluster properties. The question is, how can we determine the correct alpha value? Especially, when the set of points is non-uniformly distributed including different densities and different shapes it will be difficult to determine a fixed and appropriate alpha value. Potential consequences are over-clustering by connecting neighboring objects (repeated localizations from one emitter) or the loss of structural cluster details like interstices, sharp turns and joints.

To determine the correct value of alpha which allows to cluster the exact number of repeated localizations coming from one antibody is nearly impossible. Nevertheless, it can be approximated very precisely by varying alpha over a large range which results in an acceptable estimation of the absolute number of clusters (or antibodies) (Figure 4.9 D–E). In detail, let it be supposed that clusters (=antibodies or CD19 molecules) are evenly distributed and separated from each other with distances far larger than the cluster size (Figure 4.9 A). The expectation would be that the number of localizations per cluster increases with increasing alpha. If only one isolated cluster is considered, the number of localizations per cluster saturates with increasing alpha.

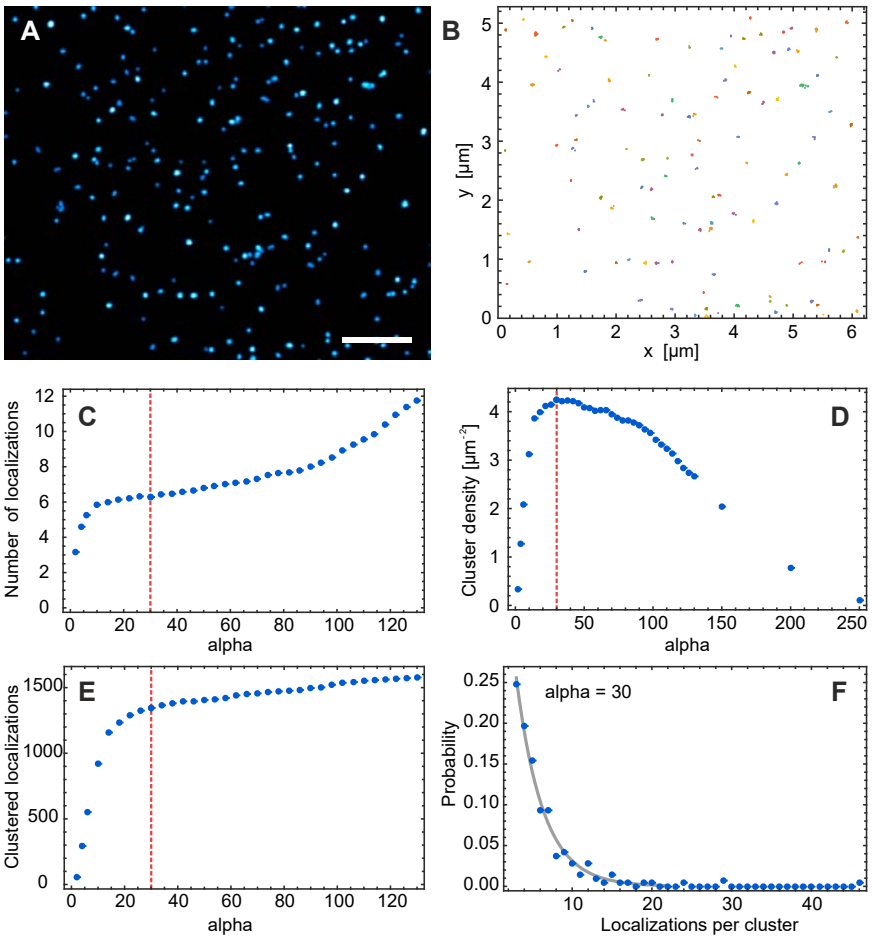

Figure 4.9: Clustering CD19 molecules on MM cells using alpha shapes. (**A**) Section of a reconstructed dSTORM image of CD19 molecules stained with anti-human CD19 Alexa Fluor 647 antibody. (**B**) Correspondent alpha shape diagram illustrating the obtained clusters in different colors. Repeated localizations coming from single fluorescent spots were clustered with alpha shapes and an alpha value of 30 nm. (**C**–**E**) A suitable alpha value was determined by serial cluster finding, i.e. varying α from small to large values which influences the number of localizations per cluster (**C**), cluster density (**D**) and the number of clustered localizations (**E**)(non-clustered localizations were discarded). Red dotted lines mark positions at α = 30 nm. (**F**) Relative distribution of the number of localizations per cluster for α = 30 nm (mean ≈ 6.3 localizations per cluster). Scale bar, 1 μm.

An alpha value at the saturation level would be appropriate for quantification. However, after saturation, the curve increases again with increasing alpha if other clusters are in the neighborhood (Figure 4.9 C). This is also the case for the cluster density, except that the correct alpha value is at the maximum density which is in this case 30 nm (Figure 4.9 D, red dotted line). Furthermore, at an alpha value of

30 nm, the majority of localizations are located in clusters (~80%) whereas non-clustered localizations are discarded (Figure 4.9 E). The mean number of localizations per cluster for an alpha value of 30 nm was about 6.3 localizations per cluster (Figure 4.9 F).

Even at a robust determination of alpha (in this case 30 nm) one cannot be absolutely sure that the output number of molecules is correct. It has to be mentioned that all quantified numbers are estimations with a range of error sources and that the risk of over- and underestimation cannot be completely impeded. However, the precise comparison with data of control experiments leads to a significant and robust approximation of molecule numbers. There are several improvements and extensions to the definition of alpha shapes which alleviate these problems. For example anisotropic scaling, where the spherical alpha disc varies in shape; density scaling, where the value of α is varied depending on the local point density (Teichmann and Capps, 2002, c1998), as well as weighted alpha shapes (Edelsbrunner, 1992). Besides alpha shapes, there exists a range of alternatives for clustering localization data or point sets in general (Griffié *et al.*, 2016; Pageon *et al.*, 2016; Nicovich *et al.*, 2017). A very robust and often applied algorithm is the density-based spatial clustering of applications with noise (DBSCAN) which classifies candidates of a point set as core points, density-reachable points, and outliers, dependent on a minimal number of neighbors (minPts) in a certain distance (ε) (Ester *et al.*, 1996; Sander *et al.*, 1998). Since quantification and cluster analysis of SMLM data becomes more and more important, useful algorithms can now be easily implemented using a range of free-available software packages as for example LAMA (Malkusch and Heilemann, 2016), ELKI (Achtert *et al.*, 2008) and Locan (see Chapter 2.2.3).

4.3 Endocytosis and Transferrin

The plasma membrane is not only a natural barrier between a cell's exterior and its cytoplasm. Nutrient supply, signal transduction and the release of enzymes as well as messenger molecules are just some processes which lead to the requirement of a highly structured and active membrane. Most of these processes are energy dependent and thus require physiological temperatures (Hamilton, 1983; Mamdouh *et al.*, 1996). For visualizing conjugates on a plasma membrane's outside it is necessary to inactivate these processes to prevent unintended endocytosis and thereby fluorophore-filled vesicles which may lead to enhanced background and artifacts (see Chapter 4.1). This is usually realized by performing all cell treatments and labeling steps at 4 °C or on ice before cell fixation. Endocytosis can be simply visualized with fluorescently labeled ligands which bind to their receptor and subsequently are taken up by the cell. One of the best-characterized representatives of receptor-mediated endocytosis is transferrin, a serum glycoprotein which transports iron into cells. When iron-loaded transferrin binds to its receptor, the ligand–receptor complex clusters in coated pits and is internalized in so called clathrin-coated vesicles (CCV). (Dautry-Varsat, 1986; McMahon and Boucrot, 2011)

In order to test this, HeLa cells were treated with Alexa Fluor 647-conjugated transferrin for 2 min on ice on the one hand and at 37 °C as control on the other hand (Figure 4.10). At low temperature, *d*STORM reveals single transferrin molecules attached to the plasma membrane, or to be more exact, to the transferrin receptor in the plasma membrane (Figure 4.10, A and B). A distinct line of transferrin molecules contours the cell's shape whereas the cytoplasm is completely free from labeled protein (fluorescent spots located between two or more HeLa cells are projections of three-dimensionally shaped membranes (Figure 4.10B)). By contrast, when incubating HeLa cells at 37 °C for only two minutes the plasma membrane seems to be vanished due to a complete uptake of labeled transferrin (Figure 4.10C). Moreover, the cell interior is filled with mainly round, vesicle-like structures of 135 ± 18 nm in diameter (n=17, Figure 4.10, D–G). This size distribution is in good accordance with those of CCV in epithelial cells determined by electron microscopy (100–150 nm, Heuser, 1989; McMahon and Boucrot, 2011; Kirchhausen *et al.*, 2014). In this context, it is important to mention that the size of CCVs is not consistent. It varies between different species and between different cell types within the same species, and is dependent on the size of cargo. The size of CCVs in brains, for example, is only 70–90 nm in diameter which may be because brain vesicles do not internalize large extracellular cargo (McMahon and

Boucrot, 2011). The above-described observations elucidate the temperature dependence of receptor-mediated endocytosis and once again highlight the importance of live-cell labeling at low temperatures when intending to perform structural and quantitative analyses of membrane proteins on the single-molecule level.

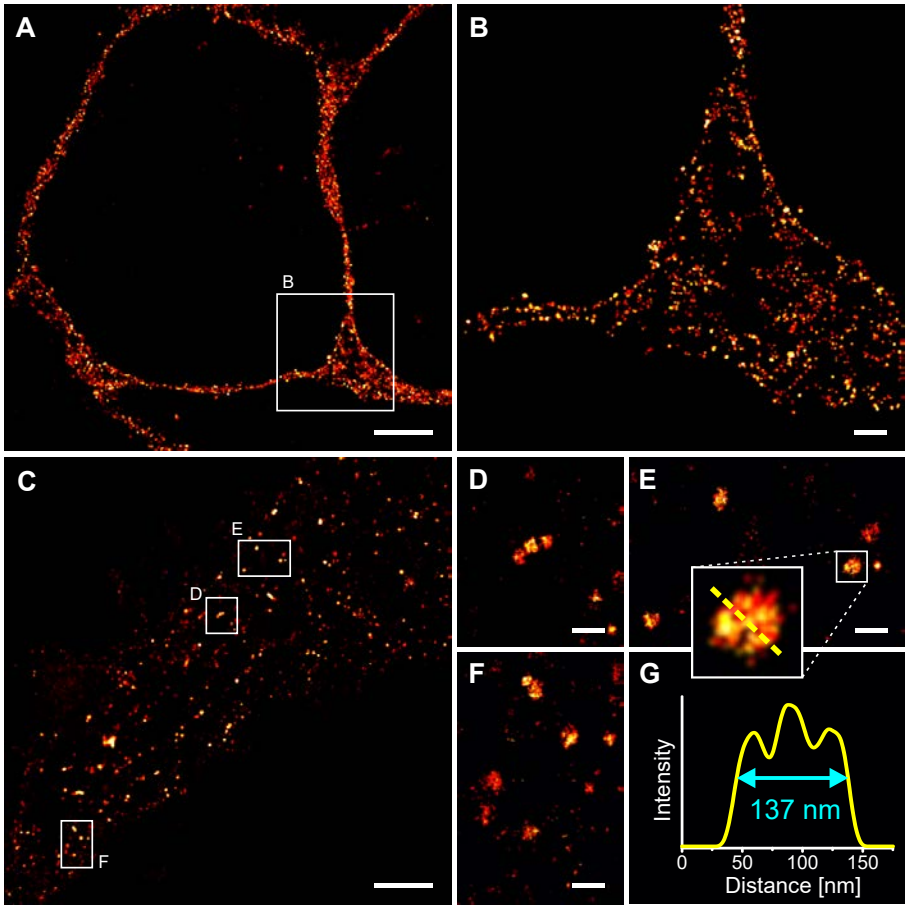

Figure 4.10: *d*STORM imaging of transferrin uptake in mammalian cells. HeLA cells were incubated with human transferrin conjugated to Alexa 647 for 2 min (**A**) on ice and (**C**) at 37 °C, respectively. (**B**) Enlarged section of boxed region in (**A**) depicting single transferrin molecules sitting on the outside of the plasma membrane. (**D**–**F**) Enlarged sections of boxed regions in (**C**) showing transferrin-filled, endocytic vesicles in the cytoplasm of a HeLa cell. (**G**) A diameter of 137 nm was measured by determining FWHM of the cross section profile of a representative vesicle. The images were recorded in HILO mode close to the glass surface (**C**) and a bit further up (**A**), respectively. Scale bars, 3 μm (**A**, **C**) and 300 nm (**B**, **D**–**F**).

To further investigate endocytosis with *d*STORM, transferrin incubation times were prolonged to 10 minutes and after a washing step another 10 to 30 minutes in PBS before fixation. The aim was to visualize the complete transferrin cycle, which starts with receptor binding, formation of CCVs and fusion with early endosomes. In the acidic environment of early endosomes, iron detaches while the transferrin–receptor complex is recycled and transferred back to the plasma membrane. The cycle ends with the release of apotransferrin —that is transferrin without iron— to the exterior. These events are rapid as the complete cycle of transferrin and its receptor takes only about 15 minutes (Dautry-Varsat, 1986). Here, after 2 and 10 minutes of transferrin incubation, tubulo-vesicular structures surrounded by vesicles could be detected in the cytoplasm of HeLa cells (Figure 4.11A). After another 10 to 30 minutes, up to 7 μm long tubular and partially cross-linked organelles with 56 ± 6 nm in diameter (n=21, Figure 4.11B) appeared.

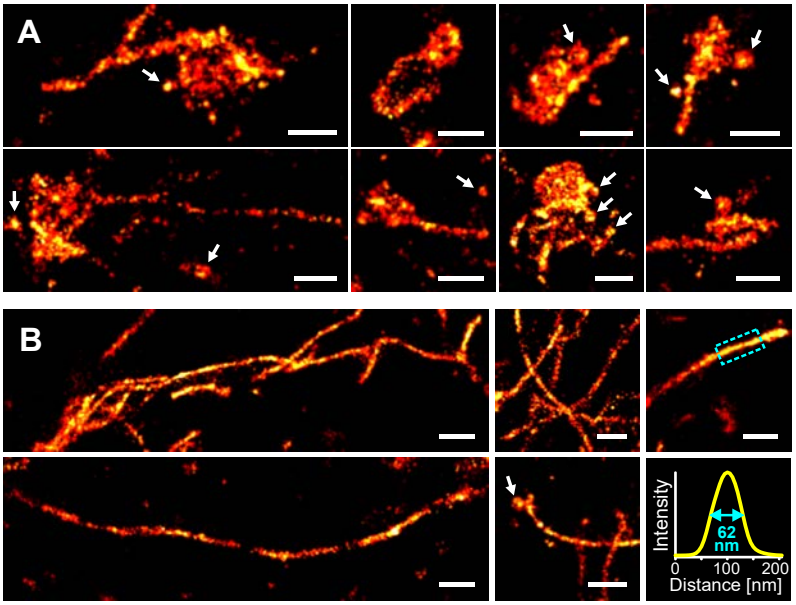

Figure 4.11: *d*STORM images of early endosomes in mammalian cells. Alexa Fluor 647-conjugated Transferrin was taken up by HeLa cells and transported in vesicles to early endosomes which consist of (**A**) sorting endosomes and (**B**) endocytic recycling compartments (ERCs). (**A**) Sorting endosomes with tubules budding out from the vesicular body. (**B**) The ERC lacks large vesicular bodies and consists only of long, interconnected tubules. The tubule in the right panel has a diameter of 62 nm. The average diameter of 21 tubules was 56 ± 6 nm. Arrows indicate endocytic vesicles. Scale bars, 400 nm.

It turned out that the observed structures are essential elements of the endocytosis apparatus. After transferrin uptake, CCVs lose their clathrin coat and fuse with sorting endosomes which are one of two types of early endosomes. Sorting endosomes are morphologically quite heterogeneous but regularly appear as up to 1 μm large vesicles with narrow, 50–60 nm large tubules (Dautry-Varsat, 1986; Mukherjee *et al.*, 1997, compare with structures in Figure 4.11A). This process takes only ~1 minute (Mukherjee *et al.*, 1997) and explains the complete uptake of transferrin after 2 minutes of incubation as described above (Figure 4.10C). Sorting endosomes, as their names suggest, use a simple physical mechanism to sort and recycle membrane components on the one hand and to retain solubilized ligands on the other hand. From the vesicular domain narrow-diameter tubules bud out which contain around 80 % of the sorting endosome's membrane. As a consequence, large fractions of membrane components are carried away while, due to the small luminal volume of tubules, solubilized ligands (e.g. iron in the case of transferrin) mainly retain in the vesicular domain. Later on, the vesicular part containing all the ligands and certain membrane proteins with special signal sequences, matures to late endosomes (Maxfield and McGraw, 2004).

Whereas the late endosome's content will be degraded, recycling molecules are transferred from sorting endosomes to the endocytic recycling compartment (ERC), the second type of early endosomes. The ERC consists mainly of tubular organelles which are about 60 nm in diameter (Maxfield and McGraw, 2004). Its tubules are extensively interconnected and often associated with microtubules (compare with Figure 4.11B). While the tubules are dispersed throughout the cytoplasm, in many cell lines they are additionally concentrated in the pericentriolar region which is around the microtubule organizing center (Ullrich, 1996). With conventional wide-field and confocal microscopy, the pericentriolar ERC appears as blurry fluorescent spot close to the nucleus (Haberman *et al.*, 2003; Casbon *et al.*, 2009; Naughtin *et al.*, 2010) whereas *d*STORM reveals substructural information like tubules and fragments of those often radiating from circular, fluorescent-free centers (Figure 4.12, A and B).

The second last step of transferrin cycle is the transport back to the plasma membrane. This can be achieved by rapid recycling ($t_{1/2} \approx 2$ min) which is the direct transport from sorting endosomes back to the plasma membrane, or by slow recycling via ERC ($t_{1/2} \approx 12$ min). In the case of the latter one, the ERC tubules in the cell periphery appear to break up into elongated vesicles which then are carried along microtubules before fusing with the plasma membrane (Pastan and Willingham, 1985; Lauffer, 1992; Grant and Donaldson, 2009; Ali, 2014). Strik-

ingly similar structures could be detected with *d*STORM, especially in the periphery of HeLa cells (Figure 4.12C). These short, rod-like vesicles exhibited dimensions of 338 ± 58 nm × 87 ± 11 nm (n = 20) and were oriented in the same way which may be because of their attachment to microtubules.

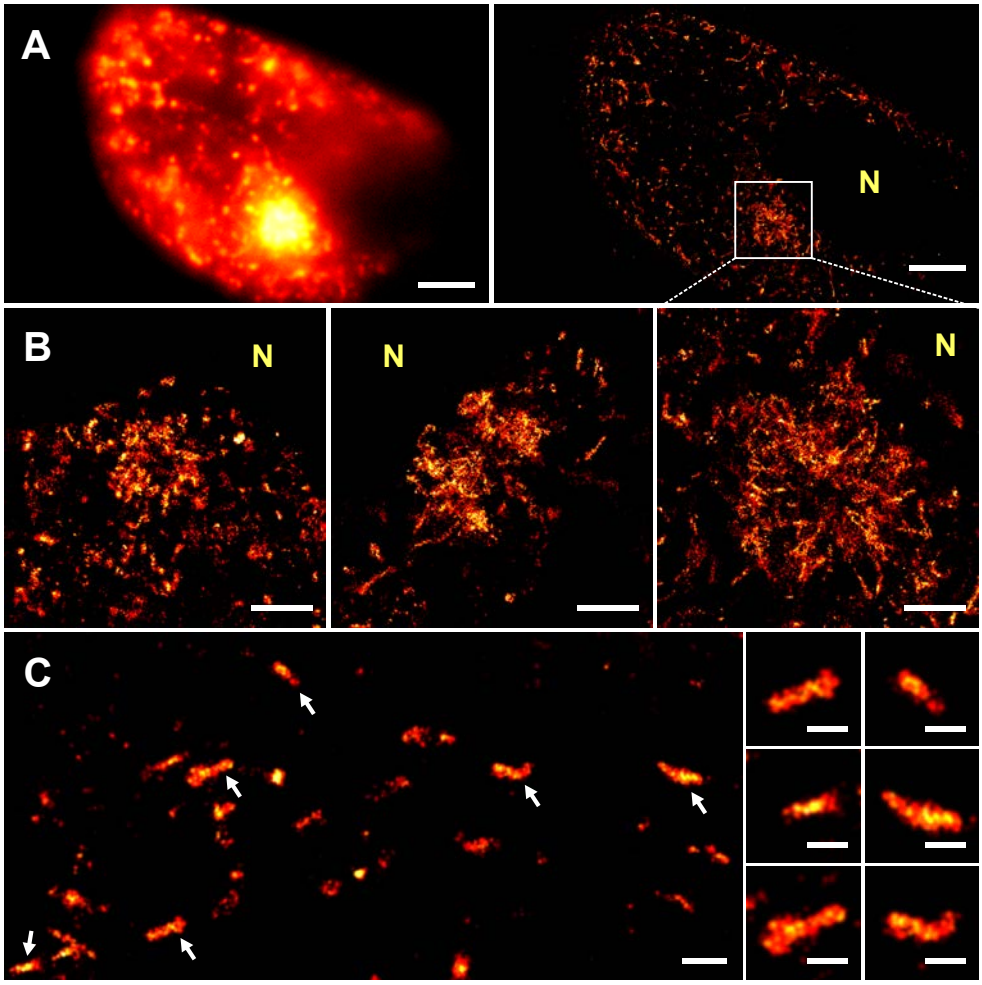

Figure 4.12: Transferrin recycling in HeLa cells imaged with *d*STORM. (**A**) Conventional wide-field (*left*) and *d*STORM (*right*) images of a HeLa cell filled with Alexa 647-conjugated transferrin bound to its receptor in endocytic organelles. (**B**) Enlarged *d*STORM images of pericentriolar ERCs located next to the nucleus (N). (**C**) Rod-shaped and transferrin-filled recycling vesicles presumably on their way to the plasma membrane. Right panels are enlarged sections of arrow-marked regions in the left panel. Scale bars, 4 μm (**A**), 1 μm (**B**), 400 nm (**C**, left panel) and 200 nm (**C**, right panels).

So far, there are only few super-resolution studies addressing endocytic trafficking (e.g. Barysch *et al.*, 2009; Leyton-Puig *et al.*, 2017) but none of them highlights the morphological analysis of complete receptor cycles and endocytic recycling processes. For example, many of them use CCVs as reference structures and as "proof-of-principal" tools for new methods (*d*STORM: Valley *et al.*, 2015, STORM: Bates *et al.*, 2007; Huang and Wang *et al.*, 2008; Jones *et al.*, 2011). Moreover, new and extended labeling approaches (e.g. aptamers as cellular markers) were presented with endocytic vesicles and early endosomes as reference structures (Opazo *et al.*, 2012; Riedel *et al.*, 2016) and clathrin-coated structures and other endocytic vesicles were used as objects of study for fixation protocols (Leyton-Puig *et al.*, 2016) or multicolor imaging (Winter *et al.*, 2017).

The above described results elucidate the possibilities of *d*STORM to visualize endocytosis and recycling processes like the transferrin cycle. However, here it has to be mentioned that the described results are morphological comparisons between observed structures and mostly electron microscopy images from literature. To further consolidate the classification of observed structures in different endocytic states and types, it would be of advantage to perform two- or multicolor *d*STORM measurements and colocalization studies with transferrin and special endocytosis markers. For example, there are several members of the Rab protein family which are involved in endocytosis and receptor recycling. These proteins could be addressed by e.g. immunocytochemistry and used to visualize distinct endocytic trafficking compartments, as e.g. RAB5 which is mainly located in sorting endosomes, or RAB11 which can be found in ERCs (Sönnichsen *et al.*, 2000; Hutagalung and Novick, 2011; Galvez *et al.*, 2012). Furthermore, colocalization with microtubules could unravel the dependence of recycling processes to the cytoskeleton, especially in the case of the ERC as well as tubule forming and branching. As mentioned above, CCVs vary in size which mainly depends on the size of their cargo (McMahon and Boucrot, 2011). This relationship could be also analyzed with localization microscopy by treating cells with ligands of different sizes (e.g. small proteins up to virus particles) and subsequent colocalization with clathrin-coated pit formation and vesicle budding.

4.4 Mitochondria

This chapter makes sub-diffraction imaging of mitochondria and especially the inner mitochondrial membrane a subject of discussion. Mitochondria are eukaryotic, intracellular organelles that play a critical role in the generation of metabolic energy (Cooper, 2000). At a first glance, there seems to be little in common between mitochondria and biological membranes. Nevertheless, mitochondria are surrounded by a double-membrane system, consisting of inner and outer mitochondrial membranes separated by an intermembrane space. The inner membrane forms numerous highly structured folds that are termed cristae. The width of cristae —the distance between two inner membrane segments forming one folding— was measured to be around 27 nm using electron microscopy (Frey and Mannella, 2000) which makes it a perfect object for testing the structural resolution of super-resolution microscopy.

The aim was to unravel the structural organization of mitochondrial cristae in human adherent cells using *d*STORM. This necessitated that the inner mitochondrial membrane was densely labeled in consideration of the Nyquist-Shannon sampling theorem (Chapter 1.2.2) to resolve the pattern of repeated, parallel cristae. To do so, it was aimed to immunostain as many proteins inside the inner mitochondrial membrane as possible. 13 proteins are encoded by the human mitochondrial genome that are core constituents of the mitochondrial respiratory complexes I–IV, and that are embedded, together with the ATP synthase (complex V), in the inner membrane (Friedman and Nunnari, 2014). In this work, fixed and permeabilized human osteosarcoma cells (U2OS) were treated with a cocktail of primary antibodies directed against all mitochondria complexes (I–V). The sample was subsequently stained with secondary antibodies (Fab fragments) conjugated to Alexa Fluor 647 dye molecules (for details regarding the staining procedure see Chapter 2.1.2). In Figure 4.13, reconstructed *d*STORM images are depicted which show long mitochondrial tubules and branches. In some regions, the mitochondrion was orientated in a way that consecutive gaps and densely labeled line segments perpendicular to the tubule axis could be observed (Figure 4.13 B–D).

These observations indicate that the repeated structures are densely labeled membrane segments forming cristae, as has recently been reported by using STORM and STED microscopy (Schmidt *et al.*, 2009; Shim *et al.*, 2012). Regions without fluorescence signal (“stripes”) could be the space between inner membranes (e.g. mitochondrial matrix). However, the visualization of the described patterns is strongly dependent on the label density, as well as the orientation of

the mitochondrion close to the glass surface. The established staining protocol was additionally used for two collaboration projects whose detailed descriptions would go beyond the scope of this work. For the sake of completeness, the reader may refer to Eyss *et al.*, 2015 and Jung *et al.*, 2017.

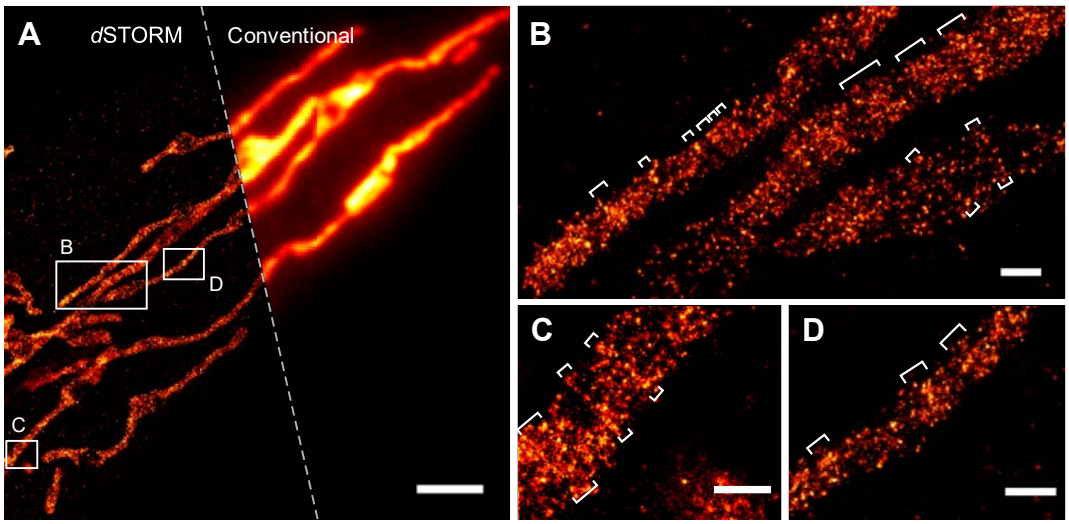

Figure 4.13: *d*STORM imaging of mitochondria in fixed U2OS cells uncovers the structural arrangement of cristea. A cocktail of primary antibodies directed against all protein complexes of the respiratory chain in the inner membrane was used to obtain sufficient label densities. (**A**, *left*) *d*STORM and (**A**, *right*) conventional image of mitochondria located in the peripheral part of a U2OS cell and close to the glass surface. (**B**–**D**) Enlarged sections of boxed regions in (**A**). Square brackets indicate areas with cristae-like structures which are perpendicular to the tubular mitochondrion. Scale bars, 3 μm (**A**) and 300 nm (**B**–**D**).

5 Conclusion and Outlook

Biological membranes are highly complex, dynamic and adaptive structures which makes it very challenging to study membranes and their molecular organization. Even after decades of extensive membrane research and the proposal of dozens of models and theories, the structural organization of plasma membranes remains largely unknown. In other words, the state of the art can be also described by the title of La Bernardino de Serna *et al.*, 2016: "There Is No Simple Model of the Plasma Membrane Organization". However, there is a growing number of methods attempting to shed light on the field of molecular membrane organization. This work also provides insights into the application of super-resolution imaging by *d*STORM as a tool for studying biological membranes. It suggests different methodologies for labeling of cell surface as well as intracellular membrane molecules, super-resolution imaging of plasma membranes, as well as quantification of membrane-associated molecules. In addition, it highlights the important role of appropriate photoswitching conditions to prevent artifacts in reconstructed *d*STORM images, and, in this context, indicates potential problems caused by projections of three-dimensional membrane structures.

Artifacts in Single-Molecule Localization Microscopy. Single-molecule localization microscopy such as *d*STORM requires fluorophores that can be switched between a fluorescent *on* and a non-fluorescent *off* state. Experimental conditions ensure that most fluorophores are in the dark state whereas only a small subset resides in the *on* state at any time (van de Linde *et al.*, 2011). Photoswitching and time separation of fluorescence emission are controlled by a range of parameters such as switching buffer composition, irradiation intensity, and label density. An inappropriate adjustment of these parameters can result in multi-emitter localizations which further can lead to image artifacts (van de Linde *et al.*, 2010). In this work, the impact of irradiation intensity, label density and photoswitching behavior on the distribution of membrane proteins in reconstructed super-resolution images was investigated (Burgert *et al.*, 2015; Mateos-Gil *et al.*, 2016, Manuscripts 2 and 3). It could be demonstrated that the combination of densely labeled plasma

membranes and inappropriate photoswitching rates induces artificial membrane clusters. Additionally, these "clusters" could even be detected and characterized by localization-based cluster analysis giving rise to potential sources of biological misinterpretations in the field of molecular clustering and membrane organization. Further investigations demonstrated that often inhomogeneous localization distributions arise from three-dimensional membrane structures, and are the result of their projections onto the two-dimensional image plane. Where the user expects a plane membrane surface, 3D structures such as microvilli, filopodia, vesicles and membrane foldings can occur which all are potential sources of projections and thus locally increased localization accumulations (Burgert *et al.*, 2015). These findings highlight the importance of accurately set photoswitching rates of standard probes in *d*STORM experiments. Even if all other parameters are set appropriately, low irradiation intensities can cause super-resolution artifacts. Especially in cases where a priori knowledge about the cellular structure is lacking, e.g., the distribution of membrane-associated proteins and lipids, caution should be exercised when interpreting reconstructed super-resolution images. An alternative way of imaging densely labeled structures without the need for high irradiation intensities might be the use of SOFI and appropriate fitting algorithms (Lukeš *et al.*, 2017).

dSTORM Imaging of Glycans. A plasma membrane's function is determined by its molecular composition as well as the spatial arrangement of its components. Since most membrane proteins and lipids are glycosylated, fluorescence tagging of glycans in combination with super-resolution imaging can be used to study large subclasses of membrane conjugates and their molecular distribution in the plasma membrane. In this work, glycans were fluorescently tagged by bioorthogonal glycoengineering which is the combination of metabolic labeling and click chemistry (Letschert *et al.*, 2014; Mateos-Gil *et al.*, 2016), (Manuscripts 1 and 3). Its advantage lies in the small label sizes of azide-functionalized glycan building blocks (sugar derivatives) and the corresponding dye–alkynes, compared to antibodies, lectins and fluorescent proteins (Laughlin and Bertozzi, 2009; Mateos-Gil *et al.*, 2016). It could be shown, that the quality of membrane staining was substantially enhanced when copper-catalyzed click chemistry was performed for only 5 min on living cells and in the presence of the copper-chelating ligand THPTA. Same results could be attained by copper-free click chemistry using strain-promoted dye alkynes when incubation times were slightly increased to 15 min (Letschert *et al.*, 2014; Mateos-Gil *et al.*, 2016). By using *d*STORM, high-resolution images of membrane-associated glycans could be generated showing a homogeneous molecule distribution on mammalian cells without the presence of clusters. This was additionally verified by localization-based cluster analysis using Ripley's H function. By

using the single-molecule information provided in each localization file, localization densities were calculated and molecule densities of three different glycan subtypes could be estimated ranging between 70 (GlcNAz) and 600 glycans/μm^2 (GalNAz). Based on this, an absolute number of 5×10^6 glycans/cell was estimated (Letschert *et al.*, 2014). These results show that labeling of glycans with chemical reporters in combination with *d*STORM can be efficiently used to study cell surface glycoconjugates and hold promise for a refined understanding of structural membrane organization and function.

Counting Receptors for Personalized Immunotherapies. Since single-molecule localization microscopy has become a general tool for quantitative analysis of molecular distributions, it also has become more and more relevant in biomedical applications. A very promising approach is the quantification of very low-expressing receptors on cancer cells which can act as targets in personalized immunotherapies. Usually, potential target receptors on healthy and tumor cells are routinely analyzed by flow cytometry. However, due to a limited sensitivity especially of standard instruments used in clinics and hospitals, low-expressing surface molecules can be overlooked. In this work, quantitative *d*STORM imaging was used to analyze primary multiple myeloma cells for CD19 expression as a potential target for CAR T cell therapy (Manuscript 4, Nerreter *et al.*, in submission).

First, it could be demonstrated, that immunostaining of primary myeloma cells was qualitatively increased when living cells were labeled on ice with fluorophore-conjugated primary antibodies before being fixed. For one thing, this ensures the structural integrity of the plasma membrane, and secondly, the cell's activity is substantially downregulated to prevent receptor and antibody endocytosis which could additionally be demonstrated by a range of transferrin experiments (Chapter 4.3). Surprisingly, CD19 could be detected on a fraction of myeloma cells in 10 out of 14 patients whereas flow cytometry only detected two CD19-positive patients. Based on these findings, the absolute number of CD19 molecules was quantified using *d*STORM and an alpha shape algorithm. To ensure that all CD19 receptors were labeled on the plasma membrane, a titration experiment with primary antibodies on a myeloma cell line was conducted (Figure 5.1). An experimental evidence for antibody (or alternatives) saturation should be always included in quantitative analyses to prevent underestimation of the number of target molecules. Depending on the patient, ~60–1,600 CD19 molecules per cell were estimated demonstrating a considerable increase in detection sensitivity of *d*STORM compared to flow cytometry (Nerreter *et al.*, in submission). However, data acquisition in *d*STORM experiments is more time consuming especially in cases where several tens to hundreds of cells per condition have to be measured

in order to statistically evaluate quantification results. This calls for more efficiency and process optimization which could be achieved by automatization of data acquisition (liquid handling, microchips, cell positioning, cell identification, autofocus and drift correction, quality control etc.) and data analysis (automated reconstruction, region of interest detection, quantification and statistics).

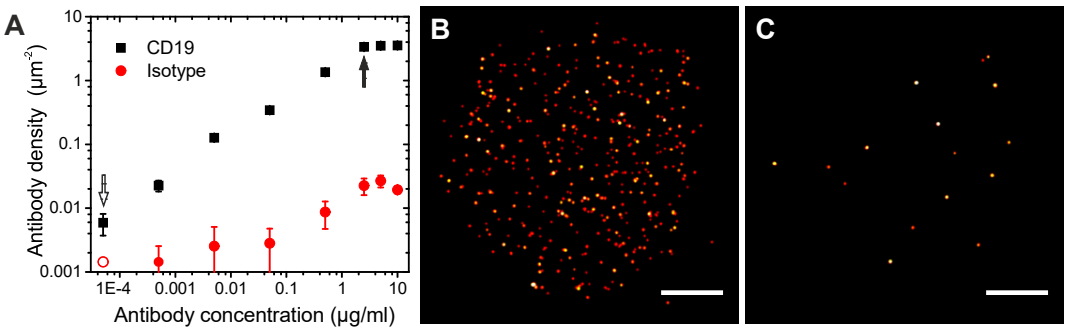

Figure 5.1: Titration of CD19 antibody on NALM-6 cells. (**A**) NALM-6 cells were incubated with different amounts of Alexa Fluor 647-conjugated anti-CD19 (black squares) and isotype control (red circles) antibodies, respectively. Densities of bound antibody were determined by alpha shape clustering of localizations coming from isolated fluorescent spots. At a concentration of 2.5 µg/ml, the density saturated at a level of 3.4 ± 0.2 CD19 antibodies/µm^2 (filled arrow). The lowest detectable density was 0.006 ± 0.002 CD19 antibodies/µm^2 at 5×10^{-5} µg/ml (open arrow). At very low isotype concentrations of 5×10^{-5} µg/ml, no fluorescent signal could be detected anymore (0 antibodies/µm^2, red open circle. (**B** and **C**) Representative *d*STORM images of the bottom membrane of NALM-6 cells stained with (**B**) 2.5 µg/ml and (**C**) 5×10^{-4} µg/ml CD19 antibody, respectively. Scale bars, 2 μm (Adapted from Nerreter *et al.*, in submission).

To summarize, the combination of appropriate labeling techniques, single-molecule localization microscopy, and well-chosen clustering algorithms promise to become one of the standard methods for the absolute quantification of cell surface molecules. Moreover, standardization and automatization regarding the measuring and analyzing workflow in combination with appropriate controls may pave the way for a daily use in diagnostic and analysis laboratories.

Abbreviations

Ac_4GalNAz	Tetraacetylated N-azidoacetylgalactosamine
Ac_4GlcNAz	Tetraacetylated N-azidoacetylglucosamine
Ac_4ManNAz	Tetraacetylated N-azidoacetyl-D-mannosamine
ATP	Adenosine triphosphate
BiTE	Bispecific T cell engager
BSA	Bovine serum albumin
CAR	Chimeric antigen receptor
CCV	Clathrin-coated vesicles
CD	Cluster of differentiation
CuAAC	Copper(I)-catalyzed azide alkyne cycloaddition
DBCO	Azadibenzocyclooctyne (ADIBO)
DBSCAN	Density-based spatial clustering of applications with noise
DIBO	Dibenzocyclooctyne
DMSO	Dimethyl sulfoxide
DOL	Degree of labeling
***d*STORM**	*direct* stochastic optical reconstruction microscopy
EMCCD	Electron multiplying charge-coupled device
ERC	Endocytic recycling compartment
FA	Formaldehyde
FC	Flow cytometry
FCS	Fetal calf serum
FWHM	Full width at half maximum
GA	Glutaraldehyde
GPI	Glycosyl-phosphatidylinositol
HILO	Highly inclined and laminated optical sheet
IgG	Immunoglobulin G

MEA	β-Mercaptoethylamine (Cysteamine)
MM	Multiple myeloma
mqH_2O	Milli-Q water
PA-FP	Photoactivatable fluorescent protein
PAINT	Points accumulation for imaging in nanoscale topography
PALM	Photoactivatable localization microscopy
PBS	Phosphate buffered saline
PDL	Poly-D-Lysine
PFA	Paraformaldehyde
PSF	Point spread function
ROS	Reactive oxygen species
RT	Room temperature
SD	Standard deviation
SEM	Standard error of the mean
SIM	Structured illumination microscopy
SMLM	Single molecule localization microscopy
SOFI	Super-resolution optical fluctuation imaging
SPAAC	Strain-promoted azide alkyne cycloaddition
SPT	Single-particle tracking
STED	Stimulated emission depletion
STORM	Stochastic optical reconstruction microscopy
TCR	T cell receptor
THPTA	Tris(3-hydroxypropyltriazolylmethyl)amine
TIRF	Total internal reflection microscopy
TRABI	Temporal, radial-aperture-based intensity estimation

Bibliography

Abbe, E. (1873) Beiträge zur Theorie des Mikroskops und der mikroskopischen Wahrnehmung. *Archiv f. Mikroskop. Anatomie* 9 (1):413–418.

Achtert, E., Kriegel, H.-P., and Zimek, A. (2008) ELKI: A Software System for Evaluation of Subspace Clustering Algorithms. In *Scientific and statistical database management: 20th international conference*, Lecture Notes in Computer Science vol. 5069, edited by B. Ludäscher, Springer, Berlin, Heidelberg, New York, pp 580–585.

Agard, N.J., Baskin, J.M., Prescher, J.A., Lo, A., and Bertozzi, C.R. (2006) A Comparative Study of Bioorthogonal Reactions with Azides. *ACS Chem. Biol.* 1 (10):644–648.

Ali, S. (2014) *Cell organisation and Function*, Pearson India.

Almén, M.S., Nordström, K.J.V., Fredriksson, R., and Schiöth, H.B. (2009) Mapping the human membrane proteome: A majority of the human membrane proteins can be classified according to function and evolutionary origin. *BMC Biol.* 7:50.

Atanackovic, D., Radhakrishnan, S.V., Bhardwaj, N., and Luetkens, T. (2016) Chimeric Antigen Receptor (CAR) therapy for multiple myeloma. *Br. J. Haematol.* 172 (5):685–698.

Bar-On, D., Wolter, S., van de Linde, S., Heilemann, M., Nudelman, G., Nachliel, E., Gutman, M., Sauer, M., and Ashery, U. (2012) Super-resolution imaging reveals the internal architecture of nano-sized syntaxin clusters. *J. Biol. Chem.* 287 (32):27158–27167.

Barysch, S.V., Aggarwal, S., Jahn, R., and Rizzoli, S.O. (2009) Sorting in early endosomes reveals connections to docking- and fusion-associated factors. *Proc. Natl. Acad. Sci. U.S.A.* 106 (24):9697–9702.

Baskin, J.M., Prescher, J.A., Laughlin, S.T., Agard, N.J., Chang, P.V., Miller, I.A., Lo, A., Codelli, J.A., and Bertozzi, C.R. (2007) Copper-free click chemistry for dynamic in vivo imaging. *Proc. Natl. Acad. Sci. U.S.A.* 104 (43):16793–16797.

Bates, M., Huang, B., Dempsey, G.T., and Zhuang, X. (2007) Multicolor Super-Resolution Imaging with Photo-Switchable Fluorescent Probes. *Science* 317 (5845):1749–1753.

Beare, A., Stockinger, H., Zola, H., and Nicholson, I. (2008) Monoclonal antibodies to human cell surface antigens. *Curr. Protoc. Immunol.* Appendix 4:4A.

Ben-Shlomo, I., Yu Hsu, S., Rauch, R., Kowalski, H.W., and Hsueh, A.J.W. (2003) Signaling receptome: A genomic and evolutionary perspective of plasma membrane receptors involved in signal transduction. *Science's STKE* 2003 (187):RE9.

Berg, J.M., Tymoczko, J.L., and Gatto, G.J. (2018) *Stryer Biochemie*, Lehrbuch, Springer Spektrum, Berlin.

Besanceney-Webler, C., Jiang, H., Zheng, T., Feng, L., Soriano del Amo, David, Wang, W., Klivansky, L.M., Marlow, F.L., Liu, Y., and Wu, P. (2011) Increasing the Efficacy of Bioorthogonal Click Reactions for Bioconjugation: A Comparative Study. *Angew. Chem. Int. Ed.* 50 (35):8051–8056.

Betzig, E., Patterson, G.H., Sougrat, R., Lindwasser, O.W., Olenych, S., Bonifacino, J.S., Davidson, M.W., Lippincott-Schwartz, J., and Hess, H.F. (2006) Imaging Intracellular Fluorescent Proteins at Nanometer Resolution. *Science* 313 (5793):1642–1645.

Bowie, J.U. (2005) Solving the membrane protein folding problem. *Nature* 438 (7068):581–589.

Brown, D.A. and London, E. (2000) Structure and function of sphingolipid- and cholesterol-rich membrane rafts. *J. Biol. Chem.* 275 (23):17221–17224.

Burgert, A., Letschert, S., Doose, S., and Sauer, M. (2015) Artifacts in single-molecule localization microscopy. *Histochem. Cell Biol.* 144 (2):123–131.

Burgert, A., Schlegel, J., Bécam, J., Doose, S., Bieberich, E., Schubert-Unkmeir, A., and Sauer, M. (2017) Characterization of Plasma Membrane Ceramides by Super-Resolution Microscopy. *Angew. Chem. Int. Ed.* 56 (22):6131–6135.

Casbon, A.-J., Allen, L.-A.H., Dunn, K.W., and Dinauer, M.C. (2009) Macrophage NADPH oxidase flavocytochrome B localizes to the plasma membrane and Rab11-positive recycling endosomes. *J. Immunol.* 182 (4):2325–2339.

Coons, A.H., Creech, H.J., and Jones, R.N. (1941) Immunological Properties of an Antibody Containing a Fluorescent Group. *Exp. Biol. M.* 47 (2):200–202.

Coons, A.H. and Kaplan, M.H. (1950) Localization of antigen in tissue cells; improvements in a method for the detection of antigen by means of fluorescent antibody. *J. Exp. Med.* 91 (1):1–13.

Cooper, G.M. (2000) *The Cell: A molecular approach*, ASM Press; Sinauer Associates, Washington, D.C., Sunderland (Mass.).

Danielli, J.F. and Davson, H. (1935) A contribution to the theory of permeability of thin films. *J. Cell. Physiol.* 5 (4):495–508.

Dautry-Varsat, A. (1986) Receptor-mediated endocytosis: The intracellular journey of transferrin and its receptor. *Biochimie* 68 (3):375–381.

Debets, M.F., van Berkel, S.S., Schoffelen, S., Rutjes, F.P.J.T., van Hest, Jan C. M., and van Delft, F.L. (2010) Aza-dibenzocyclooctynes for fast and efficient enzyme PEGylation via copper-free (3+2) cycloaddition. *Chem. Commun.* 46 (1):97–99.

Dertinger, T., Colyer, R., Iyer, G., Weiss, S., and Enderlein, J. (2009) Fast, background-free, 3D super-resolution optical fluctuation imaging (SOFI). *Proc. Natl. Acad. Sci. U.S.A.* 106 (52):22287–22292.

Dupuy, A.D. and Engelman, D.M. (2008) Protein area occupancy at the center of the red blood cell membrane. *Proc. Natl. Acad. Sci. U.S.A.* 105 (8):2848–2852.

Edelsbrunner, H. (1992) *Weighted Alpha Shapes*, UILU-ENG 17 92,1740, Dep. of Computer Science Univ. of Illinois at Urbana-Champaign, Urbana, Ill.

Edelsbrunner, H., Kirkpatrick, D., and Seidel, R. (1983) On the shape of a set of points in the plane. *IEEE Trans. Inform. Theory* 29 (4):551–559.

Edelsbrunner, H. and Mucke, E.P. (1992) *Three-dimensional alpha shapes*, Report no. UIUCDCS-R-92-1734, Dept. of Computer Science, University of Illinois at Urbana-Champaign, Urbana, Ill.

Ehmann, N., van de Linde, S., Alon, A., Ljaschenko, D., Keung, X.Z., Holm, T., Rings, A., DiAntonio, A., Hallermann, S., Ashery, U., Heckmann, M., Sauer, M., and Kittel, R.J. (2014) Quantitative super-resolution imaging of Bruchpilot distinguishes active zone states. *Nat. Commun.* 5:4650.

Endesfelder, U., Malkusch, S., Flottmann, B., Mondry, J., Liguzinski, P., Verveer, P.J., and Heilemann, M. (2011) Chemically Induced Photoswitching of Fluorescent Probes—A General Concept for Super-Resolution Microscopy. *Molecules* 16 (4):3106–3118.

Ester, M., Kriegel, H.P., Sander, J., and Xu, X. (1996) A Density-Based Algorithm for Discovering Clusters in Large Spatial Databases with Noise. In *Proc. 2 nd Int. Conf. on Knowledge Discovery and Data Mining(KDD ' 96)*, pp 226–231.

Evans, R.A. (2007) The Rise of Azide–Alkyne 1,3-Dipolar 'Click' Cycloaddition and its Application to Polymer Science and Surface Modification. *Aust. J. Chem.* 60 (6):384.

Eyss, B. von, Jaenicke, L.A., Kortlever, R.M., Royla, N., Wiese, K.E., Letschert, S., McDuffus, L.-A., Sauer, M., Rosenwald, A., Evan, G.I., Kempa, S., and Eilers, M. (2015) A MYC-Driven Change in Mitochondrial Dynamics Limits

YAP/TAZ Function in Mammary Epithelial Cells and Breast Cancer. *Cancer Cell* 28 (6):743–757.

Farkona, S., Diamandis, E.P., and Blasutig, I.M. (2016) Cancer immunotherapy: The beginning of the end of cancer? *BMC Med.* 14:73.

Fernandis, A.Z. and Wenk, M.R. (2007) Membrane lipids as signaling molecules. *Curr. Opin. Lipidol.* 18 (2):121–128.

Fiebig, H., Behn, I., Gruhn, R., Typlt, H., Kupper, H., and Ambrosius, H. (1984) Charakterisierung einer Serie von monoklonalen Antikörpern gegen humane T-Zellen. *Allerg. Immunol.* 30 (4):242–250.

Franke, C., Sauer, M., and van de Linde, S. (2017) Photometry unlocks 3D information from 2D localization microscopy data. *Nat. Methods* 14 (1):41–44.

Frey, T.G. and Mannella, C.A. (2000) The internal structure of mitochondria. *Trends Biochem. Sci.* 25 (7):319–324.

Fricke, F., Beaudouin, J., Eils, R., and Heilemann, M. (2015) One, two or three? Probing the stoichiometry of membrane proteins by single-molecule localization microscopy. *Sci. Rep.* 5:14072.

Friedman, J.R. and Nunnari, J. (2014) Mitochondrial form and function. *Nature* 505 (7483):335–343.

Fry, S.C. (1998) Oxidative scission of plant cell wall polysaccharides by ascorbate-induced hydroxyl radicals. *Biochem. J.* 332:507–515.

Frye, L.D. and Edidin, M. (1970) The rapid intermixing of cell surface antigens after formation of mouse-human heterokaryons. *J. Cell Sci.* 7 (2):319–335.

Fujiwara, T., Ritchie, K., Murakoshi, H., Jacobson, K., and Kusumi, A. (2002) Phospholipids undergo hop diffusion in compartmentalized cell membrane. *J. Cell Biol.* 157 (6):1071–1081.

Fürstenberg, A. and Heilemann, M. (2013) Single-molecule localization microscopy-near-molecular spatial resolution in light microscopy with photoswitchable fluorophores. *Phys. Chem. Chem. Phys.* 15 (36):14919–14930.

Galvez, T., Gilleron, J., Zerial, M., and O'Sullivan, G.A. (2012) SnapShot: Mammalian Rab proteins in endocytic trafficking. *Cell* 151 (1):234-234.e2.

Garfall, A.L., Maus, M.V., Hwang, W.-T., Lacey, S.F., Mahnke, Y.D., Melenhorst, J.J., Zheng, Z., Vogl, D.T., Cohen, A.D., Weiss, B.M., Dengel, K., Kerr, N.D.S., Bagg, A., Levine, B.L., June, C.H., and Stadtmauer, E.A. (2015) Chimeric Antigen Receptor T Cells against CD19 for Multiple Myeloma. *New Engl. J. Med.* 373 (11):1040–1047.

Garfall, A.L., Stadtmauer, E.A., Maus, M.V., Hwang, W.-T., Vogl, D.T., Cohen, A.D., Weiss, B.M., Porter, D.L., Frey, N., Milone, M., Mangan, P., Krevvata,

M., Ayers, E., Dengel, K., Kerr, N.D.S., Lacey, S.F., Melenhorst, J.J., Ambrose, D.E., Chen, F., Gonzalez, V.E., Kulikovskaya, I., Gupta, M., Finklestein, J., Lamontagne, A., O'Rourke, M., Davis, M.S., Malykhin, A., Levine, B.L., and June, C.H. (2016) Pilot Study of Anti-CD19 Chimeric Antigen Receptor T Cells (CTL019) in Conjunction with Salvage Autologous Stem Cell Transplantation for Advanced Multiple Myeloma. *Blood* 128 (22):974.

Geissbuehler, S., Dellagiacoma, C., and Lasser, T. (2011) Comparison between SOFI and STORM. *Biomed. Opt. Express* 2 (3):408–420.

Ghosh, A., Mailankody, S., Giralt, S.A., Landgren, C.O., Smith, E.L., and Brentjens, R.J. (2017) CAR T cell therapy for multiple myeloma: Where are we now and where are we headed? *Leuk. Lymphoma*:1–12.

Gorter, E. and Grendel, F. (1925) On Biomolecular Layers of Lipoids on the Chromocytes of the Blood. *J. Exp. Med.* 41 (4):439–443.

Grant, B.D. and Donaldson, J.G. (2009) Pathways and mechanisms of endocytic recycling. *Nat. Rev. Mol. Cell Biol.* 10 (9):597–608.

Grecco, H.E., Schmick, M., and Bastiaens, P.I.H. (2011) Signaling from the living plasma membrane. *Cell* 144 (6):897–909.

Griffié, J., Shannon, M., Bromley, C.L., Boelen, L., Burn, G.L., Williamson, D.J., Heard, N.A., Cope, A.P., Owen, D.M., and Rubin-Delanchy, P. (2016) A Bayesian cluster analysis method for single-molecule localization microscopy data. *Nat. Protoc.* 11 (12):2499–2514.

Gustafsson, M.G.L. (2000) Surpassing the lateral resolution limit by a factor of two using structured illumination microscopy. SHORT COMMUNICATION. *J. Microsc.* 198 (2):82–87.

Gutmann, M., Memmel, E., Braun, A.C., Seibel, J., Meinel, L., and Lühmann, T. (2016) Biocompatible Azide-Alkyne "Click" Reactions for Surface Decoration of Glyco-Engineered Cells. *ChemBioChem* 17 (9):866–875.

Haberman, Y., Grimberg, E., Fukuda, M., and Sagi-Eisenberg, R. (2003) Synaptotagmin IX, a possible linker between the perinuclear endocytic recycling compartment and the microtubules. *J. Cell Sci.* 116 (Pt 21):4307–4318.

Hamilton, T.A. (1983) Receptor-mediated endocytosis and exocytosis of transferrin in Concanavalin A-stimulated rat lymphoblasts. *J. Cell. Physiol.* 114 (2):222–228.

Hang, H.C., Yu, C., Kato, D.L., and Bertozzi, C.R. (2003) A metabolic labeling approach toward proteomic analysis of mucin-type O-linked glycosylation. *Proc. Natl. Acad. Sci. U.S.A.* 100 (25):14846–14851.

Harper, I.S. (1986) Glutaraldehyde-induced permeabilization of cell membranes. *J. Microsc.* 141 (Pt 2):RP3-4.

Heilemann, M., van de Linde, S., Schüttpelz, M., Kasper, R., Seefeldt, B., Mukherjee, A., Tinnefeld, P., and Sauer, M. (2008) Subdiffraction-Resolution Fluorescence Imaging with Conventional Fluorescent Probes. *Angew. Chem. Int. Ed.* 47 (33):6172–6176.

Heilemann, M., van de Linde, S., Mukherjee, A., and Sauer, M. (2009) Super-Resolution Imaging with Small Organic Fluorophores. *Angew. Chem. Int. Ed.* 48 (37):6903–6908.

Heintzmann, R. and Cremer, C.G. (1999) Laterally modulated excitation microscopy: Improvement of resolution by using a diffraction grating, SPIE Proceedings, BiOS Europe '98, edited by I.J. Bigio, H. Schneckenburger, J. Slavik, K. Svanberg, and P.M. Viallet, SPIE, pp 185–196.

Hell, S.W. (2007) Far-Field Optical Nanoscopy. *Science* 316 (5828):1153–1158.

Hell, S.W. and Wichmann, J. (1994) Breaking the diffraction resolution limit by stimulated emission: stimulated-emission-depletion fluorescence microscopy. *Opt. Lett.* 19 (11):780.

Hess, S.T., Girirajan, Thanu P K, and Mason, M.D. (2006) Ultra-high resolution imaging by fluorescence photoactivation localization microscopy. *Biophys. J.* 91 (11):4258–4272.

Heuser, J.E. (1989) Hypertonic media inhibit receptor-mediated endocytosis by blocking clathrin-coated pit formation. *J. Cell Biol.* 108 (2):389–400.

Holden, S.J., Uphoff, S., and Kapanidis, A.N. (2011) DAOSTORM: An algorithm for high- density super-resolution microscopy. *Nat. Methods* 8 (4):279.

Homann, A., Qamar, R.-U., Serim, S., Dersch, P., and Seibel, J. (2010) Bioorthogonal metabolic glycoengineering of human larynx carcinoma (HEp-2) cells targeting sialic acid. *Beilstein. J. Org. Chem.* 6:24.

Hong, V., Presolski, S.I., Ma, C., and Finn, M.G. (2009) Analysis and Optimization of Copper-Catalyzed Azide-Alkyne Cycloaddition for Bioconjugation. *Angew. Chem. Int. Ed.* 48 (52):9879–9883.

Horisawa, K. (2014) Specific and quantitative labeling of biomolecules using click chemistry. *Front. Physiol.* 5:457.

Huang, B., Jones, S.A., Brandenburg, B., and Zhuang, X. (2008) Whole-cell 3D STORM reveals interactions between cellular structures with nanometer-scale resolution. *Nat. Methods* 5 (12):1047–1052.

Huang, B., Wang, W., Bates, M., and Zhuang, X. (2008) Three-Dimensional Super-Resolution Imaging by Stochastic Optical Reconstruction Microscopy. *Science* 319 (5864):810–813.

Hudak, J.E. and Bertozzi, C.R. (2014) Glycotherapy: New Advances Inspire a Reemergence of Glycans in Medicine. *Chemistry & Biology* 21 (1):16–37.

Hudecek, M. and Einsele, H. (2016) Myeloma CARs are rolling into the clinical arena. *Blood* 128 (13):1667–1668.

Huehls, A.M., Coupet, T.A., and Sentman, C.L. (2015) Bispecific T-cell engagers for cancer immunotherapy. *Immunol. Cell. Biol.* 93 (3):290–296.

Huisgen, R. (1963) 1,3-Dipolar Cycloadditions. Past and Future. *Angew. Chem. Int. Ed.* 2 (10):565–598.

Hummer, G., Fricke, F., and Heilemann, M. (2016) Model-independent counting of molecules in single-molecule localization microscopy. *Mol. Biol. Cell* 27 (22):3637–3644.

Hutagalung, A.H. and Novick, P.J. (2011) Role of Rab GTPases in membrane traffic and cell physiology. *Physiol. Rev.* 91 (1):119–149.

Jewett, J.C., Sletten, E.M., and Bertozzi, C.R. (2010) Rapid Cu-free click chemistry with readily synthesized biarylazacyclooctynones. *J. Am. Chem. Soc.* 132 (11):3688–3690.

Johnson, J.E. and Cornell, R.B. (2009) Amphitropic proteins: Regulation by reversible membrane interactions (Review). *Mol. Membr. Biol.* 16 (3):217–235.

Jones, S.A., Shim, S.-H., He, J., and Zhuang, X. (2011) Fast, three-dimensional super-resolution imaging of live cells. *Nat. Methods* 8 (6):499–508.

Jung, L.A., Gebhardt, A., Koelmel, W., Ade, C.P., Walz, S., Kuper, J., Eyss, B. von, Letschert, S., Redel, C., d'Artista, L., Biankin, A., Zender, L., Sauer, M., Wolf, E., Evan, G., Kisker, C., and Eilers, M. (2017) OmoMYC blunts promoter invasion by oncogenic MYC to inhibit gene expression characteristic of MYC-dependent tumors. *Oncogene* 36 (14):1911–1924.

Kabbani, A.M. and Kelly, C.V. (2017) The Detection of Nanoscale Membrane Bending with Polarized Localization Microscopy. *Biophys. J.* 113 (8):1782–1794.

Kaiser, D. (2001) Building a multicellular organism. *Annu. Rev. Genet.* 35:103–123.

Karathanasis, C., Fricke, F., Hummer, G., and Heilemann, M. (2017) Molecule Counts in Localization Microscopy with Organic Fluorophores. *ChemPhysChem* 18 (8):942–948.

Khan, S. and Newaz, G. (2010) A comprehensive review of surface modification for neural cell adhesion and patterning. *J. Biomed. Mater. Res. A* 93 (3):1209–1224.

Kirchhausen, T., Owen, D., and Harrison, S.C. (2014) Molecular structure, function, and dynamics of clathrin-mediated membrane traffic. *Cold Spring Harb. Perspect. Biol.* 6 (5):a016725.

Klein, T., Löschberger, A., Proppert, S., Wolter, S., van de Linde, S., and Sauer, M. (2011) Live-cell dSTORM with SNAP-tag fusion proteins. *Nat. Methods* 8 (1):7–9.

Klein, T., Proppert, S., and Sauer, M. (2014) Eight years of single-molecule localization microscopy. *Histochem. Cell Biol.*

Klotzsch, E. and Schütz, G.J. (2013) A critical survey of methods to detect plasma membrane rafts. *Philos. Trans. R. Soc. Lond. B, Biol. Sci.* 368 (1611):20120033.

Kochenderfer, J.N. and Rosenberg, S.A. (2013) Treating B-cell cancer with T cells expressing anti-CD19 chimeric antigen receptors. *Nat. Rev. Clin. Oncol* 10 (5):267–276.

Kolb, H.C., Finn, M.G., and Sharpless, K.B. (2001) Click Chemistry: Diverse Chemical Function from a Few Good Reactions. *Angew. Chem. Int. Ed.* 40 (11):2004–2021.

Kolb, H.C. and Sharpless, K.B. (2003) The growing impact of click chemistry on drug discovery. *Drug Discovery Today* 8 (24):1128–1137.

Kusumi, A., Nakada, C., Ritchie, K., Murase, K., Suzuki, K., Murakoshi, H., Kasai, R.S., Kondo, J., and Fujiwara, T. (2005) Paradigm shift of the plasma membrane concept from the two-dimensional continuum fluid to the partitioned fluid: High-speed single-molecule tracking of membrane molecules. *Annu. Rev. Biophys. Biomol. Struct.* 34:351–378.

Kusumi, A. and Suzuki, K. (2005) Toward understanding the dynamics of membrane-raft-based molecular interactions. *Biochim. Biophys. Acta* 1746 (3):234–251.

La Bernardino de Serna, J., Schütz, G.J., Eggeling, C., and Cebecauer, M. (2016) There Is No Simple Model of the Plasma Membrane Organization. *Front. Cell Dev. Biol.* 4:106.

Lakowicz, J.R. (2006) *Principles of fluorescence spectroscopy*, Springer, New York.

Lauffer, R.B. (1992) *Iron and human disease*, CRC Press, Boca Raton.

Laughlin, S.T., Baskin, J.M., Amacher, S.L., and Bertozzi, C.R. (2008) In Vivo Imaging of Membrane-Associated Glycans in Developing Zebrafish. *Science* 320 (5876):664–667.

Laughlin, S.T. and Bertozzi, C.R. (2009) Imaging the glycome. *Proc. Natl. Acad. Sci. U.S.A.* 106 (1):12–17.

Legant, W.R., Shao, L., Grimm, J.B., Brown, T.A., Milkie, D.E., Avants, B.B., Lavis, L.D., and Betzig, E. (2016) High-density three-dimensional localization microscopy across large volumes. *Nat. Methods* 13 (4):359.

Letschert, S., Göhler, A., Franke, C., Bertleff-Zieschang, N., Memmel, E., Doose, S., Seibel, J., and Sauer, M. (2014) Super-resolution imaging of plasma membrane glycans. *Angew. Chem. Int. Ed.* 53 (41):10921–10924.

Leyton-Puig, D., Isogai, T., Argenzio, E., van den Broek, B., Klarenbeek, J., Janssen, H., Jalink, K., and Innocenti, M. (2017) Flat clathrin lattices are dynamic actin-controlled hubs for clathrin-mediated endocytosis and signalling of specific receptors. *Nat. Commun.* 8:16068.

Leyton-Puig, D., Kedziora, K.M., Isogai, T., van den Broek, B., Jalink, K., and Innocenti, M. (2016) PFA fixation enables artifact-free super-resolution imaging of the actin cytoskeleton and associated proteins. *Biol. Open* 5 (7):1001–1009.

Li, J., Mach, P., and Koehl, P. (2013) Measuring the shapes of macromolecules - and why it matters. *Comput. Struct. Biotechnol. J.* 8:e201309001.

Lillemeier, B.F., Mörtelmaier, M.A., Forstner, M.B., Huppa, J.B., Groves, J.T., and Davis, M.M. (2010) TCR and Lat are expressed on separate protein islands on T cell membranes and concatenate during activation. *Nat. Immunol.* 11 (1):90–96.

Lillemeier, B.F., Pfeiffer, J.R., Surviladze, Z., Wilson, B.S., and Davis, M.M. (2006) Plasma membrane-associated proteins are clustered into islands attached to the cytoskeleton. *Proc. Natl. Acad. Sci. U.S.A.* 103 (50):18992–18997.

Link, A.J., Vink, M.K.S., Agard, N.J., Prescher, J.A., Bertozzi, C.R., and Tirrell, D.A. (2006) Discovery of aminoacyl-tRNA synthetase activity through cell-surface display of noncanonical amino acids. *Proc. Natl. Acad. Sci. U.S.A.* 103 (27):10180–10185.

Lippincott-Schwartz, J. and Patterson, G.H. (2003) Development and use of fluorescent protein markers in living cells. *Science* 300 (5616):87–91.

Lommerse, P.H.M., Spaink, H.P., and Schmidt, T. (2004) In vivo plasma membrane organization: Results of biophysical approaches. *Biochim. Biophys. Acta* 1664 (2):119–131.

Löschberger, A., Niehörster, T., and Sauer, M. (2014) Click chemistry for the conservation of cellular structures and fluorescent proteins: ClickOx. *Biotechnol. J.*

Lukeš, T., Glatzová, D., Kvíčalová, Z., Levet, F., Benda, A., Letschert, S., Sauer, M., Brdička, T., Lasser, T., and Cebecauer, M. (2017) Quantifying protein densities on cell membranes using super-resolution optical fluctuation imaging. *Nat. Commun.* 8:1731.

Mahal, L.K., Yarema, K.J., and Bertozzi, C.R. (1997) Engineering chemical reactivity on cell surfaces through oligosaccharide biosynthesis. *Science* 276 (5315):1125–1128.

Malkusch, S. and Heilemann, M. (2016) Extracting quantitative information from single-molecule super-resolution imaging data with LAMA - LocAlization Microscopy Analyzer. *Sci. Rep.* 6:34486.

Mamdouh, Z., Giocondi, M.-C., Laprade, R., and Le Grimellec, C. (1996) Temperature dependence of endocytosis in renal epithelial cells in culture. *BBA-Biomembranes* 1282 (2):171–173.

Mateos-Gil, P., Letschert, S., Doose, S., and Sauer, M. (2016) Super-Resolution Imaging of Plasma Membrane Proteins with Click Chemistry. *Front. Cell Dev. Biol.* 4:98.

Maus, M.V. and June, C.H. (2016) Making Better Chimeric Antigen Receptors for Adoptive T-cell Therapy. *Clin. Cancer Res.* 22 (8):1875–1884.

Maxfield, F.R. and McGraw, T.E. (2004) Endocytic recycling. *Nat. Rev. Mol. Cell Biol.* 5 (2):121–132.

Mazia, D. (1975) Adhesion of cells to surfaces coated with polylysine. Applications to electron microscopy. *J. Cell Biol.* 66 (1):198–200.

McMahon, H.T. and Boucrot, E. (2011) Molecular mechanism and physiological functions of clathrin-mediated endocytosis. *Nat. Rev. Mol. Cell Biol.* 12 (8):517–533.

Melan, M.A. (op. 1994) Overview of Cell Fixation and Permeabilization. In *Monoclonal antibody protocols*, Methods in molecular biology 45, edited by W.C. Davis, Humana Press, Totowa, pp 55–66.

Mertsch, A., Letschert, S., Memmel, E., Sauer, M., and Seibel, J. (2016) Synthesis and application of water-soluble, photoswitchable cyanine dyes for bioorthogonal labeling of cell-surface carbohydrates. *Z. Naturforsch. C Bio. Sci.* 71 (9-10):347–354.

Mikkilineni, L. and Kochenderfer, J.N. (2017) Chimeric Antigen Receptor T-cell Therapies for Multiple Myeloma. *Blood*.

Möckl, L., Horst, A.K., Kolbe, K., Lindhorst, T.K., and Bräuchle, C. (2015) Microdomain Formation Controls Spatiotemporal Dynamics of Cell-Surface Glycoproteins. *ChemBioChem* 16 (14):2023–2028.

Morone, N., Fujiwara, T., Murase, K., Kasai, R.S., Ike, H., Yuasa, S., Usukura, J., and Kusumi, A. (2006) Three-dimensional reconstruction of the membrane skeleton at the plasma membrane interface by electron tomography. *J. Cell Biol.* 174 (6):851–862.

Mukherjee, S., Ghosh, R.N., and Maxfield, F.R. (1997) Endocytosis. *Physiol. Rev.* 77 (3):759–803.

Naughtin, M.J., Sheffield, D.A., Rahman, P., Hughes, W.E., Gurung, R., Stow, J.L., Nandurkar, H.H., Dyson, J.M., and Mitchell, C.A. (2010) The myotubularin phosphatase MTMR4 regulates sorting from early endosomes. *J. Cell. Sci.* 123 (Pt 18):3071–3083.

Nerreter, T., Letschert, S., Doose, S., Danhof, S., Einsele, H., Sauer, M., and Hudecek, M. (in submission) CD19CART cells eliminate myeloma cells that express very low levels of CD19.

Nicolson, G.L. (2014) The Fluid-Mosaic Model of Membrane Structure: Still relevant to understanding the structure, function and dynamics of biological membranes after more than 40 years. *Biochim. Biophys. Acta* 1838 (6):1451–1466.

Nicovich, P.R., Owen, D.M., and Gaus, K. (2017) Turning single-molecule localization microscopy into a quantitative bioanalytical tool. *Nat. Protoc.* 12 (3):453–460.

Opazo, F., Levy, M., Byrom, M., Schäfer, C., Geisler, C., Groemer, T.W., Ellington, A.D., and Rizzoli, S.O. (2012) Aptamers as potential tools for super-resolution microscopy. *Nat. Methods* 9 (10):938–939.

Pageon, S.V., Nicovich, P.R., Mollazade, M., Tabarin, T., and Gaus, K. (2016) Clus-DoC: A combined cluster detection and colocalization analysis for single-molecule localization microscopy data. *Mol. Biol. Cell* 27 (22):3627–3636.

Pastan, I. and Willingham, M.C. (1985) *Endocytosis*, Springer US, Boston, MA.

Patrizio, A. and Specht, C.G. (2016) Counting numbers of synaptic proteins: Absolute quantification and single molecule imaging techniques. *Neurophotonics* 3 (4):41805.

Patterson, D.M., Nazarova, L.A., and Prescher, J.A. (2014) Finding the right (bioorthogonal) chemistry. *ACS Chem. Biol.* 9 (3):592–605.

Patterson, G., Davidson, M., Manley, S., and Lippincott-Schwartz, J. (2010) Superresolution imaging using single-molecule localization. *Annu. Rev. Phys. Chem.* 61:345–367.

Pike, L.J. (2006) Rafts defined: A report on the Keystone Symposium on Lipid Rafts and Cell Function. *J. Lipid. Res.* 47 (7):1597–1598.

Poloukhtine, A.A., Mbua, N.E., Wolfert, M.A., Boons, G.-J., and Popik, V.V. (2009) Selective labeling of living cells by a photo-triggered click reaction. *J. Am. Chem. Soc.* 131 (43):15769–15776.

Prescher, J.A., Dube, D.H., and Bertozzi, C.R. (2004) Chemical remodelling of cell surfaces in living animals. *Nature* 430 (7002):873–877.

Presolski, S.I., Hong, V.P., and Finn, M.G. (2011) Copper-Catalyzed Azide-Alkyne Click Chemistry for Bioconjugation. *Curr. Protoc. Chem. Biol.* 3 (4):153–162.

Quan, T., Zhu, H., Liu, X., Liu, Y., Ding, J., Zeng, S., and Huang, Z.-L. (2011) High-density localization of active molecules using Structured Sparse Model and Bayesian Information Criterion. *Opt. Express* 19 (18):16963–16974.

Rayleigh. (1896) XV. On the theory of optical images, with special reference to the microscope. *Philosophical Magazine Series* 5 42 (255):167–195.

Richter, K.N., Revelo, N.H., Seitz, K.J., Helm, M.S., Sarkar, D., Saleeb, R.S., D'Este, E., Eberle, J., Wagner, E., Vogl, C., Lazaro, D.F., Richter, F., Coy-Vergara, J., Coceano, G., Boyden, E.S., Duncan, R.R., Hell, S.W., Lauterbach, M.A., Lehnart, S.E., Moser, T., Outeiro, T.F., Rehling, P., Schwappach, B., Testa, I., Zapiec, B., and Rizzoli, S.O. (2018) Glyoxal as an alternative fixative to formaldehyde in immunostaining and super-resolution microscopy. *EMBO J.* 37 (1):139–159.

Riedel, F., Gillingham, A.K., Rosa-Ferreira, C., Galindo, A., and Munro, S. (2016) An antibody toolkit for the study of membrane traffic in Drosophila melanogaster. *Biol. Open* 5 (7):987–992.

Ripley, B.D. (1977) Modelling Spatial Patterns. *J. Royal Stat. Soc.* 39 (2):172–212.

Robertson, J.D. (1959) The ultrastructure of cell membranes and their derivatives. *Biochem. Soc. Symp.* 16:3–43.

Robertson, J.D. (1981) Membrane structure. *J. Cell Biol.* 91 (3 Pt 2):189s-204s.

Rosenberg, S.A. and Restifo, N.P. (2015) Adoptive cell transfer as personalized immunotherapy for human cancer. *Science* 348 (6230):62–68.

Rostovtsev, V.V., Green, L.G., Fokin, V.V., and Sharpless, K.B. (2002a) A stepwise huisgen cycloaddition process: Copper(I)-catalyzed regioselective "ligation" of azides and terminal alkynes. *Angew. Chem. Int. Ed.* 41 (14):2596–2599.

Rostovtsev, V.V., Green, L.G., Fokin, V.V., and Sharpless, K.B. (2002b) A Stepwise Huisgen Cycloaddition Process: Copper(I)-Catalyzed Regioselective “Ligation” of Azides and Terminal Alkynes. *Angew. Chem. Int. Ed.* 41 (14):2596–2599.

Rust, M.J., Bates, M., and Zhuang, X. (2006) Sub-diffraction-limit imaging by stochastic optical reconstruction microscopy (STORM). *Nat. Methods* 3 (10):793–796.

Sadelain, M., Brentjens, R., and Rivière, I. (2013) The basic principles of chimeric antigen receptor design. *Cancer Discov.* 3 (4):388–398.

Saka, S.K., Honigmann, A., Eggeling, C., Hell, S.W., Lang, T., and Rizzoli, S.O. (2014) Multi-protein assemblies underlie the mesoscale organization of the plasma membrane. *Nat. Commun.* 5:4509.

Sako, Y. and Kusumi, A. (1994) Compartmentalized structure of the plasma membrane for receptor movements as revealed by a nanometer-level motion analysis. *J. Cell Biol.* 125 (6):1251–1264.

Sander, J., Ester, M., Kriegel, H.-P., and Xu, X. (1998) Density-Based Clustering in Spatial Databases: The Algorithm GDBSCAN and Its Applications. *Data Mining and Knowledge Discovery* 2 (2):169–194.

Sauer, M. (2013) Localization microscopy coming of age: from concepts to biological impact. *J. Cell Sci.* 126 (Pt 16):3505–3513.

Sauer, M., Hofkens, J., and Enderlein, J. (2011) *Handbook of fluorescence, spectroscopy and imaging: From single molecules to ensembles*, Wiley-VCH, Weinheim.

Saxon, E. and Bertozzi, C.R. (2000) Cell Surface Engineering by a Modified Staudinger Reaction. *Science* 287 (5460):2007–2010.

Schäfer, P., van de Linde, S., Lehmann, J., Sauer, M., and Doose, S. (2013) Methylene Blue- and Thiol-Based Oxygen Depletion for Super-Resolution Imaging. *Anal. Chem.* 85 (6):3393–3400.

Schindelin, J., Arganda-Carreras, I., Frise, E., Kaynig, V., Longair, M., Pietzsch, T., Preibisch, S., Rueden, C., Saalfeld, S., Schmid, B., Tinevez, J.-Y., White, D.J., Hartenstein, V., Eliceiri, K., Tomancak, P., and Cardona, A. (2012) Fiji: An open-source platform for biological-image analysis. *Nat. Methods* 9 (7):676.

Schmidt, R., Wurm, C.A., Punge, A., Egner, A., Jakobs, S., and Hell, S.W. (2009) Mitochondrial cristae revealed with focused light. *Nano Lett.* 9 (6):2508–2510.

Sezgin, E., Levental, I., Mayor, S., and Eggeling, C. (2017) The mystery of membrane organization: Composition, regulation and roles of lipid rafts. *Nat. Rev. Mol. Cell Biol.* 18 (6):361–374.

Shannon, C.E. (1949) Communication in the Presence of Noise. *Proc. IRE* 37 (1):10–21.

Sheetz, M.P., Schindler, M., and Koppel, D.E. (1980) Lateral mobility of integral membrane proteins is increased in spherocytic erythrocytes. *Nature* 285 (5765):510–511.

Shim, S.-H., Xia, C., Zhong, G., Babcock, H.P., Vaughan, J.C., Huang, B., Wang, X., Xu, C., Bi, G.-Q., and Zhuang, X. (2012) Super-resolution fluorescence imaging of organelles in live cells with photoswitchable membrane probes. *Proc. Natl. Acad. Sci. U.S.A.* 109 (35):13978–13983.

Shimomura, O., Johnson, F.H., and Saiga, Y. (1962) Extraction, Purification and Properties of Aequorin, a Bioluminescent Protein from the Luminous Hydromedusan,Aequorea. *J. Cell. Comp. Physiol.* 59 (3):223–239.

Sieber, J.J., Willig, K.I., Kutzner, C., Gerding-Reimers, C., Harke, B., Donnert, G., Rammner, B., Eggeling, C., Hell, S.W., Grubmüller, H., and Lang, T. (2007) Anatomy and dynamics of a supramolecular membrane protein cluster. *Science* 317 (5841):1072–1076.

Simons, K. and Ikonen, E. (1997) Functional rafts in cell membranes. *Nature* 387 (6633):569–572.

Singer, S.J. and Nicolson, G.L. (1972) The fluid mosaic model of the structure of cell membranes. *Science* 175 (4023):720–731.

Sletten, E.M. and Bertozzi, C.R. (2009) Bioorthogonal chemistry: Fishing for selectivity in a sea of functionality. *Angew. Chem. Int. Ed.* 48 (38):6974–6998.

Sletten, E.M. and Bertozzi, C.R. (2011) From mechanism to mouse: a tale of two bioorthogonal reactions. *Acc. Chem. Res.* 44 (9):666–676.

Small, J., Rottner, K., Hahne, P., and Anderson, K.I. (1999) Visualising the actin cytoskeleton. *Microsc. Res. Tech.* 47 (1):3–17.

Sönnichsen, B., Renzis, S. de, Nielsen, E., Rietdorf, J., and Zerial, M. (2000) Distinct Membrane Domains on Endosomes in the Recycling Pathway Visualized by Multicolor Imaging of Rab4, Rab5, and Rab11. *J. Cell Biol.* 149 (4):901–914.

Staudinger, H. and Meyer, J. (1919) Über neue organische Phosphorverbindungen III. Phosphinmethylenderivate und Phosphinimine. *HCA* 2 (1):635–646.

Stephens, D.J. and Allan, V.J. (2003) Light microscopy techniques for live cell imaging. *Science* 300 (5616):82–86.

Suzuki, M., Curran, K.J., and Cheung, N.-K.V. (2015) Chimeric antigen receptors and bispecific antibodies to retarget T cells in pediatric oncology. *Pediatric Blood & Cancer* 62 (8):1326–1336.

Takatori, S., Mesman, R., and Fujimoto, T. (2014) Microscopic methods to observe the distribution of lipids in the cellular membrane. *Biochem.* 53 (4):639–653.

Tan, S., Tan, H.T., and Chung, M.C.M. (2008) Membrane proteins and membrane proteomics. *Proteomics* 8 (19):3924–3932.

Tanaka, K.A.K., Suzuki, K.G.N., Shirai, Y.M., Shibutani, S.T., Miyahara, M.S.H., Tsuboi, H., Yahara, M., Yoshimura, A., Mayor, S., Fujiwara, T.K., and Kusumi, A. (2010) Membrane molecules mobile even after chemical fixation. *Nat. Methods* 7 (11):865–866.

Teichmann, M. and Capps, M. (2002, c1998) Surface reconstruction with anisotropic density-scaled alpha shapes. In *Visualization '98: Proceedings, October 18-23, 1998, Research Triangle Park, North Carolina*, Visualization '98, Association for Computing Machinery Press; Institute of Electrical and Electronics Engineers], [New York, N.Y., Piscataway, N.J., pp 67–72.

Thompson, R.E., Larson, D.R., and Webb, W.W. (2002) Precise Nanometer Localization Analysis for Individual Fluorescent Probes. *Biophys. J.* 82 (5):2775–2783.

Tom Dieck, S., Müller, A., Nehring, A., Hinz, F.I., Bartnik, I., Schuman, E.M., and Dieterich, D.C. (2012) Metabolic labeling with noncanonical amino acids and visualization by chemoselective fluorescent tagging. *Curr. Protoc. Cell Biol.* Chapter 7:Unit7.11.

Tornøe, C.W., Christensen, C., and Meldal, M. (2002) Peptidotriazoles on Solid Phase: [1,2,3]-Triazoles by Regiospecific Copper(I)-Catalyzed 1,3-Dipolar Cycloadditions of Terminal Alkynes to Azides. *J. Org. Chem.* 67 (9):3057–3064.

Truneh, A. and Machy, P. (1987) Detection of very low receptor numbers on cells by flow cytometry using a sensitive staining method. *Cytometry* 8 (6):562–567.

Tsien, R.Y. (1998) The green fluorescent protein. *Annu. Rev. Biochem.* 67:509–544.

Ullrich, O. (1996) Rab11 regulates recycling through the pericentriolar recycling endosome. *J. Cell Biol.* 135 (4):913–924.

Uppoor, R. and Niebergall, P.J. (1996) beta-D(+) glucose-glucose oxidase-catalase for use as an antioxidant system. *Pharm. Dev. Technol.* 1 (2):127–134.

Uttamapinant, C., Sanchez, M.I., Liu, D.S., Yao, J.Z., and Ting, A.Y. (2013) Site-specific protein labeling using PRIME and chelation-assisted click chemistry. *Nat. Protoc.* 8 (8):1620–1634.

Uttamapinant, C., Tangpeerachaikul, A., Grecian, S., Clarke, S., Singh, U., Slade, P., Gee, K.R., and Ting, A.Y. (2012) Fast, cell-compatible click chemistry with copper-chelating azides for biomolecular labeling. *Angew. Chem. Int. Ed.* 51 (24):5852–5856.

Valley, C.C., Liu, S., Lidke, D.S., and Lidke, K.A. (2015) Sequential superresolution imaging of multiple targets using a single fluorophore. *PLoS ONE* 10 (4):e0123941.

van de Linde, S., Aufmkolk, S., Franke, C., Holm, T., Klein, T., Löschberger, A., Proppert, S., Wolter, S., and Sauer, M. (2013) Investigating cellular structures at the nanoscale with organic fluorophores. *Chemistry & Biology* 20 (1):8–18.

van de Linde, S., Löschberger, A., Klein, T., Heidbreder, M., Wolter, S., Heilemann, M., and Sauer, M. (2011) Direct stochastic optical reconstruction microscopy with standard fluorescent probes. *Nat. Protoc.* 6 (7):991–1009.

van de Linde, S. and Sauer, M. (2014) How to switch a fluorophore: from undesired blinking to controlled photoswitching. *Chem. Soc. Rev.* 43 (4):1076–1087.

van de Linde, S., Wolter, S., Heilemann, M., and Sauer, M. (2010) The effect of photoswitching kinetics and labeling densities on super-resolution fluorescence imaging. *J. Biotechnol.* 149 (4):260–266.

van Zanten, T.S. and Mayor, S. (2015) Current approaches to studying membrane organization. *F1000Research* 4.

Walter, T., Schlegel, J., Burgert, A., Kurz, A., Seibel, J., and Sauer, M. (2017) Incorporation studies of clickable ceramides in Jurkat cell plasma membranes. *Chem. Commun.* 53 (51):6836–6839.

Wang, M., Yin, B., Wang, H.Y., and Wang, R.-F. (2014) Current advances in T-cell-based cancer immunotherapy. *Immunotherapy* 6 (12):1265–1278.

Wang, Q., Chan, T.R., Hilgraf, R., Fokin, V.V., Sharpless, K.B., and Finn, M.G. (2003) Bioconjugation by copper(I)-catalyzed azide-alkyne 3 + 2 cycloaddition. *J. Am. Chem. Soc.* 125 (11):3192–3193.

Whelan, D.R. and Bell, Toby D M. (2015) Image artifacts in Single Molecule Localization Microscopy: why optimization of sample preparation protocols matters. *Sci. Rep.* 5:7924.

Winter, F.R., Loidolt, M., Westphal, V., Butkevich, A.N., Gregor, C., Sahl, S.J., and Hell, S.W. (2017) Multicolour nanoscopy of fixed and living cells with a single STED beam and hyperspectral detection. *Sci. Rep.* 7:46492.

Wolter, S., Endesfelder, U., van de Linde, S., Heilemann, M., and Sauer, M. (2011) Measuring localization performance of super-resolution algorithms on very active samples. *Opt. Express* 19 (8):7020–7033.

Wolter, S., Löschberger, A., Holm, T., Aufmkolk, S., Dabauvalle, M.-C., van de Linde, S., and Sauer, M. (2012) rapidSTORM: accurate, fast open-source software for localization microscopy. *Nat. Methods* 9 (11):1040–1041.

Wolter, S., Schüttpelz, M., Tscherepanow, M., van de Linde, S., Heilemann, M., and Sauer, M. (2010) Real-time computation of subdiffraction-resolution fluorescence images. *J. Microsc.* 237 (1):12–22.

Yu, J., Fischman, D.A., and Steck, T.L. (1973) Selective solubilization of proteins and phospholipids from red blood cell membranes by nonionic detergents. *J. Supramol. Struct.* 1 (3):233–248.

Zhou, W. and Yan, H. (2014) Alpha shape and Delaunay triangulation in studies of protein-related interactions. *Brief. Bioinform.* 15 (1):54–64.

Zhu, L., Zhang, W., Elnatan, D., and Huang, B. (2012) Faster STORM using compressed sensing. *Nat. Methods* 9 (7):721–723.

Zhukovsky, E.A., Morse, R.J., and Maus, M.V. (2016) Bispecific antibodies and CARs: Generalized immunotherapeutics harnessing T cell redirection. *Curr. Opin. Immunol.* 40:24–35.

Zola, H. (2004) High-sensitivity immunofluorescence/flow cytometry: Detection of cytokine receptors and other low-abundance membrane molecules. *Curr. Protoc. Cytom.* Chapter 6:Unit 6.3.

Acknowledgements

I am very grateful to everyone who supported me during the last few years and helped me making this work possible.

First of all, I want to thank Markus Sauer for giving me the chance to write my PhD thesis in his group and for the possibility to participate in many exciting research projects, collaborations and conferences. Thank you, Markus, for your great support, your constant interest in my work, and your boundless enthusiasm.

I would like to thank Jürgen Seibel for co-supervision of this work and especially for a fruitful collaboration which introduced me to the exciting field of membrane biology. I highly appreciated the enriching discussions and got fascinated by the range of applications a sugar molecule can be used for.

A special thanks goes to Sören Doose for a myriad of helpful and constructive discussions and for his great scientific input in many projects. Thank you, Sören, for your time, your support, and for introducing me to the world of single molecules many years ago.

I would like to mention thankfully Thomas Nerreter, Michael Hudecek and Hermann Einsele for a highly interesting and intensive collaboration. Thanks for many helpful discussions, for the inexhaustible source of new ideas and suggestions, and for introducing me to the very exciting and new field of personalized immunotherapy. Furthermore, I want to express my gratitude to all others collaboration partners for their excellent cooperation. Many thanks to Martin Eilers, Björn von Eyss, Carsten Ade and Cossa Giacomo (Department of Biochemistry and Molecular Biology, University of Würzburg), as well as Nadja Bertleff-Zieschang, Elisabeth Memmel and Alexander Mertsch (Seibel Group, Institute of Organic Chemistry, University of Würzburg).

For an excellent working atmosphere I would like to thank my colleagues and friends at the Department of Biotechnology and Biophysics. I would like to acknowledge Petra Geßner and Lisa Behringer-Pliess for numerous happy cells and their support in practical lab-related matters, as well as Marcus Behringer, Albert

Gessner, Matthias ”Willi” Bauer, and Oliver Reichert for lots of mechanical, electrical and computer-related work. For many fruitful discussions and for sharing their expertise I would like to thank Anne Burgert, Teresa Klein, Pablo Mateos-Gil, Christian Franke, as well as the whole cluster-of-differentiation-crew Patrick Eiring, Alexander Kuhlemann and Ralph Götz.
What would the world (or the department) be like without laughing, discussing, helping each other, celebrating, playing (table) football, barbecuing, skiing, and much, much more. All of this I could share with Fabi, Andi, Simon, Tracy, Jan, Nora, Julia, Rotbart, Gerti, Sepp and Ando - Thank you! In addition, I especially want to thank Franzi, Sina, Felix, Juli, Sarah and Lena for lots of action and indescribable moments on the bike, on climbing walls and rocks, in the Main River, and on the ski slope. It was a gift for me to meet you.

Special thanks to my friends Manu, Markus, Katharina, Robert, Anne, Patrick, Carsten, Anna, Daniel, Hanni and Basti. Thank you for always being there - for eons.

Last but not least I want to thank my family. My parents, my sister and my brother who always take care, try to understand my concerns and plans, and help me wherever it is possible.
Andrea – thank you for your unconditional trust, your never ending patience, your inspiration and motivation, and for simply everything.

Publications

Manuscript 1

Letschert, S., Göhler, A., Franke, C., Bertleff-Zieschang, N., Memmel, E., Doose, S., Seibel, J., Sauer, M. (2014): Super-Resolution Imaging of Plasma Membrane Glycans. *Angewandte Chemie International Edition* 53 (41), 10921–10924

Bioorthogonal Chemistry Hot Paper

DOI: 10.1002/ange.201406045

Super-Resolution Imaging of Plasma Membrane Glycans**

Sebastian Letschert, Antonia Göhler, Christian Franke, Nadja Bertleff-Zieschang, Elisabeth Memmel, Sören Doose, Jürgen Seibel,* and Markus Sauer**

Abstract: *Much of the physiology of cells is controlled by the spatial organization of the plasma membrane and the glycosylation patterns of its components, however, studying the distribution, size, and composition of these components remains challenging. A bioorthogonal chemical reporter strategy was used for the efficient and specific labeling of membrane-associated glycoconjugates with modified monosaccharide precursors and organic fluorophores. Super-resolution fluorescence imaging was used to visualize plasma membrane glycans with single-molecule sensitivity. Our results demonstrate a homogeneous distribution of N-acetylmannosamine (ManNAc)-, N-acetylgalactosamine (GalNAc)-, and O-linked N-acetylglucosamine (O-GlcNAc)-modified plasma membrane proteins in different cell lines with densities of several million glycans on each cell surface.*

The glycosylation state of proteins controls their function, localization, and stability.[1,2] Cell-surface glycans are involved in many cell–cell recognition processes, as well as tumor development, and they reflect the developmental stage and the transformation state of a cell.[3–5] Visualization of the glycoprotein patterns in plasma membranes with regard to diseases could thus pave the way for the development of refined diagnostic tools.

However, until now two obstacles have impeded the exploitation of quantitative data concerning the architecture of membrane-associated glycoproteins: the difficulty of selective and efficient labeling of glycosylated membrane proteins, and the resolution limit of optical microscopy. This is of special importance considering the existence of confined plasma membrane compartments, that is, nanodomains or clusters with a supposed size of 5–300 nm that are required for subcompartmentalization and associated functions.[6–10] Recently, the difficulty in labeling glycans by traditional molecular and cell biology techniques has been overcome by the introduction of a bioorthogonal chemical reporter strategy termed "click chemistry".[11]

Herein, the tolerance of mammalian cells to small modifications of monosaccharide precursors is exploited. Upon cellular uptake, azido- or alkyne-modified monosaccharides are covalently incorporated by the biosynthetic machinery into the substrates of glycosyltransferases to create non-native glycans. Once incorporated into components of the cell surface, these azido- or alkyne-modified glycans can be covalently labeled with alkyne- or azido-modified fluorophores, respectively, to form triazole-linked products for the in vitro and in vivo imaging of various glycoproteins.[12–14]

In our study, we combined click chemistry for labeling and super-resolution fluorescence microscopy for visualization of membrane-associated glycoproteins with subdiffraction resolution. For the metabolic labeling of sialic acid containing and mucin-type O-linked glycans, we used analogues of their biosynthetic precursors *N*-acetylmannosamine (ManNAc), and *N*-acetylgalactosamine (GalNAc), respectively; O-GlcNAc-modified plasma membrane proteins were labeled by using a GlcNAc analogue in human osteosarcoma (U2OS) and neuroblastoma (SK-M-NC) cell lines. For subdiffraction resolution fluorescence imaging with single-molecule sensitivity, we used *direct* stochastic optical reconstruction microscopy (*d*STORM).[15–17]

Since the biosynthetic machinery tolerates the addition of chemical reporters to the N-acyl group, we fed cells with the peracetylated monosaccharides *N*-azidoacetylmannosamine (Ac_4ManNAz), *N*-azidoacetylgalactosamine (Ac_4GalNAz), and *N*-azidoacetylglucosamine (Ac_4GlcNAz), which are incorporated into cell-surface glycans upon cell permeation and deacetylation.[12–14] Ac_4ManNAz and Ac_4GalNAz have been used to visualize sialic acids and mucin-type O-linked glycans in different cell types as well as in living mice and zebrafish.[12–14] Ac_4GlcNAz is modified by the GlcNAc salvage pathway enzymes to give uridine diphosphate (UDP)-GlcNAz, which is used as a substrate by the intracellular cytosolic O-GlcNAc transferase (OGT). The resulting modification with O-GlcNAc modulates signaling and regulates protein expression, degradation, and trafficking.[12–14] O-GlcNAc addition is catalyzed by a recently discovered epidermal growth factor (EGF) domain specific O-linked GlcNAc transferase (EOGT).

In a first set of experiments, we optimized the labeling of neuroblastoma cells with different azidoacetyl monosaccharides and alkyne-bearing Alexa Fluor 647 by applying Cu^I-catalyzed azide–alkyne cycloaddition in the absence and

[*] S. Letschert, Dr. A. Göhler, C. Franke, Priv.-Doz. Dr. S. Doose, Prof. Dr. M. Sauer
Department of Biotechnology & Biophysics
Julius Maximilian University Wuerzburg
Am Hubland, 97074 Würzburg (Germany)
E-mail: soeren.doose@uni-wuerzburg.de
m.sauer@uni-wuerzburg.de
Homepage: http://www.super-resolution.de

N. Bertleff-Zieschang, E. Memmel, Prof. Dr. J. Seibel
Institute of Organic Chemistry
Julius Maximilian University Wuerzburg
Am Hubland, 97074 Würzburg (Germany)
E-mail: seibel@chemie.uni-wuerzburg.de

[**] We thank L. Pliess and P. Geßner for assistance in cell culture. This work was supported by the Biophotonics Initiative of the Bundesministerium für Bildung und Forschung (grants 13N11019 and 13N12507, M.S.), the Deutsche Forschungsgemeinschaft (DFG SA829/13-1 to M.S. and DFG Se 1410/6-1 to J.S.) and the Universität Bayern e.V. (E.M.), FCI (N.B.-Z.), ISF and IRG (S.D.).

Supporting information for this article is available on the WWW under http://dx.doi.org/10.1002/anie.201406045.

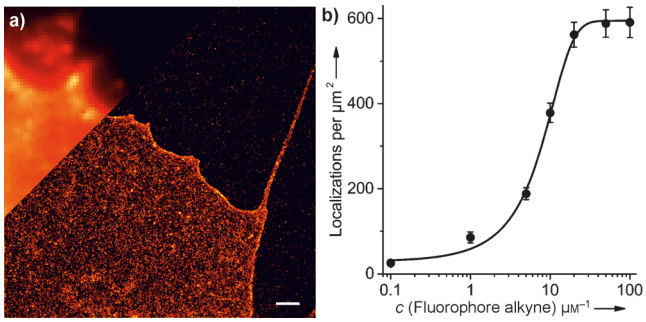

Figure 1. Membrane glycans of SK-N-MC neuroblastoma cells stained through the metabolic incorporation of azido-sugar analogues followed by copper-catalyzed azide–alkyne cycloaddition (CuAAC). a) A standard fluorescence image (upper left corner) and a high-resolution *d*STORM image (main image) of Ac_4GalNAz-treated neuroblastoma cells stained with alkyne-bearing Alexa Fluor 647. b) Localization densities of Ac_4GlcNAz-treated neuroblastoma cells for different alkyne–fluorophore concentrations. At an alkyne–fluorophore concentration of about 20 μM, the number of localizations per unit of membrane area as determined by *d*STORM becomes saturated. Scale bar: 1 μm.

presence of Cu^I and the Cu^I-stabilizing reagent Tris(3-hydroxypropyltriazolylmethyl)amine (THPTA). Cells were incubated with 25 μM aqueous solutions of modified monosaccharides in their culture medium for two days and then labeled and fixed in 4% formaldehyde with 0.2% glutaraldehyde at 25°C to minimize the lateral diffusion of membrane molecules (Figure 1, and Figures S1, S2 in the Supporting Information).[18] A fluorophore concentration of 20 μM and an incubation time of 5 min proved to be sufficient for efficient labeling in the presence of Cu^I and THPTA (Figure 1b). Higher fluorophore concentrations do not result in higher labeling efficiencies.

The resulting *d*STORM images of Ac_4ManNAz-, Ac_4GalNAz-, and Ac_4GlcNAz-derivatized plasma membrane proteins demonstrate substantially improved resolution compared to wide-field fluorescence images and reveal the localization of single glycans homogeneously distributed over the entire basal plasma membrane of U2OS and SK-*N*-MC cells (Figure 1, Figure 2, and Figure S3 in the Supporting Information). The use of blocking agents (e.g., bovine serum albumin) to reduce unspecific binding of the fluorophores to the surface was not necessary. In control experiments, the number of non-specific localizations was found to be less than 1% (Figure S4 in the Supporting Information). To exclude the influence of the addition of copper ions and THPTA on the distribution of glycoconjugates on the basal plasma membrane, we performed copper-free experiments with Alexa Fluor 647 conjugated to dibenzocyclooctyne (DIBO) for strain-promoted azide–alkyne cycloaddition. Furthermore, we imaged the apical membrane of cells by *d*STORM to investigate the influence of the proximal coverslip. The resulting *d*STORM images appear identical and display homogeneously distributed glycans in the apical plasma membrane as well (Figure S5 in the Supporting Information). To extract reliable estimates for localization densities, 12–32 cells were imaged in all experiments and averaged data are presented (Figure 2a). Interestingly, we do not see any characteristic glycan nanodomains or clusters as have been identified in recent super-resolution imaging studies of membrane proteins.[9,10,19–21] The calculation of Ripley's K-function and nearest-neighbor distance distributions only reveals characteristic clusters on the 25 nm length scale that originate from the repeated localization of a single fluorophores (Figure S6 in the Supporting Information). Ripley's K-function might indicate some more clustering for GalNAz and ManNAz glycoconjugates when compared with simulated data for complete spatial randomness. However, no characteristic length scale could reproducibly be identified either visually or by statistical analysis (Figure S6 in the Supporting Information).

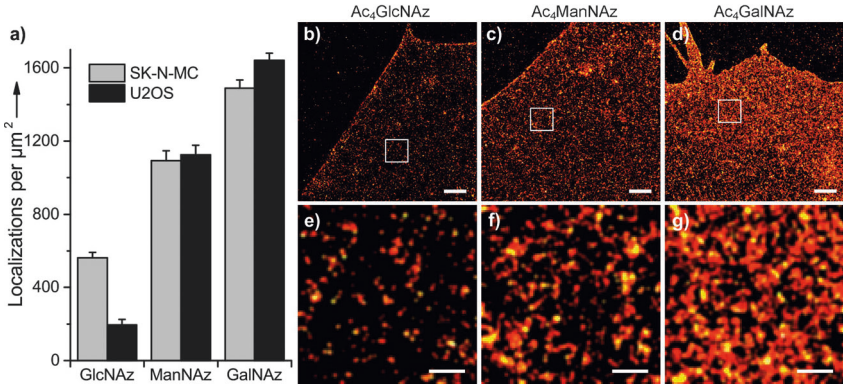

Figure 2. Super-resolution imaging and analysis of cell-surface glycoproteins. SK-N-MC neuroblastoma cells and U2OS cells were fed with one of the reactive azido sugars (Ac_4GlcNAz, Ac_4ManNAz, or Ac_4GalNAz) and then visualized and analyzed by click chemistry and *d*STORM. a) Localization density of membrane-associated glycans labeled with Alexa Fluor 647 (20 μM). Error bars represent the standard error of the mean of 12–32 imaged cells. b–d) *d*STORM images of glycoconjugates in the basal membrane of SK-*N*-MC neuroblastoma cells. Enlarged images of the sections in white boxes are shown in the lower panels (e–g). Scale bars: 1 μm (b–d) and 200 nm (e–g).

Our *d*STORM images further demonstrate that the plasma membranes of neuroblastoma and osteosarcoma cells exhibit the highest density of labeled glycans for GalNAz glycoconjugates, with 1500–1700 localizations per μm^2, followed by ManNAz-derived glycoconjugates, with approximately 1100 localizations per μm^2 (Figure 2a). GlcNAz glycoconjugates show the lowest density with a peculiar dependence on the investigated cell type (Figure 2a). For neuroblastoma cells, we find on average approximately 600 localizations per μm^2, whereas in osteosarcoma cells (U2OS), the density is substantially lower (Figure 2a). While Ac_4GalNAz and Ac_4ManNAz modify various glycoproteins and glycolipids, Ac_4GlcNAz modifies the extracellular epidermal growth factor (EGF)-like domain of just

a handful of membrane proteins,[22,23] thus explaining the lower localization density.

To estimate the number of localizations per fluorophore, spots with repeated localizations of isolated fluorophore-labeled glycans were grouped by using the tracking function of rapi*d*STORM.[24,25] To ensure that only single fluorophores were analyzed, we decreased the fluorophore concentration to 10 nM to give a very low labeling density (<20 localizations μm^{-2}). Fluorescent spots that were switched on for longer than 10 frames were discarded from further analysis. The remaining spatially isolated fluorescent spots were tracked over the whole image stack (15000 frames) within a defined area (tracking radius) to determine the number of localizations per spot. In order to determine the optimal tracking radius, we varied the tracking radius between 0 and 200 nm. By using the mean values of the resulting distributions under saturation conditions, we extracted 2.7 ± 0.4 localizations per isolated fluorescent spot (Figure 3a and Figure S7 in the Supporting Information). By aligning the coordinates of the localizations for each isolated fluorescent spot to its center of mass, we generated a 2D histogram of all localizations, which resembles a Gauss distribution. The standard deviation of the Gauss function fitted to the projection in the *xy* plane reveals an average localization precision of 10.7 ± 0.1 nm (Figure 3b).

By using the value of 2.7 ± 0.4 localizations per isolated fluorescent spot, we can now estimate the density of GalNAz and ManNAz glycans on the basal plasma membrane to be approximately 600 μm^{-2} and 400 μm^{-2}, respectively. Accordingly, we estimate there to be approximately 220 μm^{-2} and 70 μm^{-2} GlcNAz glycans on the basal plasma membrane of neuroblastoma and osteosarcoma cells, respectively. With a basal plasma membrane area of approximately 2000 μm^2, these values correspond to around 5×10^6 fluorophore-labeled plasma membrane glycans per neuroblastoma cell (considering all three glycan modifications and including the apical and basal sides of the cell). Considering other studies, in which it has been estimated that derivatives of azidoacetyl monosaccharides replace only 4–56% of their natural analogues depending on the cell line used,[26,27] the plasma membrane of a single cell may easily contain over 10 million glycans.[28]

To conclude, our data demonstrate that the cell surface of mammalian cells is homogeneously covered with several million glycans. None of the glycoconjugates form plasma membrane clusters or nanodomains on the length scale of ten to several hundred nanometers. Since the spatial and temporal organization and functions of all of these mammalian glycans is diverse, super-resolution imaging methods in combination with click chemistry hold promise for a refined understanding of the essential cellular functions associated with cell-surface glycans.

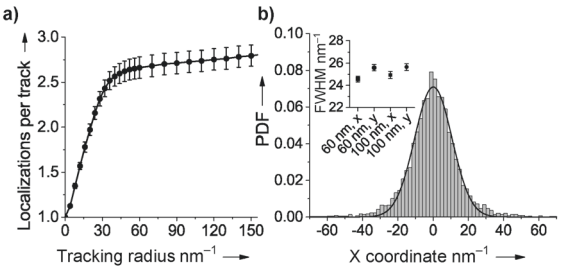

Figure 3. Quantitative analysis of *d*STORM data. a) Spots from isolated fluorophore-labeled glycans were tracked with different tracking radii over all frames. To be sure that only single fluorophores were analyzed, Ac_4GlcNAz treated SK-N-MC cells were incubated with only 10 nM alkyne-bearing Alexa Fluor 647. The curve saturates at a level of 2.68 ± 0.12 ($\pm$SEM, $n=12$ cells), which is the mean number of localizations per track. b) Probability density function (PDF) of all localizations belonging to a fluorescent spot, that is, an isolated fluorophore-labeled glycan, with a full width at half maximum (FWHM) of 25.2 ± 0.3 nm (mean $\pm$ standard error from the four estimates, inset), which corresponds to a localization precision (σ) of 10.7 ± 0.1 nm.

Received: June 10, 2014
Published online: August 22, 2014

Keywords: bioorthogonal chemistry · click chemistry · membrane glycans · microscopy · super-resolution imaging

[1] H. H. Freeze, *Nat. Rev.* **2006**, *7*, 537–549.
[2] G. W. Hart, M. P. Housley, C. Slawson, *Nature* **2007**, *446*, 1017–1022.
[3] K. Ohtsubo, J. D. Marth, *Cell* **2006**, *126*, 855–867.
[4] R. S. Haltiwanger, J. B. Lowe, *Annu. Rev. Biochem.* **2004**, *73*, 491–537.
[5] M. M. Fuster, J. D. Esko, *Nat. Rev. Cancer* **2005**, *5*, 526–542.
[6] K. Simons, M. J. Gerl, *Nat. Rev. Mol. Cell Biol.* **2010**, *11*, 688–699.
[7] A. Kusumi, T. K. Fujiwara, R. Chadda, M. Xie, T. A. Tsunoyama, Z. Kalay, R. S. Kasai, K. G. N. Suzuki, *Annu. Rev. Cell Dev. Biol.* **2012**, *28*, 215–250.
[8] B. F. Lillemeier, J. R. Pfeiffer, Z. Surviladze, B. S. Wilson, M. M. Davis, *Proc. Natl. Acad. Sci. USA* **2006**, *103*, 18992–18997.
[9] C. Eggeling, C. Ringemann, R. Medda, G. Schwarzmann, K. Sandhoff, S. Polyakova, V. N. Belov, B. Hein, C. von Middendorf, A. Schönle, S. W. Hell, *Nature* **2009**, *457*, 1159–1162.
[10] G. van den Bogaart, K. Meyenberg, H. J. Risselada, H. Amin, K. I. Willig, B. E. Hubrich, M. Dier, S. W. Hell, H. Grubmüller, U. Diederichsen, R. Jahn, *Nature* **2011**, *479*, 552–555.
[11] M. Boyce, C. R. Bertozzi, *Nat. Methods* **2011**, *8*, 638–642.
[12] S. T. Laughlin, C. R. Bertozzi, *Proc. Natl. Acad. Sci. USA* **2009**, *106*, 12–17.
[13] J. A. Prescher, D. H. Dube, C. R. Bertozzi, *Nature* **2004**, *430*, 873–877.
[14] S. T. Laughlin, J. M. Baskin, S. L. Amacher, C. R. Bertozzi, *Science* **2008**, *320*, 664–667.
[15] M. Heilemann, S. van de Linde, M. Schüttpelz, R. Kasper, B. Seefeldt, A. Mukherjee, P. Tinnefeld, M. Sauer, *Angew. Chem.* **2008**, *120*, 6266–6271; *Angew. Chem. Int. Ed.* **2008**, *47*, 6172–6176.
[16] S. van de Linde, A. Löschberger, T. Klein, M. Heidbreder, S. Wolter, M. Heilemann, M. Sauer, *Nat. Protoc.* **2011**, *6*, 991–1009.
[17] P. Zessin, K. Finan, M. Heilemann, *J. Struct. Biol.* **2012**, *177*, 344–348.
[18] K. A. K. Tanaka, K. G. N. Suzuki, Y. M. Shirai, S. T. Shibutani, M. S. M. Miyahara, H. Tsuboi, M. Yahara, A. Yoshimura, S. Mayor, T. K. Fujiwara, A. Kusumi, *Nat. Methods* **2010**, *11*, 865–866.

[19] J. J. Sieber, K. I. Willig, C. Kutzner, C. Gerding-Reimers, B. Harke, G. Donnert, B. Rammner, C. Eggeling, S. W. Hell, H. Grubmüller, Th. Lang, *Science* **2007**, *317*, 1072 – 1076.
[20] H. Mizuno, M. Abe, P. Dedecker, A. Makino, S. Rocha, Y. Ohno-Iwashita, J. Hofkens, T. Kobayashi, T. Miyawaki, *Chem. Sci.* **2011**, *2*, 1548 – 1553.
[21] D. J. Williamson, D. M. Owen, J. Rossy, A. Magenau, M. Wehrmann, J. J. Gooding, K. Gaus, *Nat. Immunol.* **2011**, *12*, 655 – 662.
[22] Y. Sakaidani, T. Nomura, A. Matsuura, M. Ito, E. Suzuki, K. Murakami, D. Nadano, T. Matsuda, K. Furukawa, T. Okajima, *Nat. Commun.* **2011**, *2*, 583.
[23] J. F. Alfaro, C.-X. Gong, M. E. Monroe, J. T. Aldrich, T. R. W. Clauss, S. O. Purvine, Z. Wang, D. G. Camp, J. Shabanowitz, P. Stanley, G. W. Hart, D. F. Hunt, F. Yang, R. D. Smith, *Proc. Natl. Acad. Sci. USA* **2012**, *109*, 7280 – 7285.
[24] S. Wolter, M. Schüttpelz, M. Tscherepanow, S. van de Linde, M. Heilemann, M. Sauer, *J. Microsc.* **2010**, *237*, 12 – 22.
[25] S. Wolter, A. Löschberger, T. Holm, S. Aufmkolk, M.-C. Dabauvalle, S. van de Linde, M. Sauer, *Nat. Methods* **2012**, *9*, 1040 – 1041.
[26] S. J. Luchansky, S. Argade, B. K. Hayes, C. R. Bertozzi, *Biochemistry* **2004**, *43*, 12358 – 12366.
[27] P. V. Chang, X. Chen, C. Smyrniotis, A. Xenakis, T. Hu, C. R. Bertozzi, P. Wu, *Angew. Chem.* **2009**, *121*, 4090 – 4093; *Angew. Chem. Int. Ed.* **2009**, *48*, 4030 – 4033.
[28] R. D. Cummings, J. M. Pierce, *Chem. Biol.* **2014**, *21*, 1 – 15.

Manuscript 2

Burgert, A.*, Letschert, S.*, Doose, S., Sauer, M. (2015): Artifacts in single-molecule localization microscopy. *Histochemistry and cell biology* 144 (2), 123–131

**authors equally contributed*

Histochem Cell Biol (2015) 144:123–131
DOI 10.1007/s00418-015-1340-4

ORIGINAL PAPER

Artifacts in single-molecule localization microscopy

Anne Burgert[1] · Sebastian Letschert[1] · Sören Doose[1] · Markus Sauer[1]

Accepted: 13 June 2015 / Published online: 3 July 2015

Abstract Single-molecule localization microscopy provides subdiffraction resolution images with virtually molecular resolution. Through the availability of commercial instruments and open-source reconstruction software, achieving super resolution is now public domain. However, despite its conceptual simplicity, localization microscopy remains prone to user errors. Using *direct* stochastic optical reconstruction microscopy, we investigate the impact of irradiation intensity, label density and photoswitching behavior on the distribution of membrane proteins in reconstructed super-resolution images. We demonstrate that high emitter densities in combination with inappropriate photoswitching rates give rise to the appearance of artificial membrane clusters. Especially, two-dimensional imaging of intrinsically three-dimensional membrane structures like microvilli, filopodia, overlapping membranes and vesicles with high local emitter densities is prone to generate artifacts. To judge the quality and reliability of super-resolution images, the single-molecule movies recorded to reconstruct the images have to be carefully investigated especially when investigating membrane organization and cluster analysis.

Keywords Super-resolution microscopy · Localization microscopy · *d*STORM · Artifacts · Photoswitching

Introduction

Super-resolution microscopy allows cellular processes and structures to be observed with molecular specificity and high spatial resolution. Among all powerful techniques introduced in recent years, super-resolution fluorescence imaging by single-molecule photoactivation or photoswitching and position determination (localization microscopy) demonstrated so far the highest spatial resolutions in fixed and living cells albeit at limited temporal resolution (Patterson et al. 2010; Maglione and Sigrist 2013; Klein et al. 2014). Due to the relative simplicity of the microscope setup (Holm et al. 2014), the availability of experimental protocols (van de Linde et al. 2011; Dempsey et al. 2011) and open-source reconstruction software (Henriques et al. 2010; Wolter et al. 2012, Sage et al. 2015), localization microscopy has been quickly picked up by the community. Since super-resolved images are built up from single-molecule coordinates, localization microscopy methods such as photoactivated localization microscopy (PALM) (Betzig et al. 2006) and *direct* stochastic optical reconstruction microscopy (*d*STORM) (Heilemann et al. 2008) are ideally suited to generate nanomaps of the molecular organization of multiprotein complexes such as the nuclear pore complex (Löschberger et al. 2012; Szymborska et al. 2013) and the synaptonemal complex (Schücker et al. 2015). Suited controls presupposed PALM and *d*STORM

Histochemistry and Cell Biology Lecture presented at the 57th Symposium of the Society for Histochemistry in Vienna, Austria, 20 August 2015.

Anne Burgert and Sebastian Letschert have contributed equally to this work.

Electronic supplementary material The online version of this article (doi:10.1007/s00418-015-1340-4) contains supplementary material, which is available to authorized users.

✉ Sören Doose
soeren.doose@uni-wuerzburg.de

✉ Markus Sauer
m.sauer@uni-wuerzburg.de

[1] Department of Biotechnology and Biophysics, University Würzburg, Am Hubland, 97074 Würzburg, Germany

can even give quantitative information about the distribution of proteins and the ratio of molecules residing inside and outside of subcellular compartments such as plasma membrane domains (Williamson et al. 2011; Lando et al. 2012; Bar-On et al. 2012; Puchner et al. 2013; Ehmann et al. 2014; Letschert et al. 2014; Löschberger et al. 2014; Saka et al. 2014; Honigmann et al. 2014; Fricke et al. 2014; Gao et al. 2015; Chen et al. 2015).

However, localization microscopy has also its unique peculiarities evoked by the assumption that the super-resolved image is reconstructed from localizations of individual, stochastically activated, spatially isolated and independently emitting fluorophores. If for any reason more than one fluorophore out of all fluorophores present within a two-dimensional diffraction-limited area reside in their fluorescent on-state, then overlapping point-spread-functions (PSFs) are generated resulting in false multiple-fluorophore localizations (van de Linde et al. 2010; Sauer 2013; van de Linde and Sauer 2014). Since the photoswitching and photobleaching efficiencies in *d*STORM and PALM, respectively, control the lifetime of the fluorophore's on-state, areas with higher fluorophore density require higher irradiation intensities to ensure efficient transfer of fluorophores to the nonfluorescent or bleached off-state. If the irradiation intensity is too low, the lifetime of the on-state increases resulting in overlapping PSFs, which can give rise to the appearance of artifacts in the super-resolved images (van de Linde and Sauer 2014).

To ensure artifact-free image reconstruction, i.e., reliable spot finding and fitting, the density of fluorescent spots has to be kept strictly below one emitter per μm^2 (Wolter et al. 2011), except if specialized algorithms for fitting multiple-emitter PSFs, like compressed sensing or DAO-Storm (Zhu et al. 2012; Holden et al. 2011), are used. Not only low irradiation intensities but also false buffer compositions (*d*STORM), high photoactivation intensities (PALM), very high local fluorophore concentrations, local inhomogeneities in photoswitching rates, slightly defocused signals and background fluorescence from other image planes can seriously deteriorate image quality.

Here we demonstrate that critical observation of the original single-molecule movies with respect to emitter density, background fluorescence, emitters with altered photoswitching behavior, e.g., very long on-state lifetimes, and contributions from three-dimensional (3D) structures is essential for correct and reliable *d*STORM. Performing experiments with cellular reference structures and various plasma membrane molecules, we show that the nonobservance of this problem, e.g., due to the use of insufficient laser power, generates serious image artifacts which can, in the last resort, result in the reconstruction of nonexistent membrane clusters and other artificial structures.

Methods

Cell culture

Human osteosarcoma (U2OS) cells were cultured in DMEM Ham's F12 containing 10 % FCS, 100 U/ml penicillin and 0.1 mg/ml streptomycin at 37 °C and 5 % CO_2. Cells were grown in standard T25-culture flasks (Greiner Bio-One) up to a confluence of about 80–90 %. For passaging, cells were washed once with PBS and incubated for 5 min with accutase. Cells were seeded at a concentration of 1×10^4 cells/well into eight well LabTek II chamber slides (Nunc, Thermo Fischer Scientific) and stained after 2 days of incubation. For studying glycans with click chemistry, cells were grown in medium supplemented with 25 µM tetraacetylated *N*-azidoacetylgalactosamine (Ac_4GalNAz, Life Technologies) for 2 days.

Fluorescence labeling

For fluorescent staining of sialic acid and *N*-acetylglucosamine residues, cells were fixed with 4 % pre-warmed (37° C) formaldehyde for 40 min at room temperature (RT). After washing cells three times with PBS, cells were incubated with 5 µg/ml Alexa Fluor 647-conjugated wheat germ agglutinin (WGA; Invitrogen) in PBS for 10 min at RT. Then, cells were washed three times with PBS before the measurement.

Membrane-associated glycans were stained using metabolic labeling and copper-free click chemistry. After cells were grown for 2 days in the presence of Ac_4GalNAz, metabolized sugar-azides were labeled with 25 µM azadibenzocyclooctyne-Cy5 (DBCO-Cy5, Sigma-Aldrich) for 10 min at RT via the so-called strain-promoted azide–alkyne cycloaddition (Boyce and Bertozzi 2011). Subsequently, cells were washed three times with PBS and fixed with 4 % formaldehyde and 0.2 % glutaraldehyde for 1 h.

For microtubule staining, cells were fixed with a pre-warmed (37° C) solution of 3 % formaldehyde and 0.1 % glutaraldehyde for 10 min at 37 °C. After fixation, free aldehyde groups were reduced with 0.1 % sodium borohydride in PBS for 7 min. Cells were washed three times with PBS before blocking and permeabilization with 3 % BSA and 0.5 % Triton-X100 in PBS for 10 min. Subsequently, samples were incubated with 1:100 diluted mouse anti-β-tubulin antibody (2.4 mg/ml; Sigma) in blocking buffer for 1.5 h. After six washing steps with PBS, cells were stained with 1:200 diluted Alexa Fluor 647-conjugated goat anti-mouse $F(ab')_2$ antibody (2 mg/ml; Life Technologies) in blocking buffer for 1 h followed by six washing steps. Post-fixation was realized with 3 % formaldehyde and 0.1 % glutaraldehyde in PBS for 15 min at RT.

Mitochondria were stained by incubating fixed (4 % formaldehyde) and permeabilized (−20 °C methanol) cells with a cocktail of primary antibodies for 90 min in blocking buffer. The cocktail consisted of monoclonal antibodies directed against all subunits (*I*–*V*) of the respiratory chain in the inner mitochondrial membrane (1:100, OxPhos Mouse anti-Human Kit, Life Technologies). Afterward, cells were treated with Alexa Fluor 647 $F(ab')_2$ fragments of goat anti-mouse IgG (1:200, Life Technologies) for 60 min, followed by postfixation in 4 % formaldehyde. Between each incubation steps, cells were washed three times with PBS.

*d*STORM imaging

Super-resolution imaging was conducted as described previously (van de Linde et al. 2011). Briefly, *d*STORM images were acquired using an inverted wide-field fluorescence microscope (IX-71; Olympus). For excitation of Alexa Fluor 647 and Cy5, a 641-nm diode laser (Cube 640-100C, Coherent) which was spectrally cleaned by a clean-up filter (Laser Clean-up filter 640/10, Chroma) was used. The laser beam was focused onto the back focal plane of the oil-immersion objective (60×, NA 1.45; Olympus). Emission light was separated from the illumination light using a dichroic mirror (HC 560/659; Semrock), spectrally filtered by a bandpass filter (HC697/75 and LP647; Semrock) and projected onto an electron-multiplying CCD camera chip (iXon DU-897; Andor). Placing additional lenses in the detection path, a final pixel size of 134 nm was generated. For each *d*STORM measurement, 15,000 images with an exposure time of 20 ms and irradiation intensities of ~0.1–0.5 or ~7 kW/cm^2 were recorded. Basal membranes were imaged by internal reflection fluorescence (TIRF) illumination, apical membranes by EPI illumination and mitochondria and microtubules by highly inclined and laminated optical sheet (HILO)-illumination. Experiments were performed in PBS-based photoswitching buffer containing 100 mM β-mercaptoethylamine (MEA, Sigma-Aldrich) and an oxygen scavenger system (2 % (w/v) glucose, 4 U/ml glucose oxidase and 80 U/ml catalase) adjusted to pH 7.4.

For cluster analysis, localization lists generated with rapi*d*STORM (Wolter et al. 2012) were loaded into the python-based software package LocAlization Microscopy Analysis (Lama) (free download: http://www.uni-frankfurt.de/54258347/Software) (Malkusch et al. 2013). Localization-based cluster analysis performed with this open-source software is based on Ripley's *K* function (Ripley 1977):

$$K(r) = \frac{1}{n}\sum_i \sum_j \frac{N_r(d_{ij})}{\lambda} \quad (1)$$

where r is a distance, n is the total number of localizations within the observation area, d_{ij} is the distance between two localizations i and j, N_r is an indicator function that is equal to 1 if the distance $d_{ij} < r$ and zero otherwise, and λ a weighting factor correcting for the average density of the total observation area. Ripley's *K* function is linearized:

$$L(r) = \sqrt{\frac{K(r)}{\pi}} \quad (2)$$

and r is subtracted so that homogeneous Poisson-distributed localizations lead to $H(r) = 0$ for all r:

$$H(r) = L(r) - r \quad (3)$$

To identify clusters, several regions of interest with a size of 2 × 2 μm^2 were analyzed using the Ripley's *H* function. The maximum of the Ripley's *H* function lies in the range between cluster radius and diameter and thus provides an estimate for the average cluster size.

Results and discussion

The first step of super-resolution imaging by localization microscopy represents efficient labeling of the protein of interest with photoswitchable or photoactivatable fluorophores. When using *d*STORM with commercially available standard fluorescent probes, the majority of fluorophores has to be transferred to a metastable non-fluorescent off-state upon irradiation with light at the beginning of the experiment. Then, during the experiment, only a stochastic subset of single fluorophores is switched on for a given observation time and localized. This cycle of photoactivation of fluorescent probes and subsequent readout is repeated to record a stack of 1000s of images and to reconstruct a super-resolution image from typically several ten thousands to millions of localizations.

Whereas the imaging resolution may be defined as the minimal distance resolvable between two emitters, it is important to consider that the extractable structural information from localization microscopy data is not only determined by the imaging resolution of the instrument but, equally, by the labeling density. According to information theory, the required density of fluorescent probes has to be sufficiently high to satisfy the Nyquist–Shannon sampling theorem (Shannon 1949). In essence, the theorem states that the mean distance between neighboring localized fluorophores (the sampling interval) must be at least twice as fine as the desired resolution. In order to resolve structural features of 20 nm in one dimension, a fluorophore must be localized at least every 10 nm. Considering a two-dimensional structure, a labeling density of about 10^4 fluorophores μm^{-2} or about 600 fluorophores within a circular diffraction-limited region is required to resolve

20 × 20 nm^2 features (Sauer 2013). Accordingly, imaging in three dimensions at high resolution requires a labeling density between 10^5 and 10^6 μm^{-3} or more than 10^4 fluorophores within the diffraction-limited region. In order to allow the isolated localization of individual fluorophores, only one fluorophore out of all fluorophores present within the diffraction-limited area, accounting for a specific structure, is allowed to reside in its fluorescent state at any time during the experiment. This implies that the lifetime of the off-state has to be substantially longer than the lifetime of the on-state, or in other words the photoswitching ratio $r = k_{off}/k_{on}$ has to be high enough to minimize false multiple-fluorophore localizations (van de Linde et al. 2010; Sauer 2013; van de Linde and Sauer 2014).

Because the density of fluorophores and thus indirectly also the size of the fluorescent probes controls the achievable structural resolution, efficient and specific labeling with small probes and optimization of labeling procedures are crucial for artifact-free localization microscopy (van de Linde and Sauer 2014; Whelan and Bell 2015). On the other hand, the irradiation intensity determines the photoswitching ratio and thus the probability for false localizations and the generation of artifacts. To demonstrate this interrelation, we imaged different cellular molecules labeled with Alexa Fluor 647 by *d*STORM under different irradiation intensities at 641 nm (~0.1 to ~7 kW cm^{-2}) (Figs. 1, 2; Supplementary Videos 1–6).

Microtubules and mitochondrial proteins are often used as standard examples to demonstrate the improved resolution of super-resolution microscopy methods. For a high irradiation intensity of ~7 kW cm^{-2}, the photoswitching ratio *r* is high enough to ensure that the average emitter density is well below one emitter per μm^2 (Wolter et al. 2011) in these samples. Hence, false multiple-emitter localizations are negligible and microtubule filaments appear as continuously labeled filaments (Fig. 1a). Also, labeling and imaging of respiratory chain proteins in the inner mitochondrial membrane nicely visualizes the multiple folded membranes of mitochondria (Fig. 1j).

Super-resolution imaging of cell surface glycoconjugates (glycans) is difficult to achieve by traditional molecular and cell biology-based labeling techniques albeit they are involved in many important cell–cell recognition processes and tumor development (Ohtsubo and Marth 2006; Haltiwanger and Lowe 2004). Recently, *d*STORM imaging of the molecular distribution of plasma membrane glycans was accomplished using a bioorthogonal chemical reporter strategy ("click chemistry") (Letschert et al. 2014) and fluorophore-labeled wheat germ agglutinin, respectively (Chen et al. 2015). Here we used both approaches to visualize plasma membrane glycans. We applied an irradiation intensity of ~7 kW cm^{-2} at 641 nm corresponding to a laser power of ~80 mW entering the microscope objective and did not use additional 405 nm irradiation for photoactivation of Alexa Fluor 647 (Heilemann et al. 2008; van de Linde et al. 2010; van de Linde and Sauer 2014). Image reconstruction was performed using rapi*d*STORM (Wolter et al. 2012), applying an intensity threshold (photon counts) of 600 photons. Using these optimized irradiation conditions, the emitter densities are well below one emitter per μm^2 (see single frame insets in Fig. 1) and both labels show homogeneously distributed glycans on the basal (Figs. 1d, g, 2e) and apical cell membrane (Fig. 2b) This demonstrates that the carbohydrate surface of cells does not exhibit special patterns, i.e., subclasses of glycans are not organized in confined plasma membrane compartments such as nanodomains or clusters corroborating previous experiments (Letschert et al. 2014).

If, however, in contrast to these optimized imaging conditions, the same cells are imaged at an irradiation intensity of <1 kW cm^{-2} under otherwise identical conditions and reconstruction of super-resolved images is performed using the same parameter settings, microtubules and mitochondria no longer appear as homogeneous filaments and structures (Fig. 1b, c, k, l). Figure 3 shows the impact of the intensity threshold on cluster-like artifacts in reconstructed *d*STORM images of microtubules for the lowest irradiation intensity of ~0.1 kW cm^{-2}. With increasing intensity threshold applied to the raw single-molecule data, the number of localizations and consequently background as well as the structural information decreases, but the impact of artificial clusters is not reduced. Here it has to be considered that in all experiments presented *d*STORM data have been acquired first at the lowest irradiation intensity to rule out possible photodamage effects.

Investigating the single-molecule signals in the unprocessed data reveals that in areas of higher fluorophore density such as crossing microtubule filaments (Figs. 1b, c, 3), the irradiation intensity is too low to efficiently transfer the fluorophores to an off-state that is long enough to fulfill the emitter density requirement of <1 μm^{-2}. Hence, the emitter density is too high resulting in false multiple-fluorophore localizations which often appear as clustered localizations indicating blurred crossing points. In contrast, in areas of straight and well-isolated microtubule filaments (Fig. 1b, c), false multiple-fluorophore localizations are less likely and not as critical due to the fact that they are located along the filaments and thus undistinguishable from regular single fluorophore localizations.

However, the situation becomes even more critical if we take a look at the structural organization of proteins in cellular membranes. The homogeneous distribution of plasma membrane-conjugated glycoproteins and glycolipids (Figs. 1d, g, 2b, e) changes into an inhomogeneous

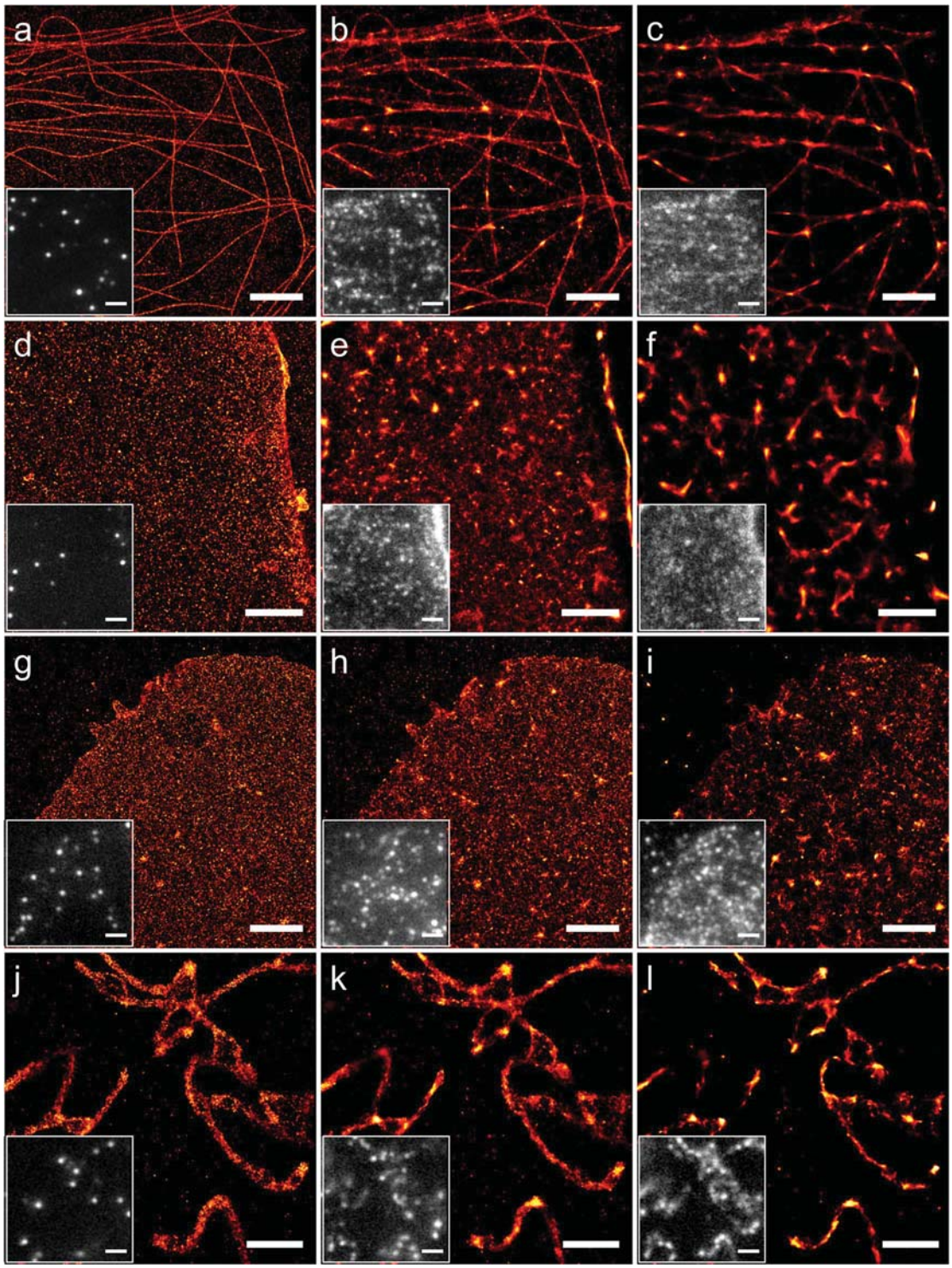

Fig. 1 Impact of irradiation intensity on artifact generation in reconstructed *d*STORM images. **a**, **d**, **g**, **j** *d*STORM images of fixed cellular structures acquired at an irradiation intensity of ~7 kW cm^{-2}. **b**, **c**, **e**, **f**, **h**, **i**, **k**, **l** *d*STORM images of the same cells and regions acquired at an irradiation intensity of ~0.3 kW cm^{-2} (**b**, **e**), ~1.0 kW cm^{-2} (**h**, **k**), ~0.5 kW cm^{-2} (**i**, **l**) and ~0.1 kW cm^{-2} (**c**, **f**). Due to inappropriate photoswitching rates and local inhomogeneities, the number of multiple-emitter events increases dramatically. Consequently, the resulting reconstructed images feature cluster-like artifacts and inhomogeneously labeled structures. *Insets* are single frames from the respective raw data movies. Images show microtubules (**a**–**c**) and mitochondria (**j**–**l**) of U2OS cells labeled by indirect immunocytochemistry with Alexa Fluor 647 and glycans on the basal plasma membrane of U2OS cells stained by Alexa Fluor 647-conjugated wheat germ agglutinin (WGA, **d**–**f**) and metabolic labeling combined with click chemistry with a sugar-azide (Ac_4GalNAz) and a fluorophore-alkyne (DBCO-Cy5) (Letschert et al. 2014) (**g**–**i**). *Scale bars* 2 µm

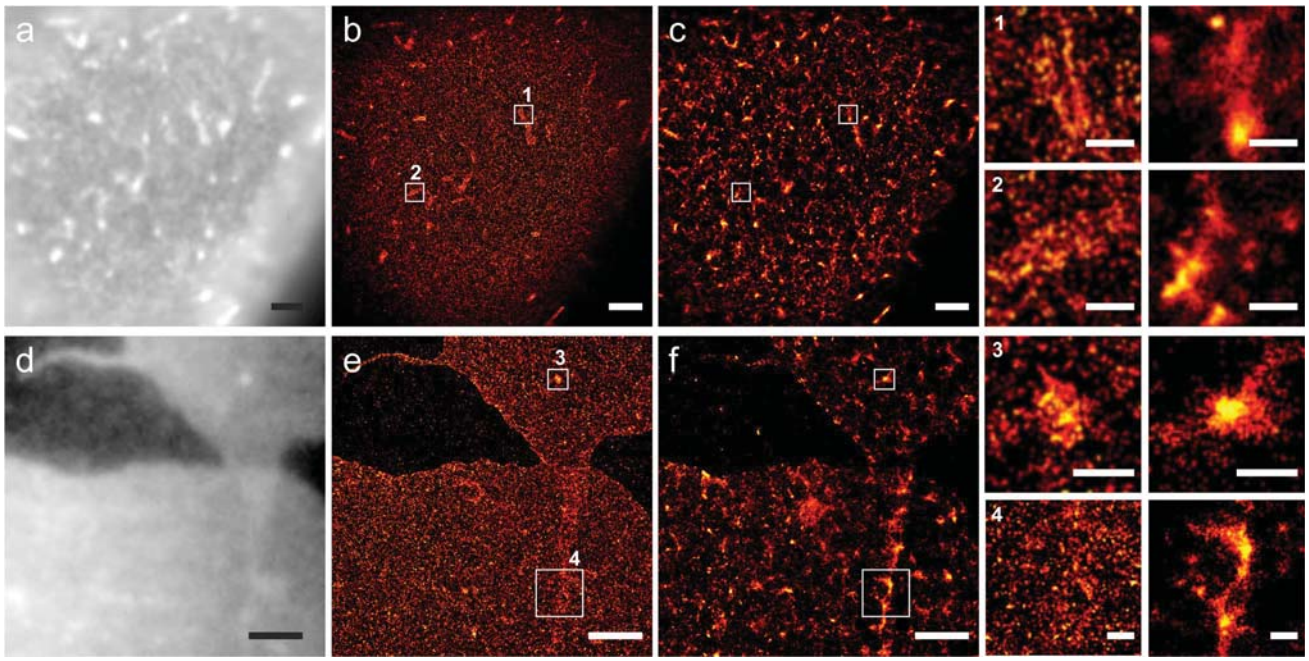

Fig. 2 *d*STORM imaging of densely labeled structures with low irradiation intensity results in reconstruction of artificial clusters. Wide-field fluorescence image of the apical membrane of a U2OS cell stained with WGA-Alexa Fluor 647 (**a**) and basal membrane stained by metabolic labeling and copper-free click chemistry (**d**). Densely labeled apical microvilli which are also visible in the wide-field fluorescence image are visualized clearly at an irradiation intensity of ~7 kW cm^{-2} (**b**). Large clusters appear at lower irradiation intensity ($\leq$0.5 kW cm^{-2}) (**c**). Two enlarged microvilli are shown exemplarily in the corresponding *d*STORM images (**1**, **2**). **e** *d*STORM image of the basal glycans reveals vesicle-like structures (**3**) and overlapping membranes (**4**) at high irradiation intensity (~7 kW cm^{-2}). **f** At lower intensity ($\leq$0.5 kW cm^{-2}), artificial clusters appear at regions of higher fluorophore density, e.g., along overlapping membranes. *Scale bars* 2 µm (**a**–**f**) and 300 nm (**1**–**4**)

distribution with clusters when the irradiation intensity is decreased below 1 kW cm^{-2} corresponding to an average laser power of ~10 mW (Figs. 1e, f, h, i, 2c, f). These cluster-like artifacts appear more often in membrane areas where the density of emitters is slightly higher than in neighboring areas increasing the apparent spatial inhomogeneity in the fluorophore distribution. Areas with lower emitter densities (such as areas with unspecifically bound labels between microtubule filaments) and areas around high-density spots (e.g., near crossing microtubule filaments) often feature almost no localizations (black regions in the reconstructed image) due to lower fluorescence intensities and the grouping of high-density spots (Fig. 1c, f, i, l). This effect is strongly enhanced by increasing the intensity threshold in the used software (Fig. 3) and is related to the fact that the reconstructed image in rapi*d*STORM is based on a pixel density representing localization number weighted by localization intensity.

Artificial clusters must not be interpreted as laterally organized nanodomains or protein clusters. Often two-dimensional projections of labeled structures above and below the image plane lead to inhomogeneities in the density of the projected localization pattern. To illustrate this, we imaged the apical membrane of U2OS cells labeled with Alexa Fluor 647-WGA at different irradiation intensities (Fig. 2a–c). The wide-field image in Fig. 2a shows bright WGA clusters on the apical cell surface. However, at the same positions, the *d*STORM image recorded under optimized conditions with sufficient excitation power (Fig. 2b) reveals that regions with dense localizations originate from 3D-distributed labels from microvilli or microvilli-like structures. In contrast, areas without microvilli exhibit a completely homogeneous distribution of WGA-labeled glycans.

If the irradiation intensity is now decreased below 0.5 kW cm^{-2}, large artifacts appear at the same positions as the microvilli that can be misinterpreted as organized protein clusters (Fig. 2c). Due to the low irradiation intensity and the local higher concentration of emitters, the chance for multiemitter events increases. The resulting bright, almost non-blinking fluorescent spots present local centers for the appearance of clusters in the reconstructed super-resolved image. Here it has to be considered that there are a range of other possible 3D projections in plasma membranes which can occur even if the cell surface is imaged with total internal reflection microscopy (TIRFM). For instance regions at the edge of the basal plasma membrane

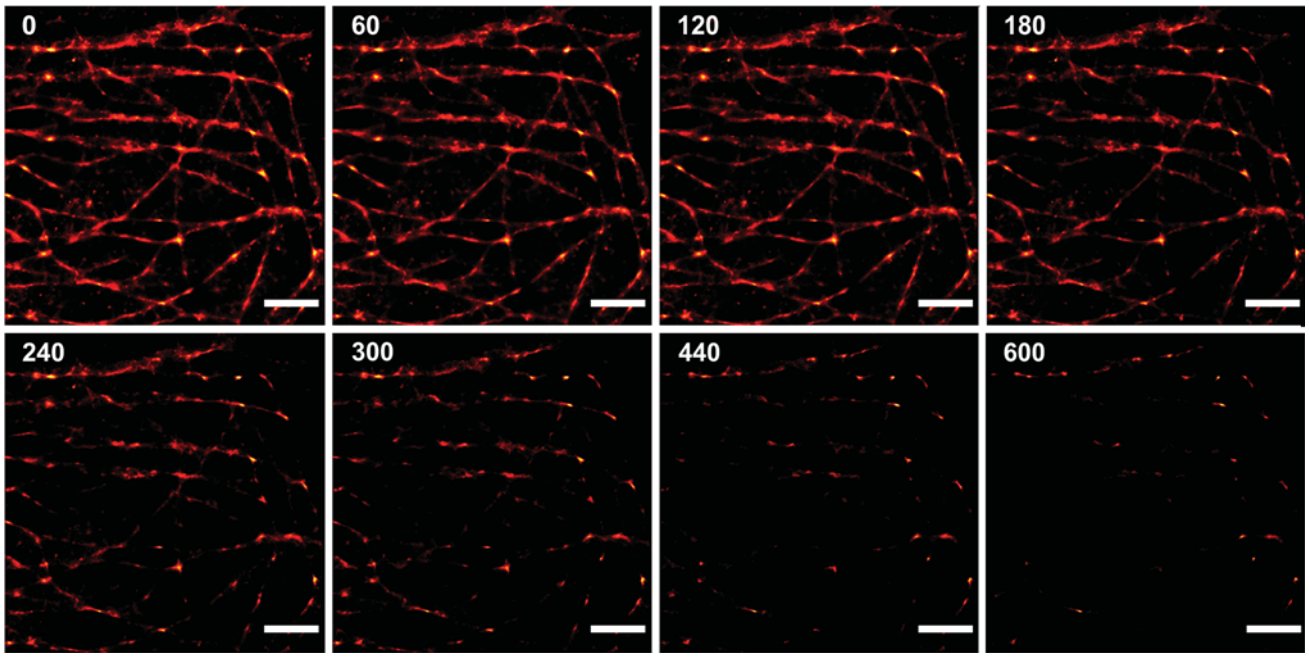

Fig. 3 Impact of intensity threshold on cluster-like artifacts in reconstructed *d*STORM images of microtubules. U2OS cells labeled by indirect immunocytochemistry with Alexa Fluor 647 were measured at an irradiation intensity of ~0.1 kW cm^{-2}. *d*STORM images were reconstructed with rapi*d*STORM using different intensity thresholds in the range of 0–600 photons. With increasing intensity threshold, areas without localizations increase. Localizations which are still visible at the highest threshold value stem from multiemitter events in areas of higher emitter densities such as crossing microtubules. *Scale bars* 2 µm

(Fig. 1d–f), overlapping membranes (Fig. 2d–f), membrane invaginations and vesicle-like structures including fluorophore-filled endosomes conjugated to or located near the plasma membrane (Fig. 2d–f).

To further analyze inhomogeneities and cluster-like artifacts, we calculated the localization-based Ripley's *H* function from the localizations of WGA-labeled glycans (sialic acid and *N*-acetylglucosamine residues) in the apical and basal plasma membrane of U2OS cells (Fig. 4). At an irradiation intensity of ~7 kW cm^{-2}, Ripley's *H* function reveals a maximum that indicates characteristic clusters on the 30-nm-length scale which originate from repeated localizations of single fluorophores. At intensities of ~0.3 and ~0.1 kW cm^{-2}, however, Ripley's *H* analysis of the same structures revealed a broader range of clustering with characteristic sizes of 95 and 175 nm in apical membranes and 180 and 195 nm in basal membranes, respectively (Fig. 4).

To conclude, our results highlight the importance of accurately set photoswitching rates of standard fluorescent probes in *d*STORM experiments. Thus, even if the sample is efficiently labeled and the optimal switching buffer is used, low irradiation intensities can cause super-resolution imaging artifacts. In standard *d*STORM instruments often with limited laser power available, the illumination intensity is always Gauss-distributed such that only the central area allows imaging with sufficiently high and uniform excitation power. Typically, the chip sizes of EMCCD cameras are larger than the illuminated areas such that most users will be able to crop artifact-prone boundary areas and select a suitable region of interest exhibiting uniform excitation power. These results are of minor importance for the interpretation of filamentous structures in super-resolution images such as microtubules because even non-experts will immediately recognize interrupted structures.

On the other hand, the correct interpretation of the distribution and organization of molecules in the plasma membrane, especially in regions with inhomogeneous and locally high emitter densities, can be seriously impeded by the use of low irradiation intensities. Images of membrane stains are particularly prone to these artifacts since various membrane structures introduce local inhomogeneities by membrane modulation or by membrane invagination and formation of vesicles carrying very high fluorophore concentrations in close proximity to the membrane (Fig. 5). Especially in cases where a priori knowledge about the cellular structure is lacking, e.g., the distribution of membrane-associated proteins and lipids, caution should be exercised when interpreting reconstructed super-resolution images. *d*STORM imaging should always include a test for possible artifacts by judging the quality of a reconstructed super-resolution image. This might include the careful investigation of

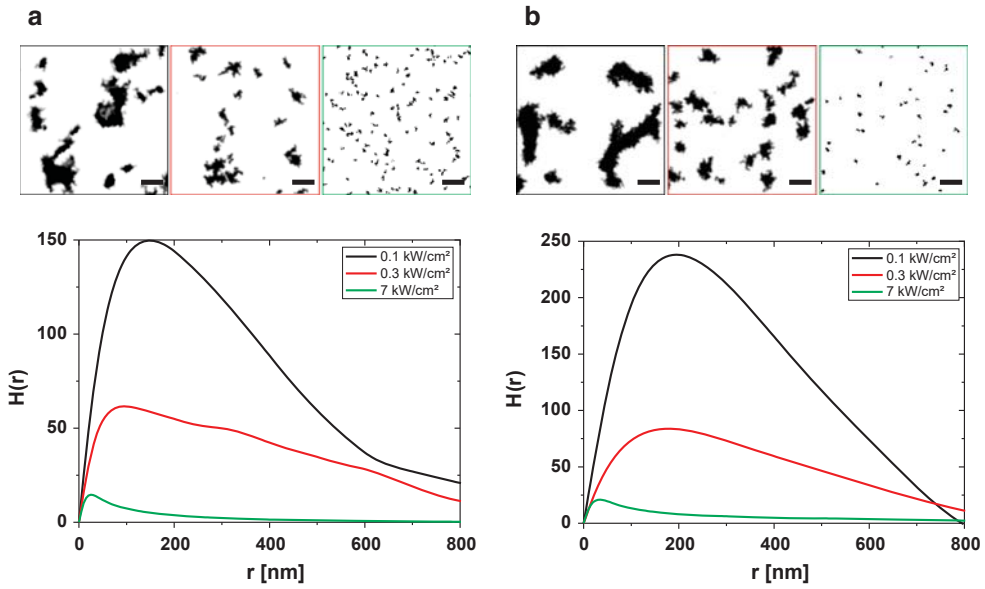

Fig. 4 Cluster analysis of sialic acid and *N*-acetylglucosamine residues stained with WGA-Alexa Fluor 647. Binary *d*STORM images of apical (**a**) and basal (**b**) U2OS cells stained with WGA and measured with an irradiation intensity of ~7 kW cm^{-2} (*green boxes*), ~0.3 kW cm^{-2} (*red boxes*), and ~0.1 kW cm^{-2} (*black boxes*). At laser intensities of ~7 kW cm^{-2} (*green curves*) cluster analysis with Ripley's *H* function reveals maxima at $r \sim 30$ nm, which represent repeated localizations of individual fluorophores. At lower intensities ~0.3 kW cm^{-2} (*red curves*) and ~0.1 kW cm^{-2} (*black curves*), Ripley's *H* curves of the same structures show broader peaks with maxima at $r \sim 95$ and ~175 nm in apical images and $r \sim 180$ and ~195 nm in basal images, respectively. The *broader peaks* indicate that the cluster size varies on larger length scales. *Scale bars* 300 nm

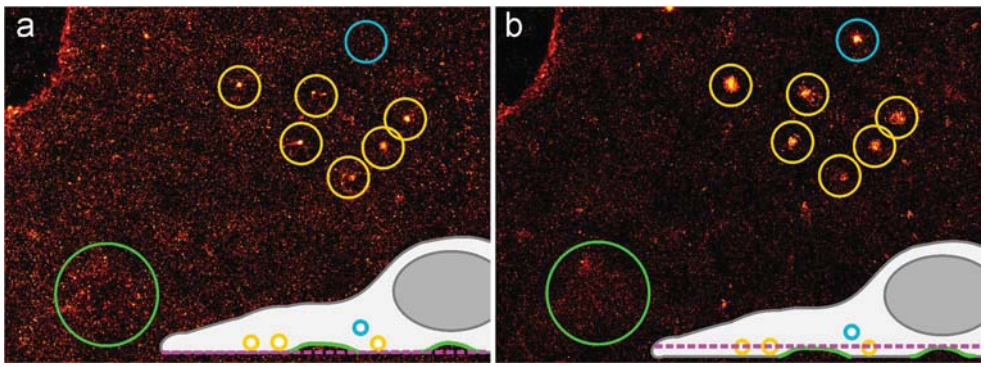

Fig. 5 Artificial clusters and 2D projections in the plasma membrane induced by vesicle-like structures and membrane modulations. *d*STORM images of glycoconjugates in the basal plasma membrane of U2OS cells stained by metabolic labeling and click chemistry with Alexa Fluor 647. Images were recorded at an irradiation intensity of ~7 kW cm^{-2} by TIRF (**a**) and EPI (**b**) illumination with focal planes slightly shifted (0.5–1 µm) into the cytosol (*dashed magenta line*). The artificial clusters in **a** (*yellow circles*) are generated due to non-blinking background signals resulting from endosome-like vesicles filled with fluorophores which are located *right above* the plasma membrane (*yellow circles*) or further up (*blue circles*) in the cytosol (**b**). Two-dimensional projections of plasma membrane modulations lead to artificial inhomogeneities in the emitter pattern (*green circles*)

the raw data movie which directly reveals information about the photoswitching behavior, emitter density, photobleaching behavior, drift and robustness of the microscope setup. In addition, 3D-*d*STORM (or alternatively imaging slightly shifted focal planes below and above the features of interest) might reveal contributions from truly 3D structures that are only imaged as two-dimensional projections.

Acknowledgments This work was supported by the Deutsche Forschungsgemeinschaft (DFG, Grant No. SA 829/13-9). We thank Sebastian Malkusch for providing us the cluster analysis software Lama.

References

Bar-On D, Wolter S, van de Linde S, Heilemann M, Nudelman G, Nachliel E, Gutman M, Sauer M, Ashery U (2012) Super-resolution imaging reveals the internal architecture of nano-sized syntaxin clusters. J Biol Chem 287:27158–27167

Betzig E, Patterson GH, Sougrat R, Lindwasser OW, Olenych S, Bonifacino JS, Davidson MW, Lippincott-Schwartz J, Hess HF (2006) Imaging intracellular fluorescent proteins at nanometer resolution. Science 313:6172–6176

Boyce M, Bertozzi CR (2011) Bringing chemistry to life. Nat Methods 8:638–642

Chen J, Gao J, Wu J, Zhang M, Cai M, Xu H, Jiang J, Tian Z, Wang H (2015) Revealing the carbohydrate pattern on a cell surface by super-resolution imaging. Nanoscale 7:3373–3380

Dempsey GT, Vaughan JC, Chen KH, Bates M, Zhuang X (2011) Evaluation of fluorophores for optimal performance in localization-based super-resolution imaging. Nat Methods 8:1027–1036

Ehmann N, van de Linde S, Alon A, Ljaschenko D, Keung XZ, Holm T, Rings A, DiAntonio A, Hallermann S, Ashery U, Heckmann M, Sauer M, Kittel RJ (2014) Quantitative super-resolution imaging of Bruchpilot distinguishes active zone states. Nat Commun 5:4650

Fricke F, Malkusch S, Wangorsch G, Greiner JF, Kaltschmidt B, Kaltschmidt C, Widera D, Dandekar T, Heilemann M (2014) Quantitative single-molecule localization microscopy combined with rule-based modeling reveals ligand-induced TNF-R1 reorganization toward higher-order oligomers. Histochem Cell Biol 142:91–101

Gao J, Wang Y, Cai M, Pan Y, Xu H, Jiang J, Ji H, Wang H (2015) Mechanistic insights into EGFR membrane clustering revealing by super-resolution imaging. Nanoscale 7:2511–2519

Haltiwanger RS, Lowe JB (2004) Role of glycosylation in development. Annu Rev Biochem 73:491–537

Heilemann M, van de Linde S, Schüttpelz M, Kasper R, Seefeldt B, Mukherjee A, Tinnefeld P, Sauer M (2008) Subdiffraction-resolution fluorescence imaging with conventional fluorescent probes. Angew Chem Int Ed 47:6172–6176

Henriques R, Lelek M, Fornasiero EF, Valtorta F, Zimmer C, Mhlanga MM (2010) QuickPALM: 3D real-time photoactivation nanoscopy image processing in ImageJ. Nat Methods 7:339–340

Holden SJ, Uphoff S, Kapanidis AN (2011) DAOSTORM: an algorithm for high-density super-resolution microscopy. Nat Methods 8:279–280

Holm T, Klein T, Löschberger A, Klamp T, Wiebusch G, van de Linde S, Sauer M (2014) A blueprint for cost-efficient localization microscopy. ChemPhysChem 15:651–654

Honigmann A, Mueller V, Ta H, Schoenle A, Sezgin E, Hell SW, Eggeling C (2014) Scanning STED-FCS reveals spatiotemporal heterogeneity of lipid interaction in the plasma membrane of living cells. Nat Commun 5:5412

Klein T, Proppert S, Sauer M (2014) Eight years of single-molecule localization microscopy. Histochem Cell Biol 141:561–575

Lando D, Endesfelder U, Berger H, Subramanian L, Dunne PD, McColl J, Klenerman D, Carr AM, Sauer M, Allshire RC, Heilemann M, Laue ED (2012) Quantitative single-molecule microscopy reveals that CENP-ACnp1 deposition occurs during G2 in fission yeast. Open Biol 2:120078

Letschert S, Göhler A, Franke C, Bertleff-Zieschang N, Memmel E, Doose S, Seibel J, Sauer M (2014) Super-resolution imaging of plasma membrane glycans. Angew Chem 53:10921–10924

Löschberger A, van de Linde S, Dabauvalle M, Rieger B, Heilemann M, Krohne G, Sauer M (2012) Super-resolution imaging visualizes the eightfold symmetry of gp210 proteins around the nuclear pore complex and resolves the central channel with nanometer resolution. J Cell Sci 125:570–575

Löschberger A, Franke C, Krohne G, van de Linde S, Sauer M (2014) Correlative super-resolution fluorescence and electron microscopy of the nuclear pore complex with molecular resolution. J Cell Sci 127:4351–4355

Maglione M, Sigrist SJ (2013) Seeing the forest tree by tree: super-resolution light microscopy meets the neurosciences. Nat Neurosci 16:790–797

Malkusch S, Muranyi W, Müller B, Kräusslich H, Heilemann M (2013) Single-molecule coordinate-based analysis of the morphology of HIV-1 assembly sites with near-molecular spatial resolution. Histochem Cell Biol 139:173–179

Ohtsubo K, Marth JD (2006) Glycosylation in cellular mechanisms of health and disease. Cell 126:855–867

Patterson G, Davidson M, Manley S, Lippincott-Schwartz J (2010) Superresolution imaging using single-molecule localization. Annu Rev Phys Chem 61:345–367

Puchner EM, Walter JM, Kasper R, Huang B, Lim WA (2013) Counting molecules in single organelles with superresolution microscopy allows tracking of the endosome maturation trajectory. Proc Natl Acad Sci 110:16015–16020

Ripley BD (1977) Modelling spatial patterns. J R Stat Soc Ser B 39:172–212

Sage D, Kirshner H, Pengo T, Stuurman N, Min J, Manley S, Unser M (2015) Quantitative evaluation of software packages for single-molecule localization microscopy. Nat Methods. doi:10.1038/nmeth.3442

Saka SK, Honigmann A, Eggeling C, Hell SW, Lang T, Rizzoli SO (2014) Multi-protein assemblies underlie the mesoscale organization of the plasma membrane. Nat Commun 5:4509

Sauer M (2013) Localization microscopy coming of age: from concepts to biological impact. J Cell Sci 126:3505–3513

Schücker K, Holm T, Franke C, Sauer M, Benavente R (2015) Elucidation of synaptonemal complex organization by super-resolution imaging with isotropic resolution. Proc Natl Acad Sci USA 112:2029–2033

Shannon CE (1949) Communication in the presence of noise. Proc IRE 37:10–21

Szymborska A, de Marco A, Daigle N, Cordes VC, Briggs JAG, Ellenberg J (2013) Nuclear pore scaffold structure analyzed by super-resolution microscopy and particle averaging. Science 341:655–658

van de Linde S, Sauer M (2014) How to switch a fluorophore: from undesired blinking to controlled photoswitching. Chem Soc Rev 43:1076–1087

van de Linde S, Wolter S, Heilemann M, Sauer M (2010) The effect of photoswitching kinetics and labeling densities on super-resolution fluorescence imaging. J Biotechnol 149:260–266

van de Linde S, Löschberger A, Klein T, Heidbreder M, Wolter S, Heilemann M, Sauer M (2011) Direct stochastic optical reconstruction microscopy with standard fluorescent probes. Nat Protoc 6:991–1009

Whelan DR, Bell TDM (2015) Image artifacts in single molecule localization microscopy: why optimization of sample preparation protocols matters. Sci Rep 5:7924

Williamson DJ, Owen DM, Rossy J, Magenau A, Wehrmann M, Gooding JJ, Gaus K (2011) Pre-existing clusters of the adaptor Lat do not participate in early T cell signaling events. Nat Immunol 12:655–662

Wolter S, Endersfelder U, van de Linde S, Heilemann M, Sauer M (2011) Measuring localization performance of super-resolution algorithms on very active samples. Opt Express 19:7020–7033

Wolter S, Löschberger A, Holm T, Aufmkolk S, Dabauvalle M, van de Linde S, Sauer M (2012) rapidSTORM: accurate, fast open-source software for localization microscopy. Nat Methods 9:1040–1041

Zhu L, Zhang W, Elnatan D, Huang B (2012) Faster STORM using compressed sensing. Nat Methods 9:721–723

Manuscript 3

Mateos-Gil, P., Letschert, S., Doose, S., Sauer, M. (2016): Super-resolution imaging of plasma membrane proteins with click chemistry. *Frontiers in Cell and Developmental Biology*. 4, 98

frontiers in Cell and Developmental Biology

METHODS
published: 09 September 2016
doi: 10.3389/fcell.2016.00098

Super-Resolution Imaging of Plasma Membrane Proteins with Click Chemistry

*Pablo Mateos-Gil *, Sebastian Letschert, Sören Doose and Markus Sauer **

Department of Biotechnology and Biophysics, Julius Maximilian University of Würzburg, Würzburg, Germany

Besides its function as a passive cell wall, the plasma membrane (PM) serves as a platform for different physiological processes such as signal transduction and cell adhesion, determining the ability of cells to communicate with the exterior, and form tissues. Therefore, the spatial distribution of PM components, and the molecular mechanisms underlying it, have important implications in various biological fields including cell development, neurobiology, and immunology. The existence of confined compartments in the plasma membrane that vary on many length scales from protein multimers to micrometer-size domains with different protein and lipid composition is today beyond all questions. As much as the physiology of cells is controlled by the spatial organization of PM components, the study of distribution, size, and composition remains challenging. Visualization of the molecular distribution of PM components has been impeded mainly due to two problems: the specific labeling of lipids and proteins without perturbing their native distribution and the diffraction-limit of fluorescence microscopy restricting the resolution to about half the wavelength of light. Here, we present a bioorthogonal chemical reporter strategy based on click chemistry and metabolic labeling for efficient and specific visualization of PM proteins and glycans with organic fluorophores in combination with super-resolution fluorescence imaging by *direct* stochastic optical reconstruction microscopy (*d*STORM) with single-molecule sensitivity.

Keywords: super-resolution fluorescence microscopy, localization microscopy, *d*STORM, plasma membrane organization, click chemistry, protein clusters

OPEN ACCESS

Edited by:
David Holowka,
Cornell University, USA

Reviewed by:
Sarah Shelby,
University of Michigan, USA
Tijana Jovanovic-Talisman,
Beckman Research Institute, USA

****Correspondence:***
Pablo Mateos-Gil
pablo.mateos_gil@uni-wuerzburg.de
Markus Sauer
m.sauer@uni-wuerzburg.de

Specialty section:
This article was submitted to Membrane Physiology and Membrane Biophysics, a section of the journal Frontiers in Cell and Developmental Biology

Received: *22 June 2016*
Accepted: *24 August 2016*
Published: *09 September 2016*

Citation:
Mateos-Gil P, Letschert S, Doose S and Sauer M (2016) Super-Resolution Imaging of Plasma Membrane Proteins with Click Chemistry. Front. Cell Dev. Biol. 4:98. doi: 10.3389/fcell.2016.00098

INTRODUCTION

The plasma membrane in eukaryotes is involved in several cell functions such as tissue formation, signal transduction, cell adhesion, and immune response. Although much evidence suggests that the spatial arrangement of its different components, i.e., membrane proteins and lipids, determines the functionality of the PM of eukaryotic cells, the precise molecular architecture remains unclear. Our current view of the cell membrane goes beyond the "fluid mosaic model," proposed more than 40 years ago by *Singer and Nicolson*, where proteins freely diffuse in a homogeneous sea of lipids (Singer and Nicolson, 1972). In contrast, a hierarchical subcompartmentalization, where proteins are transiently trapped in lipid rafts and actin-cytoskeleton associated corrals, has been hypothesized (Kusumi et al., 2012). Dynamic data obtained by ultra-fast single particle tracking has shown reduced diffusion behavior and hoping events of different membrane proteins suggesting the presence of protein nanodomains (Kusumi et al., 2005). The predicted size of these nanoclusters is in the order of a few tens to a few hundreds of nanometers, dependent on the cell type, protein,

or lipid. However, until now two obstacles impede the exploitation of quantitative data about the architecture of membrane-associated glycoproteins: selective and efficient labeling of membrane components and the resolution limit of optical microscopy.

During the last decade, the advent of far-field super-resolution microscopy methods, such as stochastic optical reconstruction microscopy (STORM) (Rust et al., 2006), *direct*STORM (Heilemann et al., 2008; van de Linde et al., 2011), photoactivated light microscopy (PALM) (Betzig et al., 2006), fluorescence PALM (Hess et al., 2006), stimulated emission depletion microscopy (STED) (Klar et al., 2000), ground state depletion microscopy (GSD) (Bretschneider et al., 2007), and structured illumination microscopy (SIM) (Gustafsson, 2000), has overcome this limitation. The application of these techniques revealed the existence of PM clusters with a typical size of ∼80 nm for various PM proteins (Kittel et al., 2006; Sieber et al., 2007; Williamson et al., 2011; Bar-On et al., 2012; Rossy et al., 2013). However, probing weather protein subcompartmentalization is a universal feature of PMs is still challenging. To this aim, methods devoted to stain, and visualize simultaneously a large population of PM proteins are required. Electron microscopy using immunogold labeling on isolated plasma membrane sheets revealed the existence of highly dense patches containing different membrane proteins (Lillemeier et al., 2006). More recently, the introduction of a bioorthogonal chemical reporter strategy, based on metabolic labeling and click chemistry, allowed the direct visualization of different membrane components by super-resolution microscopy (Letschert et al., 2014; Saka et al., 2014). This approach exploits the ability of the endogenous metabolic cellular machinery to recognize different metabolic surrogates containing small reactive chemical modifications ready to be conjugated with fluorophores. Non-natural methionine analogs, containing an azide, or an alkyne group, are recognized by the methionyl-tRNA synthetase and co-translationally incorporated into nascent proteins (Tom Dieck et al., 2012). On the other hand, non-native monosaccharide precursors can be used to introduce similar chemical groups into glycoproteins as post-translational modifications (Laughlin and Bertozzi, 2009a). Thus, click chemistry represents a direct labeling method for the visualization of different PM components.

Here, we report an efficient method to visualize PM proteins stained via metabolic labeling and click chemistry by super-resolution imaging with virtually molecular resolution. In particular, we present two procedures enabling quantitative super-resolution imaging of PM components on two different time-scales. First, we use L-azidohomoalanine (L-AHA), a non-natural methionine analog that is incorporated into newly synthesized proteins, typically within few hours. Second, we use peracetylated N-azidoacetylgalactosamine (Ac_4GalNAz) as a non-native monosaccharide incorporated into membrane-associated glycoproteins during 2 days of incubation. For fluorescence labeling, we compare two click chemistry reactions, copper-catalyzed azide-alkyne cycloaddition (CuAAC), and copper-free strain-promoted azide- alkyne cycloaddition (SPAAC), with regard to labeling efficiency. For fluorescence imaging with subdiffraction-resolution, we use single-molecule localization microscopy based on photoswitching of standard fluorophores, i.e., *direct* stochastic optical reconstruction microscopy (*d*STORM) (Heilemann et al., 2008; van de Linde et al., 2011). Furthermore, we describe localization microscopy based methods to determine quantitative information on density and spatial distribution of membrane proteins such as Ripley's K function. In addition, we highlight advantages of the method and limitations that might give rise to the appearance of artificial membrane clusters. Our data indicate that high emitter densities can be achieved of both apical and basal membrane components. Inhomogeneous distributions of PM proteins or glycans are revealed, especially in two-dimensional projections of intrinsically three-dimensional (3D) structures such as filopodia and overlapping membranes. More importantly, labeled vesicles located in close proximity to the PM can be misleadingly interpreted as clusters in two-dimensional super-resolution images. A certain degree of deviation from complete spatial randomness in PM proteins was found by Ripley's K function analysis.

MATERIALS

Cell Culture and Maintenance

1. Cell line and growth media: Adherent cell line growth in appropriate culture media. In this case, we use a human osteosarcoma (U2OS) cell line in standard growth media (cDMEM: Dulbecco's modified Eagle's HAM's F12 media supplemented with 10% (v/v) fetal calf serum (FCS), 4 mM glutamine, 100 U/L penicillin, and 0.1 mg/mL streptomycin).
2. Cell culture and maintenance: T25-culture flasks (Greiner Bio-One). Cell culture incubator maintained in humidified atmosphere at 5% CO_2 and 37°C. Phosphate-buffered saline (PBS), Hank's balance salt solution (HBSS), and accutase solution.
3. Cell preparation for metabolic labeling and fluorescence imaging: 8 well Lab-Tek chamber slides (Nunc, Thermo Fisher Scientific).

Metabolic Labeling with Azido Unnatural Amino Acid AHA

1. Metabolic labeling media: Methionine free media (MFM: Dulbecco's modified Eagle's HAM's F12, with 10% FCS, 4 mM glutamine, 100 U/L penicillin, and 0.1 mg/mL streptomycin, without methionine).
2. Azido methionine analog: L-azidohomoalanine (L-AHA) (Jena Bioscience) stored as powder at 4°C.
3. Protein synthesis inhibitors: Anisomycin (Sigma-Aldrich) 10 mg/mL stock solution in dimethyl sulfoxide (DMSO)

Metabolic Labeling with Peracetylated Azido Modified Monosaccharides.

1. Metabolic labeling media: Standard growth media (cDMEM) supplemented as described in cell culture and maintenance.
2. Azido modified monosaccharides: N-azidoacetylgalactosamine (Ac_4GalNAz) (Invitrogen). Stock

solutions were prepared at 25 mM in dimethyl sulfoxide (DMSO) and stored at −20°C up to 12 months.

Alternatively N-azidoacetylmannosamine (Ac_4ManNAz) and N-azidoacetylglucosamine (Ac_4GlcNAz) can be used

Copper-Catalyzed Azide-Alkyne Cycloaddition (CuAAC)

1. Staining solution additives: Copper sulfate ($CuSO_4$), copper ligand Tris(3-hydroxypropyltriazolyl-methyl)amine (THPTA), and sodium ascorbate (Sigma-Aldrich).
2. Stock solutions of 2 mM $CuSO_4$ and 10 mM THPTA in MiliQ water stored at −20°C. 100 mM sodium ascorbate in MiliQ water freshly prepared.
3. Alkyne-tagged fluorophore: 2 mM stock solution of Alexa Fluor 647 alkyne (Thermo Fischer Scientific) in DMSO stored at −20°C up to 12 months.

Strain-Promoted Azide-Alkyne Cycloaddition (Spaac)

1. DBCO-tagged fluorophore: 2 mM stock solution of Cy5 DBCO (Sigma-Aldrich) in DMSO stored at −20°C up to 12 months.

Super-Resolution Imaging with *d*STORM

1. Setup: We used a custom-made setup based on an inverted commercial microscope (IX71; Olympus) equipped with an oil-immersion objective (60x, NA 1.45; Olympus), and a nosepiece stage (IX2-NPS; Olympus) to prevent focus-drift during image acquisition. A 641-nm diode laser (Cube 640–100C; Coherent), spectrally cleaned-up with a band-pass filter (BrightLine 642/10, Semrock), was used for excitation of Cy5 and AF-647. Additionally, two lenses and a mirror, coupled to a translation stage, were used to focus the laser beam on the back focal plane of the objective and switching between different illumination modes, i.e., epi, low-angle/highly inclined and laminated light optical sheet (HILO), and total internal reflection illumination (TIR) (Sharonov and Hochstrasser, 2007; Tokunaga et al., 2008; van de Linde et al., 2011). Fluorescence emission of Cy5 and AF-647 were collected with the same objective, separated from excitation light by a dichroic beamsplitter (560/659, Semrock), filtered with appropriate band- and long-pass filters (BrightLine 697/75 and RazorEdge 647, Semrock), and projected on an EMCCD camera (Ixon DU897, Andor Technology). Additional lenses were placed into the detection path to generate a final pixel size of 134 nm.
2. Switching buffer: PBS buffer containing 100 mM β-mercaptoethylamine (MEA, Sigma-Aldrich) and an oxygen scavenger system (2% (w/v) glucose, 4 U/mL glucose oxidase and 80 U/mL catalase) adjusted to pH 7.4.
3. *d*STORM image reconstruction: Open source software for single-molecule localizations and super-resolution image reconstruction rapi*d*STORM 3.3 (Wolter et al., 2010, 2012).

Quantitative Analysis

For quantitative analysis of generated localization data based on XY coordinates lists, customized algorithms implemented with programing languages such as Python (available at http://www.python.org), and Mathematica (Wolfram Research Inc., Champaing, Il, USA) were used.

METHODS

Background

Since the development of the *Staudinger-Bertozzi ligation* between azides and phosphines in 2000 (Saxon and Bertozzi, 2000), bioorthogonal *"click chemistry"* reactions allowed the visualization of different biomolecules (e.g., proteins, glycans, lipids, and nucleic acids) in cultured cells, tissues, and living organisms (Sletten and Bertozzi, 2009). To this aim, one functional group (the label) is introduced into the biomolecule of interest followed by exogenous addition of fluorophores bearing the reactive partner (the probe). For example, unnatural amino acids and monosaccharides containing an azide group can be used as metabolic surrogates of their native counterparts to visualize proteins and glycoproteins as well as glycolipids (Laughlin and Bertozzi, 2009a; Tom Dieck et al., 2012).

Two different approaches have been used successfully to introduce amino acid analogs into proteins: (i) genetic encoding, i.e., site-specific modification, and (ii) metabolic labeling, i.e., residue-specific modification. Whereas, the first method introduces unnatural amino acids into one particular protein, the second method allows labeling of a wide part of the proteome replacing a native amino acid (e.g., methionine) by its non-natural analog (e.g., L-azidohomoalanine, L-AHA). Due to its structural similarity, L-AHA is recognized and tolerated by the methionyl-tRNA synthetase (MetRS), and incorporated into newly synthesized proteins co-translationally in a residue-specific manner. Alternatively, azido sugars (e.g., peracetylated N-azidoacetylgalactosamine Ac_4GalNAz, N-azidoacetylmanosamine Ac_4ManNAz, and N-azidoacetylglucosamine Ac_4GlcNAz), can be incorporated into different types of glycoproteins and glycolipids (Laughlin et al., 2006; Laughlin and Bertozzi, 2009a). Upon cellular uptake and deacetylation, Ac_4GalNAz, Ac_4ManNAz, and Ac_4GlcNAz are converted into activated sugars, recognized by the glycan biosynthetic machinery, and incorporated into sialic acids and mucin-type O-linked glycans, as well as into O-GlcNAc-modified proteins. After metabolic incorporation of amino acids and monosaccharide surrogates, the azide groups introduced into newly synthesized proteins and glycans can be conjugated with alkyne fluorophores via azide-alkyne cycloaddition allowing their direct visualization.

Originally, the classic reaction between terminal alkynes and azides was shown to be efficiently catalyzed by copper(I) at room temperature enabling it to proceed within minutes under physiological conditions, opening the door for biological applications (Rostovtsev et al., 2002; Tornøe et al., 2002). Since then, this reaction, now termed as the Cu(I)-catalyzed azide-alkyne cycloaddition (CuAAC), has been used to visualize

different metabolically labeled biomolecules (Sletten and Bertozzi, 2009). However, due to Cu(I) toxicity fluorescent staining by CuAAC has been restricted to fixed cells. To overcome this problem, two alternative strategies have been developed. In 2004, it was shown that azide-alkyne cycloaddition can be strain-promoted in the absence of copper(I) using cyclooctynes (Agard et al., 2004). Since then, different cyclooctyne molecules with enhanced efficiency have been developed for copper-free strain-promoted azide-alkyne cycloaddition (SPAAC) (Jewett and Bertozzi, 2010; Debets et al., 2011). On the other hand, the optimization of the CuAAC, by means of copper(I) ligands and further additives in the reaction buffer, preserves cell viability while live staining. For example, the use of THPTA in addition to sodium ascorbate allow efficient CuAAC bioconjugation within 5 min with low copper concentrations (e.g., 50 μM) minimizing Cu(I) toxic effects (Hong et al., 2009, 2010).

Standard fluorescence microscopy, combined with metabolic labeling and click chemistry, has been used extensively to visualize both proteins and membrane-associated glycoconjugates within different cellular contexts. For example, newly synthesized proteins have been imaged in mammalian cells and rat hippocampal neurons (Dieterich et al., 2006, 2010; Beatty and Tirrell, 2008), and different glycan populations in culture cells (Baskin et al., 2007), developing zebrafish embryos (Laughlin et al., 2008), and living *C. elegans* (Laughlin and Bertozzi, 2009b). Remarkably, these studies demonstrated the versatility of metabolic labeling for temporal profiling of dynamic changes in large protein populations and glycans. More recently, the same chemical reporter strategy has allowed direct visualization of different membrane components by super-resolution microscopy (Letschert et al., 2014; Saka et al., 2014). Stimulated emission depletion (STED) was used to image unnatural amino acids incorporated into membrane proteins in monkey kidney cell line COS-7, demonstrating protein confinement with reduced diffusion dynamics (Saka et al., 2014). On the other hand, *d*STORM was used to visualize different glycan types, including glycoproteins, after metabolic labeling with Ac_4GalNAz, Ac_4ManNAz, and Ac_4GlcNAz in human osteosarcoma (U2OS) and neuroblastome (SK-N-MC) cells (Letschert et al., 2014). Moreover, due to its ability for single-molecule detection and position determination *d*STORM measurements provided quantitative estimates of molecular densities and spatial distributions of membrane-associated glycoconjugates.

Protocols

In this section we provide protocols to combine metabolic labeling and fluorescent staining via click chemistry for super-resolution imaging with *d*STORM of membrane proteins with single-molecule sensitivity. The method comprises four steps:

Step 1. **Metabolic labeling with azido surrogates**, i.e., with L-azidohomoalanine (L-AHA) and peracetylated N-azidoacetylgalactosamine (Ac_4GalNAz) (**Figure 1A**).

Step 2. **Click chemistry fluorescent live staining** via copper-catalyzed (CuAAC) and copper-free strain-promoted azide-alkyne cycloadditions (SPAAC) (**Figure 1B**).

Step 3. **Localization based super-resolution imaging with *d*STORM**. Image acquisition and reconstruction, identification of two-dimensional projections of three-dimensional cell structures, and labeling efficiency estimation.

Step 4. **Quantitative analysis**. Estimation of detected molecular densities using reference samples, and clustering analysis by Ripley's K function.

Step 1- Metabolic Labeling with Azido Surrogates

Protocol 1a: Metabolic Labeling with Azido Methionine Analogs (L-Azidohomoalanine, L-AHA)

1. Cell culture and maintenance: Choose an appropriate cell line, e.g., human osteosarcoma (U2OS) cells, as a model system of adherent mammalian cells. Maintain the cells at 37°C in 5% CO_2 water-saturated atmosphere in growth culture medium (cDMEM).
   For gentler detachment of cells from T25-culture flasks incubation with accutase for 5 min is preferred rather than trypsine/EDTA treatment.
2. Azido amino acid incubation: Detach cells from culture flask by incubating with accutase for 5 min, count them and seed them in LabTek 8 well chambers at 1.2×10^4 final concentration per well in cDMEM growth media, and let them grow in the cell incubator for 48–72 h at 37°C and 5% CO_2 water saturated atmosphere until 80–90% confluency. Previous to L-AHA incubation, exchange growth medium with prewarmed HBSS, and incubate cells at 37°C during 50 min to deplete the cellular reservoirs of endogenous methionine. During this time prepare a fresh solution of 4 mM L-AHA in methionine-free medium (MFM) and prewarm it. Replace HBSS with AHA solution and incubate cells at 37°C and 5% CO_2 water saturated atmosphere for the desired time, e.g., 4–5 h.
   Control samples can be prepared incubating AHA in the presence of protein synthesis inhibitor such as anisomycin at 40 μM final concentration to evaluate fluorescent background (**Figure S1**).

Protocol 1b: Metabolic Labeling with Azido Sugars (N-Azidoacetylgalactosamine, Ac_4GalNAz)

1. Cell culture and maintenance: follow the same procedure as describe above.
2. Azido sugar incubation: After accutase incubation seed the cells onto 8 wells LabTek chamber at a final concentration of 1.2×10^4 cells per well. Add Ac_4GalNAz at 25 μM final concentration. Incubate cells at 37°C and 5% CO_2 water saturated atmosphere for 48 h before fluorescence staining and fixation.
   Control cells can be prepared in absence of azido sugars to evaluate fluorescence background (**Figure S1**).

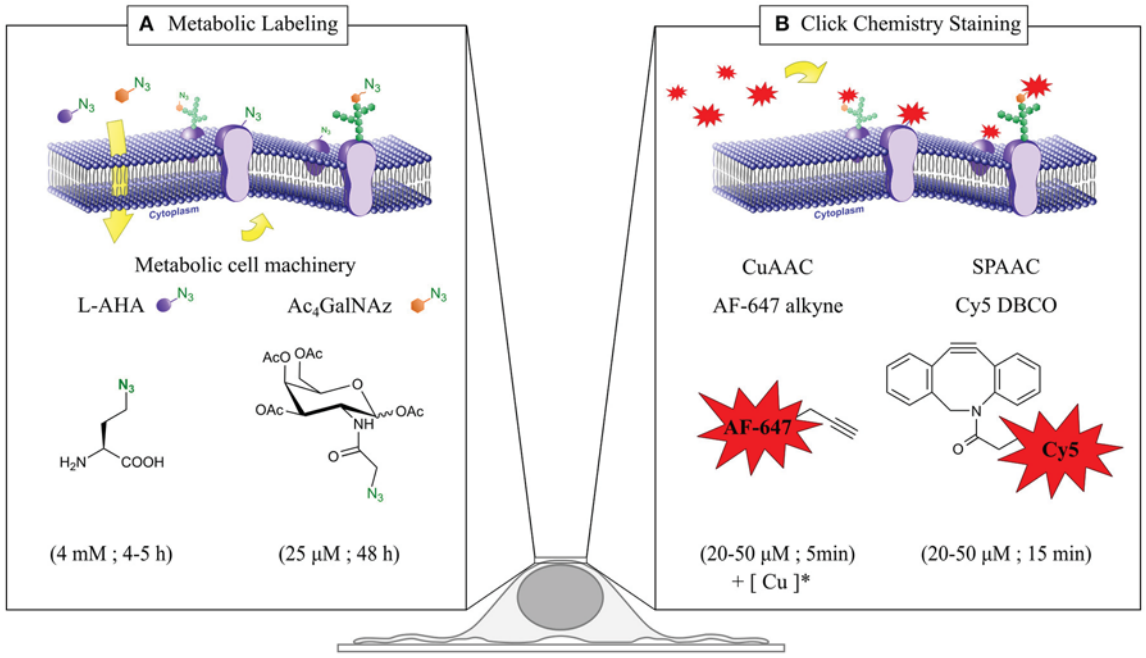

FIGURE 1 | Chemical reporter strategy based in metabolic labeling and click chemistry for *d*STORM quantitative imaging of plasma membrane (PM) proteins. (A) Incorporation of the metabolic surrogates L-azidohomoalanine (L-AHA) and N-Azidoacetylgalactosamine (Ac_4GalNAz) into newly synthesized proteins. Upon cellular uptake, L-AHA and Ac_4GalNAz are recognized by the endogenous cell machinery, and incorporated co-translationally and post-translationally into PM proteins and glycoproteins respectively. Typical incubation time and surrogate concentration for each metabolic labeling scheme are indicated at the bottom. **(B)** Click chemistry staining of PM proteins. After metabolic labeling, PM proteins bearing an azido group are stained with Alexa Fluor 647 alkyne and Cy5 DBCO via copper-catalyzed (CuAAC) and copper-free azide-alkyne cycloadditions (SPAAC) respectively. Typical incubation time and fluorophore concentration for each click chemistry reaction are indicated at the bottom. (*) Staining solution for CuAAC reaction (50 µM $CuSO_4$, 250 µM THPTA, 2.5 µM sodium ascorbate, and the desired amount of Alexa Fluor 647 alkyne in PBS).

Step 2- Fluorescence Live Staining via CuAAC and Spaac

Protocol 2a: Copper Catalyzed Azide-Alkyne Cycloaddition (CuAAC)

1. Preparation of optimal staining solution (50 µM $CuSO_4$, 250 µM THPTA, 2.5 µM sodium ascorbate, and the desired amount of Alexa Fluor 647 alkyne in PBS): For one LabTek well (final volume 200 µl). Premix 5 µl of 2 mM $CuSO_4$ with 5 µl of 10 mM THPTA stock solution. After 5 min add 5 µl of 100 mM sodium ascorbate freshly prepared stock solution in MiliQ water. Add appropriate volume of PBS and Alexa Fluor 647 depending on the desired final concentration of fluorophore. Vortex at high speed for few seconds.
   Further details in the use of copper ligands and sodium ascorbate for optimal CuAAC bioconjugation can be found elsewhere (Hong et al., 2009).
2. Fluorophore incubation: Immediately after removing the LabTek from incubator, wash cells once with prewarmed PBS and incubate them with staining solution for 5 min protected from light at room temperature. Then, wash cells three times gently with PBS and fixate them in PBS solution containing 4% formaldehyde and 0.2% glutaraldehyde respectively. Finally, wash cells three times with PBS and store them at 4°C in PBS containing sodium azide 0.2% (w/v).
   Strong fixation over long times (e.g., 1 h) in the presence of glutaraldehyde is required to minimized lateral mobility of membrane proteins (Tanaka et al., 2010).

Protocol 2b: Copper-Free Strain-Promoted Azide-Alkyne Cycloaddition (SPAAC)

1. Staining solution: Dilute Cy5 DBCO in HBSS at desired concentration without any further additives.
   To avoid cellular stress, HBSS is preferred to PBS due to longer fluorophore incubation times.
2. Fluorophore incubation: Proceed as in point 2 of protocol 2a, i.e., wash the cells once with prewarmed PBS, exchange PBS with staining solution with desired fluorophore concentration, and incubate for 15 min instead of 5 min, wash cells three times with PBS, add fixation solution for 1 h, wash three times, and store cells at 4°C in PBS with 0.2% of sodium azide.

Step 3- Localization Based Super-Resolution Imaging with *d*storm

Protocol 3: *d*STORM Super-Resolution Imaging

1. Photoswitching buffer preparation: Prior to imaging, dissolve β-mercaptoethylamine (MEA) in PBS and keep the MEA powder reagent under argon atmosphere to avoid oxidation. Thaw stock aliquots of glucose, glucose oxidase and catalase

for the oxygen scavenger system. Mix all the reagents to final concentrations of 100 mM MEA, 2% (w/v) glucose, 4 U/mL glucose oxidase and 80 U/mL catalase. Finally adjust the pH to 7.4 with 5 M KOH solution.

2. Preparing cells for *d*STORM imaging: Exchange storing buffer with switching buffer (1.1 mL per well) and seal the LabTek with a coverslip to reduce uptake of atmospheric oxygen. Finally mount the LabTek onto the oil immersed inverted objective of the microscope.
3. Measuring *d*STORM image stack: First, localize and position cell of interest at low intensities. Then, increase the irradiation intensity, e.g., 5 kW/cm^2, to induce rapid transition of the fluorophores to their non-fluorescent off-state. Before image acquisition, exchange the illumination mode from TIRF, to epi-fluorescence and then back to TIRF to maximize the conversion of out-of-focus fluorophores to the dark state. Wait until all molecules in the field of view blink properly, typically 60 s, and start recording an image stack with the desired length and frame rate, e.g., 20,000 frames at 66 Hz (15 ms exposure time per frame).
   High irradiation intensities are crucial while measuring areas with high fluorophore densities to prevent artifacts due to overlapping of single emitter.
4. Reconstruction of super-resolution image with rapi*d*STORM: Set desired values of the minimum intensity threshold for single-molecule localization and the pixel-size of the super resolution image, e.g., 1000 photons and 10 nm respectively.
5. Identification of 2D-projections of 3D cell structures: Image consecutively the region of interest with slightly shifted (0.5–1 μm) focal planes into the cytosol.
6. Estimation of labeling efficiency: Titrate fluorophore concentration for desired fixed metabolic labeling conditions. Calculate localization density using a sliding window analysis (diameter = 1 μm, step = 100 nm). To prevent contribution from overlapping membrane structures measure localization density in regions under the nucleus.

Step 4- Quantitative Analysis of Molecular Densities and Spatial Distribution at the Nanoscale.

Protocol 4: Estimation of Detected Molecular Densities of Membrane Proteins and Glycans.

1. Preparing reference samples: To ensure detection of single and well isolated fluorophores decrease the labeling density to <20 localizations per μm^2 by adjusting the fluorophore concentration to <0.1 μM. Perform *d*STORM reference measurements using the same optical and chemical conditions, i.e., laser irradiation intensity, buffer composition and TIRF angle, as for non-diluted samples.
   Grouping localizations from isolated fluorophores: Group all localizations within a certain radius detected along the whole image stack (20,000 frames), e.g., by applying a Kalman tracking routine as implemented in rapi*d*STORM. Allow the tracking algorithm to group localizations with maximum temporal separation equal to stack length within a defined area specified by the given tracking radius. To confirm the detection of single spots vary the tracking radius from 1 to 160 nm.
2. Estimation of detected molecular densities: Plot the average track length versus the tracking radius and use the saturation level of the curve as a conversion factor reflecting the number of localizations detected per isolated fluorophore. In addition, align all the localizations within tracks with length >2 to their center of mass. Calculate the experimental precision by fitting the spatial distribution to a Gauss function.
3. Computation of Ripley's h function: We computed what we call Ripley's h function $h(d)$ as function of distance d following the standard definition for Ripley's k function (Ripley, 1977) and applying an established transformation (Kiskowski et al., 2009) allowing simple optical inspection since $h(d)$ is equal to zero for all d in the case of a spatially homogeneous point process (complete spatial randomness):

$$h(d) = \sqrt{\frac{A\sum_{i=1}^{n}\sum_{j=1}^{m}k(i,j)}{\pi m(n-1)}} - d \quad (1)$$

where d is a distance, A is the area of the region containing all localizations, n is the total number of localizations, m is the number of test localizations in a random subset of localizations, and $k(i,j)$ is a weight defined as:

$$k(i,j) = \begin{cases} 1 \text{ if the distance between localization i and j is less than } d \\ 0 \text{ otherwise} \\ 0 \text{ if the localizations i and j are identical} \end{cases} \quad (2)$$

For efficient computing on large datasets, we limited the number of test localizations to a subset with typically 500 localizations. For comparison with experimental data, we generated data sets with random localizations according (i) to a Poisson point process, and (ii) to a Neyman-Scott point process (Neyman and Scott, 1952). The Poisson process yields a data set of complete spatial randomness, whereas the Neyman-Scott process yields a data set with spatially Poisson-distributed parent events. Each parent event provides a set of offspring events with a Poisson distributed number of members, on average 5 (equal to the average number of localizations per fluorophore obtained experimentally from diluted reference samples). The offspring spatial coordinates are 2D Gauss distributed around each parent event with a standard deviation equal to the localization precision of 8 nm. We generated data sets with an overall localization density equal to the densities of experimental data. Simulations and statistical analysis of five cells in each data set was carried out using Wolfram Mathematica 10.4.1.

COMMENTARY

Comparison with Other Methods

During the last decades, fluorescence microscopy has allowed the direct observation of cellular processes in a relatively non-invasive fashion with high molecular specificity and temporal

resolution. However, due to the wave nature of light the spatial resolution is limited to approximately half the wavelength of the light in the imaging plane (Abbe, 1873). Recently, super-resolution microscopy methods have circumvented this problem improving the optical resolution substantially. Localization microscopy exhibits the highest spatial resolution of less than 20 nm, as compared to other super-resolution techniques such as STED (Klar et al., 2000) or structural illumination microscopy (SIM) (Gustafsson, 2000). Moreover, due to their single molecule sensitivity, localization microscopy can potentially provide quantitative information about the spatial organization of proteins, as well as the number of molecules residing inside and outside of subcellular compartments including PM nanodomains involved in different cell functions. For example, PALM and *d*STORM, in combination with genetically encoded fluorescent photactivable proteins and immunochemistry, respectively, demonstrated nanocluster organization of synaptic proteins (Bar-On et al., 2012; Ehmann et al., 2014), membrane receptors involved in cell growth, proliferation and differentiation (Gao et al., 2015), tumor necrosis (Fricke et al., 2014), or related to the immunological response (Williamson et al., 2011; Rossy et al., 2013). Comparative studies have also proven PM heterogeneity depending on protein membrane anchor types including the transmembrane protein Lat, the lipid-anchored protein Lyn, the vesicular stomatitis viral glycoprotein VSVG, and GPI anchored proteins (Sengupta et al., 2011, 2013). However, all these studies were restricted to a limited number of proteins at a given time and thus, it became obvious that a more general approach for visualizing simultaneously a large population of membrane proteins is required to inspect the global distribution of PM proteins at the nanoscale. Moreover, fluorescent staining with antibodies and genetically encoded fluorescent proteins can induce artificial clustering of membrane proteins (Tanaka et al., 2010; Magenau et al., 2015) and limit the localization precision due to their relatively large size, especially in high density labeled samples. Metabolic labeling fills both gaps by introducing small bioorthogonal chemical groups such as azides into newly synthetized proteins.

Metabolic labeling has been used during the last decade to visualize newly synthetized proteins with standard fluorescent microscopy in cultured cells, tissues, and living animals. The advantage of this staining strategy is two-fold. First, labeling proteins with small and bioorthogonal chemical handles either by co-translational incorporation of unnatural amino acids or by post-translationally modification with non-natural monosaccharides minimizes perturbation of proteins and likely resembles physiological conditions. Second, metabolic labeling constitutes a unique tool to visualize spatial patterns of wide parts of the proteome. Whereas, immunochemistry and genetically encoded fluorescent are useful to visualize one specific protein, metabolic labeling allows to stain simultaneously newly synthesized proteins in a less specific way. Because the azido amino acid L-azidohomoalanine (L-AHA) replaces endogenous methionine, all proteins containing natively at least a single methionine are prompted to be labeled. On the other hand, the peracetylated azido sugar N-azidoacetylgalactosamine (Ac_4GalNAz) is incorporated into specific subtypes of glycans such as mucin-type O-linked glycans and O-GlcNAc-modified glycoproteins (Laughlin and Bertozzi, 2009a). Further identification of which proteins incorporated successfully L-AHA or Ac_4GalNAz has been achieved using alkyne affinity-tags (e.g., biotin-FLAG-alkyne tag) instead of alkyne fluorophores, in combination with proteomics studies (Dieterich et al., 2006; Laughlin et al., 2006). It is important to remark that the incorporation of L-AHA and Ac_4GalNAz into PM proteins occurs during protein translation and post-translational glycosylation before they are delivered to the cell membrane. Therefore, different metabolic labeling conditions (e.g., changes in incubation time or concentration of the azido surrogates) can be used to study not only the spatial but also the temporal organization of newly synthesized proteins and glycans as shown previously by standard live-cell fluorescence microscopy (Baskin et al., 2007; Beatty and Tirrell, 2008; Laughlin et al., 2008; Laughlin and Bertozzi, 2009b; Dieterich et al., 2010).

When combined with super-resolution microscopy, metabolic labeling allows to inspect the overall distribution of membrane proteins at the nanoscale. This has recently been proven by STED and *d*STORM imaging of membrane proteins containing unnatural amino acids and azido sugars respectively (Letschert et al., 2014; Saka et al., 2014). Although both techniques provide images with substantially enhanced spatial resolution, due to their peculiarities, they exhibit unique advantages and limitations. For example, *d*STORM exhibits better spatial resolution than STED and has the potential to quantify molecular densities of membrane components as well as their spatial distributions. However, due to fluorophore photoswitching kinetics, the necessity of high photon yields, and slow camera frame rates, image acquisition typically requires few minutes (van de Linde et al., 2011). On the other hand, STED achieves much higher temporal resolution and therefore it is more suitable for dynamic studies. Remarkably, STED combined with fluorescence correlation spectroscopy (STED-FCS), where very small areas are scanned at frequencies in the order of a few kHz, can be used to measure diffusion dynamics of membrane proteins and lipids demonstrating molecular confinement with both high spatial and high temporal resolution (Eggeling et al., 2009; Saka et al., 2014).

Critical Parameters, Limitations, and Perspectives

The conditions presented in the given protocols constitute a robust recipe to stain and visualize large populations of PM proteins and glycans with super-resolution localization microscopy (**Figure 2**). Nevertheless, critical aspects, as well as limitations and future perspectives, with regard to obtain reliable quantitative data and avoid artifacts are shown in the next subsections. First, we highlight potential artifacts of *d*STORM as well as the inherent problem of 2D super-resolution images due to projections of 3D structures such as membrane ruffling, filopodia, overlapping membranes, and vesicles located in close proximity to the PM. Then, we compare the fluorescence staining efficiency achieved by copper-catalyzed and copper-free click chemistry reactions for fixed metabolic labeling

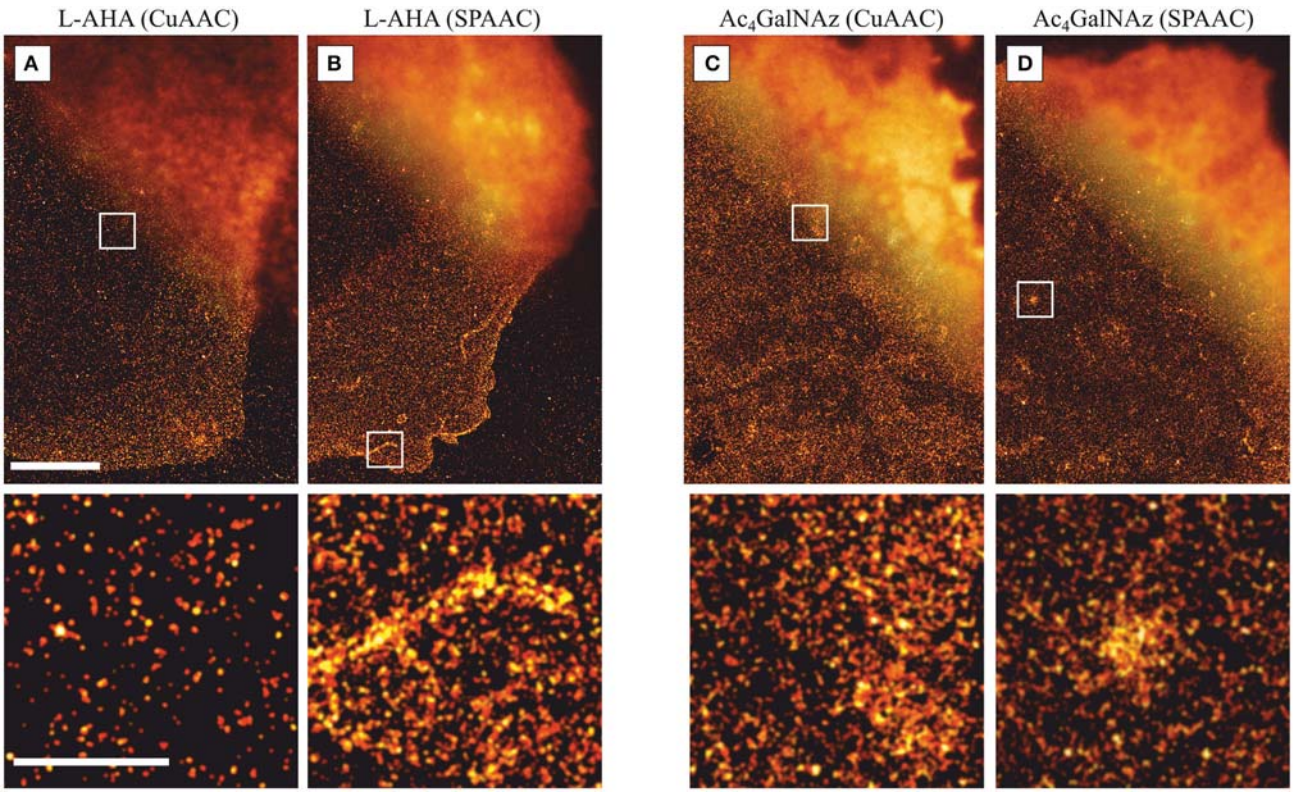

FIGURE 2 | Comparison of *d*STORM images with standard fluorescent microscopy. Representative *d*STORM and overlaid standard fluorescence images (upper right corner) of PM proteins at the basal membrane stained via **(A)** L-AHA (CuAAC), **(B)** L-AHA (SPAAC), **(C)** Ac_4GalNAz (CuAAC), and **(D)** Ac_4GalNAz (SPAAC). Comparison of L-AHA and Ac_4GalNAz stained via copper-catalyzed (CuACC) and copper-free (SPAAC) show no significant differences, indicating that the presence of copper ions or THPTA do not affect the distribution of PM components. For the four staining schemes depicted, 2D projected structures lead to spatial inhomogeneties as highlighted in the lower panels, e.g., **(A)** one fold membrane under the nucleus, **(B)** two-fold membrane structure within the lamellipodia plus one filopodia, **(C)** membrane ruffles, and **(D)** projection of a vesicle located in close proximity to the plasma membrane. All images were acquired under TIRF illumination, reconstructed with a minimum localization intensity threshold of 1000 photons, and a pixel size of 10 nm. Scale bars are 5 μm (upper panels) and 1 μm (lower panels).

conditions. Finally, we show how quantitative information about the distribution of PM components can be percolated from *d*STORM data using statistical spatial analysis approaches, such as pair-correlation and Ripley's K functions.

Artifacts and 2D Projections of 3D Structures in *d*STORM Imaging.

The intrinsic features of localization microscopy, i.e., reconstruction of super-resolution images from localization of single molecules, determine its accuracy, and reliability. The precision of position determination of single and well isolated fluorescent emitters is mainly determined by the number of collected photons, the signal-to-noise ratio, and the accuracy of the algorithm implemented in the localization software used to fit the point-spread-function (PSF) of detected fluorophores (Thompson et al., 2002; Mortensen et al., 2010; Sage et al., 2015). In contrast, other considerations must be taken into account to reconstruct reliable super-resolution images. For example, overlapping PSFs of multiple fluorophores residing in their on-state simultaneously within the same diffraction-limited area must be prevented, except specialized algorithms capable of fitting multiple emitters PSFs are used (Holden et al., 2011; Zhu et al., 2012), to avoid incorrect localizations and ensure artifact-free images reconstruction (van de Linde et al., 2010; Sauer, 2013; van de Linde and Sauer, 2014; Burgert et al., 2015). As a rule of thumb to avoid PSFs overlapping and ensure reliable spot finding and fitting, the density of fluorescent emitters has to be kept below 0.2 spots per μm^2 (Wolter et al., 2011). Therefore, appropriate measurement conditions in *d*STORM imaging such as laser irradiation intensities high enough to transfer the majority of organic dyes to long-living off states as well as suitable buffer compositions are required to guarantee good image quality.

Besides the aforementioned experimental traits of *d*STORM, inherent problems and limitations appear when studying membrane components with 2D localization microscopy. Without 3D information the ability to extract unbiased information about PM can be error prone. The existence of Z-projections of inherent cell membrane structures such as invaginations and vesicle-like structures, including fluorophore-filled endosomes in contact with or located near the PM,

as well as overlapping membranes in the lamellipodia, might distort severely the quantitative analysis and interpretation of super-resolution images. For example, a sliding window analysis applied to *d*STORM images of PM under the nucleus reveals half of the localization density compared to lamellipodia indicating a two-fold membrane structure (**Figures 3A,B**). Furthermore, circular clusters with apparent sizes ranging from a few tens to a few hundred nanometers can be visually identified from more homogeneous distributions, however it is difficult to discern weather they represent nanodomains enriched in membrane proteins or projections from fluorophore-filled vesicles in close proximity to the membrane. Whereas, a 3D-*d*STORM measurement would reduce any information bias on PM organization due to vertical projections, instrumentation, and implementation for 3D-*d*STORM is more complex and expensive compared to 2D-*d*STORM, and they usually achieve a lower axial than lateral resolution (Klein et al., 2014). In contrast, consecutive imaging of the same cell with slightly shifted focal planes above the feature of interest constitutes a fast control to determine the two-dimensional projection contribution from inherent 3D structures as shown in **Figures 3C,D** for vesicle-like structures located right above the plasma membrane (yellow circles) or further up (blue circle), and membrane ruffles (green circle) (Burgert et al., 2015).

Optimal Staining Efficiencies by Copper-Catalyzed and Copper-Free Click-Chemistry.

The first step of any fluorescent microscopy technique is the efficient staining of the protein of interest with a fluorophore. Moreover, in localization microscopy higher staining efficiencies, reflected as higher labeling densities, affects the maximum resolution in localization microscopy (Sauer, 2013). Whereas,

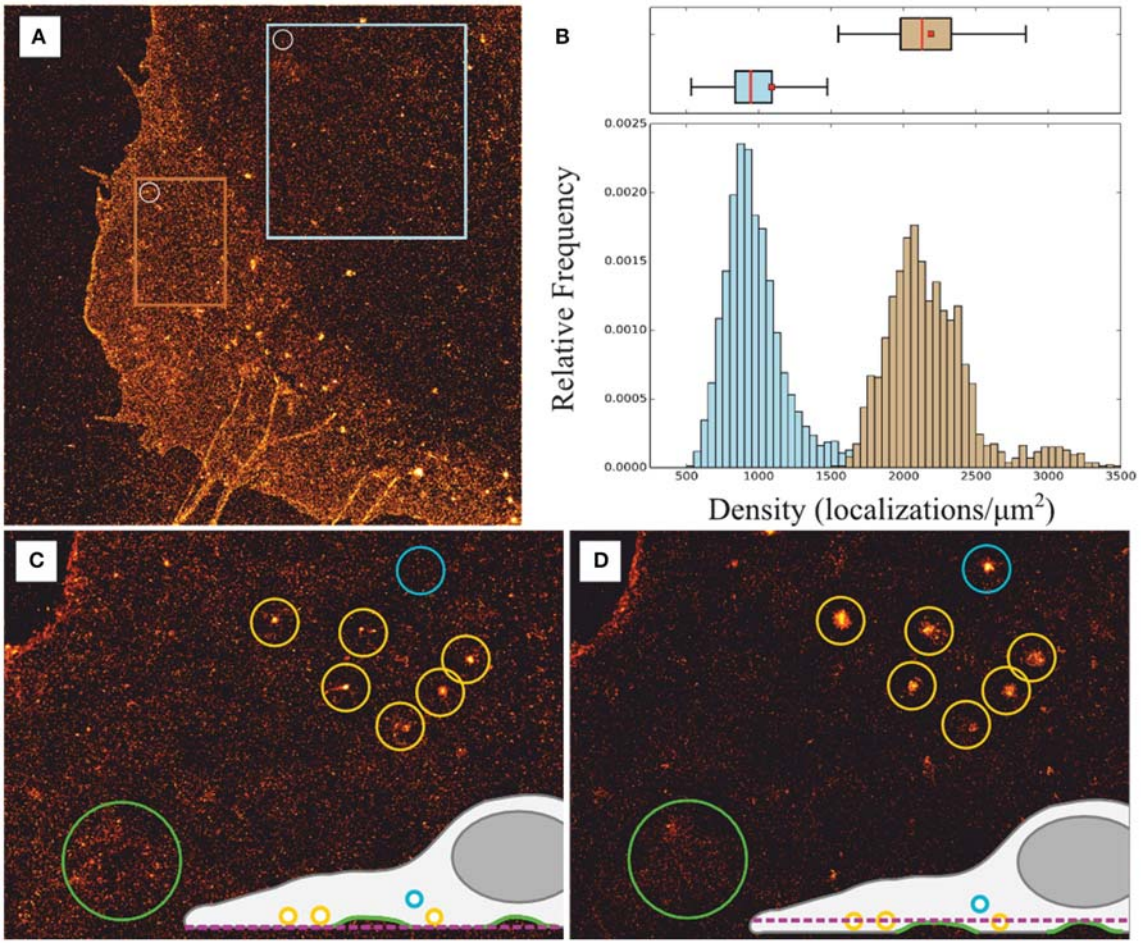

FIGURE 3 | Effect of two-dimensional projections of membrane structures. (A) *d*STORM image of PM proteins metabolically labeled with L-AHA showing overlapping membranes, vesicle-like structures, and filipodia. **(B)** Sliding window analysis to estimate PM content (white circle in **(A):** diameter = 1 μm, step = 100 nm) lead to median values of 884 localizations per μm^2 within a region under the nucleus, i.e., single membrane structure blue square in **(A)**, and 2130 localizations per μm^2 within the lamellipodia, i.e., two-fold overlapping membranes orange square in **(A)**. Box plot: red bar = median, box = 25th and 75th percentile, □ = mean. **(C,D)** Consecutive images with focal planes slightly shifted (0.5–1 μm) into the cytosol reveal artificial cluster structures generated due to vesicle-like structures located above the plasma membrane blue and yellow circles as well as inhomogeneities due to membrane ruffles green circle; adapted from Burgert et al. (2015).

imaging resolution is usually defined as the minimal resolvable distance between two emitters, the extractable structural information is also related to the sampling frequency, i.e., fluorophore labeling density, as described by the Nyquist-Shannon theorem (Shannon, 1949). In essence, the theorem states that the sampling interval, i.e., the mean distance between neighboring localized fluorophores, must be at least twice as fine as the structural details to be resolved. Therefore, higher labeling densities prevent under sampling and improve spatial resolution.

The conditions given here for click chemistry staining of membrane proteins and glycoconjugates lead to maximum labeling densities ranging from 400 to 2000 localizations per μm^2 (**Figure 4**). For the four bioconjugated systems inspected, we observed that fluorophore concentrations around 20–50 μM are required to maximize fluorescent signal. Moreover, copper-free strain-promoted azide-alkyne cycloaddition (SPAAC) is equally efficient as CuAAC to stain Ac_4GalNAz-derived glycoconjugates, and two-fold better to detect membrane proteins containing AHA. Thus, optimal conditions for click chemistry can also be achieved in absence of copper avoiding toxicity effects and simplifying the protocol.

Quantitative Analysis with *d*STORM

In *d*STORM measurements, localization densities in a certain area of the sample can be directly calculated from the coordinate lists exported by the localization software. Whereas, the number of localizations per unit area can be used to estimate the staining efficiency for different labeling conditions, it only provides relative information on the detected numbers of membrane proteins present. Since organic dyes undergo several photoswitching cycles during a *d*STORM measurement,

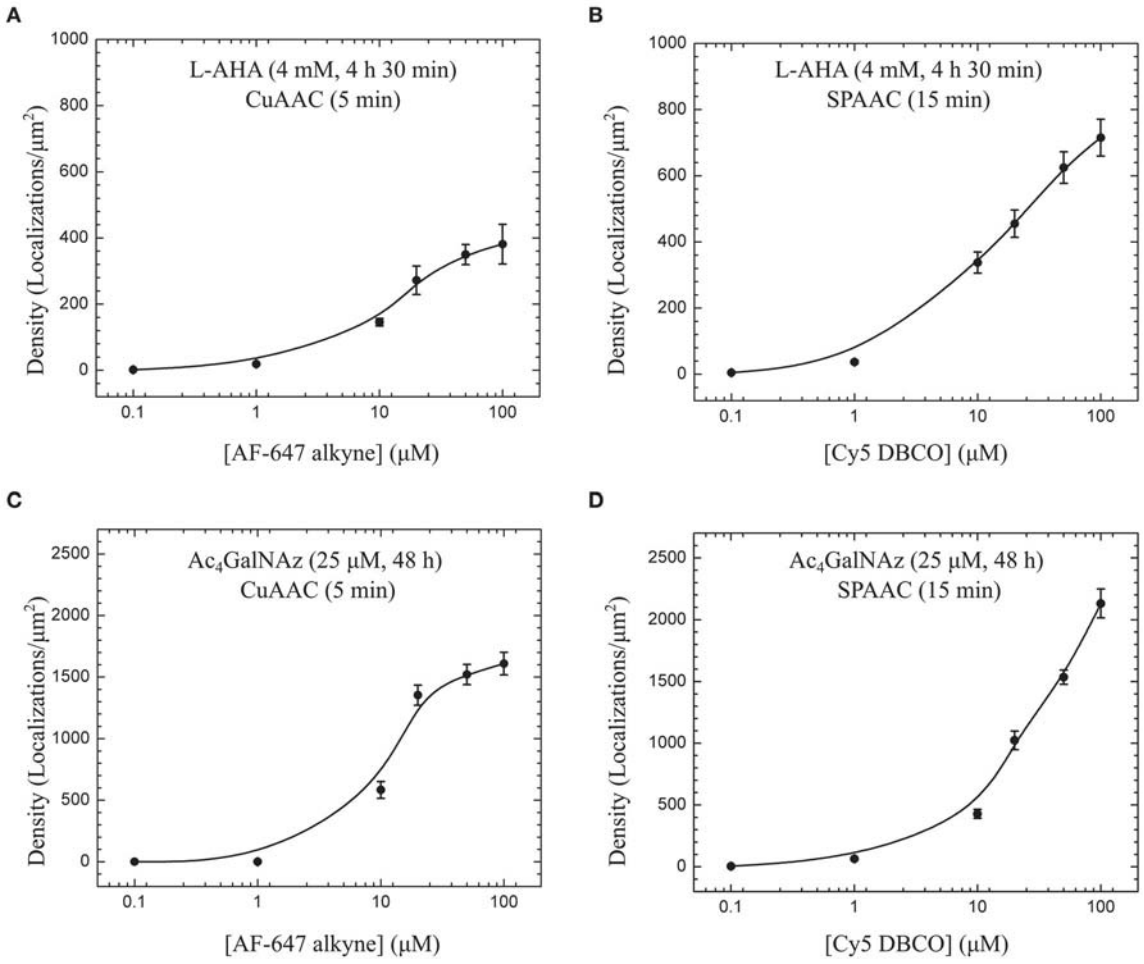

FIGURE 4 | Labeling efficiency of copper-catalyzed (CuAAC) and copper-free azide-alkyne cycloadditions (SPAAC). Fluorophore titration for the same metabolic labeling conditions, i.e., 4 mM L-AHA during 4 h 30 min **(A,B)**, and 25 μM Ac_4GalNAz during 48 h **(C,D)**, show optimal staining efficiency with AF-647 alkyne and Cy5 DBCO in the range of 20 to 50 μM for 5 min CuAAC and 15 min SPAAC reactions. For each cell, detected localizations were first obtained with a sliding window analysis (diameter = 1 μm, step = 100 nm) applied to big areas defined at bottom plasma membrane under the cell nucleus as described in **Figure 3B**. Plotted values and error bars represent median and SE of several cells imaged and analyzed for each fluorophore concentration [**(A)** 7–10 cells, **(B)** 8–15 cells, **(C)** 7–8 cells, and **(D)** 12–16 cells].

counting molecular numbers with localization microscopy requires further correction for multiple detections of the same molecule. The typical number of localizations recorded per fluorophore under the same optical and chemical conditions can be determined in diluted samples (**Figure 5**). If the blinking of isolated spots can be unequivocally assigned to single fluorophores, a conversion factor can be extracted to estimate the detected number of labeled membrane proteins (**Table 1**). For example, we estimate the density of PM proteins labeled with AHA during 4 h 30 min to be approximately ~50 μm^{-2} and ~125 μm^{-2} when stained via CuAAC and SPAAC respectively. On the other hand, we detected higher densities of glycans, in the range of ~345 μm^{-2} and ~280 μm^{-2}, metabolic labeled with Ac_4GalNAz during 48 h. It is important to mention that dividing the number of localizations in a region of interest by the average number of localizations detected per isolated fluorophore in reference experiments represents only an average correction value. To prevent over-counting effects in highly dense sample areas, more sophisticated methods based on the temporal and spatial fingerprint of single fluorophore blinking, such as off-time gap (Zhao et al., 2014) and pair correlation function analysis (PCF) (Veatch et al., 2012; Sengupta et al., 2013), can be applied.

Beyond density determination, coordinate lists obtained by localization microscopy can be used advantageously to inspect spatial distributions of membrane proteins. Analysis

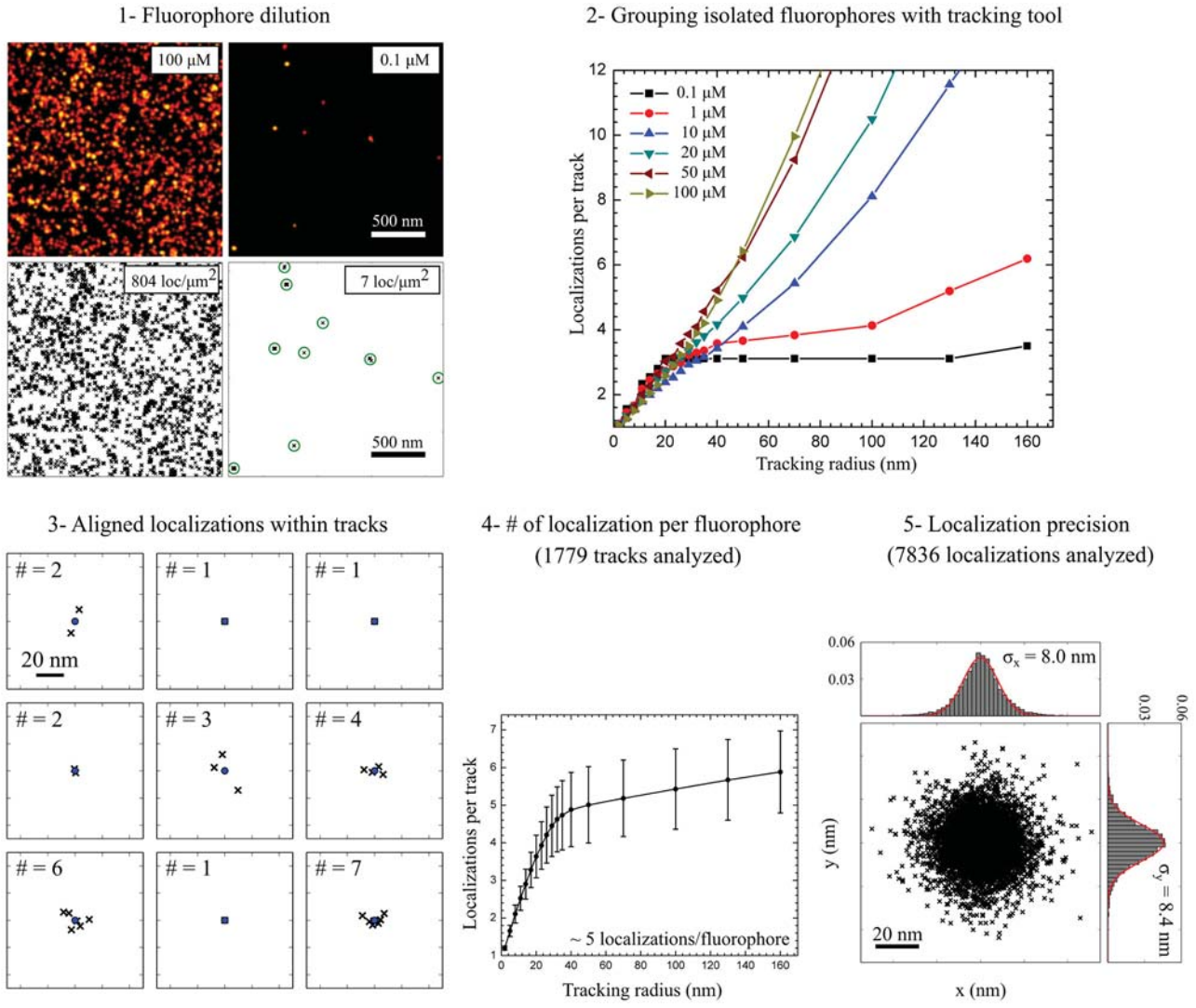

FIGURE 5 | Estimation of molecular densities and experimental localization precision. (1) Fluorophore dilution (<0.1 µM) leads to very low localization densities (<20 localizations per μm^2) allowing the detection of well isolated fluorophores. (2) Grouping localizations from isolated fluorophores was performed with a tracking algorithm. To confirm the detection of isolated fluorophores the tracking radius was varied from 1 to 160 nm for different fluorophore concentrations. (3) Localizations within tracks detected using a tracking radius = 50 nm aligned to the center of mass of each track. (4) For diluted samples the saturation level (tracking radius = 50 nm) indicates the number of localization per track, i.e., the number of localizations per isolated fluorophore. (5) Aligned localizations are used to estimate the experimental localization precision by fitting X and Y projections of the probability density function to a Gauss function.

TABLE 1 | Quantification of molecular density and experimental localization precision.

	Localization density[a] (loc/μm^2)	Conversion factor[b] (loc/fluorophore)	Molecular density (fluorophore/μm^2)[c]	σ_x (nm)[d] σ_y (nm)[e]
AHA (CuAAC)	350 ± 30	6.7 ± 1.1	52 ± 13	8.7 ± 0.1 8.9 ± 0.1
AHA (SPAAC)	625 ± 48	5.0 ± 1.0	125 ± 35	8.0 ± 0.1 8.4 ± 0.1
Ac_4GalNAz (CuAAC)	1520 ± 82	4.4 ± 1.4	345 ± 128	8.6 ± 0.1 9.9 ± 0.1
Ac_4GalNAz (SPAAC)	1536 ± 58	5.5 ± 1.0	279 ± 61	8.2 ± 0.1 8.4 ± 0.1

[a]Localization densities reflect median values calculated with a sliding window (diameter = 1 μm step = 100 nm) in regions under the cell nucleus to avoid overlapping membranes as shown in ***Figure 3****. Data presented correspond to 50 μM fluorophore concentration, i.e., AF-647 alkyne for 5 min CuACC staining and Cy5 DBCO for 15 min SPAAC staining. [b]Number of localizations per fluorophore obtained in diluted samples as described in* ***Figure 4*** *for 0.1 μM fluorophore concentrations. [c]Detected molecular densities calculated from localization densities divided by localizations per fluorophore. [d,e]Standard deviations obtained from Gauss function fits of the probability density functions calculated from aligned localizations as described in* ***Figure 4****.*

based on pair-correlation function (PCF) (Veatch et al., 2012; Sengupta et al., 2013) or nearest-neighbor based algorithms (including *Ripley's K* function) (Owen et al., 2012) can indicate weather proteins are more aggregated forming clusters or more dispersed than they were under a distribution of complete spatial randomness. All analysis routines need to take into account local self-clustering induced by single fluorophore blinking. Moreover, quantitative estimation of cluster size and densities can be difficult to extract without prior biological knowledge (Coltharp et al., 2014). Nevertheless, comparison with simulated spatial distributions mimicking experimental data can alleviate these problems and avoid miss-interpretations (Kiskowski et al., 2009; Veatch et al., 2012; Letschert et al., 2014). Finally, clustering algorithms, such as K-Means, DBSCAN, and polygon-based tessellation methods, have been used for morphological analysis of membrane proteins (Bar-On et al., 2012; Ehmann et al., 2014; Löschberger et al., 2014; Levet et al., 2015; Andronov et al., 2016). In contrast to pair-correlation and nearest-neighbor based algorithms, these methods rely on segmentation of the super-resolution image and thus the size and shape of each cluster, as well as their XY position, can be directly visualized.

To characterize the spatial distribution of PM components, we calculated Ripley's h functions from experimental data and two different sets of simulated spatial patterns. In particular, we simulated XY coordinates according to (i) a Poisson process and (ii) a Neyman-Scott process within 5 × 5 μm^2 with similar density as the number of localizations per μm^2 obtained from *d*STORM images. Whereas, a Poisson process resembles complete spatial randomness, it lacks to mimic individual fluorophore blinking inherent to *d*STORM measurements. In contrast, data sets simulated according to the Neyman-Scott process (Neyman and Scott, 1952) account photoswitching cycles from single fluorophores by including Gauss distributed offspring events around each parent position. Number of the offspring events and the standard deviation of the Gauss distribution (σ) where set from experimental data, i.e., on average ∼5 blinks per fluorophore and experimental localization precision ∼8 nm, respectively.

Ripley's k function reveals possible combinations of homogeneous distributions on large scales and clustering on small scales (e.g., due to the repeated blinking of individual labels). **Figure 6** shows direct comparison between experimental (blue line) and simulated data for a Poisson and Neyman-Scott process (black and red line respectively). For all the labeling schemes inspected, our data showed maximum clustering on a length scale similar to the estimated localization precision (i.e., d ∼20–30 nm). Therefore, clustering might reflect single fluorophore photoswitching. Since the maximum value of Ripley's h function for a simulated Neyman-Scott process is close to that of experimental data, we conclude that single fluorophore blinking is the only significant clustering process on this length scale. In addition, all the data indicate a small but significant deviation from complete spatial randomness on length scales from 30 to 800 nm. It is important to note that there is no characteristic length scale above 30 nm for any clusters of a well-defined size that can be identified. The indicated deviations from complete spatial randomness can have their origin in the various PM deformations e.g., due to the onset of vesicle formation or membrane ruffling. Whereas, it is possible to find small areas with a distribution that perfectly resemble a Neyman-Scott process (with clusters originating only from single emitter blinking), Ripley's h function for data in areas of 5 × 5 μm^2 in well-labeled cells under the nucleus (excluding double membrane contributions) typically appear as presented.

CONCLUSIONS AND REMARKS

We report a chemical reporter strategy, based on metabolic labeling and click chemistry, in combination with super-resolution imaging by *d*STORM to stain and visualize PM proteins and glycans. The labeling methodology results in staining efficiencies ranging from ∼50 to ∼350 fluorophore per μm^2 depending on the labeling scheme used. Besides the estimation of PM protein content, our data show potential

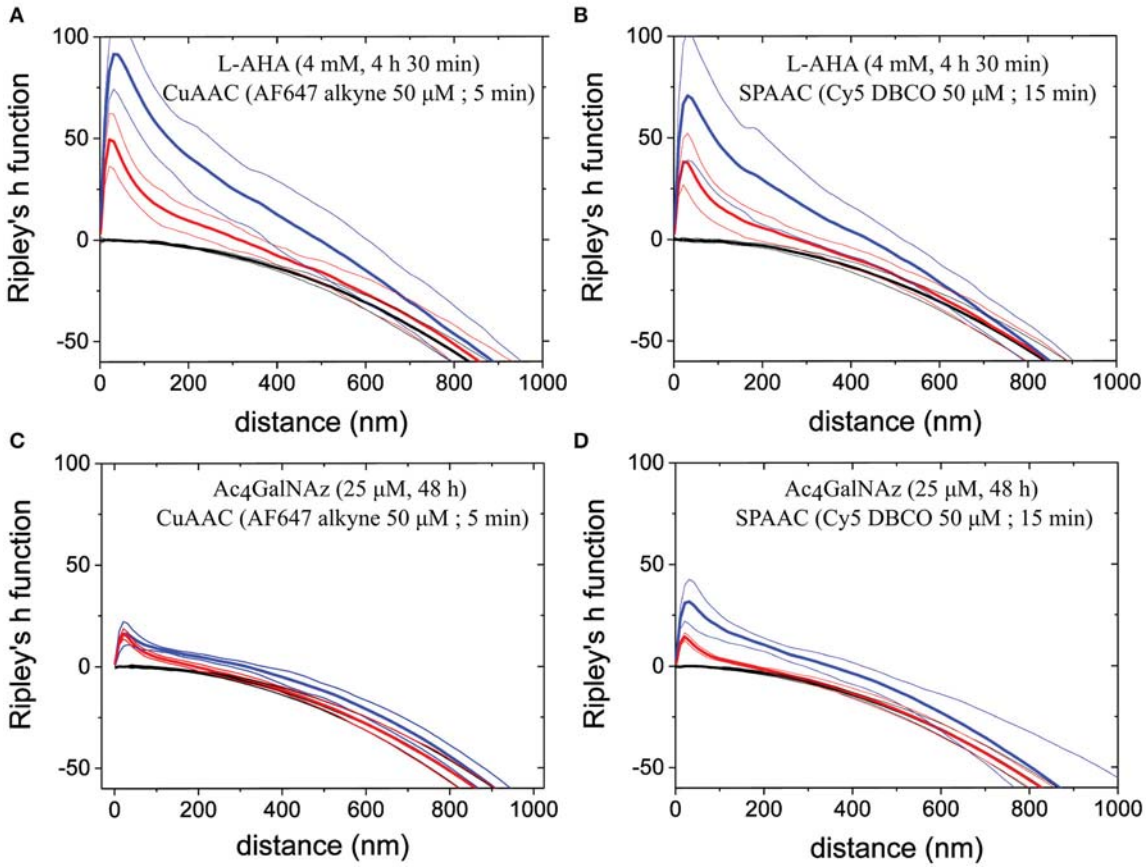

FIGURE 6 | Spatial distribution analysis by Ripley's h function. The data show Ripley's h functions computed from experimental data (blue lines) of PM proteins stained via **(A)** L-AHA (CuAAC), **(B)** L-AHA (SPAAC), **(C)** Ac_4GalNAz (CuAAC), and **(D)** Ac_4GalNAz (SPAAC). Plotted curves represent mean values (thick lines) together with 95% confidence intervals (thin) over 5 regions in total ($5 \times 5\ \mu m^2$ size) from independent cells, which appeared rather homogeneous by visual inspection. For comparison Ripley's function was computed from two simulated random point process, i.e., Neyman-Scott process (red lines) and Poisson point process (black lines). Simulation parameters, such as process intensity, average of offspring events, and spatial distribution around their parent event, where chosen to mimic localization density, photoswitching cycles, and localization precision obtained experimentally. The peak observed on short length scales for Neyman-Scott process and experimental data indicates artificial clustering due to repeated localizations from identical fluorophores within a Gauss distributions equal to localization precision, i.e., standard deviation ~8 nm. For all four staining schemes presented, Ripley's h functions show further clustering on longer length scales but more pronounced for L-AHA samples.

artifacts in super-resolution images due to 2D-projections of 3D-inherent cell structures. For example, overlapping membranes lead to overestimation of protein content, and vesicle-like structures located in closed proximity to the cell membrane appear as protein clusters and, thus, can potentially result in false interpretation of PM organization. Consecutive imaging with slightly shifted focal planes below and above the structure of interest can be used to reveal the contribution of 3D structures as two-dimensional projections. Furthermore, statistical analysis based on Ripley's function combined with point pattern simulations, can be used to identify deviations from complete spatial randomness. Our data clearly show artificial clustering due to fluorophore photoswitching at length scales related to the experimental localization precision (i.e., ~20–30 nm). Ripley's analysis also indicates a small deviation from spatial randomness at larger scales (e.g., ~30–800 nm). However, whereas these deviations from randomness might reflect some spatial organization of PM proteins at the nanoscale, their origin due to membrane modulations and ruffles, or the onset of vesicle formation cannot be completely excluded.

Finally, the examples presented here where performed at fixed metabolic conditions to incorporate azide groups in newly synthesized proteins. Experimental designs varying concentration and incubation time of metabolic surrogates combined with drug treatments can be used to study how fast proteins are delivered and trafficked from the cytosol to the plasma membrane. Reversibly, proteins can be followed after live cell staining to study membrane turnover involving different endocytic pathways. All in all, click chemistry constitutes a powerful tool to study PM composition at the molecular level as well as its dynamic organization. Moreover, the synthesis of new bioorthogonal molecules as well as their commercial availability will expand the applicability and usability of this methodology.

AUTHOR CONTRIBUTIONS

PM and MS designed the experiments. PM and SL performed the experiments. PM and SD analyzed the data. All authors discussed results and contributed to the manuscript.

ACKNOWLEDGMENTS

PM acknowledges financial support from Marie Curie Actions (FP7/PEOPLE-IEF-2013-625720). This work was also supported by the Deutsche Forschungsgemeinschaft, DFG grant SA829/13-1 to MS. We also want to acknowledge Lisa Behringer-Pließ and Petra Geßner for cell culture and technical support.

SUPPLEMENTARY MATERIAL

The Supplementary Material for this article can be found online at: http://journal.frontiersin.org/article/10.3389/fcell.2016.00098

Figure S1 | Click chemistry staining specificity. (A) To evaluate non-specific signal, control cells were incubated with AHA in the presence of 40 μM anisomycin, a protein synthesis inhibitor, and subsequently stained via CuAAC or SPAAC with 50 μM of Alexa Fluor 647 alkyne for 5 min or Cy5 DBCO for 15 min respectively. **(B)** In the case of azido sugar, control cells were incubated in absence of Ac_4GalNAz and subsequently stained via CuAAC or SPAAC with 20 μM of AF 647 alkyne for 5 min or Cy5 DBCO for 15 min respectively. All controls showed relatively low background of ∼19, 42, 10, and 20 localizations per μm^2 for L-AHA (CuAAC), L-AHA (SPAAC), Ac_4GalNAz (CuAAC), and Ac_4GalNAz (SPAAC) respectively. Values and error bars represent median and SE of localization densities obtained with sliding window analysis under the nucleus ($N = 7$ cells in all cases).

REFERENCES

Abbe, E. (1873). Beiträge zur Theorie des Mikroskops und der mikroskopischen Wahrnehmung. *Arch. Mikrosk. Anat.* 9, 413–418. doi: 10.1007/BF02956173

Agard, N. J., Prescher, J. A., and Bertozzi, C. R. (2004). A strain-promoted [3 + 2] azide-alkyne cycloaddition for covalent modification of biomolecules in living systems. *J. Am. Chem. Soc.* 126, 15046–15047. doi: 10.1021/ja044996f

Andronov, L., Orlov, I., Lutz, Y., Vonesch, J.-L., and Klaholz, B. P. (2016). ClusterViSu, a method for clustering of protein complexes by Voronoi tessellation in super-resolution microscopy. *Sci. Rep.* 6:24084. doi: 10.1038/srep24084

Bar-On, D., Wolter, S., van de Linde, S., Heilemann, M., Nudelman, G., Nachliel, E., et al. (2012). Super-resolution imaging reveals the internal architecture of nano-sized syntaxin clusters. *J. Biol. Chem.* 287, 27158–27167. doi: 10.1074/jbc.M112.353250

Baskin, J. M., Prescher, J. A., Laughlin, S. T., Agard, N. J., Chang, P. V., Miller, I. A., et al. (2007). Copper-free click chemistry for dynamic *in vivo* imaging. *Proc. Natl. Acad. Sci. U.S.A.* 104, 16793–16797. doi: 10.1073/pnas.0707090104

Beatty, K. E., and Tirrell, D. A. (2008). Two-color labeling of temporally defined protein populations in mammalian cells. *Bioorg. Med. Chem. Lett.* 18, 5995–5999. doi: 10.1016/j.bmcl.2008.08.046

Betzig, E., Patterson, G. H., Sougrat, R., Lindwasser, O. W., Olenych, S., Bonifacino, J. S., et al. (2006). Imaging intracellular fluorescent proteins at nanometer resolution. *Science* 313, 1642–1645. doi: 10.1126/science.1127344

Bretschneider, S., Eggeling, C., and Hell, S. W. (2007). Breaking the diffraction barrier in fluorescence microscopy by optical shelving. *Phys. Rev. Lett.* 98:218103. doi: 10.1103/PhysRevLett.98.218103

Burgert, A., Letschert, S., Doose, S., and Sauer, M. (2015). Artifacts in single-molecule localization microscopy. *Histochem. Cell Biol.* 144, 123–131. doi: 10.1007/s00418-015-1340-4

Coltharp, C., Yang, X., and Xiao, J. (2014). Quantitative analysis of single-molecule superresolution images. *Curr. Opin. Struct. Biol.* 28C, 112–121. doi: 10.1016/j.sbi.2014.08.008

Debets, M. F., van Berkel, S. S., Dommerholt, J., Dirks, A. T., Rutjes, F. P., and van Delft, F. L. (2011). Bioconjugation with strained alkenes and alkynes. *Acc. Chem. Res.* 44, 805–815. doi: 10.1021/ar200059z

Dieterich, D. C., Hodas, J. J., Gouzer, G., Shadrin, I. Y., Ngo, J. T., Triller, A., et al. (2010). *In situ* visualization and dynamics of newly synthesized proteins in rat hippocampal neurons. *Nat. Neurosci.* 13, 897–905. doi: 10.1038/nn.2580

Dieterich, D. C., Link, A. J., Graumann, J., Tirrell, D. A., and Schuman, E. M. (2006). Selective identification of newly synthesized proteins in mammalian cells using bioorthogonal noncanonical amino acid tagging (BONCAT). *Proc. Natl. Acad. Sci. U.S.A.* 103, 9482–9487. doi: 10.1073/pnas.0601637103

Eggeling, C., Ringemann, C., Medda, R., Schwarzmann, G., Sandhoff, K., Polyakova, S., et al. (2009). Direct observation of the nanoscale dynamics of membrane lipids in a living cell. *Nature* 457, 1159–1162. doi: 10.1038/nature07596

Ehmann, N., van de Linde, S., Alon, A., Ljaschenko, D., Keung, X. Z., Holm, T., et al. (2014). Quantitative super-resolution imaging of Bruchpilot distinguishes active zone states. *Nat. Commun.* 5, 4650. doi: 10.1038/ncomms5650

Fricke, F., Malkusch, S., Wangorsch, G., Greiner, J. F., Kaltschmidt, B., Kaltschmidt, C., et al. (2014). Quantitative single-molecule localization microscopy combined with rule-based modeling reveals ligand-induced TNF-R1 reorganization toward higher-order oligomers. *Histochem. Cell Biol.* 142, 91–101. doi: 10.1007/s00418-014-1195-0

Gao, J., Wang, Y., Cai, M., Pan, Y., Xu, H., Jiang, J., et al. (2015). Mechanistic insights into EGFR membrane clustering revealed by super-resolution imaging. *Nanoscale* 7, 2511–2519. doi: 10.1039/C4NR04962D

Gustafsson, M. G. (2000). Surpassing the lateral resolution limit by a factor of two using structured illumination microscopy. *J. Microsci.* 198(Pt 2), 82–87. doi: 10.1046/j.1365-2818.2000.00710.x

Heilemann, M., van de Linde, S., Schüttpelz, M., Kasper, R., Seefeldt, B., Mukherjee, A., et al. (2008). Subdiffraction-resolution fluorescence imaging with conventional fluorescent probes. *Angew. Chem. Int. Ed Engl.* 47, 6172–6176. doi: 10.1002/anie.200802376

Hess, S. T., Girirajan, T. P., and Mason, M. D. (2006). Ultra-high resolution imaging by fluorescence photoactivation localization microscopy. *Biophys. J.* 91, 4258–4272. doi: 10.1529/biophysj.106.091116

Holden, S. J., Uphoff, S., and Kapanidis, A. N. (2011). DAOSTORM: an algorithm for high- density super-resolution microscopy. *Nat. Methods* 8, 279–280. doi: 10.1038/nmeth0411-279

Hong, V., Presolski, S. I., Ma, C., and Finn, M. G. (2009). Analysis and optimization of copper-catalyzed azide-alkyne cycloaddition for bioconjugation. *Angew. Chem. Int. Ed Engl.* 48, 9879–9883. doi: 10.1002/anie.200905087

Hong, V., Steinmetz, N. F., Manchester, M., and Finn, M. G. (2010). Labeling live cells by copper-catalyzed alkyne–azide click chemistry. *Bioconjug. Chem.* 21, 1912–1916. doi: 10.1021/bc100272z

Jewett, J. C., and Bertozzi, C. R. (2010). Cu-free click cycloaddition reactions in chemical biology. *Chem. Soc. Rev.* 39, 1272–1279. doi: 10.1039/b901970g

Kiskowski, M. A., Hancock, J. F., and Kenworthy, A. K. (2009). On the use of Ripley's K-function and its derivatives to analyze domain size. *Biophys. J.* 97, 1095–1103. doi: 10.1016/j.bpj.2009.05.039

Kittel, R. J., Wichmann, C., Rasse, T. M., Fouquet, W., Schmidt, M., Schmid, A., et al. (2006). Bruchpilot promotes active zone assembly, $Ca2^+$ channel clustering, and vesicle release. *Science* 312, 1051–1054. doi: 10.1126/science.1126308

Klar, T. A., Jakobs, S., Dyba, M., Egner, A., and Hell, S. W. (2000). Fluorescence microscopy with diffraction resolution barrier broken by stimulated emission. *Proc. Natl. Acad. Sci. U.S.A.* 97, 8206–8210. doi: 10.1073/pnas.97.15.8206

Klein, T., Proppert, S., and Sauer, M. (2014). Eight years of single-molecule localization microscopy. *Histochem. Cell Biol.* 141, 561–575. doi: 10.1007/s00418-014-1184-3

Kusumi, A., Fujiwara, T. K., Chadda, R., Xie, M., Tsunoyama, T. A., Kalay, Z., et al. (2012). Dynamic organizing principles of the plasma membrane that regulate signal transduction: commemorating the fortieth anniversary of Singer and Nicolson's fluid-mosaic model. *Annu. Rev. Cell Dev. Biol.* 28, 215–250. doi: 10.1146/annurev-cellbio-100809-151736

Kusumi, A., Nakada, C., Ritchie, K., Murase, K., Suzuki, K., Murakoshi, H., et al. (2005). Paradigm shift of the plasma membrane concept from the two-dimensional continuum fluid to the partitioned fluid: high-speed single-molecule tracking of membrane molecules. *Annu. Rev. Biophys. Biomol. Struct.* 34, 351–378. doi: 10.1146/annurev.biophys.34.040204.144637

Laughlin, S. T., Agard, N. J., Baskin, J. M., Carrico, I. S., Chang, P. V., Ganguli, A. S., et al. (2006). Metabolic labeling of glycans with azido sugars for visualization and glycoproteomics. *Meth. Enzymol.* 415, 230–250. doi: 10.1016/S0076-6879(06)15015-6

Laughlin, S. T., Baskin, J. M., Amacher, S. L., and Bertozzi, C. R. (2008). *In vivo* imaging of membrane-associated glycans in developing zebrafish. *Science* 320, 664–667. doi: 10.1126/science.1155106

Laughlin, S. T., and Bertozzi, C. R. (2009a). Imaging the glycome. *Proc. Natl. Acad. Sci. U.S.A.* 106, 12–17. doi: 10.1016/B978-0-12-388448-0.00029-2

Laughlin, S. T., and Bertozzi, C. R. (2009b). *In vivo* imaging of Caenorhabditis elegans glycans. *ACS Chem. Biol.* 4, 1068–1072. doi: 10.1021/cb900254

Letschert, S., Göhler, A., Franke, C., Bertleff-Zieschang, N., Memmel, E., Doose, S., et al. (2014). Super-resolution imaging of plasma membrane glycans. *Angew. Chem. Int. Ed Engl.* 53, 10921–10924. doi: 10.1002/ange.201406045

Levet, F., Hosy, E., Kechkar, A., Butler, C., Beghin, A., Choquet, D., et al. (2015). SR-Tesseler: a method to segment and quantify localization-based super-resolution microscopy data. *Nat. Methods* 12, 1065–1071. doi: 10.1038/nmeth.3579

Lillemeier, B. F., Pfeiffer, J. R., Surviladze, Z., Wilson, B. S., and Davis, M. M. (2006). Plasma membrane-associated proteins are clustered into islands attached to the cytoskeleton. *Proc. Natl. Acad. Sci. U.S.A.* 103, 18992–18997. doi: 10.1073/pnas.0609009103

Löschberger, A., Franke, C., Krohne, G., van de Linde, S., and Sauer, M. (2014). Correlative super-resolution fluorescence and electron microscopy of the nuclear pore complex with molecular resolution. *J. Cell Sci.* 127(Pt 20), 4351–4355. doi: 10.1242/jcs.156620

Magenau, A., Owen, D. M., Yamamoto, Y., Tran, J., Kwiatek, J. M., Parton, R. G., et al. (2015). Discreet and distinct clustering of five model membrane proteins revealed by single molecule localization microscopy. *Mol. Membr. Biol.* 32, 11–18. doi: 10.3109/09687688.2014.990997

Mortensen, K. I., Churchman, L. S., Spudich, J. A., and Flyvbjerg, H. (2010). Optimized localization analysis for single-molecule tracking and super-resolution microscopy. *Nat. Methods* 7, 377–381. doi: 10.1038/nmeth.1447

Neyman, J., and Scott, E. L. (1952). A theory of the spatial distribution of galaxies. *Astrophys. J.* 116, 144. doi: 10.1086/145599

Owen, D. M., Williamson, D., Magenau, A., and Gaus, K. (2012). Optical techniques for imaging membrane domains in live cells (live-cell palm of protein clustering). *Meth. Enzymol.* 504, 221–235. doi: 10.1016/B978-0-12-391857-4.00011-2

Ripley, B. D. (1977). Modelling spatial patterns. *J. R. Stat. Soc. Ser. B* 39, 172–212.

Rossy, J., Owen, D. M., Williamson, D. J., Yang, Z., and Gaus, K. (2013). Conformational states of the kinase Lck regulate clustering in early T cell signaling. *Nat. Immunol.* 14, 82–89. doi: 10.1038/ni.2488

Rostovtsev, V. V., Green, L. G., Fokin, V. V., and Sharpless, K. B. (2002). A stepwise huisgen cycloaddition process: copper(I)-catalyzed regioselective "ligation" of azides and terminal alkynes. *Angew. Chem. Int. Ed Engl.* 41, 2596–2599. doi: 10.1002/1521-3773(20020715)41:14<2596:AID-ANIE2596>3.0.CO;2-4

Rust, M. J., Bates, M., and Zhuang, X. (2006). Sub-diffraction-limit imaging by stochastic optical reconstruction microscopy (STORM). *Nat. Methods* 3, 793–795. doi: 10.1038/nmeth929

Sage, D., Kirshner, H., Pengo, T., Stuurman, N., Min, J., Manley, S., et al. (2015). Quantitative evaluation of software packages for single-molecule localization microscopy. *Nat. Methods* 12, 717–724. doi: 10.1038/nmeth.3442

Saka, S. K., Honigmann, A., Eggeling, C., Hell, S. W., Lang, T., and Rizzoli, S. O. (2014). Multi-protein assemblies underlie the mesoscale organization of the plasma membrane. *Nat. Commun.* 5:4509. doi: 10.1038/ncomms5509

Sauer, M. (2013). Localization microscopy coming of age: from concepts to biological impact. *J. Cell Sci.* 126(Pt 16), 3505–3513. doi: 10.1242/jcs.123612

Saxon, E., and Bertozzi, C. R. (2000). Cell surface engineering by a modified Staudinger reaction. *Science* 287, 2007–2010. doi: 10.1126/science.287.5460.2007

Sengupta, P., Jovanovic-Talisman, T., and Lippincott-Schwartz, J. (2013). Quantifying spatial organization in point-localization superresolution images using pair correlation analysis. *Nat. Protoc.* 8, 345–354. doi: 10.1038/nprot.2013.005

Sengupta, P., Jovanovic-Talisman, T., Skoko, D., Renz, M., Veatch, S. L., and Lippincott-Schwartz, J. (2011). Probing protein heterogeneity in the plasma membrane using PALM and pair correlation analysis. *Nat. Methods* 8, 969–975. doi: 10.1038/nmeth.1704

Shannon, C. E. (1949). Communication in the Presence of Noise. *Proc. Inst. Radio Eng.* 37, 10–21. doi: 10.1109/jrproc.1949.232969

Sharonov, A., and Hochstrasser, R. M. (2007). Single-molecule imaging of the association of the cell-penetrating peptide Pep-1 to model membranes. *Biochemistry* 46, 7963–7972. doi: 10.1021/bi700505h

Sieber, J. J., Willig, K. I., Kutzner, C., Gerding-Reimers, C., Harke, B., Donnert, G., et al. (2007). Anatomy and dynamics of a supramolecular membrane protein cluster. *Science* 317, 1072–1076. doi: 10.1126/science.1141727

Singer, S. J., and Nicolson, G. L. (1972). The fluid mosaic model of the structure of cell membranes. *Science* 175, 720–731. doi: 10.1126/science.175.4023.720

Sletten, E. M., and Bertozzi, C. R. (2009). Bioorthogonal chemistry: fishing for selectivity in a sea of functionality. *Angew. Chem. Int. Ed Engl.* 48, 6974–6998. doi: 10.1002/anie.200900942

Tanaka, K. A., Suzuki, K. G., Shirai, Y. M., Shibutani, S. T., Miyahara, M. S., Tsuboi, H., et al. (2010). Membrane molecules mobile even after chemical fixation. *Nat. Methods* 7, 865–866. doi: 10.1038/nmeth.f.314

Thompson, R. E., Larson, D. R., and Webb, W. W. (2002). Precise nanometer localization analysis for individual fluorescent probes. *Biophys. J.* 82, 2775–2783. doi: 10.1016/S0006-3495(02)75618-X

Tokunaga, M., Imamoto, N., and Sakata-Sogawa, K. (2008). Highly inclined thin illumination enables clear single-molecule imaging in cells. *Nat. Methods* 5, 159–161. doi: 10.1038/nmeth1171

Tom Dieck, S., Müller, A., Nehring, A., Hinz, F. I., Bartnik, I., Schuman, E. M., et al. (2012). Metabolic labeling with noncanonical amino acids and visualization by chemoselective fluorescent tagging. *Curr. Protoc. Cell Biol.* 56, 7.11.1–7.11.29. doi: 10.1002/0471143030.cb0711s56

Tornøe, C. W., Christensen, C., and Meldal, M. (2002). Peptidotriazoles on solid phase: [1,2,3]-triazoles by regiospecific copper(i)-catalyzed 1,3-dipolar cycloadditions of terminal alkynes to azides. *J. Org. Chem.* 67, 3057–3064. doi: 10.1021/jo011148j

van de Linde, S., Löschberger, A., Klein, T., Heidbreder, M., Wolter, S., Heilemann, M., et al. (2011). Direct stochastic optical reconstruction microscopy with standard fluorescent probes. *Nat. Protoc.* 6, 991–1009. doi: 10.1038/nprot.2011.336

van de Linde, S., and Sauer, M. (2014). How to switch a fluorophore: from undesired blinking to controlled photoswitching. *Chem. Soc. Rev.* 43, 1076–1087. doi: 10.1039/C3CS60195A

van de Linde, S., Wolter, S., Heilemann, M., and Sauer, M. (2010). The effect of photoswitching kinetics and labeling densities on super-resolution fluorescence imaging. *J. Biotechnol.* 149, 260–266. doi: 10.1016/j.jbiotec.2010.02.010

Veatch, S. L., Machta, B. B., Shelby, S. A., Chiang, E. N., Holowka, D. A., and Baird, B. A. (2012). Correlation functions quantify super-resolution images and estimate apparent clustering due to over-counting. *PLoS ONE* 7:e31457. doi: 10.1371/journal.pone.0031457

Williamson, D. J., Owen, D. M., Rossy, J., Magenau, A., Wehrmann, M., Gooding, J. J., et al. (2011). Pre-existing clusters of the adaptor Lat do not participate in early T cell signaling events. *Nat. Immunol.* 12, 655–662. doi: 10.1038/ni.2049

Wolter, S., Endesfelder, U., van de Linde, S., Heilemann, M., and Sauer, M. (2011). Measuring localization performance of super-resolution algorithms on very active samples. *Opt. Express* 19, 7020–7033. doi: 10.1364/OE.19.007020

Wolter, S., Löschberger, A., Holm, T., Aufmkolk, S., Dabauvalle, M.-C., van de Linde, S., et al. (2012). Rapi*d*STORM: accurate, fast open-source software for localization microscopy. *Nat. Methods* 9, 1040–1041. doi: 10.1038/nmeth.2224

Wolter, S., Schüttpelz, , M., Tscherepanow, M., VAN DE Linde, S., Heilemann, M., and Sauer, M. (2010). Real-time computation of subdiffraction-resolution fluorescence images. *J. Microsci.* 237, 12–22. doi: 10.1111/j.1365-2818.2009.03287.x

Zhao, Z. W., Roy, R., Gebhardt, J. C., Suter, D. M., Chapman, A. R., and Xie, X. S. (2014). Spatial organization of RNA polymerase II inside a mammalian cell nucleus revealed by reflected light-sheet superresolution microscopy. *Proc. Natl. Acad. Sci. U.S.A.* 111, 681–686. doi: 10.1073/pnas.1318496111

Zhu, L., Zhang, W., Elnatan, D., and Huang, B. (2012). Faster STORM using compressed sensing. *Nat. Methods* 9, 721–723. doi: 10.1038/nmeth.1978

Conflict of Interest Statement: The authors declare that the research was conducted in the absence of any commercial or financial relationships that could be construed as a potential conflict of interest.

Manuscript 4

Nerreter, T.*, Letschert, S.*, Doose, S., Danhof, S., Einsele, H., Sauer, M., Hudecek, M.: CD19CART cells eliminate myeloma cells expressing very low levels of CD19 (**in submission**)

**authors equally contributed*

CD19CART cells eliminate myeloma cells that express very low levels of CD19

Thomas Nerreter[1a], Sebastian Letschert[2a], Sören Doose[2], Sophia Danhof[1], Hermann Einsele[1], Markus Sauer[2*] and Michael Hudecek[1*]

[1]Medizinische Klinik und Poliklinik II, Universitätsklinikum Würzburg, Würzburg, Germany

[2]Department of Biotechnology and Biophysics, Julius-Maximilians-Universität Würzburg, Würzburg, Germany

[a]These authors contributed equally to this work

[*]Corresponding authors: M.H. (Hudecek_M@ukw.de) & M.S. (m.sauer@uni-wuerzburg.de)

Word count (3.000): 2.700

Abstract (150): 158

Figures and tables (6): 5

References (40): 31

This manuscript contains a supplement

Category: Original article

Abstract:

Immunotherapy with chimeric antigen receptor (CAR)-engineered T-cells targeting CD19 (CD19CART) is being evaluated in multiple myeloma. A recent study reported complete remission in a patient that had received CD19CART even though only 0.05% of myeloma cells expressed CD19 by flow cytometry (FC). The mechanism for this response has remained unclear and sparked debate over low level CD19 expression on myeloma cells.

We generated CD19 expression profiles on myeloma cells from n=14 patients by single-molecule sensitive super-resolution microscopy (*d*STORM - *direct* stochastic optical reconstruction microscopy) and FC and treated myeloma cells with CD19CART *in vitro*.

In 10/14 patients, we detected CD19 on a fraction of myeloma cells (range: 10.3%-80%) by *d*STORM at very low levels below the FC detection limit. Treatment with CD19CART led to elimination of myeloma cells, even when CD19 was undetectable by FC. The threshold for CD19CART recognition was below 100 CD19 molecules per myeloma cell surpassing previous assumptions on the sensitivity of this novel treatment.

Introduction

Multiple myeloma (MM) is a hematologic malignancy with clonal proliferation of plasma cells that produce aberrant immunoglobulin. Despite aggressive treatment with polychemotherapy, myeloma remains incurable in the majority of patients[1]. Recently, Garfall *et al* reported the clinical efficacy of adoptive immunotherapy with gene-engineered T-cells expressing a chimeric antigen receptor (CAR) specific for the B-cell marker CD19 (CD19CART) in heavily pre-treated myeloma patients. They observed one complete and several partial responses in patients that were treated with CD19CART after myeloablative chemotherapy and autologous hematopoietic stem cell transplantation (HSCT)[2]. Notably, previous myeloablative chemotherapy and autologous HSCT had only induced a partial, transient response in the patient who achieved the complete response, and therefore, achievement of a complete response was attributed to the administration of CD19CART[2].

CD19CART therapy is approved as a potentially curative treatment for patients with relapsed/refractory B-cell acute lymphoblastic leukemia (ALL) and non-Hodgkin's lymphoma (NHL)[3-6]. In these diseases, CD19 is uniformly expressed on malignant cells, with an antigen density in the order of several thousands of molecules per cell[3, 4, 7], which is thought to be an optimal range for recognition by CD19CART. CD19 has thus far been considered a rarely and infrequently expressed target on myeloma cells[2, 8]. However, the positive outcome in some of the patients in the Garfall *et al* study has provided optimism that CD19 may also be exploited as a target for CART in MM. According to conventional detection by flow cytometry (FC), CD19 was only present on 0.05% of myeloma cells in the patient that achieved the complete response in the Garfall *et al* study, which has sparked controversy over the ability of FC to detect very low levels of CD19 that are presumed to be expressed on myeloma cells and that have been speculated to be sufficient for triggering CD19CART. At present, the role of CD19 as a therapeutic target in MM is uncertain and the antigen threshold on tumor cells required for CART recognition is debated controversially.

In previous work, we have demonstrated the capacity of *direct* stochastic optical reconstruction microscopy (*d*STORM) to determine absolute copy numbers of molecules on plasma membranes of human cells[9, 10]. This super-resolution microscopy method has single-molecule sensitivity[11, 12],

suggesting that this technique could be used to detect very low expression levels of CD19 on myeloma cells that would be otherwise undetectable by FC. Here, we hypothesized that CD19 may be expressed on a proportion of myeloma cells at a molecular density below the detection limit of FC but sufficient to trigger recognition by CD19CART. To test this, we used *d*STORM to generate expression profiles of CD19 on myeloma cells and assessed their recognition by CD19CART *in vitro*. We show that in a subset of myeloma patients, CD19 is expressed on a large fraction of myeloma cells at a very low antigen density that is below the detection limit of FC, and demonstrate that less than 100 CD19 molecules per myeloma cell trigger elimination by CD19CART.

Results

Patient characteristics and CD19-expression by FC

To generate expression profiles of CD19 on primary myeloma cells by FC and *d*STORM, we obtained bone marrow from 14 consecutive patients with MM that had measurable disease by histopathology. In this patient series, 4 patients had newly diagnosed myeloma, and 10 patients had been previously treated and were either in a state of partial remission (n=2) or had progressing disease (n=8) (Table S1). First, we performed FC to detect CD19 on myeloma cells (Figure S1). In two of the 14 patients (M012 and M016), we found a clearly distinguishable CD19-positive myeloma cell population, comprising 30.4% and 4.9% of cells, respectively (Figure 1a, b). In the remaining 12 patients, myeloma cells were either CD19-negative or contained only a minute population of myeloma cells (<3%) in which the signal obtained after staining for CD19 could not be clearly discriminated from background (Figure 1c, d; Figure S1; Table 1).

d*STORM is more sensitive than FC in detecting CD19 on myeloma cells*

We applied *d*STORM on the same samples of myeloma cells from the two patients who were CD19-positive by FC. Myeloma cells were identified by conventional fluorescence microscopy for positivity of CD38 and CD138 and CD19 was detected by *d*STORM (Figure 2a-f). In both patients, the percentage

of myeloma cells on which we detected CD19 by *d*STORM was higher compared to FC: in patient M012 68% (vs. 30.4% by FC); and in patient M016 32% (vs. 4.9% by FC) (Table 1). This discrepancy suggested that *d*STORM is more sensitive than FC in detecting CD19. To test this, we performed antibody titration experiments on the human leukemia cell line NALM-6, which is known to uniformly express CD19 (Figure S2). The results showed that the detection limit of our *d*STORM approach is 0.006 ± 0.002 CD19 molecules/μm^2, which corresponds approximately to 3.1 ± 1.3 CD19 molecules per cell for this model cell line. This value is at least 3-log-fold lower than the detection limit of FC (Figure S2; Table S2). Taken together, our data demonstrate that *d*STORM is more sensitive than FC in detecting CD19, and able to visualize CD19 molecules on tumor cells with single-molecule resolution.

Expression profile of CD19 on myeloma cells by* d*STORM

Based on the higher detection sensitivity of *d*STORM compared to FC, we hypothesized that, in addition to $CD19^{high}$ myeloma cells that are detected by FC, there is an as-yet undetected population of $CD19^{low}$ myeloma cells that is invisible to FC. To test this, we attempted flow cytometry-based cell sorting to separate CD19-positive and CD19-negative myeloma cells but found that the number of cells that survived this procedure was insufficient to perform subsequent *d*STORM-analyses. Therefore, we generated CD19 density plots based on the *d*STORM data obtained from myeloma cells of patient M012 (examples shown in Figure S3a,e). A schematic density plot and classification is provided in Figure S4. The plot showed a clear segregation into CD19-positive and CD19-negative myeloma cells as anticipated (Figure 3a). The average density of CD19 on all CD19-positive myeloma cells from patient M012 was 1,200 ± 580 molecules per cell (Table 1). We reasoned that FC had only detected myeloma cells with the highest CD19-expression and quantified CD19 molecules from cells in the top 30.4% of the density plot (which was the percentage of CD19-positive myeloma cells by FC). We found that the average number of CD19 molecules on these $CD19^{high}$ myeloma cells was 2,240 ± 260 molecules per cell compared with 750 ± 60 molecules in the remaining, $CD19^{low}$ myeloma cells. (Figure 3a, Table 1). The cut-off value separating $CD19^{high}$ and $CD19^{low}$ myeloma cells at the 30.4^{th} percentile of the density plot was 1,350 CD19 molecules per cell. We obtained similar data for patient M016 (Figure 3b, Figure

S3b,f). Collectively, these data show that single-molecule sensitive fluorescence imaging by *d*STORM detects CD19^{low} myeloma cells that express less than 1,350 CD19 molecules per cell and are not detectable by FC.

d*STORM detects CD19^{low} myeloma cells in patients that are classified as CD19-negative by FC*

Next, we examined CD19-expression by *d*STORM on myeloma cells from the 12 patients who were classified as CD19-negative by FC. We detected CD19-positive myeloma cells in 8 out of these 12 patients by *d*STORM (Figure 4, Figure S5, Figure S6) and determined that they comprised between 10.3 and 80.3% of the entire myeloma cell population (mean: 55 ± 9%, Figure 4a, Table 1). In five of these 8 patients, myeloma cells were exclusively CD19^{low}. In three of these 8 patients, we also detected a proportion of myeloma cells with CD19^{high} expression (mean: 29 ± 10%) (Table 1, Figure S5). In the remaining four patients, we detected only CD19-negative myeloma cells by *d*STORM. Taken together, our data show that CD19 is expressed at low levels on a substantial proportion of myeloma cells in a significant number of patients that are falsely classified as CD19-negative by FC.

CD19^{low} (and CD19^{high}) myeloma cells are eliminated by CD19CART

To investigate whether CD19-expression on CD19^{high} and CD19^{low} myeloma cells is sufficient for CART recognition, we treated them with CD19CART for 4 hours *in vitro* and then repeated the *d*STORM-analysis. In all patients that contained CD19^{high} and CD19^{low} myeloma cells, we found that CD19-expressing myeloma cells detected by *d*STORM were completely eliminated and only CD19-negative myeloma cells were present after the treatment (Figure 3, Figure S5). Control T-cells derived from the same donor and not equipped with the CD19CAR did not confer any relevant reactivity against CD19^{high} and CD19^{low} myeloma cells (Figure 3, Figure S5). The complete elimination of CD19^{low} myeloma cells indicated that CD19CART required an antigen density of less than 100 CD19 molecules to recognize and eliminate a myeloma cell. To exclude the potential that elimination of CD19^{low} myeloma cells had occurred due to bystander killing (i.e. due to cytolytic granules released from CD19CART after being triggered by CD19^{high} myeloma cells), we repeated the CD19CART treatment

assay with myeloma cells that were exclusively CD19^{low}. In all patients, we found, that CD19CART eliminated CD19^{low} myeloma cells, including CD19^{low} myeloma cells from patients M017 and M013, that expressed on average 64 ± 8 and 93 ± 10 CD19 molecules per cell, respectively (Figure S5, Figure S6). Collectively, these data demonstrate that CD19CART are capable of rapidly eliminating myeloma cells that express very low levels of CD19. Further, the data demonstrate that the antigen threshold required for triggering CD19CART is well below 100 CD19 molecules per target cell.

IFNγ-secretion by CD19CART does not predict the presence of CD19^{low} myeloma cells

We sought to determine whether intracellular staining for IFNγ production in CD19CART after co-culture with myeloma cells could be used as a simple surrogate assay to test for the presence of CD19^{low} myeloma cells instead of super-resolution microscopy. However, the IFNγ assay worked in only two of the ten patients that we had shown to contain CD19-positive myeloma cells by FC and *d*STORM (Figure S7). These data suggest that the antigen threshold required for inducing cytokine production in CD19CART is higher compared to the threshold required for inducing cytolytic activity, consistent with prior data on triggering distinct T-cell effector functions[13]. In summary, these data show that conventional detection (FC) and analytical methods (IFNγ secretion assay) are not sensitive enough to reveal very low level CD19 expression on myeloma cells.

Discussion

CD19 is pursued as a target for CART immunotherapy in MM. A recent study by Garfall *et al* reported complete remission in a myeloma patient who received CD19CART after myeloablative chemotherapy and autologous HSCT, even though only 0.05% of myeloma cells were CD19-positive as assessed by FC and qt-RT[2]. The discrepancy of the latter to our findings may be related to the reference genes used for normalization as it is known that individually validated reference genes for every tissue and experimental condition are a crucial prerequisite for valid interpretation of sequencing data that can be otherwise over- or underestimated.[14] Therefore, also the cell population classified as CD19-negative by qPCR in this specific assay could in fact potentially contain CD19dim cells that could have been visualized using dSTORM microscopy. Given the patient outcomes, Garfall *et al* speculated that CD19 may be expressed on a higher proportion of myeloma cells than had been identified by FC in their study, including myeloma cells that express CD19 at very low levels, which may, however, be sufficient for recognition by CD19CART[2, 15, 16]. An obstacle to testing this hypothesis was the relatively high detection limit of FC, the prevailing detection method in clinical routine, with a detection limit in the order of few a thousands of molecules per cell[7,17, 18]. In addition, the precise antigen threshold on tumor cells required to trigger and subsequently activate CART has thus far been unknown. Several studies have attempted to extrapolate the lower detection limit of CARTs with model cell lines, providing estimates in the range of hundreds of target molecules per cell[13, 19]. However, these estimates have not been rigorously verified owing again to the lacking ability of FC to detect such low antigen levels on target cells. Here, we applied single-molecule sensitive super-resolution microscopy by *d*STORM and show that in 10 out of 14 myeloma patients, CD19 is expressed on a considerable fraction of myeloma cells comprising up to 80% of the entire myeloma cell population. However, on the majority of myeloma cells, the expression level of CD19 is below the detection limit of FC and could only be visualized by *d*STORM. We also show that very low level expression of CD19 is sufficient for recognition and elimination by CD19CART and establish that the sensitivity threshold of CD19CART is well below 100 CD19 molecules per myeloma cell.

Our data show that FC dramatically underestimates the percentage of myeloma cells that express CD19 and falsely classifies myeloma cells in 8 out of 10 patients as CD19-negative, even though CD19 is

expressed on a fraction of myeloma cells at low levels as revealed by *d*STORM imaging. Our data suggest that myeloma cells that express less than 1,350 CD19 molecules are not detected by FC, which is consistent with previous reports on the sensitivity of this method in clinical routine[13, 17-19]. We show that in each of the 10 myeloma patients, where we detected a proportion of CD19-expressing myeloma cells (either at high or low density), they were readily eliminated after a short treatment with CD19CART *in vitro*. These data suggest that CD19CART could be effective against CD19-expressing myeloma cells *in vivo*, even though functionality in vitro does not necessarily imply a one-to-one comparable function in vivo as factors like receptor affinity [20, 21], the tumor microenvironment, antigen-loss and other factors do influence the therapeutic outcome [22]. The CD19CAR employed in our study has been validated in clinical trials in ALL and NHL[3, 4]. However, our data also show that in each of the 10 patients, there was a fraction of CD19-negative myeloma cells that were not eliminated by CD19CART. These data suggest that complete responses of MM after CD19CART therapy may only be accomplished in conjunction with another effective antimyeloma treatment, e.g. melphalan (140 mg per square meter) as in the Garfall *et al* study. Indeed, recent studies with CD19CART in ALL and with B-cell maturation antigen (BCMA)-CART in myeloma have shown that the presence of antigen-negative leukemia or myeloma cells leads to outgrowth of these cells and rapid relapse[23, 24].

CARs are synthetic receptors and even though CD19CART have accomplished clinical approval in ALL and NHL, their mechanism of action is still a black box at the molecular level. A particular interest has been to determine the antigen sensitivity of CART, both for predicting efficacy and for assessing safety. Here, we provide for the first time direct evidence that CD19CART are able to recognize and eliminate myeloma cells that express less than 100 CD19 molecules on their surface. These data establish the sensitivity threshold for CART-cells and surpass predictions that have been made in previous studies with model tumor cell lines[13, 19], but were limited by the inability of FC to enumerate antigens with single-molecule resolution. Our data support the prior notion that CART are more sensitive than conventional antibodies and bi-specific antibodies in detecting surface molecules on tumor cells[13]. Further, our study illustrates the challenge that CART are more sensitive in detecting antigens on tumor cells than established analytical tools in clinical practice. Consequently, more sensitive detection methods than FC (and immunohistochemistry) need to be implemented into clinical routine in order to

guide patient and antigen selection for CART therapy, and to detect low-level expression in healthy tissues to prevent toxicity. Efforts to implement *d*STORM-analysis into clinical pathology are ongoing at our institution.

In summary, our data encourage the continued evaluation of CD19 as a target for CART in MM. We show that single-molecule sensitive super-resolution imaging methods such as *d*STORM can aid in stratifying patients according to CD19-expression to identify myeloma patients who have the highest chance to benefit from this novel, highly innovative treatment. These insights are relevant not only for CD19CART in MM, but also for CART approaches targeting alternative antigens in other hematologic and solid tumor malignancies to exploit their full therapeutic potential and to ensure patient safety.

Online Methods

Human subjects

Bone marrow aspirates were obtained from patients with multiple myeloma, and T-cells for CAR-modification were isolated from the peripheral blood of healthy donors. All participants provided written informed consent to participate in research protocols approved by the institutional review board of the University of Würzburg.

Primary myeloma cells

Freshly aspirated bone marrow was diluted 1:10 in phosphate-buffered saline (PBS), and leukocytes were isolated using Ficoll-hypaque density centrifugation in 50 mL LeukoSep tubes (Greiner Bio One, Frickenhausen, Germany). $CD138^+$ myeloma cells were isolated using positive selection with CD138-MicroBeads (Miltenyi, Bergisch-Gladbach, Germany) and used for functional assays next-day.

Cell lines and cell culture media

NALM-6 (DSMZ, Heidelberg, Germany), MM.1S and K562 (both ATCC, Manassas, VA, USA) cells were maintained in RPMI-1640 medium containing 8% fetal calf serum (FCS), 2 mM L-glutamine, and 100 U/mL penicillin/streptomycin (all components from Gibco, Thermo Scientific, Schwerte,

Germany). K562_CD19 cells were generated by lentiviral transduction with human *CD19*. Primary myeloma cells and T-cells were maintained in RPMI-1640 medium containing 8% human serum, 2 mM Glutamax, 0,1% β-mercaptoethanol and 100 U/mL penicillin/streptomycin (T-cell medium; all other components from Gibco). T-cell cultures were supplemented with 50 U/ml IL-2 (Proleukin, Novartis, Basel, Switzerland).

Generation of CD19CART

The vector design and experimental procedure has been described in a previous study[25]. In brief, peripheral blood mononuclear cells (PBMCs) of healthy donors were purified using Ficoll-hypaque density centrifugation in 50 mL LeukoSep tubes (Greiner Bio One), and $CD8^+$ T-cells were isolated using negative magnetic sorting ($CD8^+$ T-cell Isolation Kit, human, Miltenyi). T-cells were stimulated with anti-CD3/CD28 magnetic beads (Dynabeads® Human T-Activator CD3/CD28, ThermoScientific) and transduced with an epHIV7 lentivirus encoding a CAR construct comprising the following: an anti-CD19 single chain variable fragment derived from FMC63; an IgG4-Fc hinge spacer; a CD28 transmembrane region; a 4-1BB_CD3ζ signaling module; and a truncated epidermal growth factor receptor (EGFR) transduction marker[26]. T-cells were enriched for $EGFRt^+$ using the biotinylated anti-EGFR monoclonal antibody (mAb) Cetuximab (Merck, Darmstadt, Germany) and anti-Biotin Microbeads (Miltenyi). Purified CD19CART and non-transduced control T-cells were expanded with irradiated $CD19^+$ feeder cells as previously described[27] and stored in aliquots in liquid nitrogen until functional testing.

Antibodies and flow cytometry

Antibodies against CD19 (clone HIB19, AF647), CD38 (clone HIT2, AF488), CD138 (clone MI15, PE and unconjugated) from BioLegend (London, United Kingdom); IFN-γ (clone B27, FITC) from BD Biosciences (Heidelberg, Germany), and CD8 (clone BW135/80, VioBlue) from Miltenyi as well as 7-AAD to exclude dead cells from analysis were used. For *d*STORM-microscopy, an anti-CD138 antibody was conjugated to AF555 (ThermoFisher Scientific). Flow analyses were performed with a FACS Canto II (BD) machine and analyzed using FlowJo software (TreeStar, Ashland, OR).

Experimental procedures

CD19CART and non-transduced control T-cells were thawed, washed and maintained overnight in T-cell medium with low-dose IL-2 (10 IU/mL). Then, $1x10^5$ T-cells were co-cultured with 2.5×10^4 primary myeloma cells or control tumor cell lines for 4 h in 96-well round-bottom plates in the absence (for microscopy measurements) or presence of GolgiStop™ (BD). GolgiStop™-treated cells were permeabilized using the Cytofix/Cytoperm Kit (BD) and stained for intracellular IFN-γ. For flow cytometric analysis of CD19 expression, untouched primary myeloma cells were washed and stained with anti-CD38-AF488, anti-CD138-PE and anti-CD19-AF647 or AF647 isotype control according to the manufacturer's instructions and subsequently washed and analyzed. For microscopy measurements, LabTek chamber slides (Nunc™ Lab-Tek™ II Chamber Slide™ System, ThermoFisher Scientific) were coated with poly-D-lysine and primary myeloma cells (or cell lines / co-cultures) and allowed to adhere for 90 min at 37°C. Afterwards, cells were washed with PBS and stained with anti-CD38-AF488, anti-CD138-AF555 and anti-CD19-AF647 or AF647 isotype control. Cells were washed and fixed with 4% paraformaldehyde and used for *d*STORM-analyses.

Super-resolution imaging

For reversible photoswitching of Alexa Fluor 647, a PBS-based imaging buffer (pH 7.4) was used that contained 80 mM β-mercaptoethylamine (Sigma-Aldrich, Taufkirchen, Germany) and an oxygen scavenger system containing 3% (w/v) glucose, 4 U/mL glucose oxidase and 80 U/mL catalase. *d*STORM measurements were performed as previously described[11, 12]. We used an Olympus IX-71 inverted microscope (Olympus, Hamburg, Germany) equipped with an oil-immersion objective (APON 60XOTIRF, Olympus) and a nosepiece stage (IX2-NPS, Olympus). AF647, AF555 and AF488 were excited with the appropriate laser systems (Genesis MX 639 and MX 561 from Coherent, Göttingen, Germany; iBeam smart 488 nm, Toptica, Gräfelfing, Germany). The excitation light was spectrally cleaned by appropriate bandpass filters and then focused onto the backfocal plane of the objective. To switch between different illumination modes (epi and TIRF illumination), the lens system and mirror were arranged on a linear translation stage. A polychromatic mirror (HC 410/504/582/669, Semrock,

Rochester, NY, USA) was used to separate excitation (laser) and emitted (fluorescent) light. The fluorescence emission was collected by the same objective and transmitted by the dichroic beam splitter and several detection filters (HC 440/521/607/700, Semrock; HC 679/41, Semrock, for Alexa 647; HQ 610/75, Chroma (Bellows Falls, VT, USA), for Alexa 555; ET 525/50, Chroma, for Alexa 488), before being projected onto two electron-multiplying CCD cameras (both iXon Ultra 897, Andor, Belfast, UK; beam splitter 635 LP, Semrock). A final pixel size of 128 nm was generated by placing additional lenses in the detection path. Excitation intensity was approximately 3.3 kW/cm^2. Typically, 15,000 frames were recorded with a frame rate of ~67 Hz (15 ms exposure time).

Image reconstruction and data analysis

From the recorded image stack, a table with all localizations as well as a reconstructed *d*STORM image was generated using the single-molecule localization software rapidSTORM 3.3[28]. Only CD38/CD138 double-positive cells (i.e., myeloma cells) were further analyzed for CD19 expression. Quantification of CD19 was performed with a custom-written Mathematica (Wolfram Research, Inc., Mathematica, Version 11.2, Champaign, IL, USA) script. The analysis routine included the following steps: fluorescent spots containing less than 800 photons per frame were discarded. Repeated localizations coming from one antibody were grouped using an alpha-shape algorithm with an alpha value of 30. It was confirmed that the overall density of detected antibodies was small enough to yield well-separated alpha-shapes. Antibody densities (CD19 or isotype) were calculated from the number of grouped localizations divided by the area of the bottom plasma membrane of each cell, as determined with a region of interest (ROI)-selector. A total of 10–80 cells per patient and condition were analyzed to obtain CD19 and isotype antibody density distributions. To distinguish between non-specific (negative subpopulation) and specific (positive subpopulation) binding of CD19 antibodies, detected antibody density distributions were fitted to a one- or two-component log-normal distribution. Relative contributions of non-specifically and specifically bound antibodies were estimated, together with the average density (localizations μm^{-2}) of specifically bound antibodies. The significance of all distribution estimates was statistically tested using an Anderson-Darling test (rejected for p-values < 0.05).

Acknowledgements

This work was supported by the project “Center for Personalized Molecular Immunotherapy” funded within the EFRE-program of the European Union (Europäischer Fond für regionale Entwicklung); a grant from the German Ministry for Science and Education (BMBF, Bundesministerium für Bildung und Forschung, Grant # 13N14414); and a grant within the Max Eder Program of German Cancer Aid (Deutsche Krebshilfe e.V., Grant number 110313 to M.H.). M.H. is a member of the Young Scholar Program (Junges Kolleg) and Extraordinary Member of the Bavarian Academy of Sciences (Bayerische Akademie der Wissenschaften).

Author contributions

T.N. and S.L. designed and performed experiments, analyzed data and wrote the manuscript. S.Do. designed experiments and analyzed data. S.Da. provided biological material and analyzed data. H.E. designed experiments, analyzed data, and wrote the manuscript. M.H. and M.S. designed experiments, analyzed data, wrote the manuscript and supervised the project.

Competing interests

M.H. is co-inventor on patents related to CAR technologies that have been filed by the University of Würzburg, Würzburg, Germany, and the Fred Hutchinson Cancer Research Center, Seattle, WA and licensed by JUNO Therapeutics Inc. (Seattle, WA). M.S. is co-inventor on patents related to *d*STORM.

References

1. Kumar, S.K. et al. Continued improvement in survival in multiple myeloma: changes in early mortality and outcomes in older patients. *Leukemia* **28**, 1122-1128 (2014).
2. Garfall, A.L. et al. Chimeric Antigen Receptor T Cells against CD19 for Multiple Myeloma. *The New England journal of medicine* **373**, 1040-1047 (2015).
3. Turtle, C.J. et al. Immunotherapy of non-Hodgkin's lymphoma with a defined ratio of CD8+ and CD4+ CD19-specific chimeric antigen receptor-modified T cells. *Science translational medicine* **8**, 355ra116 (2016).
4. Turtle, C.J. et al. CD19 CAR-T cells of defined CD4+:CD8+ composition in adult B cell ALL patients. *J Clin Invest* **126**, 2123-2138 (2016).
5. Bach, P.B., Giralt, S.A. & Saltz, L.B. FDA Approval of Tisagenlecleucel: Promise and Complexities of a $475000 Cancer Drug. *JAMA : the journal of the American Medical Association* (2017).
6. Roberts, Z.J., Better, M., Bot, A., Roberts, M.R. & Ribas, A. Axicabtagene ciloleucel, a first-in-class CAR T cell therapy for aggressive NHL. *Leukemia & lymphoma*, 1-12 (2017).
7. Uckun, F.M., Qazi, S., Dibirdik, I. & Myers, D.E. Rational design of an immunoconjugate for selective knock-down of leukemia-specific E2A-PBX1 fusion gene expression in human Pre-B leukemia. *Integr Biol (Camb)* **5**, 122-132 (2013).
8. Tembhare, P.R. et al. Flow cytometric differentiation of abnormal and normal plasma cells in the bone marrow in patients with multiple myeloma and its precursor diseases. *Leukemia research* **38**, 371-376 (2014).
9. Ehmann, N. et al. Quantitative super-resolution imaging of Bruchpilot distinguishes active zone states. *Nat Commun* **5**, 4650 (2014).
10. Letschert, S. et al. Super-resolution imaging of plasma membrane glycans. *Angewandte Chemie* **53**, 10921-10924 (2014).
11. Heilemann, M. et al. Subdiffraction-resolution fluorescence imaging with conventional fluorescent probes. *Angewandte Chemie* **47**, 6172-6176 (2008).
12. van de Linde, S. et al. Direct stochastic optical reconstruction microscopy with standard fluorescent probes. *Nature protocols* **6**, 991-1009 (2011).
13. Stone, J.D., Aggen, D.H., Schietinger, A., Schreiber, H. & Kranz, D.M. A sensitivity scale for targeting T cells with chimeric antigen receptors (CARs) and bispecific T-cell Engagers (BiTEs). *Oncoimmunology* **1**, 863-873 (2012).
14. Kirschneck, C. et al. Valid gene expression normalization by RT-qPCR in studies on hPDL fibroblasts with focus on orthodontic tooth movement and periodontitis. *Sci Rep* **7**, 14751 (2017).
15. Hajek, R., Okubote, S.A. & Svachova, H. Myeloma stem cell concepts, heterogeneity and plasticity of multiple myeloma. *British journal of haematology* **163**, 551-564 (2013).
16. Paiva, B. et al. Differentiation stage of myeloma plasma cells: biological and clinical significance. *Leukemia* (2016).
17. Zola, H. High-sensitivity immunofluorescence/flow cytometry: detection of cytokine receptors and other low-abundance membrane molecules, Vol. Chapter 6. (2004).
18. Truneh, A. & Machy, P. Detection of very low receptor numbers on cells by flow cytometry using a sensitive staining method. *Cytometry* **8**, 562-567 (1987).
19. Watanabe, K. et al. Target antigen density governs the efficacy of anti-CD20-CD28-CD3 zeta chimeric antigen receptor-modified effector CD8+ T cells. *Journal of immunology* **194**, 911-920 (2015).

20. Liu, X. et al. Affinity-Tuned ErbB2 or EGFR Chimeric Antigen Receptor T Cells Exhibit an Increased Therapeutic Index against Tumors in Mice. *Cancer research* **75**, 3596-3607 (2015).
21. Hudecek, M. et al. Receptor affinity and extracellular domain modifications affect tumor recognition by ROR1-specific chimeric antigen receptor T cells. *Clinical cancer research : an official journal of the American Association for Cancer Research* **19**, 3153-3164 (2013).
22. Rotolo, A., Karadimitris, A. & Ruella, M. Building upon the success of CART19: chimeric antigen receptor T cells for hematologic malignancies. *Leukemia & lymphoma*, 1-16 (2017).
23. Ali, S.A. et al. T cells expressing an anti-B-cell maturation antigen chimeric antigen receptor cause remissions of multiple myeloma. *Blood* **128**, 1688-1700 (2016).
24. Ruella, M. & Maus, M.V. Catch me if you can: Leukemia Escape after CD19-Directed T Cell Immunotherapies. *Comput Struct Biotechnol J* **14**, 357-362 (2016).
25. Sommermeyer, D. et al. Chimeric antigen receptor-modified T cells derived from defined CD8(+) and CD4(+) subsets confer superior antitumor reactivity in vivo. *Leukemia* **30**, 492-500 (2016).
28. Wolter, S. et al. rapidSTORM: accurate, fast open-source software for localization microscopy. *Nat Methods* **9**, 1040-1041 (2012).

Supplementary references

26. Wang, X. et al. A transgene-encoded cell surface polypeptide for selection, in vivo tracking, and ablation of engineered cells. *Blood* **118**, 1255-1263 (2011).
27. Terakura, S. et al. Generation of CD19-chimeric antigen receptor modified CD8+ T cells derived from virus-specific central memory T cells. *Blood* **119**, 72-82 (2012).
29. Durie, B.G. & Salmon, S.E. A clinical staging system for multiple myeloma. Correlation of measured myeloma cell mass with presenting clinical features, response to treatment, and survival. *Cancer* **36**, 842-854 (1975).
30. Chng, W.J. et al. IMWG consensus on risk stratification in multiple myeloma. *Leukemia* **28**, 269-277 (2014).
31. Kumar, S. et al. International Myeloma Working Group consensus criteria for response and minimal residual disease assessment in multiple myeloma. *Lancet Oncol* **17**, e328-e346 (2016).

Figure Legends

Figure 1. Detection of CD19 on myeloma cells by flow cytometry. Flow cytometric analysis of CD19-expression on primary myeloma cells purified from bone marrow aspirates. Gating strategy for dot plots shown in a-d: FSC/SSC plasma cell gate → 7-AAD$^-$ → CD138$^+$/CD38$^+$. **a-d** show exemplary patients where myeloma cells comprised a CD19-positive fraction by FC (**a**, patient M012 & **b**, patient M016), or were CD19-negative or ambiguous (**c**, patient M019 & **d**, patient M022). Data for all patients are shown in Table 1 and Figure S1.

Figure 2. Detection of CD19 on multiple myeloma cells using *d*STORM.

Myeloma cells were identified by transmitted light microscopy (**a**) and expression of CD138 (**b**) and CD38 (**c**) as detected by conventional wide-field fluorescence microscopy. CD19 was detected on primary myeloma cells using conventional wide-field fluorescence (**d**) and *d*STORM (**e,f**). Images depict CD19 molecules in the bottom plasma membrane (attached to glass surface) of a CD19$^+$ (top row) and a CD19$^-$ myeloma cell (bottom row). Small panels (**f**) display magnification of boxed regions revealing the markedly enhanced sensitivity of *d*STORM. Scale bars, 3 µm (**d**, **e**) and 0.4 µm (**f**).

Figure 3. *d*STORM analysis of CD19-expression on myeloma cells before and after treatment with CD19CART. Expression profiles for CD19 on myeloma cells from patient M012 (**a**), M016 (**b**), M019 (**c**) and M022 (**d**) generated by *d*STORM. Far left and left column: Distribution plots showing the relative CD19 density obtained after staining with isotype control (far left column) and anti-CD19 antibody (left column) on myeloma cells before treatment with CD19CART. Densities are provided as logarithmic numbers of molecules per µm^2. Density plots were divided into CD19-positive and CD19-negative subpopulations (corresponding to CD19-positive and CD19-negative myeloma cells, respectively). The latter group was defined by the density distribution pattern of the isotype control antibody (non-specific binding to plasma cell membrane and glass surface). Density plots were fitted with a one or two log-normal function that was dependent on the fit-accuracy calculated with an Anderson-Darling test (rejected at a p-value < 0.05). For each patient, the percentage of myeloma cells that had been determined to be CD19-positive by flow cytometry is provided for comparison (red

segments). Right and far right column: Distribution plots showing the relative CD19 density obtained after staining with anti-CD19 antibody on myeloma cells after treatment with CD19CART (right column) or untransduced control T cells (far right column). Data for all patients are shown in Table 1 and Figure S5.

Figure 4: Frequency of CD19-expressing myeloma cells and average density of CD19 quantified by *d*STORM. (**a**) Distribution of $CD19^+$ (dark grey) and $CD19^-$ (light grey) myeloma cells as assessed by *d*STORM imaging in n=10 CD19-positive myeloma patients, and one CD19-negative patient (M014) for comparison. (**b**) Mean CD19 molecule density on $CD19^+$ myeloma cell in molecules per μm^2.

Table 1 – Summary of data obtained by *d*STORM and flow cytometry

Patients		**Flow Cytometry**	***d*STORM**						
#	**Identifier**	**Δ% CD19$^+$** (% anti-CD19- % isotype)	**% CD19$^+$**	**No of CD19$^+$ cells analyzed**	**CD19 molecules/cell***			**Elimination by CD19CART**	**% IFNγ producing CD19CART**
					CD19$^+$ (range)	**CD19^{low}**	**CD19^{high}**		
1	**M007**	**0** (0.1-0.1)	**0**	-	**N/A**	N/A	N/A	N/A	0
2	**M008**	**0** (1.2-0.9)	**69.2**	65	**110** (22–340)	110	0	+	**4.9**
3	**M011**	**(s)** (0.8-0.6)	**0**	-	**N/A**	N/A	N/A	N/A	0
4	**M012**	**29** (30.4-1.6)	**67.6**	34	**1,200** (250–3,700)	750	2,240 (30%)	**+**	**8.9**
5	**M013**	**0.9** (1.2-0.3)	**75.1**	45	**93** (19–290)	93	0	+	0.3
6	**M014**	**1.7** (4.0-2.3)	**0**	-	**N/A**	N/A	N/A	N/A	0
7	**M015**	**(s)** (1.1-1.3)	**0**	-	**N/A**	N/A	N/A	N/A	0
8	**M016**	**3.7** (4.9-1.2)	**32.1**	31	**530** (110–1,650)	470	1,850 (4%)	+	1.2
9	**M017**	**0** (0.7-1.4)	**66.0**	20	**64** (13–200)	64	0	+	0.8

10	**M018**	**0** (0.4-1.7)	**60.4**	33	**270** (55–830)	270	0	+	0
11	**M019**	**0** (1.9-2.3)	**80.3**	25	**140** (28–420)	140	0	+	0.4
12	**M020**	**2.4** (5.7-2.3)	**46.0**	36	**950** (200–3,000)	680	2,090 (19%)	+	ndt
13	**M021**	**1.3** (3.1-1.8)	**30.2**	38	**630** (130–2,000)	530	1,900 (7%)	+	0
14	**M022**	**0.8** (1.5-0.7)	**10.3**	80	**1,600** (330–5,000)	830	2,500 (47%)	+	0

(s): single events

ndt: cytokine production was not assessed for patient M020

(*) Mean values are indicated in bold. In brackets: Calculated data ranging from small (median−2σ) to high (median+2σ) values (95.45% of all values lie within this range). $CD19^+$ cells with more than 1,350 molecules per cell were classified as $CD19^{high}$ and were otherwise classified as $CD19^{low}$ (simulated data). Δ % $CD19^+$: the percentage of the cells in the $CD19^+$ gate for the isotype control was subtracted from the percentage of cells in the $CD19^+$ gate for the respective CD19 staining.

Figure 1

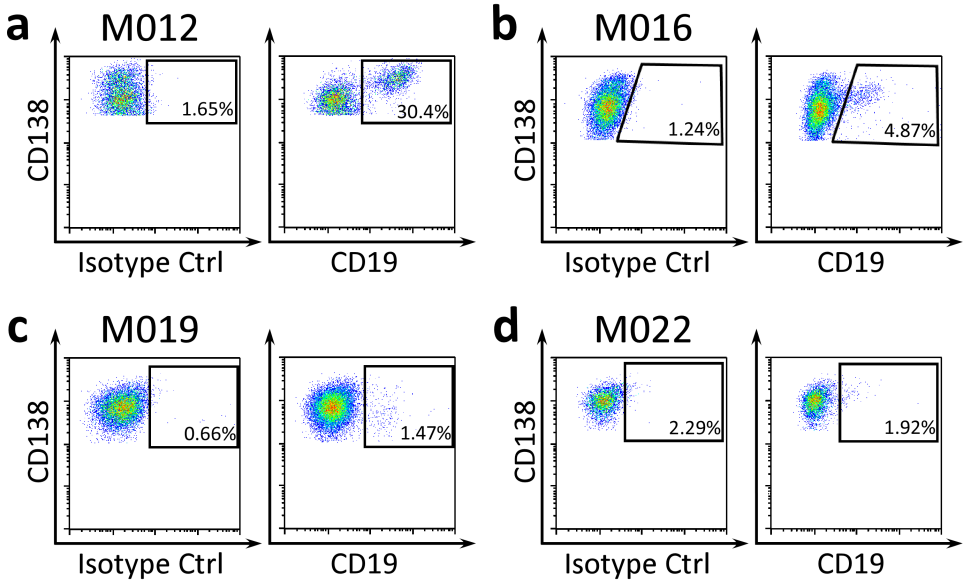

Figure 2

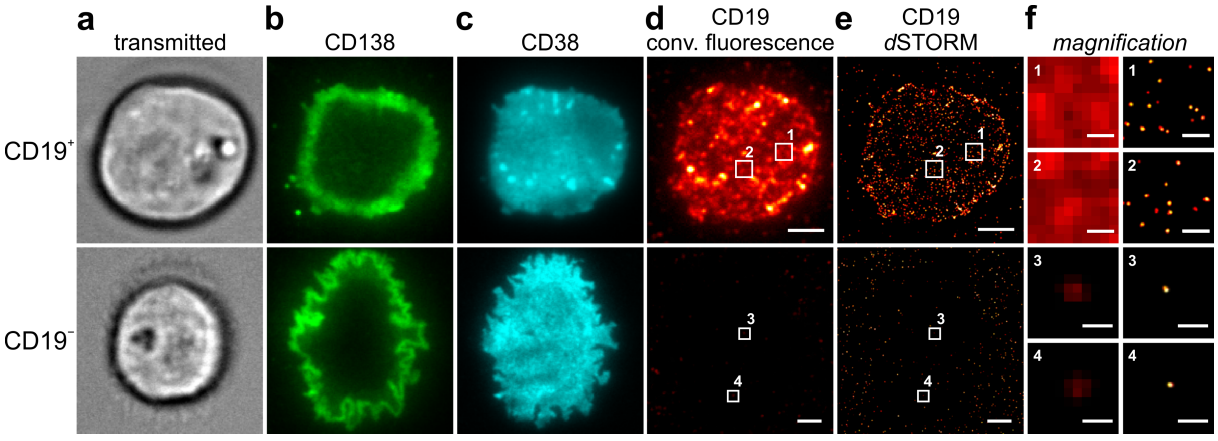

Figure 3

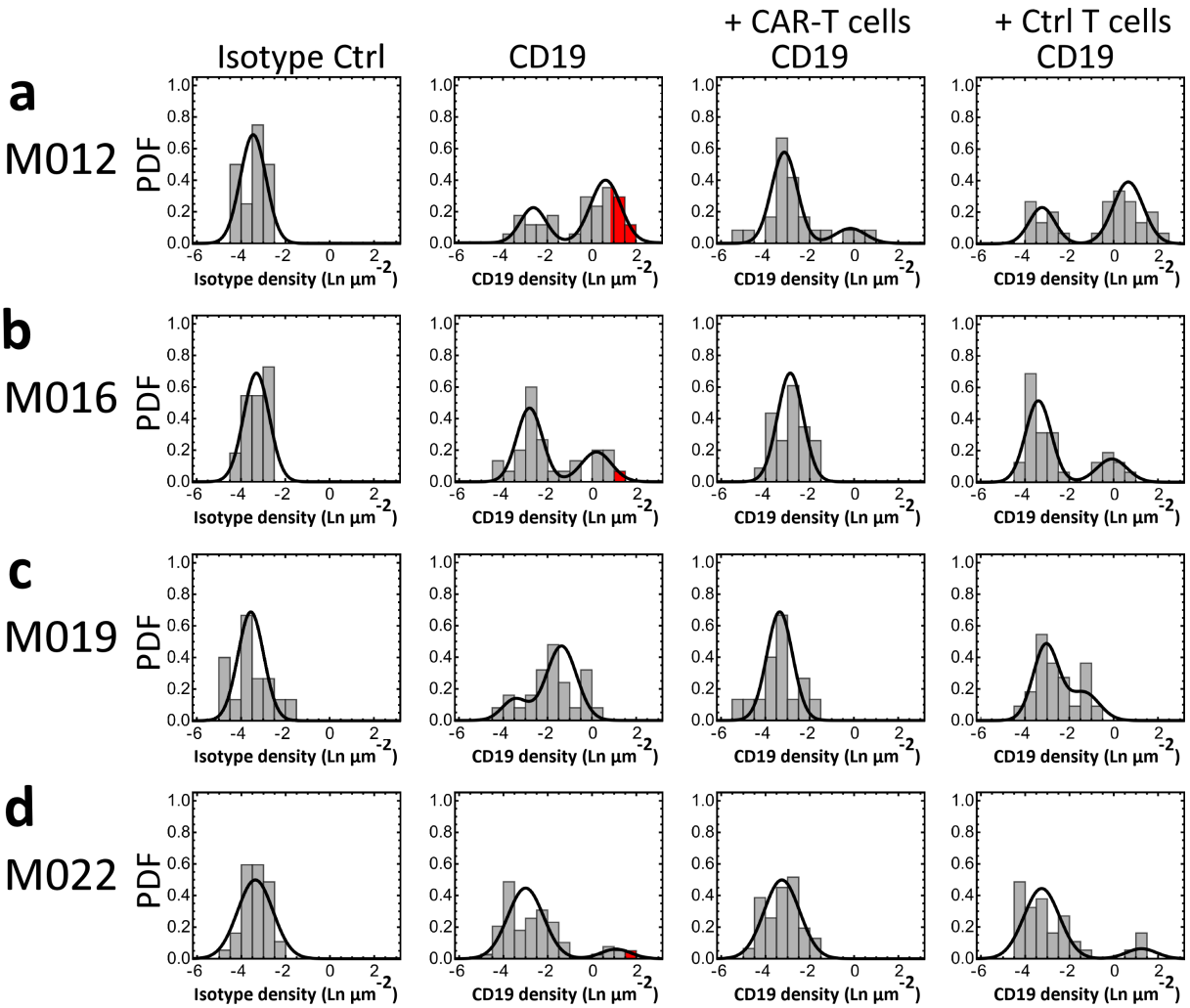
Isotype Ctrl
CD19
+ CAR-T cells CD19
+ Ctrl T cells CD19
a
M012
b
M016
c
M019
d
M022
PDF
Isotype density (Ln µm-2)
CD19 density (Ln µm-2)

Figure 4

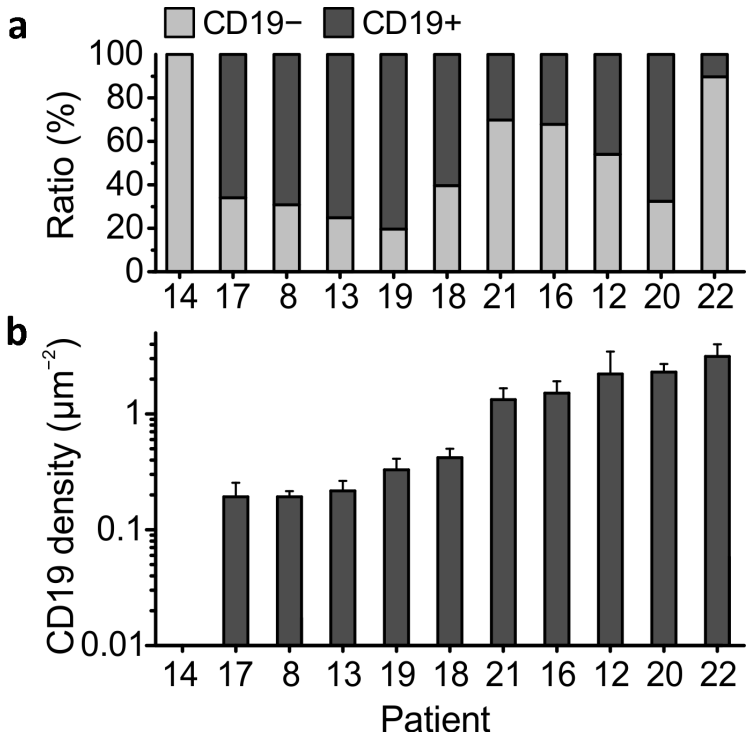
a
CD19−
CD19+
Ratio (%)
100
80
60
40
20
0
14 17 8 13 19 18 21 16 12 20 22
b
CD19 density (μm^{-2})
1
0.1
0.01
14 17 8 13 19 18 21 16 12 20 22
Patient

Erklärungen nach §4 Abs. 3 Satz 3, 5, 8 der Promotionsordnung der Fakultät für Biologie

Affidavit

I hereby declare that my thesis entitled: "Quantitative Analysis of Membrane Components using Super-Resolution Microscopy" is the result of my own work.

I did not receive any help or support from commercial consultants. All sources and / or materials applied are listed and specified in the thesis.

Furthermore I verify that the thesis has not been submitted as part of another examination process neither in identical nor in similar form.

Eidesstattliche Erklärung

Hiermit erkläre ich an Eides statt, die Dissertation: „Quantitative Analysis of Membrane Components using Super-Resolution Microscopy", eigenständig, d. h. insbesondere selbständig und ohne Hilfe eines kommerziellen Promotionsberaters, angefertigt und keine anderen, als die von mir angegebenen Quellen und Hilfsmittel verwendet zu haben.

Ich erkläre außerdem, dass die Dissertation weder in gleicher noch in ähnlicher Form bereits in einem anderen Prüfungsverfahren vorgelegen hat.

Würzburg, _____

Sebastian Letschert